

University of Alberta

Experimental Investigation of Ice Floe Stability

by

Karen Elizabeth Dow Ambtman

A thesis submitted to the Faculty of Graduate Studies and Research
in partial fulfillment of the requirements for the degree of

Doctor of Philosophy

in

Water Resources Engineering

Department of Civil and Environmental Engineering

©Karen Elizabeth Dow Ambtman

Fall 2009

Edmonton, Alberta

Permission is hereby granted to the University of Alberta Libraries to reproduce single copies of this thesis and to lend or sell such copies for private, scholarly or scientific research purposes only. Where the thesis is converted to, or otherwise made available in digital form, the University of Alberta will advise potential users of the thesis of these terms.

The author reserves all other publication and other rights in association with the copyright in the thesis and, except as herein before provided, neither the thesis nor any substantial portion thereof may be printed or otherwise reproduced in any material form whatsoever without the author's prior written permission.

Examining Committee

Dr. Faye Hicks, Department of Civil and Environmental Engineering

Dr. Peter Steffler, Department of Civil and Environmental Engineering

Dr. Mark Loewen, Department of Civil and Environmental Engineering

Dr. Alireza Nouri , Department of Civil and Environmental Engineering

Dr. Carlos Lange, Department of Mechanical Engineering

Dr. Yee-Chung Jin, Faculty of Engineering, University of Regina

Dedicated to Erick and Homer:

Here's to the adventure!

ABSTRACT

It is known that discrete ice floes approaching an ice cover from upstream will either contribute to the lengthening of the ice cover, or will become entrained in the flow. Knowledge of the hydrodynamic forces acting on individual ice floes is an important component of any model attempting to predict ice cover progression. Currently ice process models rely on empirical relationships to predict the behaviour of ice floes at the leading edge of an intact ice cover.

Experimental studies were conducted in a re-circulating flume in the T. Blench Hydraulics Laboratory at the University of Alberta to increase the knowledge of the physical behaviour of ice floes in water, and the hydrodynamic forces that act upon them. The dynamic pressure was measured beneath a floating “ice” block for various block thickness-to-depth ratios and flow velocities and leading edge shapes. The effect of block rotation on the resulting pressure distribution was also investigated by tilting the block until its top upstream corner reached the water surface. Digital particle image velocimetry was used also to characterize the velocity field beneath a floating ice block investigating the effect of block thickness and leading edge shape on the resulting velocity field.

A method was developed for predicting the pressure distribution beneath a floating ice block and as well as the submerging forces and moments. A stability analysis was performed to determine the conditions under which a floating block would become entrained through a force – moment analysis. The velocity field

revealed a separation zone forms at the leading edge of the rectangular block which was eliminated by rounding the leading edge of the block. The velocity results were found to be correlated with the resulting pressure reduction beneath the block. This confirms the importance of localized flow behaviour due to flow acceleration and separation on the stability of a block.

The work presented in this thesis presents the first rigorous method for determining ice block stability based on actual flow physics and the first detailed characterization of the velocity field beneath a floating ice block.

ACKNOWLEDGEMENTS

This thesis would not have been possible without the dedication and support of many people. First I would like to express my sincere gratitude to my thesis supervisors, Dr. Faye Hicks and Dr. Peter Steffler for their tremendous support and encouragement. They are wonderful mentors who inspired me to pursue excellence through their dedication, passion for research, valuable advice, attention to detail, and tireless work. I cannot imagine a more perfect supervisory combination!

Thank you to Dr. Mark Loewen for his support and advice in the experimental setup and examining committees. I am deeply grateful to have had the opportunity to work with him as he provided wisdom that significantly contributed to my education.

I would like to acknowledge my thesis review committee for their time, effort and valuable suggestions for this thesis. Their participation on such short notice is greatly appreciated.

I would like to offer a huge thank you to Perry Fedun and Chris Krath without whom the experiments would never have been possible. They provided tremendous technical expertise and emotional support through many moments of frustration. I thank them for their friendship.

Thank you to undergraduate students Brett Howard and Kimberly Alcorn for their assistance in conditioning the flume and for performing the most tedious of tasks.

Thank you to graduate student Moniz Mukto for his invaluable advice on the setup of the particle image velocimetry system and for his hard work in the development of the image analysis software.

I gratefully acknowledge the financial support that was provided through an Alberta Ingenuity Studentship Award, NSERC postgraduate scholarship, R (Larry) Gerard Memorial Graduate Scholarship, and various research and teaching assistantships provided by the University of Alberta. Additional funding for this research was provided by NSERC grants obtained by Dr. Faye Hicks and Dr. Peter Steffler.

I would not be where I was today without the love and support of my wonderful family. To my parents and my sister for always standing by me, to both my grandparents for inspiring me to learn, and to my Hot t'Am Ali's for embracing me as one of their own.

Finally I would like to thank my greatest supporter and my best friend, my husband Erick. Thank you for challenging me, for knowing when to push me and when to hug me, for traveling this path with me, and for your unwavering love and support. Life together is always an adventure.

TABLE OF CONTENTS

CHAPTER 1: INTRODUCTION.....	1
1.1 RESEARCH OBJECTIVES.....	3
1.2 LITERATURE REVIEW	4
1.2.1 Problem Definition.....	4
1.2.2 Current state of knowledge	6
1.2.3 Particle image velocimetry technique	10
1.3 OUTLINE OF THESIS	12
1.4 REFERENCES	18
CHAPTER 2: EXPERIMENTAL INVESTIGATION OF THE PRESSURE DISTRIBUTION BENEATH A FLOATING ICE BLOCK.....	21
2.1 INTRODUCTION	21
2.2 BACKGROUND	23
2.3 EXPERIMENTAL METHODS	25
2.3.1 Rectangular Block, Centerline Pressure Measurements....	25
2.3.2 Rectangular Block, Transverse Measurements	27
2.3.3 Rounded Block, Centerline Pressure.....	28
2.3.4 Data Accuracy and Reproducibility	28
2.4 EXPERIMENTAL RESULTS	28
2.4.1 Rectangular Block, Centerline Pressure Measurements....	29
2.4.2 Rectangular Block, Transverse Measurements	30

2.4.3	Rounded Block, Centerline Pressure.....	31
2.4.4	Manometer Fluctuations.....	32
2.5	DATA ANALYSIS	32
2.5.1	Force and Moment Analysis	37
2.6	DISCUSSION.....	38
2.6.1	Comparison to Previous Research.....	41
2.7	CONCLUSIONS	42
2.8	REFERENCES	75

CHAPTER 3: ANALYSIS OF THE STABILITY OF FLOATING ICE

	BLOCKS.....	77
3.1	INTRODUCTION.....	77
3.2	BACKGROUND ON ICE BLOCK STABILITY.....	79
3.3	EXPERIMENTAL SETUP AND RESULTS	86
3.4	ANALYSIS OF BLOCK STABILITY	90
3.5	DISCUSSION.....	94
3.6	CONCLUSIONS AND RECOMMENDATIONS.....	99
3.7	REFERENCES	114

CHAPTER 4: DPIV INVESTIGATION OF THE FLOW FIELD

	BENEATH A FLOATING ICE BLOCK.....	116
4.1	INTRODUCTION.....	116
4.2	EXPERIMENTAL METHODS	119
4.3	DATA PROCESSING.....	122

4.4	EXPERIMENTAL RESULTS	123
4.4.1	Flow Development	123
4.4.2	Length of Separation Zone (rectangular block cases).....	126
4.4.3	Reynolds Stresses	127
4.4.4	Comparison to pressure distribution	127
4.5	CONCLUSIONS AND RECOMMENDATIONS	129
4.6	REFERENCES	163
 CHAPTER 5: CONCLUSIONS AND RECOMMENDATIONS.....		165
5.1	SUMMARY AND KEY FINDINGS	166
5.2	FUTURE WORK	168
 APPENDIX A: DETAILS FOR PIV STUDY		195
A.1	TIMING SEQUENCE	195
A.2	DATA PROCESSING	196
 APPENDIX B: INVESTIGATION OF ICE BLOCK STABILITY – NUMERICAL MODELING ISSUES.....		215
B.1	INTRODUCTION	215
B.2	DIMENSIONAL ANALYSIS.....	217
B.3	MODEL IMPLEMENTATION	218
B.3.1	Modeling Platform.....	218
B.3.2	Test Case for Ice Block Stability	220
B.3.3	Model Implementation	221

B.4	MODEL RESULTS.....	224
B.4.1	Sensitivity Analysis on Inlet Development Length and Inflow Boundary Condition	224
B.4.2	Sensitivity Analysis on Shape of the Leading Edge of the Ice Cover	226
B.5	SUMMARY AND CONCLUSIONS.....	227
B.6	REFERENCES	236

APPENDIX C: DATA FROM PRESSURE EXPERIMENTS..... 238

LIST OF TABLES

Table 2-1: Rectangular block pressure tap locations, $y = 0$ cm is the centerline of the block.	45
Table 2-2. Summary of experimental data.....	46
Table 2-3: Rounded block pressure tap locations.	48
Table 2-4: Observed change in water surface elevation.	49
Table 2-5: Range in manometer levels observed through each trail.....	50
Table 2-6: Summary of data used for non-dimensionalization of rectangular block data.	51
Table 2-7: Compare the measured minimum pressure to the calculated minimum pressure using Equation [19].	52
Table 2-8: Rectangular block submerging forces, F_s , overturning moments, M_u and location of the resultant submerging force, \bar{x}	53
Table 2-9: Submerging forces, overturning moments and resultant force location for the rounded block cases.	54
Table 3-1: Summary of experimental variables.....	101
Table 3-2: Summary of data used for non-dimensionalization.....	101
Table 3-3: Summary of calculated submerging forces and overturning moments.	101
Table 4-1: Summary of experimental data.....	131
Table 4-2: Summary of variables used to process the images.	131
Table 4-3: Summary of experimental variables from pressure measurements in Dow-Ambtman et al. (2009).....	132

Table A-1: Spurious vectors.	201
Table A-2: Raw pixel displacements.	201
Table C-1: Water Surface Profile for $t/H = 0.05$; Top Block = 52.47 cm; $t = 1.59$ cm; $H = 30.64$ cm.	239
Table C-2: Water Surface Profile for $t/H = 0.15$; Top Block = 58.25 cm; $t = 4.82$ cm; $H = 30.65$ cm.	241
Table C-3: Water Surface Profile for $t/H = 0.25$; Top Block = 55.64 cm; $t = 7.76$ cm; $H = 30.74$ cm.	243
Table C-4: Water Surface Profile for Transverse $t/H = 0.1$; Top Block = 59.25 cm; $t = 2.67$ cm; $H = 29.67$ cm.	245
Table C-5: Water Surface Profile for Transverse $t/H = 0.3$; Top Block = 54.11 cm; $t = 8.13$ cm; $H = 29.56$ cm.	246
Table C-6: Water Surface Profile for Round $t/H = 0.05$; Top Block = 59.1 cm; $t =$ 1.89 cm; $H = 30.45$ cm.	247
Table C-7: Water Surface Profile for Round $t/H = 0.3$; Top Block = 56.18 cm; $t =$ 9.51 cm; $H = 30.43$ cm.	249
Table C-8: Water Surface Profile for Flat $t/H = 0.1$; Top Block = 48.65 cm; $t =$ 3.08 cm; $H = 30.19$ cm.	251
Table C-9: Water Surface Profile for Tilt $t/H = 0.1$; Top Block = 48.42 cm; $t =$ 3.53 cm; $H = 30.38$ cm.	252

LIST OF FIGURES

Figure 1-1: Problem definition sketch.	14
Figure 1-2: Primary modes of ice block entrainment: a) vertical submergence and b) submergence by overturning.	14
Figure 1-3: Evidence of block entrainment from experiment on ice jam formation dynamics (adapted from Healy, 2006).	15
Figure 1-4: Instability observed in field video of breakup on the Athabasca River at Fort McMurray, 2005 (video courtesy of Alberta Environment).	16
Figure 1-5: Field of view of previous DPIV studies with flow separation: a) Huang and Fiedler (1997); b) Higuchi et al. (2006); c) Burgmann and Schroder (2008); d) Agelinchabb and Tachie (2008).	17
Figure 2-1: Problem definition sketch.	55
Figure 2-2: Primary modes of ice block entrainment: a) submergence by overturning and b) vertical submergence.	55
Figure 2-3. Schematic of experimental setup.	56
Figure 2-4. Experimental flume - Ice block setup, looking downstream.	56
Figure 2-5: Rectangular block pressure tap locations as seen from below: solid circles indicate taps used for centerline pressure measurements while hollow circles indicate taps used for the transverse pressure measurements.	57
Figure 2-6: Rounded block profile and pressure tap locations.	58
Figure 2-7: Example of the variation between the two trials for a test run.	58
Figure 2-8: Dynamic pressure measured under the ice block for various thickness- to-depth ratios.	60

Figure 2-9: Dynamic pressures measured for transverse pressure runs.....	61
Figure 2-10: Comparison of pressure measured in the mirror taps from the transverse pressure tests.	62
Figure 2-11: Dynamic Pressure measured from transverse pressure tests plotted longitudinally for various thickness-to-depth ratios.....	63
Figure 2-12: a) Dynamic pressure for rounded block $t/H = 0.06$ with profile of block above b) Dynamic pressure for rounded block $t/H = 0.31$ with profile of block above.	64
Figure 2-13: Comparison of leading edge effects on the dynamic pressure distribution for various thickness-to-depth ratios.....	65
Figure 2-14: Example of the fluctuations observed for a test run in the manometer levels.....	66
Figure 2-15: Definition of pressure zones and variables used for non- dimensionalization of rectangular block data.....	67
Figure 2-16: Measured pressure plateau compared to the calculated venturi pressure.....	67
Figure 2-17: a) Non-dimensionalized pressure distribution for all rectangular test cases; b) Non-dimensional relationship to determine the minimum pressure coefficient for a rectangular block; c) Non-dimensional relationship for the location at which the pressure is midway between the initial and final pressure plateau values for a rectangular block measured from the leading edge.....	69

Figure 2-18: Comparing the measured and predicted pressure distributions for various thickness-to-depth ratios.....	71
Figure 2-19: Approximate profile of the rounded block using a circle of radius 9 cm.....	72
Figure 2-20: Generalized block stability cases: I. Leading edge effects dominated, II. Leading edge partial recovery, III. Leading edge full recovery, and IV. Venturi effects dominated.....	73
Figure 2-21: a) C_{leading} and b) $\frac{\bar{x}}{x_{50}}$ for a rectangular block of length $0.5x_{50} < L < 3x_{50}$	74
Figure 2-22: Comparison of a) predicted force to measured force and b) predicted moment to measured moment per unit width for the rectangular ice block.....	74
Figure 3-1: Problem definition sketch.....	102
Figure 3-2: Progression of sinking instability: a) Block at rest, forces are in perfect balance; b) Flow is introduced, a submerging force due to pressure reduction is created which will pull the block down; c) The critical position where the net buoyancy force and the submerging force are at a maximum; d) Block entrained in the flow is subjected to additional forces.....	102
Figure 3-3: Progression of overturning instability: a) Block at rest, moments are in perfect balance; b) Flow is introduced, a resultant submerging force creates overturning moment which will cause block to rotate; c) The critical position for entrainment; d) Block entrained in the flow, is subjected to additional forces.....	103

Figure 3-4: Instability observed in field video of breakup on the Athabasca River at Fort McMurray.	103
Figure 3-5: Variation of hydrostatic righting moment with block angle of rotation calculated using the experimental data of Table 3-1.	104
Figure 3-6: Schematic of experimental setup (Dow-Ambtman et al., 2009).....	104
Figure 3-7: Rectangular block pressure tap locations, as seen from below.	105
Figure 3-8: Dynamic pressures measured for the tilted block cases.	106
Figure 3-9: a) Non-dimensionalized pressure distribution from Dow-Ambtman et al. (2009) with flat and tilted block data; b) Non-dimensional relationship to determine the minimum pressure coefficient for a rectangular block; c) Non- dimensional relationship for the location at which the pressure is midway between the initial and final pressure plateau values for a rectangular block measured from the leading edge.	108
Figure 3-10: Critical densimetric Froude numbers for sinking cases.	108
Figure 3-11: Comparison of hydrostatic righting moment to overturning moment.	109
Figure 3-12: Comparison of moment analysis to Uzuner and Kennedy (1972) observations.	111
Figure 3-13: Comparison of moment analysis to Larsen (1975) observations. ...	111
Figure 3-14: Comparison of moment analysis to Ashton (1974) relationship....	112
Figure 3-15: Comparison of moment analysis to Daly and Axelson (1990) relationship.	112

Figure 3-16: Critical densimetric Froude numbers from force-moment analysis.	113
Figure 4-1: Schematic of experimental setup.	133
Figure 4-2: Rounded block profile.....	133
Figure 4-3: Schematic of laser system setup: a) in profile; b) in plan.	134
Figure 4-4: Field of view for Case 2: tH01.....	134
Figure 4-5: Location of leading edge for the rectangular block cases.....	135
Figure 4-6: Example of typical seed density achieved in a DPIV image.	135
Figure 4-7: Profiles used in image processing.....	137
Figure 4-8: Mean velocity contours for Case 1: tH005 using a grid distance of 16 with the profile used for processing shown as the dashed line.....	138
Figure 4-9: Mean velocity vectors and contours near the leading edge for Case 1: tH005.	139
Figure 4-10: Mean velocity contours for Case 2: tH01.	140
Figure 4-11: Mean velocity vectors and contours for Case 2: tH01 near the leading edge of the block.	141
Figure 4-12: Mean velocity contours for Case 3: tH005Round.....	142
Figure 4-13: Mean velocity vectors and contours near the leading edge for Case 3: tH005Round.	143
Figure 4-14: Streamlines for the three cases.....	145
Figure 4-15: Mean velocity profile development beneath the block for Case 1:tH005.....	146

Figure 4-16: Mean velocity profile development beneath the block for Case 2:	
tH01.	147
Figure 4-17: Mean velocity profile development beneath the block for Case 3:	
tH005Round.	148
Figure 4-18: Comparison of mean velocity for the three cases.	149
Figure 4-19: Comparison of minimum velocity for the three cases.	149
Figure 4-20: Comparison of maximum velocity for the three cases.	150
Figure 4-21: Comparison of the location of the maximum velocity relative to the bottom of the block.	150
Figure 4-22: Comparison of the location of the minimum velocity relative to the bottom of the block.	151
Figure 4-23: Mean U velocity at the first grid point beneath the block for Case 1:	
tH005.	152
Figure 4-24: Mean U velocity at the first grid point beneath the block for Case 2:	
tH01.	152
Figure 4-25: Number of velocity changes beneath the block detected for Case 1:	
tH005 with a mean of 2.4.	153
Figure 4-26: Number of velocity changes beneath the block detected for Case 2:	
tH01 with a mean of 2.2.	153
Figure 4-27: Instantaneous velocity vectors and vorticity for four consecutive image pairs for Case 1: tH005.	155
Figure 4-28: Instantaneous velocity vectors and vorticity for four consecutive image pairs for Case 2: tH01.	157

Figure 4-29: Reynolds stress for Case 1: tH005: a) contour of stresses; b) maximum Reynolds stress with distance.....	158
Figure 4-30: Reynolds stress for Case 2: tH01: a) a) contour of stresses; b) maximum Reynolds stress with distance.....	159
Figure 4-31: Compare dynamic pressure to maximum, minimum and mean velocity for Case 1: tH005.....	160
Figure 4-32: Compare dynamic pressure to maximum, minimum and mean velocity for Case 2: tH01.....	160
Figure 4-33: Comparison of dynamic pressure to maximum, minimum and mean velocity for Case 3: tH005Round.....	161
Figure 4-34: Comparison of separation zone length to pressure distribution for Case 1: tH005.....	161
Figure 4-35: Comparison of separation zone length to pressure distribution for Case 2: tH01.....	162
Figure A-1: Schematic of laser pulse timings.....	202
Figure A-2: Spurious vector locations for tH005.....	203
Figure A-3: An example of the spurious vector locations tH01.....	203
Figure A-4: Example of locations of spurious vectors detected for tH005Round.	204
Figure A-5: Raw pixel displacements for tH005, grid distance of 16.....	204
Figure A-6: Raw displacements for tH01.....	205
Figure A-7: Raw displacement histogram for tH005Round for a grid distance 16.	205

Figure A-8: Velocity contours for tH005 for a grid distance of 32, 16 and 8.....	206
Figure A-9: Mean velocity contours for tH01 averaged over 100 images for a grid distance of 32, 16 and 8.....	207
Figure A-10: Mean velocity contours for tH005Round averaged over 100 images for a grid distance of 32, 16 and 8.....	208
Figure A-11: Compare maximum, minimum, and mean velocity for tH005.	209
Figure A-12: Maximum, minimum and mean velocity grid size comparison for tH01.....	210
Figure A-13: Comparison of maximum, minimum and mean velocity for tH005Round.....	211
Figure A-14: Velocity vectors at leading edge averaged over 100 images for tH005 at a grid distance of 32, 16 and 8.....	212
Figure A-15: Mean velocity vectors for tH01 averaged over 100 images for a grid distance of 32, 16, and 8.....	213
Figure A-16: Mean velocity vectors at leading edge for tH005Round averaged over 100 images for a grid distance of 32, 16, and 8.....	214
Figure B-1: Defining sketch for ice floe stability problem.....	230
Figure B-2: Model geometry for preliminary simulations.....	231
Figure B-3: YZ plane at edge of ice cover a) before mesh adaption, and b) after mesh adaption.....	232
Figure B-4: Refined mesh solution a) residual plot and b) monitor points on ice cover for pressure.....	233

Figure B-5: Sensitivity of model results to variation in flow development length.	234
Figure B-6: Sensitivity of model results to variation in inlet velocity profile.	234
Figure B-7: Model configuration for testing a beveled leading edge on the ice cover.	235
Figure B-8: Effect of ice leading edge shape on computed under ice pressure distribution.....	235
Figure C-1: Pressure measurements for $t/H = 0.05$	255
Figure C-2: Pressure measurements for $t/H = 0.1$	257
Figure C-3: Pressure measurements for $t/H = 0.15$	260
Figure C-4: Pressure measurements for $t/H = 0.2$	262
Figure C-5: Pressure measurements for $t/H = 0.25$	265
Figure C-6: Pressure measurements for $t/H = 0.3$	267
Figure C-7: Pressure measurements for transverse case $t/H = 0.1$	269
Figure C-8: Pressure measurements for transverse case $t/H = 0.3$	271
Figure C-9: Pressure measurements for rounded block $t/H = 0.05$	274
Figure C-10: Pressure measurements for rounded block $t/H = 0.3$	277
Figure C-11: Pressure measurements for flat block case $t/H = 0.1$	279
Figure C-12: Pressure measurements for tilted block case $t/H = 0.1$	281

LIST OF SYMBOLS

$$a = 0.9989$$

A = ice block plane area

$$b = -1.003$$

b = width of the ice block

$$c = 0.9893$$

C = pressure coefficient

$\bar{C}_{leading}$ = the resultant pressure coefficient from the leading edge pressure effects

C_{min} = the minimum value of the sink coefficient, C , calculated for each test case

$C_{venturi}$ = the value of C at the final pressure plateau near the end of the block

calculated using the venturi pressure

$$d = 0.3914$$

F_2 = critical Froude number of approach flow from Uzuner and Kennedy data

F_a = Froude number of approach flow

F_b = force of buoyancy acting on the block

F_D = densimetric Froude number

$F_{D_{CR}}$ = critical densimetric Froude number

$F_{D_{CR-LEADING}}$ = critical densimetric Froude number for vertical submergence for

leading edge effects dominated case

$F_{D_{CR-VENTURI}}$ = critical densimetric Froude number for vertical submergence for

venturi effects dominated case

$F_{leading}$ = the resultant force from the leading edge pressure

F_s = total submerging force acting on the ice block

$F_{venturi}$ = the resultant force from the venturi pressure

g = acceleration due to gravity

H = approach flow depth

H_u = flow depth beneath the ice block

L = length of the ice block

$M_{leading}$ = the overturning moment caused by the leading edge pressure

M_{max} = maximum hydrostatic righting moment

M_u = overturning moment acting on the ice block

M_{u1} = overturning moment acting on the ice block at angle of rotation θ_1

$M_{venturi}$ = the overturning moment caused by the venturi pressure

P = pressure differential from hydrostatic

$P_{buoyancy}$ = the buoyancy pressure acting on the block

P_{min} = the minimum pressure observed for each test case

$P_{venturi}$ = venturi pressure

Q = flow rate

R = hydrostatic righting moment at angle of rotation

R_a = Reynolds number of the approach flow

R_b = the Reynolds number using the block submerged thickness and the under
block velocity

Re = Reynolds stress

R_{max} = the maximum hydrostatic righting moment

s_i = specific gravity of ice

t = ice block thickness

t_s = submerged ice block thickness

u = turbulent velocity in the x direction

U = mean velocity in the x direction

v = turbulent velocity in the y direction

V = average velocity of the approach flow

V_u = average velocity beneath the ice block

V_{us} =critical submergence velocity

x = distance along the block measured from the block's leading edge

X =distance along flume measured from flume inlet

\bar{x} = location of resultant submerging force measured from the ice block's leading edge

x_{50} = the location at which the pressure is midway between the initial and final pressure plateau values

x_{FOV} = distance in the x direction measured from the edge of the field of view

$\bar{x}_{venturi}$ = the location measured from the leading edge of the block at which the resultant venturi force acts

y = distance across the ice block measured from the block's centerline

y_{FOV} = distance in the y direction measured from the edge of the field of view

z = distance upwards measured from the bottom of the block

ρ_w = density of water

ρ_i = density of ice

θ = angle of block rotation

θ_1 = angle of block rotation when the top upstream corner is at the water surface elevation

θ_2 = angle of block rotation when the top downstream corner is at the water surface elevation

θ_{\max} = the angle of rotation at which the hydrostatic righting moment is a maximum

ξ = non-dimensionalized length scale

ξ_{50} = non-dimensionalized length scale at x_{50}

ψ = streamline

CHAPTER 1: INTRODUCTION

The phenomenon of ice jamming causes many problems as it can be destructive to both lives and property. The process is of major concern to Canadian communities (e.g. Fort McMurray and Peace River) as ice jams can release quickly creating dangerous saves of ice and water. The transport and accumulation of ice is of great importance to the formation of ice jams and is considered one of the more complicated problems in river ice engineering.

It is known that an ice floe approaching an intact ice cover will either come to rest, extending the length of the ice cover, or become entrained. Once an ice floe becomes entrained it can be deposited beneath the intact ice cover contributing to its thickening, potentially leading to the formation of an ice jam. Beltaos (1995) suggested that the leading edge of an ice jam accumulation behaves as a ‘narrow jam’, with floe entrainment and juxtapositioning being the dominant local processes. This theory is supported by the experimental work of Healy and Hicks (2001) who observed this tendency near the leading edge of ice jams forming in a laboratory flume.

Ice floe entrainment is also of particular relevance to ice jam release events. It is likely that large ice blocks are transported under the ice jam and propelled upwards impacting the intact solid ice cover downstream, which cracks and weakens the cover. It has been speculated that these blocks create mechanical leads in the ice cover which can result in the release of the ice jam (Jasek, 2003). Due to the inherent logistical difficulties and safety issues which arise when trying to measure dynamic ice processes in the field, much of the knowledge of these processes is necessarily qualitative. Experimental and numerical work must be relied on to further the understanding of the mechanics of ice transport and accumulation.

There have been some experimental studies examining the stability of a floating ice block upstream of an intact ice cover. Investigations of this phenomenon focused on defining a critical approach velocity or critical densimetric Froude number (based on approach flow velocity and ice block thickness) at which instability was observed (Pariset and Hausser, 1961; Ashton, 1974; Uzuner and Kennedy, 1972; Larsen, 1975; Daly and Axelson, 1990; Hara et al., 1996; Kawai et al., 1997). Uzuner and Kennedy (1972), Larsen (1975), Hara et al. (1996) and Kawai et al. (1997) conducted experiments in which they recorded the critical Froude number at observed block instability. Ashton (1974) developed a relationship for estimating the critical Froude number based on the experiments of others. Daly and Axelson (1990) examined the problem analytically and identified that instability would occur when the submerging forces and moments exceeded the resisting forces and moments. All of these researchers surmised that the instability of the block arises due to a pressure reduction beneath the block caused by flow acceleration and flow separation. It has also been speculated that unsteady flow behavior due to vortex shedding at the leading edge of the block could cause an instantaneous pressure reduction sufficient to destabilize the block.

Because of the devastating nature of ice jam formation and release events, much effort has been put into the development of numerical models that would be able to predict their occurrences. If these models are to successfully predict these phenomena, determining the conditions under which an approaching ice floe becomes entrained is a fundamental component of any model; however current theory forces modellers to rely on the conventional empirical relationships that are based on critical densimetric Froude number. Many of these numerical models developed to predict ice transport and accumulation are one or two dimensional and it is not known if these three dimensional phenomena can be adequately represented in fewer dimensions. Recent research efforts have focused on developing discrete element models, such as the work from Babić et al. (1990) and Hopkins and Daly (2003). These discrete element models attempt to predict the motion of individual ice floes and their interactions often in three dimensions;

however little knowledge exists about the actual physics surrounding an individual ice floe and the hydrodynamic forces that act on it.

This research seeks to further the understanding of the physics of flow under a floating ice block and the hydrodynamic forces that act on it. A series of experiments were carried out in the T. Blench Hydraulics Laboratory in the Natural Resources Engineering Facility at the University of Alberta. The first series of experiments were designed to measure the dynamic pressure distribution beneath a floating ice block under various ice block geometries and approaching flow characteristics to quantify the submerging forces and moments that act on a floating ice block. The second series of experiments were designed to develop a more rigorous method for determining ice block stability criterion. The third series of experiments were designed to characterize the velocity field beneath a floating ice block using particle image velocimetry to correlate the measured velocity fields with the measured pressure distributions and to examine the unsteady flow behaviour at the leading edge of the block. The results of the experimental studies will provide essential validation data for a three dimensional computational fluid dynamics model that can be used to examine a broad range of scenarios.

1.1 RESEARCH OBJECTIVES

The objectives of this research are to:

1. Advance the knowledge of the physical behaviour of ice pieces in flowing water;
2. Quantify the hydrodynamic forces and moments that act on a floating ice block;
3. Develop a more rigorous method for determining ice block stability;
4. Characterize the velocity field beneath a floating ice block;
5. Correlate the velocity field to the resulting pressure reduction beneath a floating ice block;

6. Determine if unsteady flow behaviour at the leading edge of a floating ice block should be considered in determining ice block stability.

1.2 LITERATURE REVIEW

1.2.1 Problem Definition

Figure 1-1 shows a sketch of the problem definition. In this figure, an ice block of width b , length L , and thickness t , has come to rest against a floating obstacle. Here, V refers to the average velocity of the approach flow, H the approach flow depth, V_u the average velocity beneath the ice block, H_u the depth of flow under the block, t_s the submerged thickness of the block and x the distance along the block measured from the leading edge. A dimensional analysis of this problem suggests that for solid blocks of rectangular shape, the critical velocity for submergence, V_{us} , is a function of:

$$V_{us} = f(t, b, L, H, \rho_w, \rho_i, g) \quad [1-1]$$

where ρ_w refers to the density of water, ρ_i the density of ice, and g the gravitational acceleration. These variables can be combined to express in a nondimensional form as:

$$\frac{V_{us}}{\sqrt{gH}} = f\left(\frac{t}{H}, \frac{t}{L}, \frac{L}{b}, s_i\right) \quad [1-2]$$

where s_i refers to the specific gravity of ice (i.e. ρ_i / ρ_w). The validity of this dimensional analysis has been confirmed by Pariset and Hausser (1961), Uzuner and Kennedy (1972) and Chee and Haggag (1978).

Previous investigators examining ice floe entrainment have observed two principal methods of block entrainment. The first method has been termed vertical submergence or “sinking” as pictured in Figure 1-2a. In this method of entrainment the submerging force exceeds the hydrostatic resisting force and the block sinks vertically until it is carried downstream by the flow. The second method has been termed submergence by “underturning” and involves the block rotating completely about its downstream corner as pictured in Figure 1-2b. In this method of entrainment it is the moment that the submerging force creates that causes the block to rotate to entrainment. Another version of underturning has been discussed by some researchers termed “half turning” in which the block begins rotation about its downstream corner but becomes entrained in the flow in that half turned position shown in Figure 1-2b without completing the rotation.

Observations of video evidence taken during an experimental study of ice jam formation dynamics (Healy, 2006) suggested that incoming ice floes approaching an intact ice cover either juxtaposed with the intact ice cover or became entrained in the flow by underturning. Figure 1-3 shows the progression of a block becoming entrained by underturning. In that study, entrained blocks were frequently observed to continue “flipping” along the bottom of the intact ice cover before coming to rest some distance from the leading edge, and contributing to the thickening of the cover. No ice blocks were observed to begin the rotation only to stall and become stable again. No ice blocks were observed to be carried by the flow a significant distance once entrained.

Observations of video evidence from 2005 breakup on the Athabasca River at Fort McMurray, capturing an incoming ice run approaching an intact ice cover, support Jasek’s theories that entrained ice floes can impact the intact ice cover and result in the formation of open leads. In one video obtained by Alberta Environment observers, an open lead was initiated downstream of the leading edge of an intact ice cover with ice blocks observed to surface within the open lead then disappear again at the end. This open lead was observed to grow

significantly within a short period of time, with the size of ice floes appearing in the open lead increasing as the size of the lead grew. Observers of breakup have previously described hearing a loud “rumbling” noise while standing on the river bank looking at an intact ice cover. This supports the experimental observations in Healy (2006) that ice floes once entrained will continue to bump along beneath the intact ice cover until they come to rest.

A third method of submergence was commonly observed in the video from Alberta Environment as shown in Figure 1-4. This is similar to overturning; however, most of the rotation occurs out of the water. Likely this process begins by rotation about the block’s lower downstream corner, but the force of the flow is so great that the block does not have time to complete the rotation before the flow begins to push the block downstream causing the downstream end of the block to be pushed up in the air.

1.2.2 Current state of knowledge

Early investigators examined the problem by attempting to define a critical Froude number at which instability was reached. The approach Froude number, F_a , is defined as:

$$F_a = \frac{V}{\sqrt{gH}} \quad [1-3]$$

Kivisild (1959) was amongst the first to examine this problem and suggested that instability was reached at an approach Froude number of 0.08. Pariset and Hauser (1961) introduced the concept of the “no-spill” condition which suggests that instability is reached when the top upstream corner of the block becomes submerged. They noted that this condition would be exceeded when the upstream velocity head equalled the block’s freeboard, or the thickness of ice that is above the water surface. Michel (1971) extended Pariset and Hauser’s (1961) analysis to

include the effect of block porosity in reducing the block freeboard. This analysis was again extended by Chee and Haggag (1978).

Uzuner and Kennedy (1972) conducted a series of experiments to determine the critical Froude number at instability as a function of t/H , t/L and ρ_i/ρ_w . They observed that blocks within the range $0.1 < t/L < 0.8$ submerged by overturning while thick, short blocks ($t/L > 0.8$) or thin, long blocks ($t/L < 0.1$) submerged by sinking. This was attributed to the dominance of the of flow separation for the shorter blocks and flow acceleration for the longer blocks. They also examined the effect of rounding the block's leading edge to a quarter circle and found that these blocks had a higher critical Froude number. They analyzed the stability through a one dimensional moment analysis and found an empirical moment coefficient that depended on t/L and ρ_i/ρ_w , determined by disregarding t/H . They also employed the "no-spill" condition as the limit of stability. Their analysis had the disadvantage of using many empirical coefficients and only managed to achieve a rough fit to the data.

Ashton (1974) performed a simplified moment analysis using the data of Uzuner and Kennedy (1972), developing a densimetric Froude criterion (based on the block thickness and density) for the limit of stability. He suggested that the overturning instability occurs at a lower critical velocity than required for vertical submergence. Like Uzuner and Kennedy (1972) he based his analysis on the "no spill" criterion and found a dependence on the t/H ratio but thought the t/L ratio to be of little importance. His analysis was considered to be straightforward in application and was found to produce reasonable results in most practical situations (Beltaos, 1995).

Larsen (1975) conducted a series of experiments using paraffin blocks and various flow conditions, recording the critical velocity at which instability was reached. As did Uzuner and Kennedy (1972), Larsen observed submergence by both overturning and sinking. He also observed a third method of submergence for relatively short blocks ($3 < L/t < 15$) with a rounded upstream face, in which the downstream end of the block submerged enough for it to slide beneath the intact ice cover. He attributed this method of submergence to the lack of flow separation at the leading edge of the rounded block and the shifting of the pressure center under the block downstream. He found that the critical velocity for submergence was higher for blocks with a rounded upstream face than for rectangular blocks. He also studied the effect of changing the support of the block from the lower downstream corner to the upper downstream corner, but found that it had little impact on the critical velocity for submergence.

Daly and Axelson (1990) examined the problem through a moment analysis, reasoning that block instability occurs when the overturning moment exceeds the hydrostatic righting moment. They performed a detailed analysis of the hydrostatic righting moment and discounted the previous “no-spill” condition as they found the maximum hydrostatic righting moment to occur at an angle of rotation greater than the “no-spill” angle. They used the experimental data of Uzuner and Kennedy (1972) and Larsen (1975) to fit parameters to an exponential function of t/H in order to determine moment coefficients. They also use experimental data of Ashton (1974); however no experimental data was found in this paper. These parameters were then used to describe the limit of stability in terms of a densimetric Froude number and were found to match the experimentally measured densimetric Froude numbers of Uzuner and Kennedy (1972) to within ± 0.1 with some outliers, but under-predicted the densimetric Froude number for the experimental data of Larsen (1975) and over-predicted the densimetric Froude number for the experimental data of Ashton (1974) which both occurred at densimetric Froude numbers larger than 1.0.

Coutermarsh and McGilvary (1994) attempted to measure the dynamic pressure distribution beneath a floating block under different flow scenarios and angles of attack. Investigators up to this point had assumed a uniform pressure distribution across the width of the block. Coutermarsh and McGilvary (1994) found the pressures to be symmetric about the centerline of the block and in a characteristic “saddle” shape with negative pressures at the leading edge of the block becoming less negative, or positive, where flow reattachment occurred towards the downstream end of the block. They found that, with an increase in the block angle of rotation, the area of negative pressure increased and moved towards the downstream end of the block. They examined stability through a moment analysis, similar to that of Daly and Axelson (1990), employing the use of a moment coefficient. This moment coefficient was found to increase with angle of attack, weakly decrease with an increase in the average velocity of the approach flow, V , and decrease with an increase in the approach flow depth, H . They reduced their stability analysis to the form used by past researchers relating a Froude number to the block instability.

Most recently Kawai et al. (1997) and Hara et al. (1998) examined the movement of ice floes at the leading edge of an ice cover recording the densimetric Froude number at which they submerged and classifying the movement as none, overturning, half turning, sliding and pile up which was scarcely observed. They examined the effect of the leading edge shape of the intact ice cover on ice block entrainment through four different shapes: rectangular, semi-circular, an upward cut of 45° , and a downward cut of 45° . They developed critical curves based on critical Froude number as a function of the block thickness-to-block length ratio.

The more recent investigations of Daly and Axelson (1990) and Coutermarsh and McGilvary (1994) have provided the most physical information and analysis of the problem to this point; however the measured pressure data of Coutermarsh and McGilvary is not retrievable (personal communication, Coutermarsh, 01/05)

and the data available in the published literature is self-contradictory. Without such data it is impossible to take the stability analysis any further, therefore the purpose of the present study was to explore and extend the work of Coutermarsh and McGilvary (1994) to measure the pressure distribution beneath the block and examine the block stability through a force - moment analysis.

1.2.3 Particle image velocimetry technique

Digital Particle Image Velocimetry (DPIV) is a relatively new procedure in fluid mechanics that uses optical imaging techniques to measure fluid velocity vectors at thousands of points in a flow field simultaneously. DPIV is a non-intrusive technique that can be used to measure the two or three dimensional instantaneous velocity field of a fluid. Other flow properties, such as vorticity, turbulent velocities, and turbulent kinetic energy, can be computed from the measured velocity field. DPIV requires the water be seeded with tracer particles, a light source to illuminate the particles and a high speed video camera to capture images spaced a certain time apart. The images are then processed using image analysis software to determine the displacements of the particles from one image to the next and from this the instantaneous velocity fields can be calculated. With recent advancements in the DPIV technique, investigators have begun using DPIV to examine flow separation under various conditions.

Huang and Fiedler (1997) investigated the behavior of the flow developing downstream of a backward-facing step using DPIV, as shown in Figure 1-5a. They observed the flow to separate and reattach some distance downstream of the face of the step and examined the temporal development of the flow to steady state conditions. They suggested that large scale eddies of low frequency dominate the recirculation region after the flow becomes fully developed. They found that fluctuations in reattachment length are governed by vorticity rollup and shedding in the recirculation region and that the reattachment length is a function of Reynolds number. They defined the location of reattachment as the stagnation point of streamline $\psi = 0$.

Higuchi et al (2006) investigated axial flow over a blunt circular cylinder using PIV as shown in Figure 1-5b. As can be seen in this figure, a blunt circular cylinder behaves as a rectangular block in plane view which is similar to a floating ice block. They examined three cases, three different cylinder lengths and observed the same flow pattern for each. They observed a complex flow field with large scale complex eddy motion. They found that the instantaneous shear layer reattachment was far from well defined marked by the unsteady impingement of large scale vortical structures. The mean separation zone actually consisted of complex large-scale flow impinging on the surface in an unsteady manner.

Burgmann and Schroder (2008) investigated the separation zone on the suction side of an SD7003 airfoil using DPIV as shown in Figure 1-5c. The appearance of a separation zone significantly decreases airfoil performance as it decreases lift and increases the drag. They suggested that Kelvin-Helmholtz instabilities excite large vortices at the downstream end of the separation zone which then detach from the recirculation region. They observed that the vortices that form in the reattachment region and travel downstream are highly three-dimensional and time dependent. This quasi-periodic roll up of the shear layer and formation of large vortices leads to what they term “bubble flapping”, i.e. the zone length changed significantly in time. They defined the beginning of the separation region as the point where particle traces significantly deviated from the wall curvature. They found the start of the transition process responsible for the separated shear layer to reattach by examining the point where a significant rise in the growth of the Reynolds shear stress was observed and comparing this to the point at which the shape factor was a maximum. In defining the mean reattachment point, they suggested that using the mean velocity field to define this point should be avoided as it includes the influence of drifting vortices. Instead they divided the instantaneous flow fields into a main recirculation region and a region of shed vortices. The instantaneous “pseudo-reattachment” was determined for each time step and then averaged to determine the mean reattachment length. They found

that this was always significantly smaller than that obtained by analyzing the mean velocity distribution but admitted that this method suffers from certain ambiguity.

Agelinchabb and Tachie (2008) investigated separated flow over two dimensional transverse blocks of square, rectangular and semi-circular cross sections using PIV as shown in Figure 1-5d. They focused on the separation behind the obstacle and the subsequent redevelopment of the flow. They suggest that the strength of the separation zone, the degree of distortion induced by the pressure field at reattachment and subsequent redevelopment downstream of reattachment are a strong function of the geometry of the obstacle. They observed that the flow separates at the upstream edge of the square and rectangular obstacle but separates downstream of the crest for the semi-circular block. They observed a small separation zone on top of the rectangular block close to the upstream edge which is similar to a floating ice block. They defined the reattachment point as the point where the streamwise component of the mean velocity $U \sim 0$ and where dividing streamline reattaches to the floor.

1.3 OUTLINE OF THESIS

This thesis presents an experimental investigation of ice-water hydrodynamics by measuring the pressure distribution beneath a floating ice block, examining the block stability through a force-moment analysis, and measuring the velocity field beneath a floating ice block. Each of the three investigations is presented as a separate chapter. The following is a brief overview of each chapter.

Chapter 2 investigates the pressure distribution beneath a floating ice block through a series of flume experiments. The effect of changing the approach flow velocity, the block's thickness, and the block's leading edge shape are examined with the objective of understanding the submerging forces and moments that act on a floating ice block. Chapter 3 examines the stability of a floating ice block

through a force-moment analysis. It builds on the previous study by extending the results to examine the effect of tilting the block on the pressure distribution and resulting forces and moments. The objective of this chapter was to develop a more rigorous method for determining the stability of a floating block rather than the conventional empirical estimation based on Froude number. Chapter 4 investigates the velocity field beneath a floating ice block using digital particle image velocimetry. The study examines the effect of block thickness and leading edge shape on the resulting velocity field. The objective of this study was to compare the velocity field at the leading edge of the block to the measured pressure distributions and to determine if the unsteady flow behaviour should be considered. Chapter 5 presents a summary of the three contributions presented in chapters 2 to 4, indicating the key findings in each of the studies. Recommendations for future work are included in this chapter.

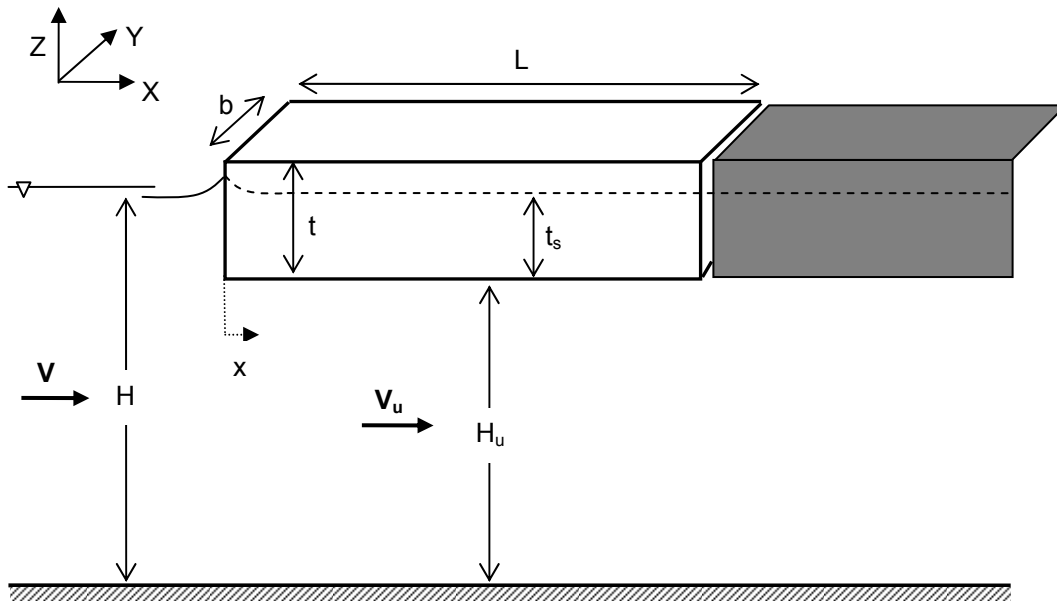


Figure 1-1: Problem definition sketch.

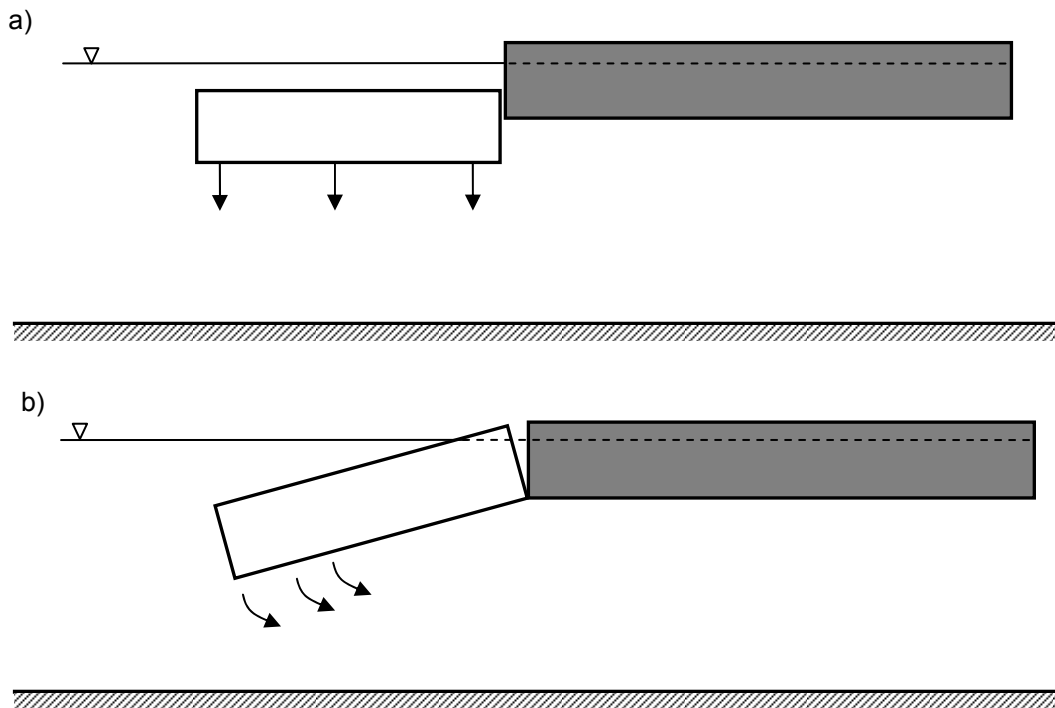


Figure 1-2: Primary modes of ice block entrainment: a) vertical submergence and b) submergence by overturning.

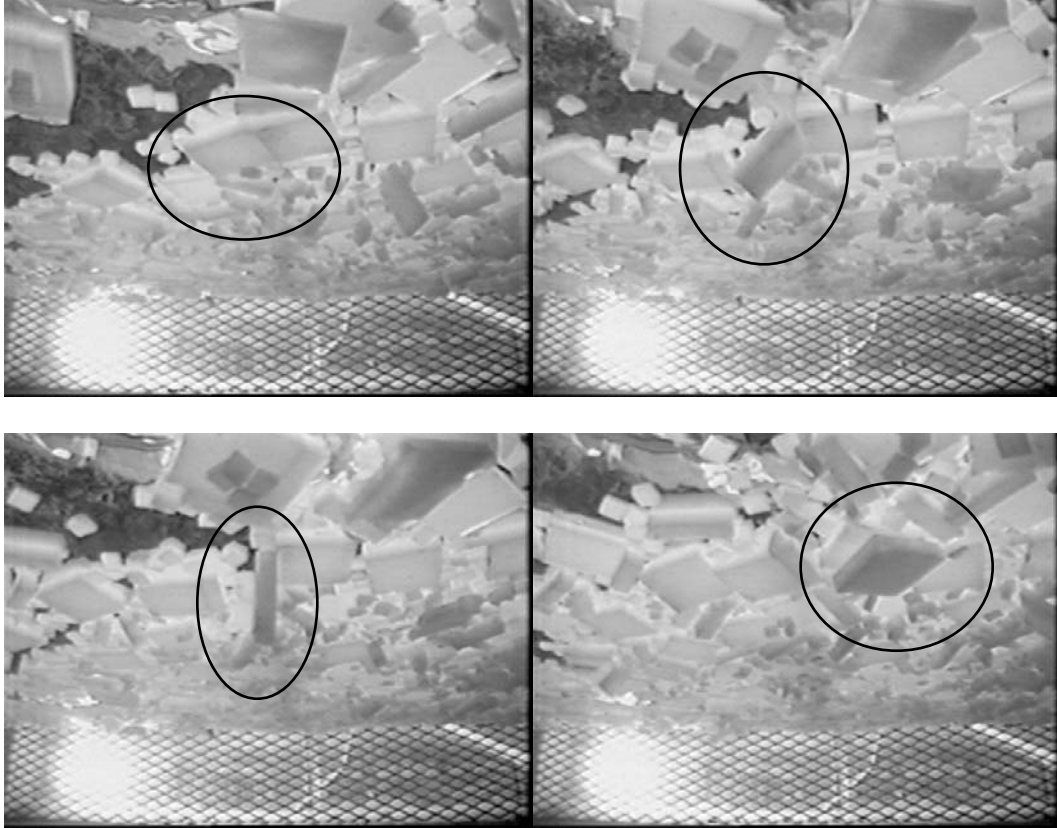


Figure 1-3: Evidence of block entrainment from experiment on ice jam formation dynamics (adapted from Healy, 2006).

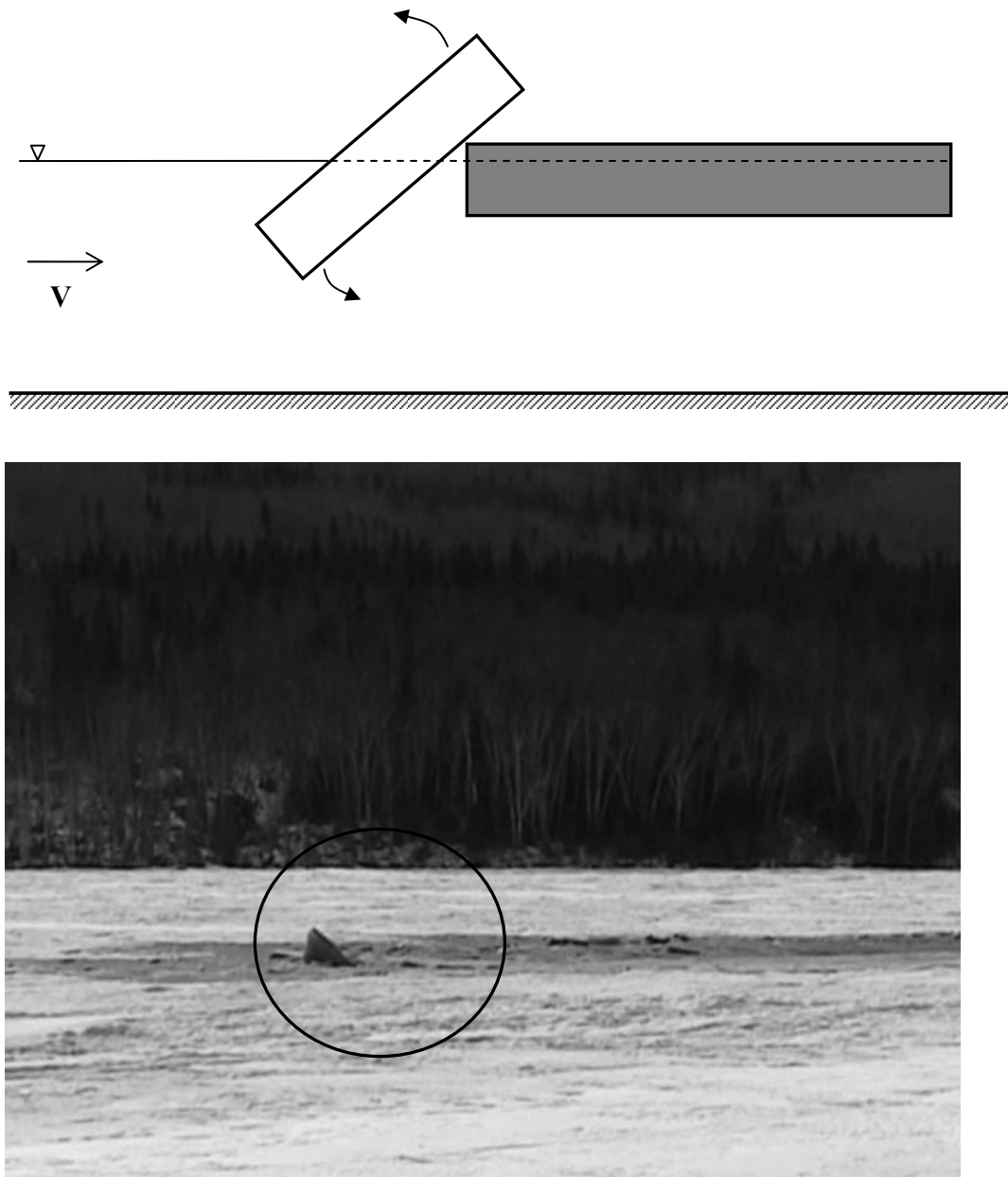


Figure 1-4: Instability observed in field video of breakup on the Athabasca River at Fort McMurray, 2005 (video courtesy of Alberta Environment).

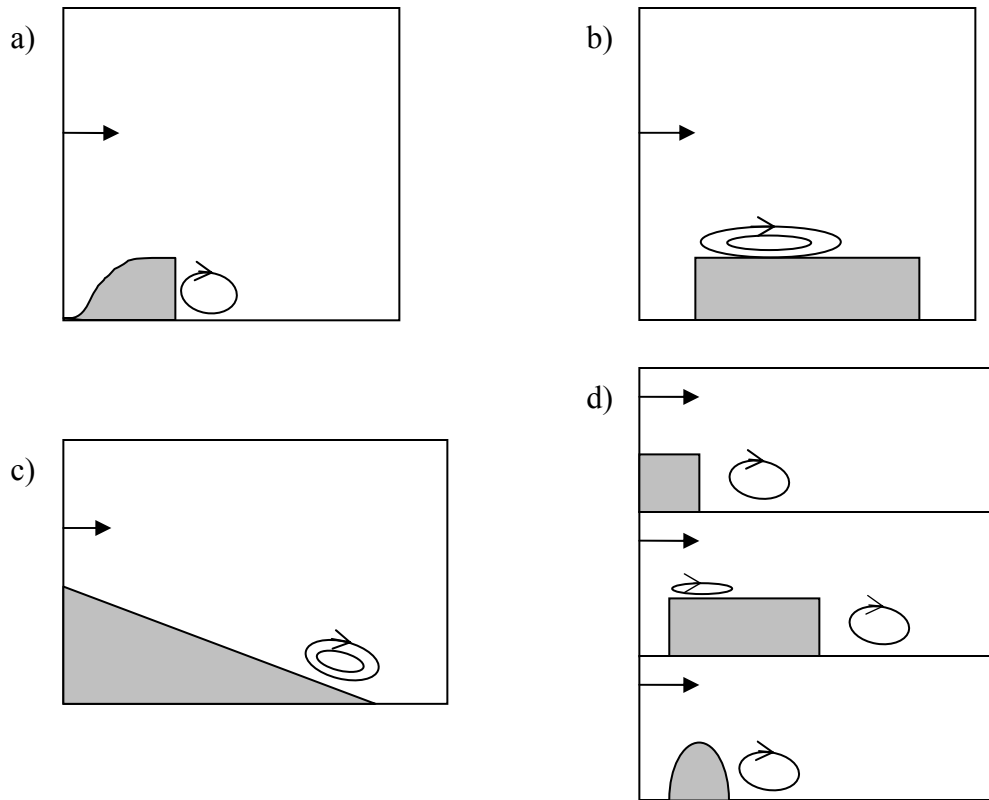


Figure 1-5: Field of view of previous DPIV studies with flow separation: a) Huang and Fiedler (1997); b) Higuchi et al. (2006); c) Burgmann and Schroder (2008); d) Agelinchabb and Tachie (2008).

1.4 REFERENCES

- Agelinchabb, M. and Tachie, M.F., 2008. PIV study of separated and reattached open channel flow over surface mounted blocks. *Journal of Fluids Engineering*, 130(6), 9 pp.
- Ashton, G.D., 1974. Froude criterion for ice-block stability. *Journal of Glaciology*, 13(68), pp. 307-313.
- Babić, M., Shen, H.T., Bjedov, G., 1990. Discrete element simulations of river ice transport. *Proceedings, IAHR Ice Symposium, Espoo, Finland*, pp. 564-574.
- Beltaos, S., 1995. *River Ice Jams*. Water Resources Publications, LLC, Highlands Ranch, Colorado, 372 pp.
- Burgmann, S. and Schröder, W., 2008. Investigation of the vortex induced unsteadiness of a separation bubble via time-resolved and scanning PIV measurements. *Experiments in Fluids*, 45(4), pp. 675-691.
- Chee, S.P. and Haggag, M.R.I., 1978. Instability characteristics of ice blocks, *Proceedings, IAHR Symposium on Ice Problems, Lulea, Sweden, August 7-9, 1978, Vol. II*, pp. 375-388.
- Coutermarsh, B. & McGilvary, W.R., 1991. Pressure distribution of an overturning ice floe. *Proc. 6th Workshop on River Ice*, pp. 143-163.
- Coutermarsh, B.A. and McGilvary, W.R., 1993. Static analysis of floating ice block stability. *Journal of Hydraulic Research*, 31(2), pp. 147-160.
- Coutermarsh, B and McGilvary, R., 1994. Analyzing the stability of floating ice floes. *CRREL Report 94-13*, 19 pp.
- Daly, S.F. and Axelson, K.D., 1990. Stability of floating and submerged blocks. *Journal of Hydraulic Research*, 28(6), pp. 737-752.
- Hara, F., Kawai, T., Hanada, M., Nishihata, A., and Saeki, H., 1996. Movement of ice blocks under an ice cover. *Proceedings of IAHR Ice Symposium, Beijing*, pp. 769-778.

- Healy, D. and Hicks, F., 2001. "Experimental Study of Ice Jam Shoving" Proc. 11th Workshop on River Ice, Ottawa, May, pp. 126-144.
- Healy, D., 2006. Experimental observations on river ice accumulations. Ph.D. Thesis, Department of Civil and Environmental Engineering, University of Alberta, Edmonton, AB, 380 pp.
- Higuchi, H., van Langen, P., Sawada, H., and Tinney, C.E., 2006. Axial flow over a blunt circular cylinder with and without shear layer reattachment. *Journal of Fluids and Structures*, 22(7), pp. 949-959.
- Hopkins, M. and Daly, S., 2003. Recent advances in discrete element modeling of river ice. Proceedings of the 12th workshop on the hydraulics of ice covered rivers, The CGU HS Committee on River Ice Processes and the Environment. June 19-20, 2003, Edmonton, AB, pp. 348-368.
- Huang, H.T. and Fiedler, H.E., 1997. A DPIV study of a starting flow downstream of a backward-facing step. *Experiments in Fluids*, 23(5), pp. 395-404.
- Jasek, M., 2003. Ice jam release and break-up front propagation. Proceedings of the 12th workshop on the hydraulics of ice covered rivers, The CGU HS Committee on River Ice Processes and the Environment. June 19-20, 2003, Edmonton, AB, pp. 348-368.
- Kawai, T., Hara, F., Masaki, S., Nishihata, A., and Saeki, H., 1997. Experimental study on the process of ice jam development. Proceedings of 9th CRIPE, pp. 245-256.
- Kivisild, H.R., 1959. Hanging ice dams, Proceedings of the 8th Congress of the International Association for Hydraulic Research, Vol. 2, paper 23-F, p. 1-30.
- Larsen, P., 1975. Notes on the stability of floating ice blocks. Proceedings of the IAHR third international symposium on ice problems. Hanover, NH, IAHR, pp. 305-313.
- Michel, B., 1971. Winter regime of rivers and lakes, U.S. Army Cold Regions Research and Engineering Laboratory, Cold Regions Science and Engineering Monograph, Pt. III, Sec. Bla., pp. 65-71.

- Pariset, E. and Hausser, R., 1961. Formation and evolution of ice covers on rivers. Transactions of the Engineering Institute of Canada, 5(1), pp. 41-49.
- Uzuner, M.S. and Kennedy, J.F., 1972. Stability of floating ice blocks. Journal of the Hydraulics Division, 98 (HY12), pp. 2117-2133.

CHAPTER 2: EXPERIMENTAL INVESTIGATION OF THE PRESSURE DISTRIBUTION BENEATH A FLOATING ICE BLOCK

2.1 INTRODUCTION

The transport and accumulation of ice is one of the more complicated problems in river ice hydraulics, because of the complex fluid dynamics surrounding individual ice floes. It is of relevance to the physics of ice cover development, ice jam formation and ice jam release. Specific knowledge of the hydrodynamic forces acting on individual ice floes will be an important component of any model which attempts to predict ice cover progression and ice jam events. Currently one dimensional and two dimensional ice process models rely on empirical relationships about leading edge behaviour of incoming ice floes for modelling ice cover progression. Researchers are also beginning to explore discrete element modeling for ice cover development. If we are to advance to modelling individual ice particles with credibility we need to know the forces that act on those particles.

A condensed version of this chapter has been submitted for publication to the Journal Hydraulic of Engineering and is currently under review.

In the practical context of this problem, there are a number of component phenomena to consider. The initial question is: do discrete ice floes approaching an ice cover or accumulation from upstream contribute to lengthening, or will they be entrained in the flow and transported beneath the ice cover? In the case of ice floes approaching an ice jam a further question is whether or not the entrained floe will be transported all the way past the ice jam toe, to be in a position to rise under the intact restraining ice cover.

At present, much of our knowledge of these processes is necessarily qualitative, due to the inherent logistical difficulties and safety issues which arise when trying to measure dynamic ice processes in the field. This is particularly difficult for ice floe transport under ice jams. As a consequence, experimental research is essential to further understand the mechanics of ice floe entrainment and transport, and that is the purpose of this investigation. Here the first phase of this experimental investigation is discussed focusing on the issue of ice floe entrainment at the leading edge of an ice cover or accumulation. Current theory and observations (e.g. Beltaos, 1995) suggest that the leading edge of an ice jam accumulation behaves as a 'narrow jam', with floe entrainment or juxtapositioning being the dominant local processes. Healy and Hicks (2001) observed this same tendency near the leading edge of ice jams forming in a laboratory flume.

Numerous studies have already been conducted to examine the problem of ice block stability. Early investigations of this phenomenon focused on defining the critical approach velocity or critical densimetric Froude number (based on approach flow velocity and block thickness) at which floating ice blocks at the leading edges of intact ice covers are submerged (Pariset and Hausser, 1961; Ashton, 1974; Uzunur and Kennedy, 1972; Larsen, 1975). Daly and Axelson (1990) examined the problem analytically and identified that instability was reached when the overturning moment exceeded the righting moment. Coutermarsh and McGilvary (1991, 1993, 1994) attempted to measure the two

dimensional pressure distribution along the bottom surface of a floating block and found both positive (stabilizing) and negative (destabilizing) pressures acted on the block, with a characteristic saddle shape in the pressure distribution. They observed that changes in flow velocity had little effect on the pressure distribution but primarily changed the pressure magnitude. More recently Hara *et al.* (1996) and Kawai *et al.* (1997) conducted a series of experiments investigating the movement of ice floes at the edge of an ice cover characterizing the movement and the critical densimetric Froude number at movement. They focused on the shape of the edge of the ice cover and the thickness of the ice block.

With recent advances in numerical and experimental technology that allow for better flow visualization and determination, more information about the mechanics of the problem can now be realized. The objective of the first phase of this study was to examine the steady state stability of floating ice blocks that have come to rest against an intact ice cover by measuring the pressure distribution beneath a floating ice block to increase the knowledge of the stability behaviour of floating ice floes and the hydrodynamic forces that act upon them.

2.2 BACKGROUND

It is known that ice floes that come to rest against an intact ice cover will either contribute to the lengthening of the ice cover or become entrained. Figure 2-1 shows a sketch of the problem definition. In this figure, an ice block of width b , length L , and thickness t , has come to rest against a floating obstacle. Here, V refers to the average velocity of the approach flow, H the approach flow depth, V_u the average velocity beneath the ice block, H_u the depth of flow under the block, t_s the submerged thickness of the block and x the distance along the block measured from the leading edge. A dimensional analysis of this problem suggests that for solid blocks of rectangular shape, the critical submergence velocity is a function of:

$$V_{us} = f(t, b, L, H, \rho_w, \rho_i, g) \quad [2-1]$$

where ρ_w refers to the density of water, ρ_i the density of ice, and g the gravitational acceleration. Combining these variables:

$$\frac{V_{us}}{\sqrt{gH}} = f\left(\frac{t}{H}, \frac{t}{L}, \frac{L}{b}, s_i\right) \quad [2-2]$$

where s_i refers to the specific gravity of ice (i.e. ρ_i/ρ_w). The validity of this dimensional analysis has been confirmed by Pariset and Hausser (1961), Uzuner and Kennedy (1972) and Chee and Haggag (1978).

Past investigators have surmised that the submerging forces acting on the block arise from a pressure reduction that is caused by flow acceleration and separation around the ice block while the buoyancy forces resist block entrainment. In the first type of instability, the case of an ice floe sinking pictured in Figure 2-2b. The total submerging force acting on the block can be calculated by integrating the dynamic pressure beneath the block as:

$$F_s = \int_A P(x, y) dA \quad [2-3]$$

where $P(x, y)$ is the pressure differential from hydrostatic, A is the ice block plane area, x is measured from the blocks leading edge along the block, and y is measured across the block.

The second type of instability, the block overturning pictured in Figure 2-2a, arises from the same forces as the sinking criteria; however, it is the moments that these forces create that lead to the instability. Following the practice of previous researchers, the assumption is that the block rotates about its lower downstream

corner. The overturning moment can be calculated from the resulting pressure distribution as:

$$M_u = \int_A P(x, y)(L - x)dA \quad [2-4]$$

The location of the resultant submerging force, measured from the leading edge of the block, can be calculated as:

$$\bar{x} = L - \frac{M_u}{F_s} \quad [2-5]$$

2.3 EXPERIMENTAL METHODS

The pressure distribution beneath a floating ice block was measured under various flow scenarios and various ice block thicknesses. The effect of the shape of the leading edge was also investigated.

The experiments were carried out in the 7.5 m (metre) long re-circulating flume located in the T. Blench Hydraulics Lab at the University of Alberta. This rectangular flume, shown in Figure 2-3, has 0.45 m high side walls and a width of 0.75 m. The flume bed and walls are made of glass to facilitate modern optical measurement techniques, such as particle image velocimetry (which was employed in Phase 3 of this study). The pump is controlled by a variable frequency drive and has a maximum discharge of 150 L/s. Flow rates are measured with a magnetic flow meter.

2.3.1 Rectangular Block, Centerline Pressure Measurements

A hollow rectangular block 50 cm long, 75 cm wide and total thickness of 10.1 cm was constructed of Plexiglas. To enable the simulation of various thicknesses of floating ice, the block was held in position by four threaded rods that allowed for height adjustment, as pictured in Figure 2-4. Approach flow velocity profiles

were measured using a micro-ADV (Acoustic Doppler Velocimeter). The block was outfitted with 20 pressure taps at various positions along the centerline in order to measure the pressure distribution beneath the block. Each pressure tap was connected to a manometer board using ¼" O.D. Tygon tubing. The pressure tap locations are summarized in Table 2-1 and shown in Figure 2-5 as the solid (filled) circles.

The block was positioned in the flume with the leading edge at $X = 4$ m to ensure the flow was fully developed before reaching the block, and to ensure it would not be affected by the outlet. This position was chosen by examining the flow development in the flume through Acoustic Doppler Velocimetry (ADV) measurements of the velocity profiles along the flume length and across the flume width. The block was positioned vertically by adjusting the threaded rods to the desired elevation and using a digital level to ensure the block was level. The effective thickness of the "ice" was determined based upon assuming a typical specific gravity of ice of 0.92 so that the submerged thickness of the block was 0.92 times the thickness of the ice block. The water depth and block height were measured using a point gauge.

De-mineralized water was de-aired for use in the manometer tubing to minimize the occurrence of air bubbles which would compromise the pressure reading. Once the block was positioned, the tubing was flushed to eliminate any air bubbles. To accomplish this, a Nalgene container filled with de-aired water was raised to the ceiling of the lab, creating sufficient head to flush the tubing effectively. While the tubing was being flushed, the underside of the block was wiped clean with a squeegee to remove any air that had become trapped beneath the block. This procedure was repeated as necessary until all of the air was removed from the system.

In each test, the manometer board was tilted to 30° to allow for more accurate readings. A digital camera on a tripod was set up above the manometer board and

a photograph was taken with the flume flow at rest, in order to obtain the initial reading for each manometer. A water surface profile upstream of the block was then measured using a point gauge. The flow was increased to the desired flow rate and allowed to stabilize for five minutes. Continuous photographs of the manometer board were then taken for 30 seconds. A water surface profile upstream of the block was taken again before turning off the flow. Each test was repeated twice.

Six different ice thicknesses were tested at three different flow rates for a total of eighteen tests, as summarized in Table 2-2. The approach flow depth, H , was held approximately constant for the tests to examine a variety of t/H ratios. In this table, F_a refers to the Froude number of the approach flow and R_a is the Reynolds number of the approach flow.

2.3.2 Rectangular Block, Transverse Measurements

The Plexiglas block described above was outfitted with 18 additional pressure taps the locations of which are summarized in Table 2-1 and shown in Figure 2-5 as the empty circles. Four pressure taps were placed on one side of the block centerline to determine the variation in the magnitude of the pressure across the block and whether this variation was important in determining the stability of the block. Two “mirrored” pressure taps were placed on the other side of centerline to determine if the pressure distribution is symmetrical about the centerline of the block. Two of the centerline taps from the centerline pressure measurements tests, Tap # 1 and # 20, were measured again for this series of experiments for a total of 20 pressure measurements. To get an indication of the pressure symmetry and uniformity across the block, two different ice thicknesses were tested at two different flow rates using the procedure described above for a total of four tests, as summarized in Table 2-2. Here “TR” refers to transverse in the run number classification.

2.3.3 Rounded Block, Centerline Pressure

To investigate the effect of the leading edge shape on the resulting pressure distribution beneath the ice block, a hollow Plexiglas block was constructed with a rounded leading edge as shown in Figure 2-6. The block was 51.45 cm long, 75 cm wide, and a total thickness of 14.2 cm. It was held in position by four threaded rods in the same manner as the rectangular block and the thickness was adjusted using the same method described above. The block was outfitted with 20 pressure taps at various positions along the block centerline. The pressure tap locations are also shown in Figure 2-6 and summarized in Table 2-3. In this table, C refers to the circumference, measured from the top upstream edge. Two different ice thicknesses at three different flowrates were tested using the procedure described above for a total of six tests as summarized in Table 2-2. Here the run numbers are labelled “RD” for rounded.

2.3.4 Data Accuracy and Reproducibility

The data accuracy of the dynamic pressures reported depends on how accurately the manometer levels could be read. The analyzed images can be considered accurate to within ± 0.5 mm on the tilted manometer board or ± 2.5 Pa. The reproducibility of the dynamic pressures is determined as the difference between the two trials conducted for each run scenario. One case, $t/H = 0.15$, was chosen to illustrate the typical discrepancy observed between the two trials conducted for each run scenario, shown in Figure 2-7. An average over all the run scenarios indicates that the two trials were within 2.5% with a standard deviation of 1 %.

2.4 EXPERIMENTAL RESULTS

Each of the photographs was analyzed using SigmaScan Pro 5 to determine the water levels in the manometer tubes. The dynamic pressures were then calculated by subtracting the manometer levels for each image from the manometer levels of the initial image for that test, which was taken before the flow was initiated, then adjusted to account for the angle of the manometer board and converted into Pa

units. Each test run had approximately 55 images and the dynamic pressures were averaged over all the images for that test. Each test run was repeated twice so the dynamic pressures were again averaged over the two repeats. Any tubes that were considered to have erroneous data due to air bubbles were omitted from the averaging between the two repeats.

The measured water surface profiles indicated that a change in water elevation upstream of the block was observed to occur once the flow was turned on. This elevation change would affect the hydrostatic pressure and was therefore taken into account by adjusting the manometer levels of the initial image for that test by this amount. The change in water elevation was calculated for each test run by averaging the change in water surface elevation observed at 1, 2 and 3 metres upstream of the block and are summarized in Table 2-4.

2.4.1 Rectangular Block, Centerline Pressure Measurements

The dynamic pressures measured at the centerline for the rectangular block are shown in Figures 2-8a through 2-8f. In general, the shape of the pressure distribution was found to be consistent for all eighteen cases. The distributions exhibit an initial pressure drop to a minimum at the leading edge of the block, then plateaus for a certain distance from the leading edge. The pressure then increases gradually to a second plateau where it remains constant for the remainder of the block length. The first four runs (Figure 2-8a and the lowest flow in Figure 2-8b) appear to have a slightly different shape with no initial pressure plateau; these distributions begin at a minimum pressure and immediately begin recovering to the second pressure plateau. This could be because the pressure taps are not close enough to the leading edge to capture the initial plateau, or it could be that the pressure distributions are of a different shape.

In each of the six cases, the pressure decreased as the flow rate increased. This reflects the increasing flow acceleration beneath the block. As the velocity beneath the block increased the corresponding pressure would decrease. Also,

comparing the six cases, it is evident that as the thickness of the block increases (i.e. as the t/H ratio increases), the pressures beneath the block decrease. A greater thickness of ice produces a larger obstruction to the flow and consequently a larger velocity beneath the block. Also as the ice thickness increases, the length of the initial pressure drop region increases. This can be attributed to the size of the separation recirculation zone at the leading edge of the ice block, which appears to increase with ice thickness. For the case of $t/H = 0.1$ this initial pressure drop region appears to increase with flow rate, as well. It could be that this case demonstrates a transition between the pressure distributions that have no initial plateau and those that do.

2.4.2 Rectangular Block, Transverse Measurements

The dynamic pressures measured transversely on the rectangular block are shown in Figures 2-9a through 2-9d. In these figures, the pressure is plotted for each transverse row of pressure taps where $y = 0$ cm is the centerline of the block and $x = 0$ cm is the leading edge of the block. Note that large air pockets were observed at the leading edge for Run # TR-tH01-Q142 (Figure 2-9b), which likely compromised the $x = 2$ cm data for this run. The purpose of these test runs was to measure the variation in the magnitude of the pressure across the block and to determine if the pressure distribution was symmetrical about the centerline of the block.

Overall, the magnitude of the pressure was found to be relatively constant across the width of the block. As seen in Figures 2-9a-d, there is little variation in the magnitude of the pressure across the block at $x = 40.5$ cm. Near the leading edge of the block, at $x = 2$ and 15 cm, a variation in pressure was observed near the walls of the flume; however, the pressure remained constant within ± 20 cm of the centerline of the block. Vortices were observed to form near the flume walls which likely caused this pressure deviation. This suggests that in terms of a stability analysis the pressure distribution beneath a floating block can be

considered a two dimensional phenomenon as no significant variation in the pressure distribution across the width of the block was observed.

Figure 2-10 shows a comparison of the pressure measured in the “mirrored” pressure taps placed to test for symmetry about the centerline of the block. In this figure, the 45° line indicates a perfect agreement between the two measurements. The pressure measurements were found to match within approximately 7%, with the largest discrepancy observed for the case shown in Figure 2-9b where large air pockets formed at the leading edge of the block. This suggests that the pressure distribution beneath the block is symmetrical about the block’s centerline.

Figure 2-11a and b shows the results from the transverse measurements plotted longitudinal distance. Figure 2-11a can be compared to the rectangular centerline pressure measurements in Figure 2-8b and Figure 2-8b can be compared to the rectangular centerline pressure measurements in Figure 2-8f. The transverse pressure results are consistent with those of the rectangular centerline results with similar distribution shapes and similar pressure magnitudes observed.

2.4.3 Rounded Block, Centerline Pressure

Figures 2-12a and b show the dynamic pressure measured for each of the rounded block tests. In each of the figures, a profile of the block is plotted above the pressure distribution to aid in interpretation, as the profile changes with the submerged thickness of the block. In each of the cases, the pressure is initially positive as the flow hits the block face, then decreases sharply to a minimum pressure where it begins to recover immediately before reaching a final pressure plateau.

These pressure distributions are compared with the corresponding rectangular block cases in Figures 2-13a and b. Note that the block thickness, approach flow depth and velocities are not a perfect match between the rounded and rectangular cases as can be seen in Table 2-2, but some observations can be made about the

differences by plotting the two together. The minimum pressure reached in the rectangular block appears to be lower than that for the rounded block. This can be attributed to the flow separation that occurs at the leading edge of the rectangular block. In contrast, no flow separation was observed for the rounded block. This separation zone would constrict the flow area, leading to a higher velocity beneath the block which would create a lower pressure (or greater pressure drop). For the largest thickness-to-depth ratio (rectangular) case, this minimum pressure extends farther along the block, the initial pressure plateau. This can be attributed to the length of the separation zone that forms at the leading edge of the rectangular block which extends further along the block for the largest thickness-to-depth ratio case. As for the second pressure plateau, both the rectangular and rounded blocks appear to have similar magnitudes particularly in the $t/H = 0.3$ case.

2.4.4 Manometer Fluctuations

One case, $t/H = 0.15$, was chosen to illustrate the range of fluctuations observed in the manometer levels over the duration of each trial. Figure 2-14 illustrates the range of pressures observed for one of the trials due to the fluctuations in the manometer levels over the duration of the test. The variation observed over each trial was on average $\pm 3.5\%$ with a standard deviation of 2%. Note: fluctuations in manometer levels were not recorded for the centerline, rectangular block cases where $t/H = 0.1, 0.2$ and 0.3 or for the transverse, rectangular block case where $t/H = 0.1$. However, based on the variation observed for the cases reported in Table 2-5, the magnitude of the fluctuations were not considered significant enough to repeat these test runs in order to determine the corresponding fluctuations.

2.5 DATA ANALYSIS

When looking at the rectangular block data it is evident that there is a consistent shape for all of the measured pressure distributions. The pressure begins at a minimum which plateaus for some distance which is a function of thickness-to-depth ratio and in some cases flow rate. It then recovers reaching a second pressure plateau if the block is sufficiently long to capture the entire pressure recovery. As shown in Figure 2-15, this general pressure profile shape can be explained by breaking the pressure reduction into two distinct components: a pressure reduction due to venturi effects and a pressure reduction due to leading edge effects.

Venturi Pressure

As the flow goes under the block there is an increase in flow velocity due to the constriction of the flow area caused by the ice block. This pressure reduction is constant over the entire length of the block, as demonstrated by the second pressure plateau, and can be calculated by the difference in the velocity heads from the Bernoulli equation.

$$P_{venturi} = \frac{1}{2} \rho_w V^2 - \frac{1}{2} \rho_w V_u^2 \quad [2-6]$$

where V refers to the average velocity of the approach flow and V_u the average velocity beneath the ice block.

In many of the cases tested, the venturi pressure plateau was reached and measured. For example, all of the rounded block cases reached the venturi pressure and for the rectangular block the first six runs (Figures 2-8a and b) and Runs # tH015-Q79 (Figure 2-8c) and Run # tH02-Q79 (Figure 2-8d) can be considered. These measured pressure plateaus were compared to the calculated venturi pressure based on Equation [2-6] and compared in Figure 2-16. Based on these results, this equation can be considered a good approximation to estimate

the magnitude of the second pressure plateau as these values are within 15% (on average).

Leading Edge Pressure Effects

The pressure reduction due to leading edge effects is caused by the local flow acceleration at the leading edge of the block, as the water accelerates under the block. In the case of the rectangular block there is a separation zone that forms at the leading edge that further constricts the flow, causing a higher velocity, and therefore, a lower pressure.

The results can be combined into a non-dimensional relationship by employing a pressure coefficient of the form:

$$C = \frac{P}{\frac{1}{2}\rho V_u^2} \quad [2-7]$$

where P is the dynamic pressure measurement and V_u is the under ice average velocity. The pressure was non-dimensionalized using the ratio $\frac{C - C_{venturi}}{C_{min} - C_{venturi}}$

where C_{min} is the minimum value of the sink coefficient, C , calculated for each test case and $C_{venturi}$ is the value of C at the final pressure plateau calculated as:

$$C_{venturi} = \frac{P_{venturi}}{\frac{1}{2}\rho V_u^2} = \left(\frac{V^2}{V_u^2} - 1 \right) \quad [2-8]$$

This removes the constant venturi pressure so that the pressure reduction due to the effect of the leading edge remains.

The length scale was non-dimensionalized using the ratio $\frac{\xi}{\xi_{50}}$ where:

$$\xi = \frac{x}{t_s} \quad [2-9]$$

where x is the distance along the block measured from the block's leading edge and t_s is the submerged ice block thickness and:

$$\xi_{50} = \frac{x_{50}}{t_s} \quad [2-10]$$

where x_{50} is the location at which the pressure is midway between the initial and final pressure plateau values, the values of which are summarized in Table 2-6.

Figure 2-17a shows the complete set of pressure distribution data in non-dimensional form, presented as a ratio of $\frac{C - C_{venturi}}{C_{min} - C_{venturi}}$ versus a ratio of $\frac{\xi}{\xi_{50}}$.

The inset in Figure 2-17a shows the figure zoomed in to show the detail in the initial part of the curve. The first run at the lowest flowrate and smallest thickness-to-depth ratio (Run # tH005-Q79) shows a slight deviation from zero at the tail of the curve due to the discrepancy in the measured pressure and the calculated venturi pressure. $\frac{C - C_{venturi}}{C_{min} - C_{venturi}}$ remains at 1.0 until a $\frac{\xi}{\xi_{50}}$ ratio of 0.5

and reaches 0 at a $\frac{\xi}{\xi_{50}}$ ratio of 3.0. A Pulse Cumulative curve is fit to the data between these two points shown in the inset of Figure 2-17a, at a coefficient of determination of 0.97, in the form of:

$$\frac{C - C_{venturi}}{C_{min} - C_{venturi}} = a + b \left(1 - \exp \left(- \frac{\left(\frac{\xi}{\xi_{50}} \right) - d \ln \left(1 - \frac{\sqrt{2}}{2} \right) - c}{d} \right) \right)^2 \quad [2-11]$$

where $a = 0.9989$, $b = -1.003$, $c = 0.9893$, and $d = 0.3914$.

In order to use this figure as a predictive tool for the pressure distribution, relationships for x_{50} and C_{\min} are required. Figure 2-17b shows the variation of $C_{\min} - C_{venturi}$ with Reynolds number calculated using the submerged block thickness and under block velocity, R_b , as:

$$R_b = \frac{V_u t_s}{\nu} \quad [2-12]$$

The values of R_b used are summarized in Table 2-6. In this figure, Run # tH005-Q79 can be considered an outlier as the measured pressure differences were close to the minimum resolution level of the apparatus. A linear regression best fit line to the data points (not including Run # tH005-Q79) shows that it may be more appropriate to simply consider that $C_{\min} - C_{venturi}$ to be constant at -0.7, the mean of the data points. The standard deviation is plotted on the figure and shows that most of the data points fit within \pm one standard deviation. The constant value of -0.7 suggests that the difference between the minimum pressure and the venturi pressure is based solely on the under block velocity.

Figure 2-17c shows the variation of x_{50} as a ratio with the approach flow depth, H , with the Reynolds number, R_b . Initially the x_{50}/H ratio increases linearly with Reynolds number to a Reynolds number of approximately $3.2 \text{ E } +04$ where the curve levels off and becomes constant at an x_{50}/H ratio of 0.95. A linear regression is fit to both sections and is shown in Figure 2-17c. This suggests that after reaching a certain Reynolds number, the location of the midpoint pressure is proportional to the approach flow depth.

Figures 2-17 a-c were used to predict the pressure distributions for the rectangular centerline test cases and are compared to the measured pressure distributions in Figures 2-18a - f. Overall the predictions do a good job of capturing the shape of the distribution and the magnitude of the pressures expected.

Figure 2-17b also leads to a relationship for the calculation of the minimum pressure acting on a floating ice block. $C_{\min} - C_{venturi}$ is known to be -0.7 so combining this with equation 2-6 and the relationship from 2-7, an equation for the minimum pressure can be determined as:

$$P_{\min} = \frac{1}{2}\rho V^2 - 0.85\rho V_u^2 \quad [2-13]$$

which shows that the minimum pressure depends on the difference in velocity heads with more emphasis on the under block velocity. The above equation was used to calculate the minimum pressure and compared with the actual measured minimum pressure in Table 2-7. With the exception of Run # tH005-Q79 for reasons that were previously discussed the predicted minimum pressures match the measured minimum pressures to within 6% (on average).

2.5.1 Force and Moment Analysis

Since the pressure across the block was shown to be symmetric about the centerline of the block and relatively constant across the width of the block, the block width can be neglected in the force and moment calculations as the block width will have no effect on the overall stability calculation. The total submerging force, F_s , can then be calculated using Equation [2-3] modified slightly to neglect the block width and the overturning moment, M_u , can then be calculated using Equation [2-4] modified slightly to neglect the block width. The total submerging force per unit width, the overturning moment per unit width and the location at which the submerging force acts are summarized in Table 2-8 for the rectangular

block cases. As can be seen from the table the submerging force and overturning moment increases with block thickness as well as flowrate.

The submerging force and overturning moment per unit width for the rounded block cases are summarized in Table 2-9. The pressures acting on the underside of the rounded block can be broken into x and y components by approximating the block profile as a circle of radius 9 cm as shown in Figure 2-19. The x-component of the force is significantly smaller than the y-component of the force and therefore has a negligible contribution to the overall overturning moment. When comparing the rounded block cases to the corresponding rectangular block cases, rounding the leading edge of the block decreases the submerging force with a greater effect as the thickness of the block or the flowrate increases. Rounding the leading edge of the block also creates a smaller overturning moment for the same flow conditions, particularly for the thicker block where the rounded block has an overturning moment that is approximately 50% lower than the corresponding rectangular block case. The location of the resultant force is shifted towards the centerline of the block for the rounded case.

2.6 DISCUSSION

Based on the pressure distributions, the block stability can be broken into four possible scenarios: I) Leading edge effects dominated, II) Leading edge partial recovery, III) Leading edge full recovery and IV) Venturi effects dominated.

I. Leading Edge Effects Dominated

If the block is short enough, it will only observe the minimum pressure plateau as shown in Figure 2-20-I. According to the non-dimensionalized pressure distribution in order for this case to occur the length of the block must be less than $0.5x_{50}$. The minimum pressure can be calculated directly from Equation [2-13] and will be uniformly distributed across the bottom of the block. Because the resulting pressure reduction is uniform across the

block, this block is more likely to sink rather than overturn since the center of gravity coincides with the center of pressure.

II. Leading Edge Partial Recovery

In this scenario the block is not long enough to see the pressure reduction recover to the venturi pressure, as shown in Figure 2-20-II. In order for this to occur the length of the block will need to be $0.5x_{50} < L < 3x_{50}$. In this scenario the venturi effects and leading edge effects can be separated.

The venturi pressure can be calculated using Equation [2-6] and the resultant force per unit width, force location and moment per unit width due to the venturi effects can be calculated as:

$$F_{venturi} = P_{venturi} L \quad [2-14]$$

$$\bar{x}_{venturi} = L/2 \quad [2-15]$$

$$M_{venturi} = P_{venturi} L(L/2) \quad [2-16]$$

The leading edge resultant force and moment can be calculated from the non-dimensionalized pressure distribution in Figure 2-17a. From this figure an average pressure coefficient can be calculated as:

$$\bar{C}_{leading} = \frac{\int C_{leading} d\left(\frac{x}{x_{50}}\right)}{\int d\left(\frac{x}{x_{50}}\right)} \quad [2-17]$$

where $C_{leading} = C - C_{venturi}$. The location of the resultant in terms of x_{50} can also be calculated using Figure 2-17a and are summarized in Figure 2-

21. The resultant force per unit width and resultant moment per unit width due to leading edge effects can then be calculated as:

$$F_{leading} = \bar{C}_{leading} \left(\frac{1}{2} \rho V_u^2 \right) (L) \quad [2-18]$$

$$M_{leading} = F_{leading} (L - \bar{x}_{leading}) \quad [2-19]$$

The total submerging force and overturning moment can then be calculated by adding the two components together as:

$$F_s = F_{leading} + F_{venturi} \quad [2-20]$$

$$M_u = M_{leading} + M_{venturi} \quad [2-21]$$

III. Leading Edge Full Recovery

In this scenario the block length is long enough to see the pressure reduction recover to the venturi pressure, as shown in Figure 2-20-III. According to the non-dimensionalized pressure distribution in order for this scenario to occur the length of the block must be in excess of $3x_{50}$. The venturi effects and leading edge effects can be separated in this scenario as well. Equations [2-14] - [2-16] can be used to calculate the venturi effects. From Figure 2-21, $\bar{C}_{leading} = -0.25$ and $\bar{x}_{leading} = 0.62x_{50}$ so the resultant force per unit width and resultant moment per unit width due to leading edge effects can be calculated as:

$$F_{leading} = -0.25 \left(\frac{1}{2} \rho V_u^2 \right) (3x_{50}) \quad [2-22]$$

$$M_{leading} = F_{leading} (L - 0.62x_{50}) \quad [2-23]$$

The total submerging force and overturning moment can be calculated using equations [2-20] and [2-21].

IV. Venturi Pressure Dominated

In this scenario the block is so long that the venturi pressure effects dominate, as shown in Figure 2-20-IV. In order for this to occur $F_{venturi} \gg F_{leading}$. This block is likely to sink as the center of pressure coincides with the center of gravity of the block. The venturi pressure can be calculated using Equation [2-6] above.

The procedures outlined above were used to predict the force and moment for the rectangular block test cases. The rectangular block test cases all fall within the category of leading edge partial recovery or leading edge full recovery. Figure 2-22 compares of the predicted forces and moments to the measured forces and moments where the 45° line indicates a perfect match. On average, the predictions match to within approximately 5%.

2.6.1 Comparison to Previous Research

The pressure distribution results presented in this paper are consistent with previous researcher's observations of block instability. Uzuner and Kennedy (1972) observed short, thick blocks to sink, which corresponds to the leading edge effects dominated case. They also observed long, thin blocks to sink, which corresponds with the venturi pressure dominated case. Both Uzuner and Kennedy (1972) and Larsen (1975) reported higher critical Froude numbers for rounded blocks which is consistent with these findings that the rounded block experiences a significantly lower destabilizing force and moment than the rectangular block under the same flow conditions. Larsen (1975) observed another method of submergence for relatively short blocks with a rounded face in which the downstream end sinks. Examining the pressure distributions of Figures 2-11a and b if the block was short it would only observe the first part of the pressure

distribution and therefore the downstream end of the block would see the largest destabilizing pressure and would be pulled down.

While it is impossible to directly compare these measured pressures to those of Coutermarsh and McGilvary (1994), certain general comparisons can be made based on their published figures. They observed the pressure distribution to be symmetric about the centerline which is consistent with the measurements made here. Similar to the findings here, they observed an increase in the magnitudes of the pressure with increasing thickness-to-depth ratio, appear to observe a weak increase in the overturning moment with an increase in velocity as well and an increase in the overturning moment with increasing block angle of attack. Upon examination of the pressure distributions presented in their paper for zero angle of attack, they found a similar distribution to what was reported here with the pressure beginning at a minimum at the leading edge of the block then recovering to a plateau near the end of the block; however, the magnitudes of these pressures appear flawed as they report positive pressures for the plateau which according to Bernoulli is not possible so likely the value used for their hydrostatic pressure is suspect. There is some evidence in their data plots of an initial pressure plateau, although it is difficult to ascertain from the plots. They also appear to present a rather large variation in the pressure across leading edge of the block while this paper found the pressures to be rather consistent across the block with minor wall effects. Their block was not the full width of their flume so it could be secondary flow effects at the block edges or it could be erroneous data due to air entrainment as these authors experienced a large amount of air entrainment particularly at the leading edge of the block. They also reported large spikes in the pressure distribution for some cases and based on the findings here this is highly implausible and more likely caused by air entrainment.

2.7 CONCLUSIONS

The results of an experimental study to determine the steady state pressure distribution beneath a floating ice block have been presented. These results further the understanding of the hydrodynamic forces that act on a floating ice block, which is an essential component to any model that attempts to predict ice floe entrainment and movement. Until this time, much of the knowledge of these processes was necessarily qualitative.

The centerline pressure distribution was measured for eighteen test cases on a rectangular model ice block. The dynamic pressure was found to decrease for increasing block thickness-to-approach flow depth ratios and increasing flowrates. The pressure distribution along the block began at a minimum pressure that persisted for a certain distance from the leading edge of the block followed by a gradual increase to a second pressure plateau. These results were broken into two separate effects: a pressure reduction due to venturi effects and a pressure reduction due to leading edge effects. The magnitude of the pressure reduction due to venturi effects was approximated using the Bernoulli equation. The pressure reduction due to leading edge effects was non-dimensionalized into a form that can be used to predict the pressure distribution beneath a floating ice block.

The transverse pressure distribution was measured for four test cases on a rectangular model ice block. The pressure was found to be symmetrical about the centerline of the block. The pressure was also found to be relatively constant across the width of the block which indicated that the block width could be neglected and the pressure distribution beneath a floating block can be considered a two dimensional phenomenon.

The effect of the shape of the leading edge was investigated by measuring the centerline pressure distribution for six test cases on a block with a rounded leading edge. The pressure for these cases began at a positive pressure decreasing sharply to a minimum pressure then immediately recovering to the same venturi

pressure plateau as the rectangular block. This emphasized the importance of the flow separation on the pressure reduction due to leading edge effects.

The submerging force and overturning moment were found to increase with increasing thickness-to-depth ratios and increasing flowrate. The rounded block experienced significantly lower submerging force and overturning moment than the rectangular block under the same flow conditions. A generalized force analysis was produced in which the pressure distribution can be broken into four possible scenarios: i) leading edge effects dominated, ii) leading edge partial recovery, iii) leading edge full recovery, and iv) venturi effects dominated. The classification depended on the length of the block and the predicted value of x_{50} . From these, an estimate of the submerging force and overturning moment can be made.

Future work in this area should verify the stability predicted by the generalized stability analysis presented in this paper by floating various model ice blocks to a floating obstacle. The effect of different leading edge shapes should be investigated to attempt to characterize the stability in a general form, as was done in this paper for blocks of rectangular shape. It was shown that once the block begins to become entrained the pressure distribution will change. A model ice block could be constructed to examine the pressure distribution on all block faces as the block becomes entrained. The question still remains: once the ice floe becomes entrained what happens? Further studies examining ice floe entrainment and deposition should be conducted. There was a small indication in this study that ice roughness may affect the pressure distribution beneath a floating ice block and this should be investigated further.

Table 2-1: Rectangular block pressure tap locations, $y = 0$ cm is the centerline of the block.

Centerline Pressure Tap Locations					
Tap #	x (cm)	y (cm)	Tap #	x (cm)	y (cm)
1	1.25	0	11	5.0	-1.25
2	1.5	1.25	12	6.5	0
3	1.75	2.5	13	8.0	0
4	2.0	-1.25	14	10	0
5	2.25	-2.5	15	12.5	0
6	2.5	0	16	15	0
7	3.0	1.25	17	20	0
8	3.5	-1.25	18	25	0
9	4.0	0	19	30.5	0
10	4.5	1.25	20	40.5	0
Transverse Pressure Tap Locations					
Tap #	x (cm)	y (cm)	Tap #	x (cm)	y (cm)
1	2	-1.25	11	15	5
2	2	-34.75	12	15	-15
3	2	-15	13	15	-34.75
4	2	5	14	40.5	-34.75
5	2	15	15	40.5	-15
6	2	27.25	16	40.5	5
7	2	34.75	17	40.5	15
8	15	34.75	18	40.5	27.25
9	15	27.25	19	40.5	34.75
10	15	15	20	40.5	0

Table 2-2. Summary of experimental data.

Rectangular Pressure Measurements								
Run #	t (cm)	H (cm)	t/H	Q (L/s)	V (cm/s)	V_u (cm/s)	F_a	R_a
tH005-Q79	1.59	30.64	0.05	79	34.4	36.2	0.20	1.06E+05
tH005-Q111	1.59	30.64	0.05	111	48.2	50.6	0.28	1.48E+05
tH005-Q142	1.59	30.64	0.05	142	61.8	64.9	0.36	1.89E+05
tH01-Q79	3.29	30.20	0.11	79	35.0	38.9	0.20	1.06E+05
tH01-Q111	3.29	30.20	0.11	111	49.0	54.4	0.28	1.48E+05
tH01-Q142	3.29	30.20	0.11	142	62.7	69.7	0.36	1.89E+05
tH015-Q79	4.82	30.65	0.16	79	34.4	40.2	0.20	1.05E+05
tH015-Q111	4.82	30.65	0.16	111	48.1	56.3	0.28	1.48E+05
tH015-Q142	4.82	30.65	0.16	142	61.7	72.2	0.36	1.89E+05
tH02-Q79	5.96	30.03	0.20	79	35.2	43.1	0.21	1.06E+05
tH02-Q111	5.96	30.03	0.20	111	49.2	60.2	0.29	1.48E+05
tH02-Q142	5.96	30.03	0.20	142	63.1	77.2	0.37	1.90E+05
tH025-Q79	7.76	30.74	0.25	79	34.3	44.7	0.20	1.06E+05
tH025-Q111	7.76	30.74	0.25	111	48.0	62.5	0.28	1.48E+05
tH025-Q142	7.76	30.74	0.25	142	61.6	80.2	0.35	1.89E+05
tH03-Q79	8.33	29.02	0.29	79	36.5	49.6	0.22	1.06E+05
tH03-Q111	8.33	29.02	0.29	111	51.0	69.3	0.30	1.48E+05
tH03-Q142	8.33	29.02	0.29	142	65.3	88.8	0.39	1.90E+05
Transverse Pressure Measurements								
Run #	t (cm)	H (cm)	t/H	Q (L/s)	V (cm/s)	V_u (cm/s)	F_a	R_a
TR-tH01-Q79	2.67	29.67	0.09	79	35.67	38.78	0.21	1.06E+05
TR-tH01-Q142	2.67	29.67	0.09	142	64.11	69.58	0.38	1.90E+05
TR-tH03-Q79	8.13	29.56	0.28	79	35.62	47.75	0.21	1.05E+05
TR-tH03-Q142	8.13	29.56	0.28	142	63.35	85.67	0.37	1.87E+05
Rounded Block Pressure Measurements								

Run #	t (cm)	H (cm)	t/H	Q (L/s)	V (cm/s)	V_u (cm/s)	F_a	R_a
RD-tH005-Q79	1.89	30.45	0.06	79	34.8	36.8	0.2	1.06E+05
RD-tH005-Q111	1.89	30.45	0.06	111	48.7	51.4	0.3	1.48E+05
RD-tH005-Q142	1.89	30.45	0.06	142	62.7	66.0	0.4	1.91E+05
RD-tH03-Q79	9.51	30.43	0.31	79	34.7	48.8	0.2	1.06E+05
RD-tH03-Q111	9.51	30.43	0.31	111	48.6	68.1	0.3	1.48E+05
RD-tH03-Q142	9.51	30.43	0.31	142	62.2	87.3	0.4	1.89E+05

Table 2-3: Rounded block pressure tap locations.

Tap #	C (cm)	x (cm)	z (cm)	Tap #	C (cm)	x (cm)	z (cm)
1	4	0.075	10.025	11	21.15	11	0
2	8	0.575	6.075	12	22.15	12	0
3	10	1.375	4.225	13	23.15	13	0
4	12	2.55	2.65	14	24.15	14	0
5	14	4.075	1.3	15	26.15	16	0
6	16	5.875	0.5	16	28.15	18	0
7	17	6.85	0.25	17	30.15	20	0
8	18	7.85	0.1	18	35.15	25	0
9	19	8.85	0.025	19	40.15	30	0
10	20.15	10	0	20	50.15	40	0

Table 2-4: Observed change in water surface elevation.

Run #	ΔH (cm)	Run #	ΔH (cm)
tH005-Q79	-0.08	tH025-Q142	0.18
tH005-Q111	-0.12	tH03-Q79	0.04
tH005-Q142	-0.17	tH03-Q111	0.17
tH01-Q79	-0.07	tH03-Q142	0.30
tH01-Q111	-0.07	TR-tH01-Q79	-0.09
tH01-Q142	-0.11	TR-tH01-Q142	-0.13
tH015-Q79	-0.02	TR- tH03-Q79	0.04
tH015-Q111	-0.03	TR- tH03-Q142	0.30
tH015-Q142	-0.04	RD-tH005-Q79	-0.10
tH02-Q79	0.00	RD-tH005-Q111	-0.14
tH02-Q111	0.01	RD-tH005-Q142	-0.25
tH02-Q142	0.06	RD-tH03-Q79	-0.02
tH025-Q79	0.03	RD-tH03-Q111	-0.03
tH025-Q111	0.06	RD-tH03-Q142	0.01

Table 2-5: Range in manometer levels observed through each trail.

Run #	+/-	Run #	+/-
tH005Q79 - Trial 1	7.4%	tH025Q142 - Trial 2	1.8%
tH005Q79 - Trial 2	10.4%	TR - tH03Q79 - Trial 1	3.0%
tH005Q111 - Trial 1	3.4%	TR - tH03Q79 - Trial 2	3.1%
tH005Q111 - Trial 2	3.6%	TR - tH03Q142 - Trial 1	2.2%
tH005Q142 - Trial 1	3.1%	TR - tH03Q142 - Trial 2	2.3%
tH005Q142 - Trial 2	3.1%	RD - tH005Q79 - Trial 1	8.8%
tH015Q79 - Trial 1	3.9%	RD - tH005Q79 - Trial 2	6.7%
tH015Q79 - Trial 2	3.3%	RD - tH005Q111 - Trial 1	4.8%
tH015Q111 - Trial 1	2.7%	RD - tH005Q111 - Trial 2	3.9%
tH015Q111 - Trial 2	3.0%	RD - tH005Q142 - Trial 1	2.2%
tH015Q142 - Trial 1	2.4%	RD - tH005Q142 - Trial 2	2.0%
tH015Q142 - Trial 2	1.9%	RD - tH03Q79 - Trial 1	2.7%
tH025Q79 - Trial 1	2.2%	RD - tH03Q79 - Trial 2	3.5%
tH025Q79 - Trial 2	2.2%	RD - tH03Q111 - Trial 1	2.1%
tH025Q111 - Trial 1	2.3%	RD - tH03Q111 - Trial 2	1.8%
tH025Q111 - Trial 2	2.1%	RD - tH03Q142 - Trial 1	3.1%
tH025Q142 - Trial 1	2.1%	RD - tH03Q142 - Trial 2	2.7%

Table 2-6: Summary of data used for non-dimensionalization of rectangular block data.

<i>Run #</i>	x_{50} (cm)	R_b
tH005-Q79	2.1	5.29E+03
tH005-Q111	4.3	7.40E+03
tH005-Q142	6.0	9.49E+03
tH01-Q79	5.4	1.18E+04
tH01-Q111	13.1	1.65E+04
tH01-Q142	18.9	2.11E+04
tH015-Q79	16.8	1.78E+04
tH015-Q111	23.1	2.49E+04
tH015-Q142	24.1	3.20E+04
tH02-Q79	25.0	2.36E+04
tH02-Q111	26.0	3.30E+04
tH02-Q142	27.3	4.23E+04
tH025-Q79	25.0	3.19E+04
tH025-Q111	30.3	4.47E+04
tH025-Q142	28.8	5.73E+04
tH03-Q79	29.0	3.80E+04
tH03-Q111	28.3	5.31E+04
tH03-Q142	27.5	6.80E+04

Table 2-7: Compare the measured minimum pressure to the calculated minimum pressure using Equation [19].

Run #	Measured P_{\min} (Pa)	Calculated P_{\min} (Pa)	Difference
tH005-Q79	-34.4	-51.9	51%
tH005-Q111	-111.8	-101.6	-9%
tH005-Q142	-159.3	-167.2	5%
tH01-Q79	-78.9	-67.2	-15%
tH01-Q111	-131.7	-131.9	0%
tH01-Q142	-201.2	-216.5	8%
tH015-Q79	-75.4	-78.3	4%
tH015-Q111	-142.8	-153.3	7%
tH015-Q142	-226.3	-252.2	11%
tH02-Q79	-92.7	-95.7	3%
tH02-Q111	-185.6	-187.1	1%
tH02-Q142	-312.8	-307.8	-2%
tH025-Q79	-121.3	-111.0	-9%
tH025-Q111	-208.1	-217.2	4%
tH025-Q142	-369.7	-357.0	-3%
tH03-Q79	-146.8	-142.3	-3%
tH03-Q111	-295.7	-278.4	-6%
tH03-Q142	-494.2	-456.6	-8%

Table 2-8: Rectangular block submerging forces, F_s , overturning moments, M_u and location of the resultant submerging force, \bar{x} .

Run #	F_s (N / m)	M_u (N-m/m)	\bar{x} (cm)
tH005-Q79	-2.1	0.7	15.9
tH005-Q111	-10.3	3.6	15.1
tH005-Q142	-19.9	6.7	16.2
tH01-Q79	-11.6	3.7	18.1
tH01-Q111	-31.0	9.9	18.1
tH01-Q142	-56.8	18.1	18.1
tH015-Q79	-18.7	6.2	17.0
tH015-Q111	-47.6	14.6	19.2
tH015-Q142	-79.5	23.8	20.1
tH02-Q79	-32.4	9.7	20.1
tH02-Q111	-67.0	19.9	20.4
tH02-Q142	-115.3	34.1	20.4
tH025-Q79	-42.6	12.8	20.0
tH025-Q111	-82.4	23.4	21.6
tH025-Q142	-142.9	41.3	21.1
tH03-Q79	-57.0	16.5	21.1
tH03-Q111	-113.4	32.8	21.1
tH03-Q142	-185.8	54.4	20.7

Table 2-9: Submerging forces, overturning moments and resultant force location for the rounded block cases.

Run #	$F_s y$ (N / m)	$F_s x$ (N / m)	M_u (N-m/m)	\bar{x} (cm)
RD-tH005-Q79	-2.2	0.07	0.6	22.8
RD-tH005-Q111	-9.5	-0.01	2.7	21.9
RD-tH005-Q142	-13.2	0.01	3.8	21.6
RD-tH03-Q79	-27.9	-1.44	7.6	22.7
RD-tH03-Q111	-58.3	-2.83	15.5	23.5
RD-tH03-Q142	-98.1	-5.09	26.5	23.1

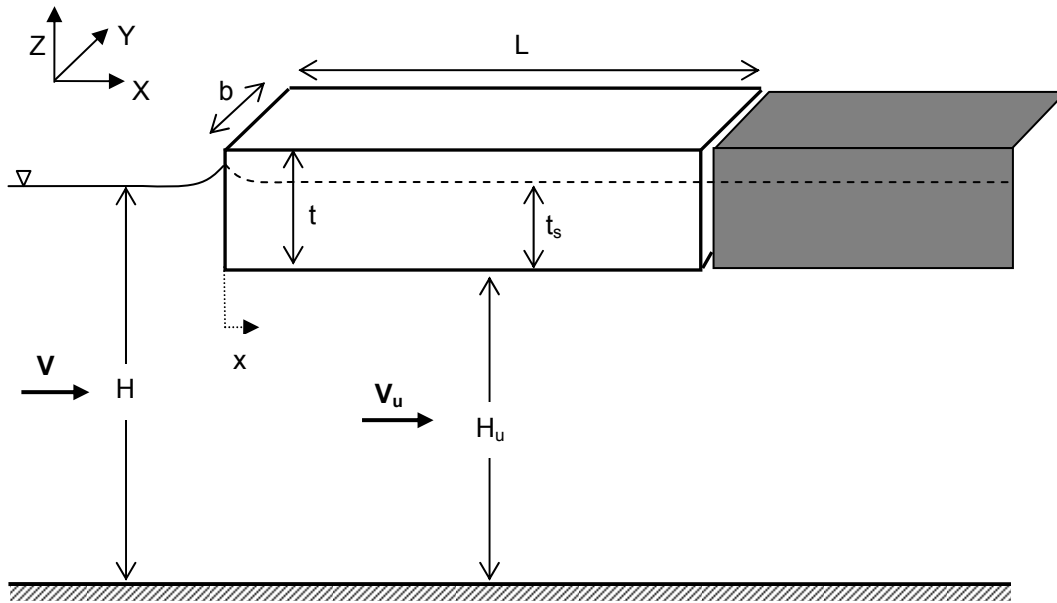


Figure 2-1: Problem definition sketch.

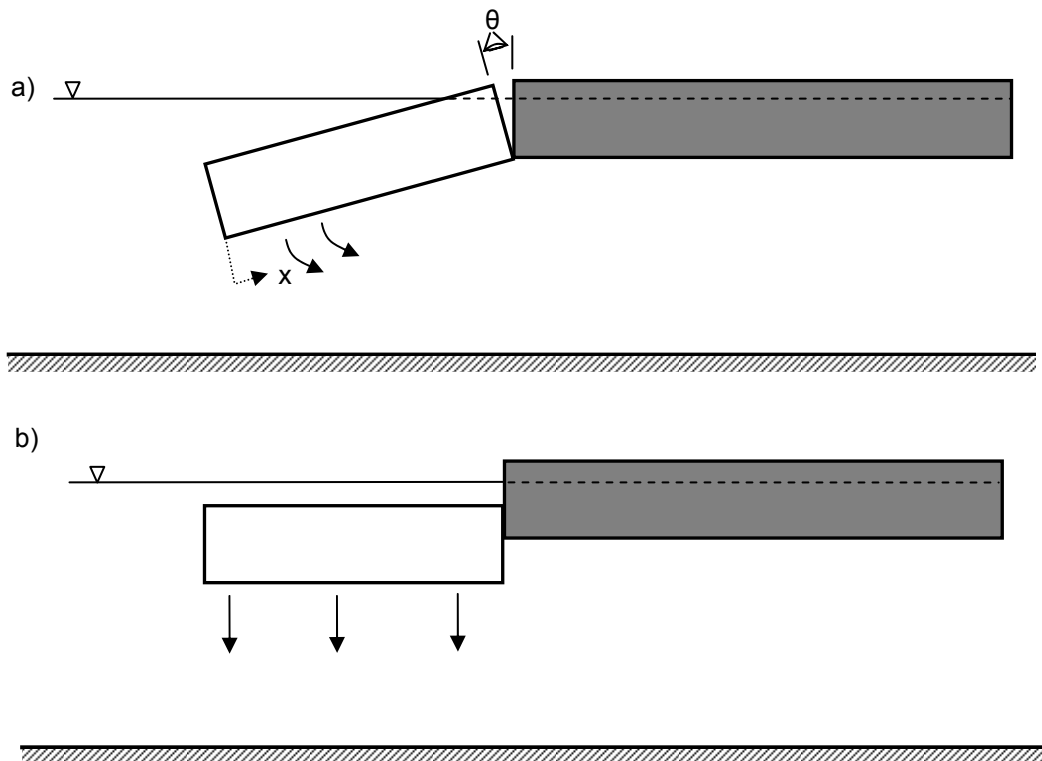


Figure 2-2: Primary modes of ice block entrainment: a) submergence by overturning and b) vertical submergence.

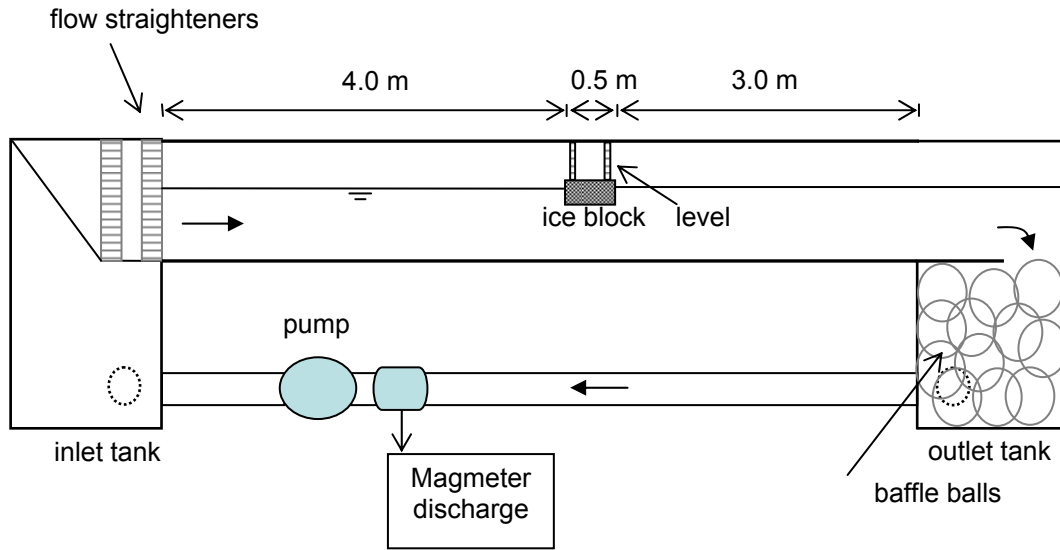


Figure 2-3. Schematic of experimental setup.

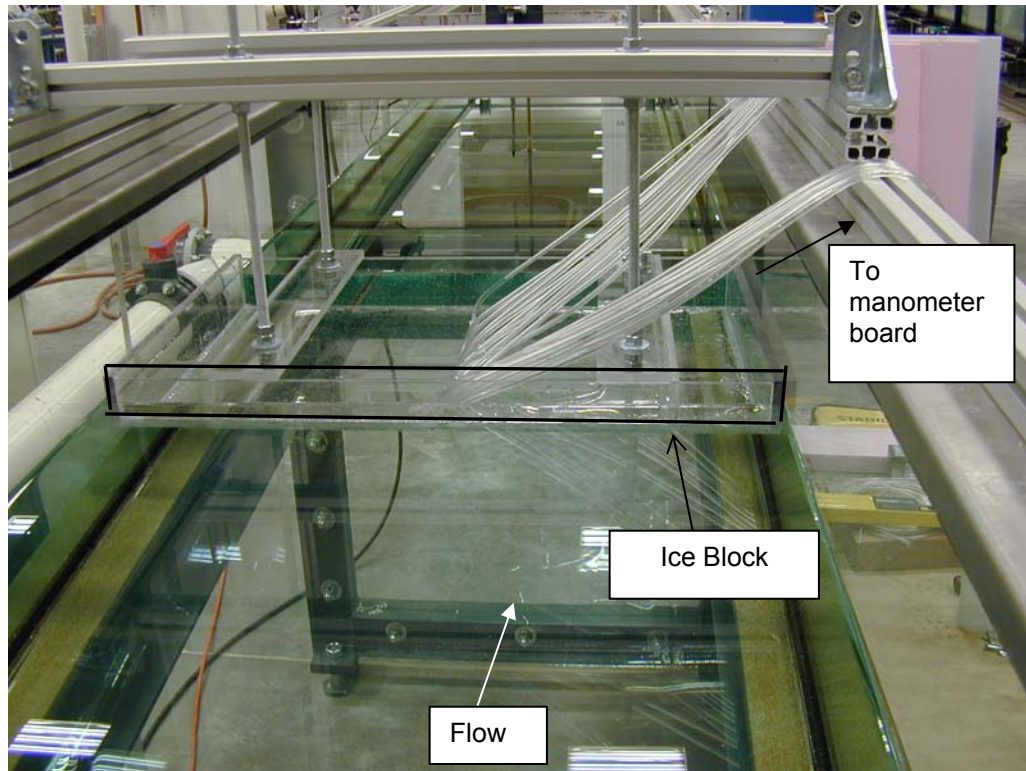


Figure 2-4. Experimental flume - Ice block setup, looking downstream.

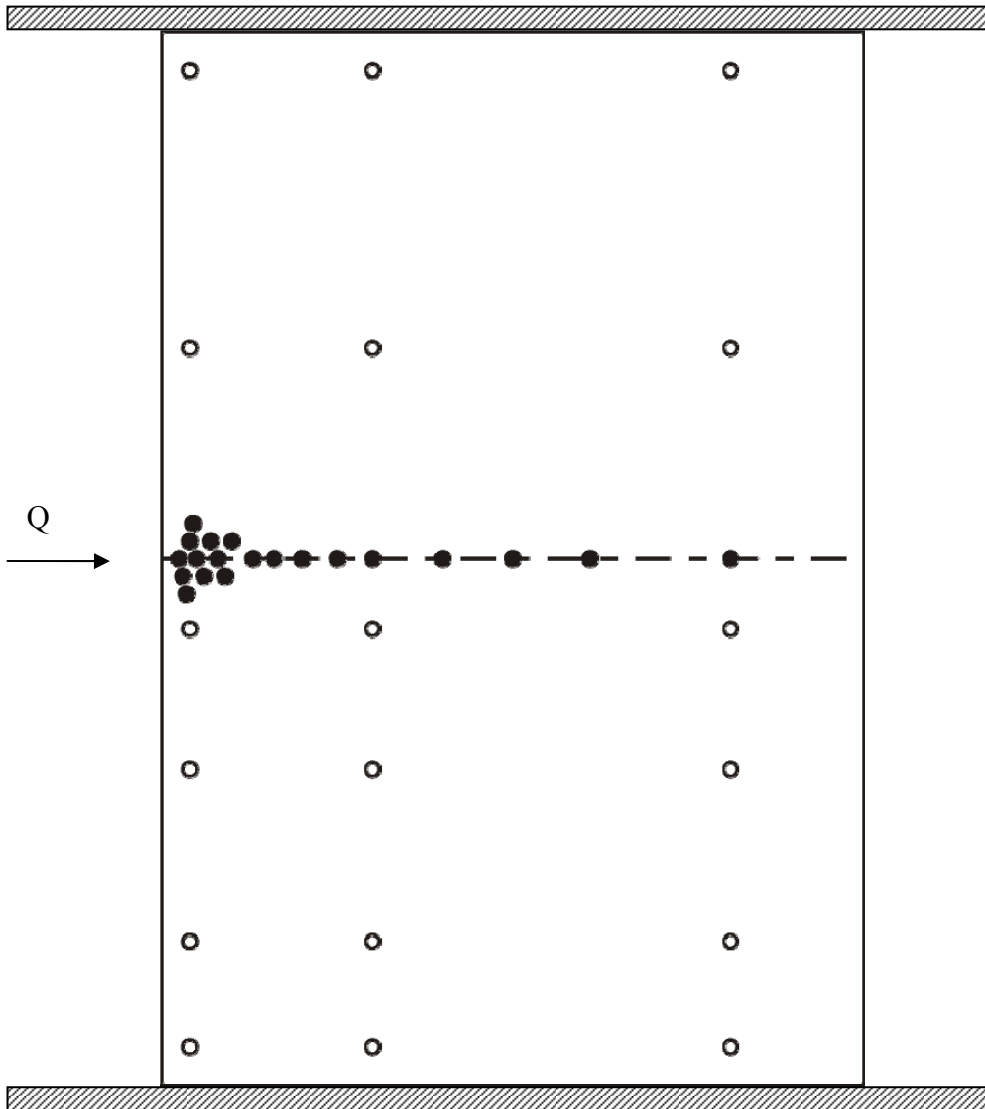


Figure 2-5: Rectangular block pressure tap locations as seen from below: solid circles indicate taps used for centerline pressure measurements while hollow circles indicate taps used for the transverse pressure measurements.

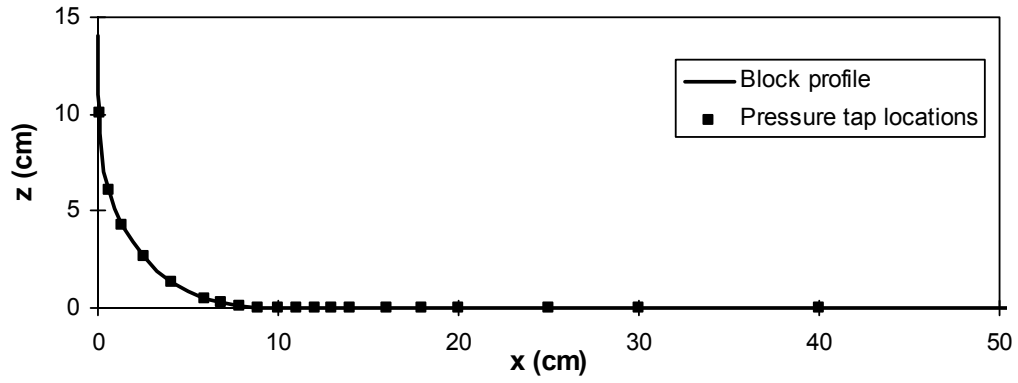


Figure 2-6: Rounded block profile and pressure tap locations.

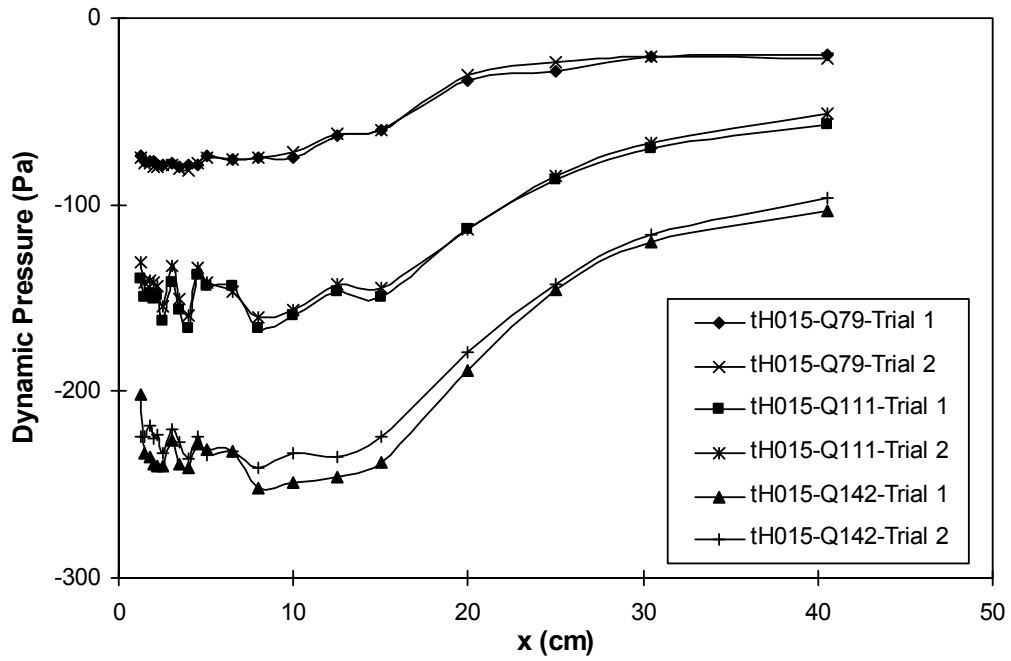
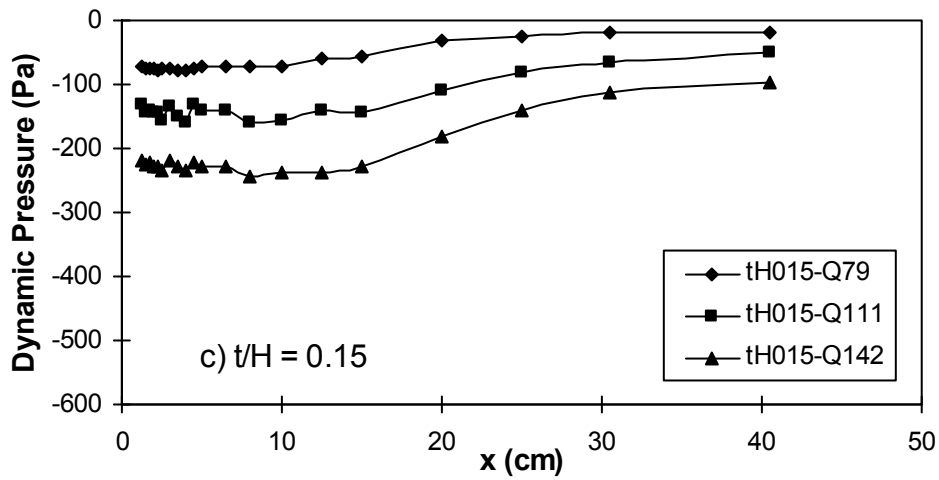
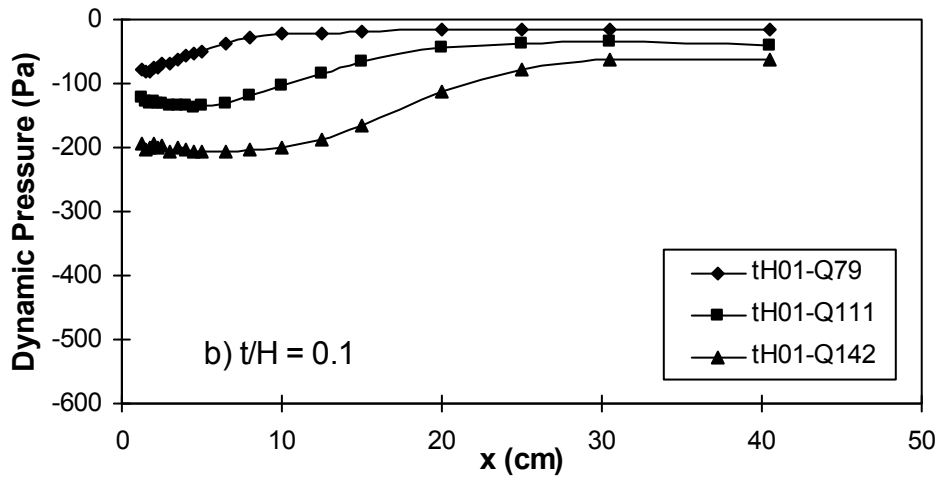
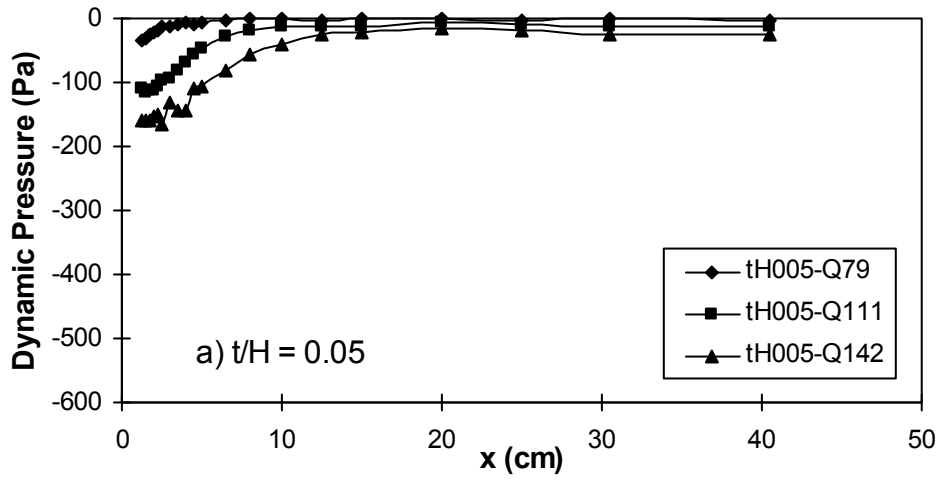


Figure 2-7: Example of the variation between the two trials for a test run.



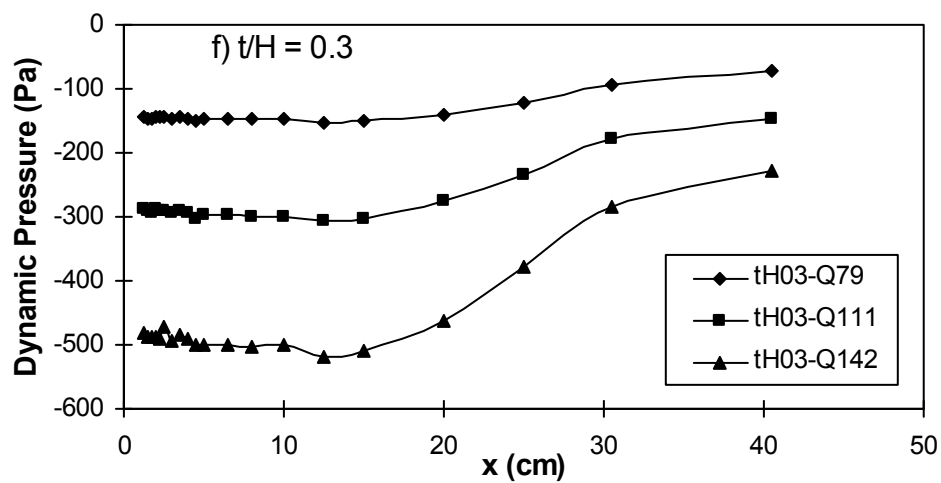
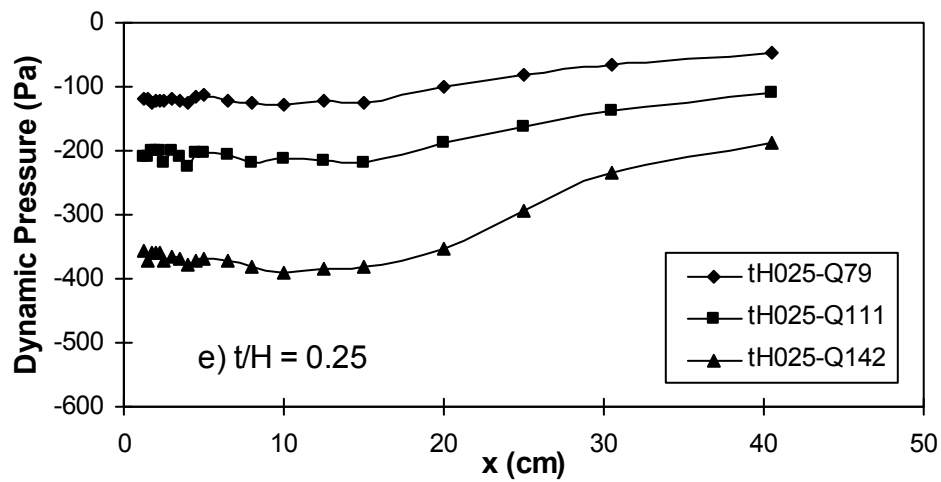
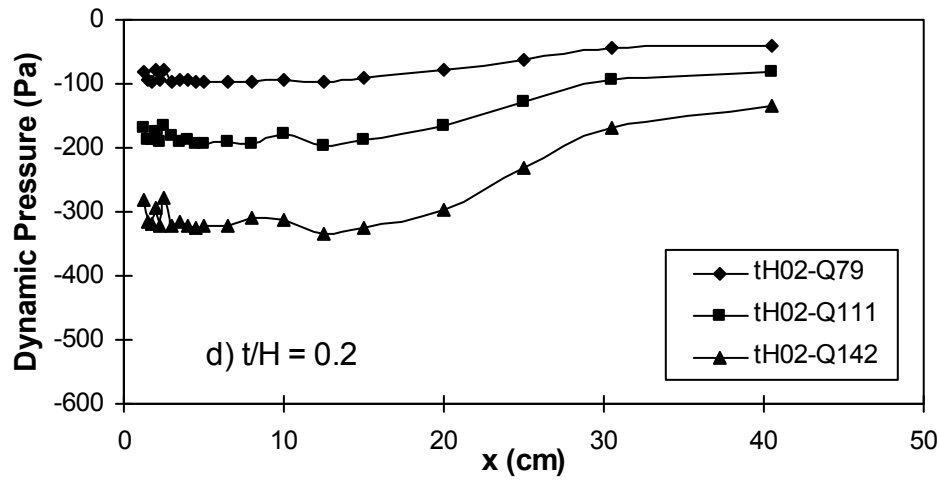


Figure 2-8: Dynamic pressure measured under the ice block for various thickness-to-depth ratios

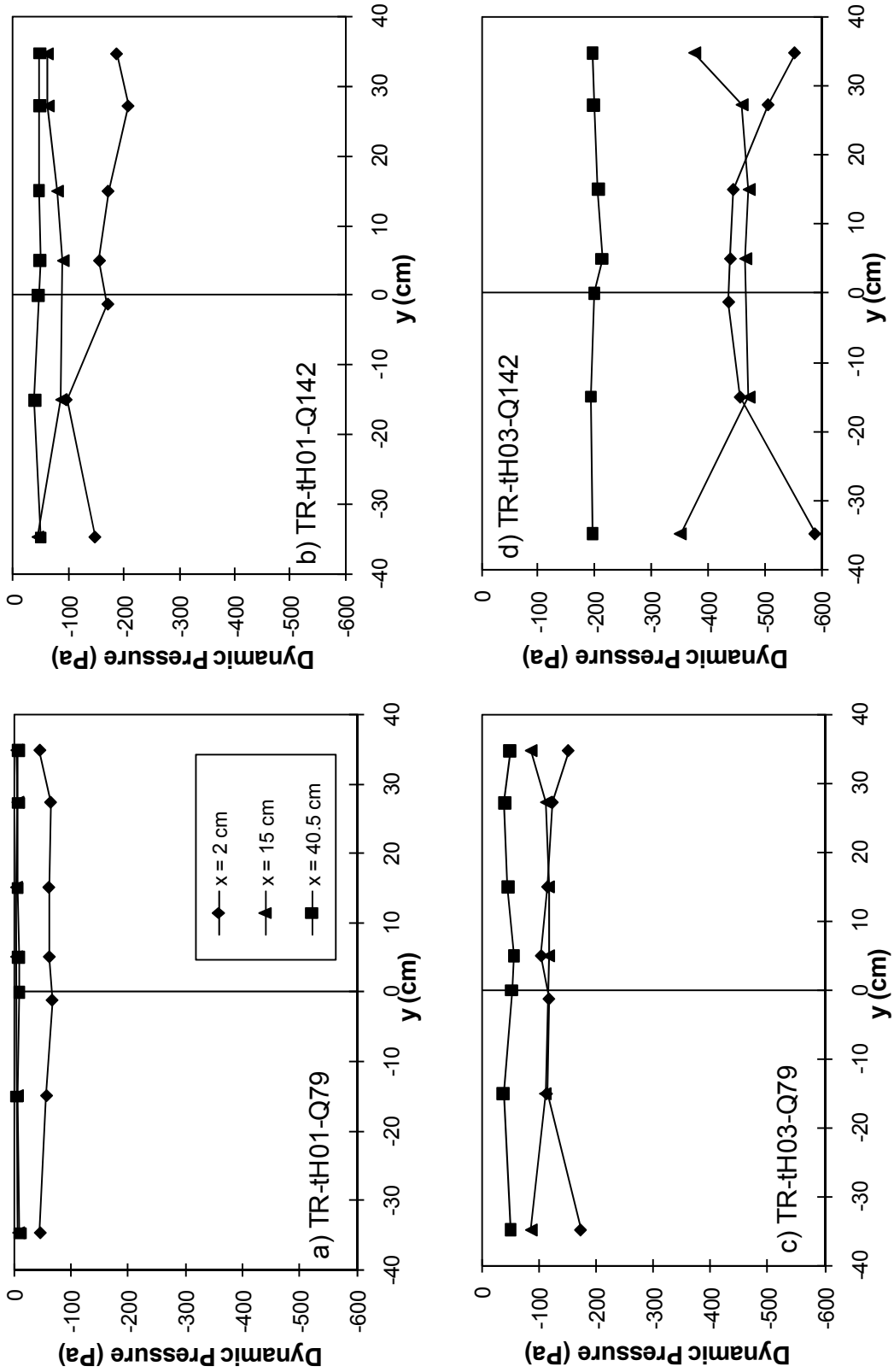


Figure 2-9: Dynamic pressures measured for transverse pressure runs.

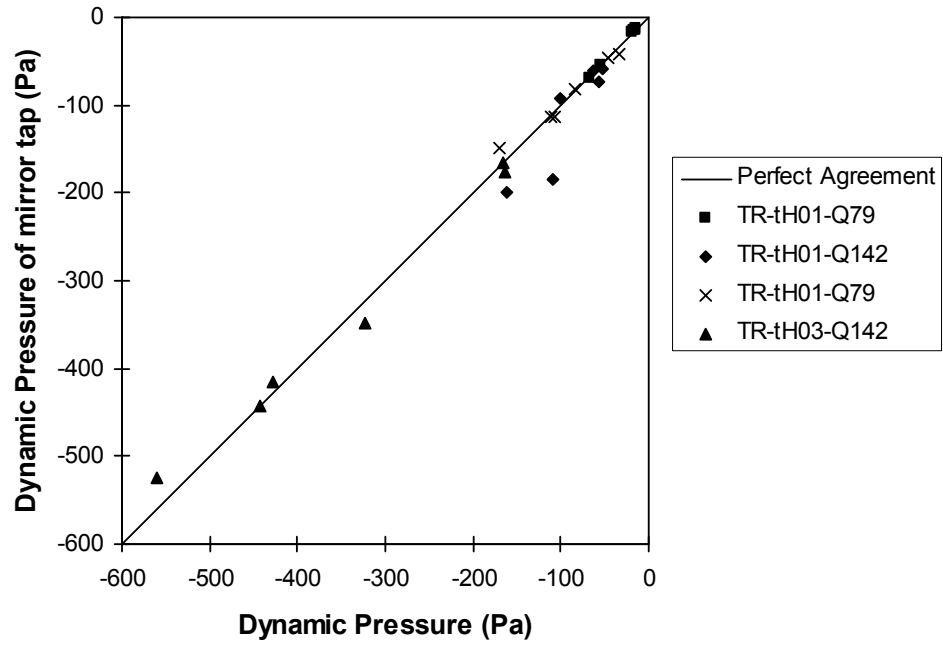


Figure 2-10: Comparison of pressure measured in the mirror taps from the transverse pressure tests.

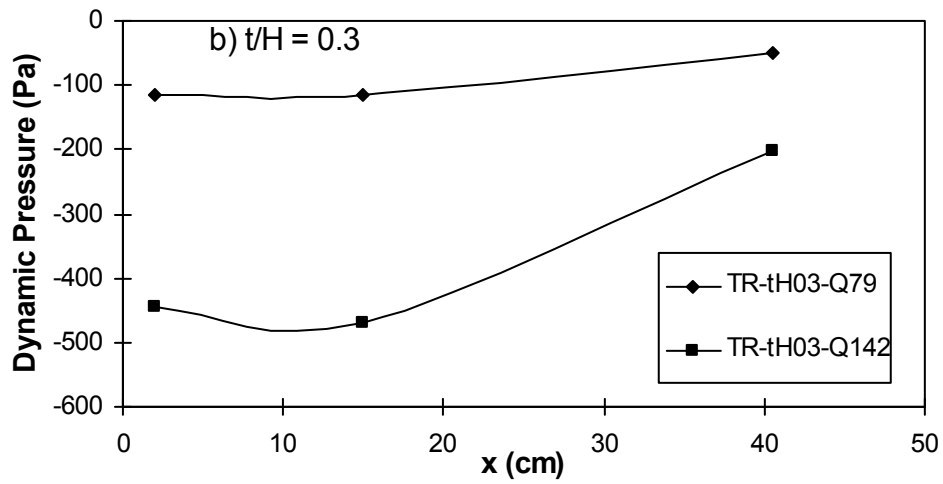
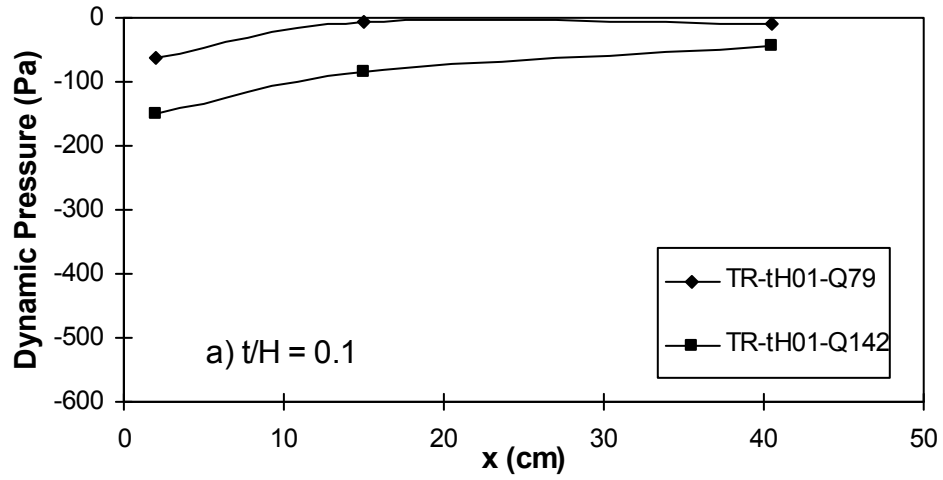


Figure 2-11: Dynamic Pressure measured from transverse pressure tests plotted longitudinally for various thickness-to-depth ratios.

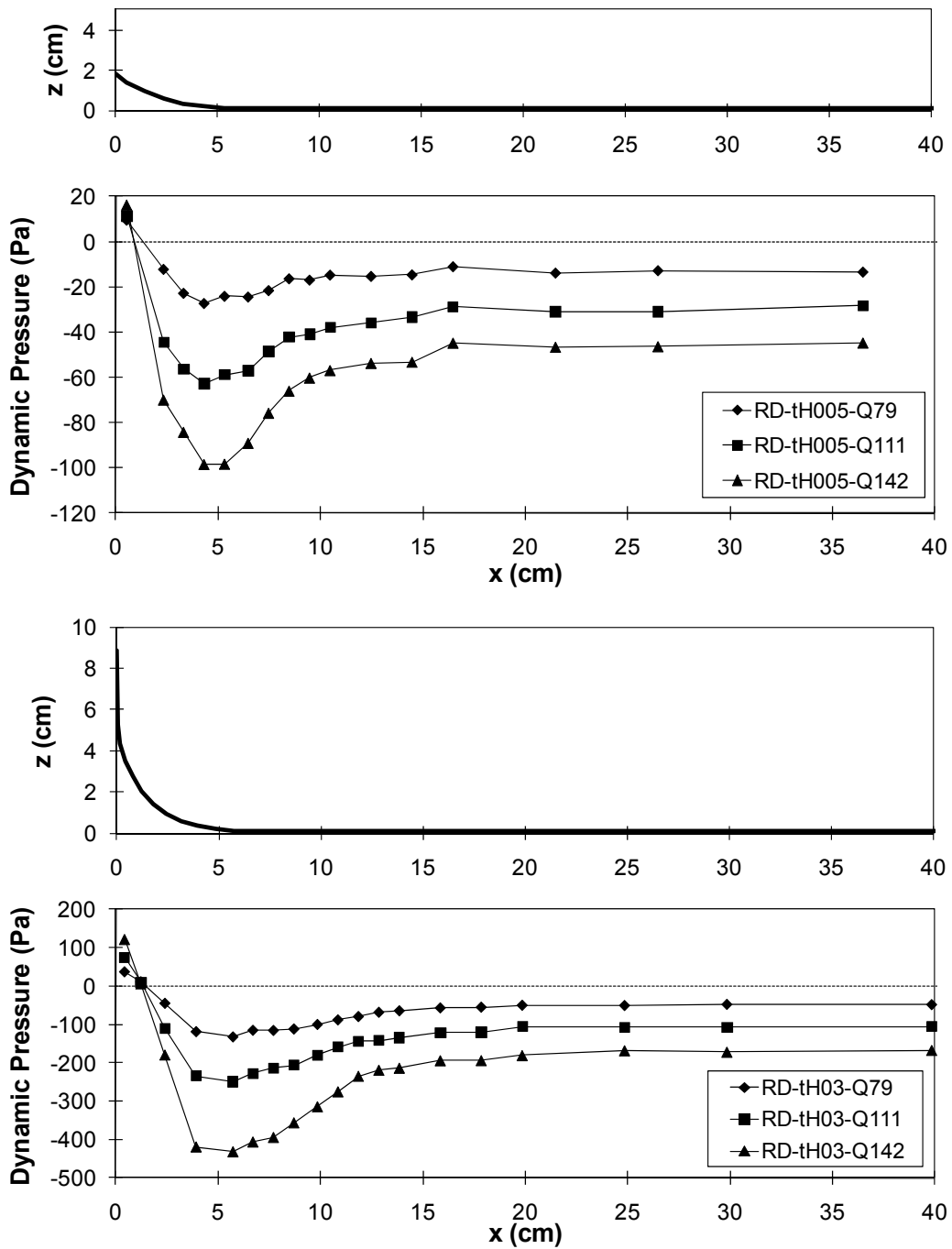


Figure 2-12: a) Dynamic pressure for rounded block $t/H = 0.06$ with profile of block above b) Dynamic pressure for rounded block $t/H = 0.31$ with profile of block above.

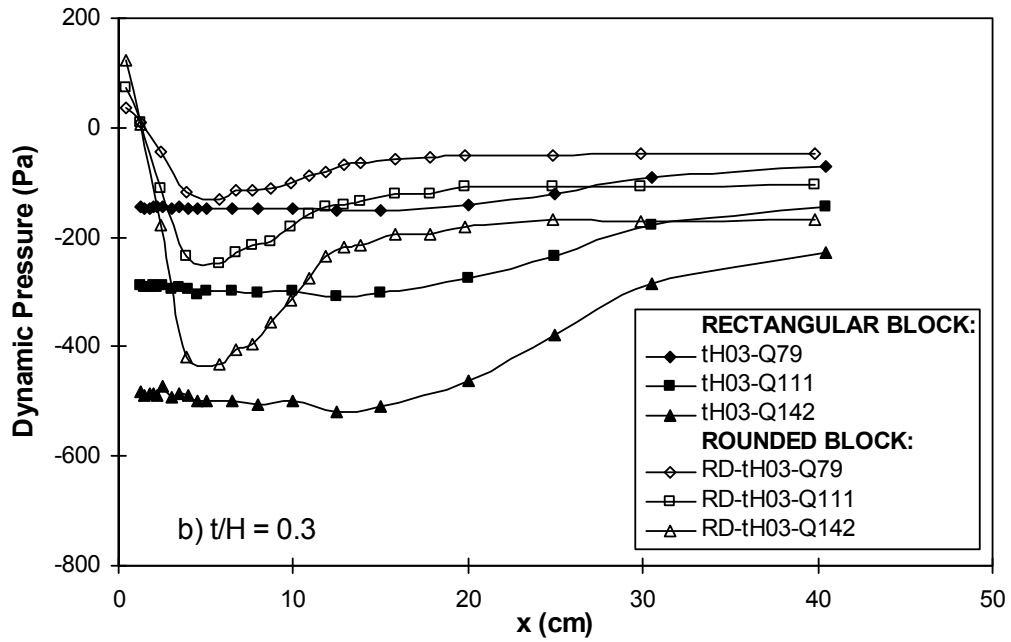
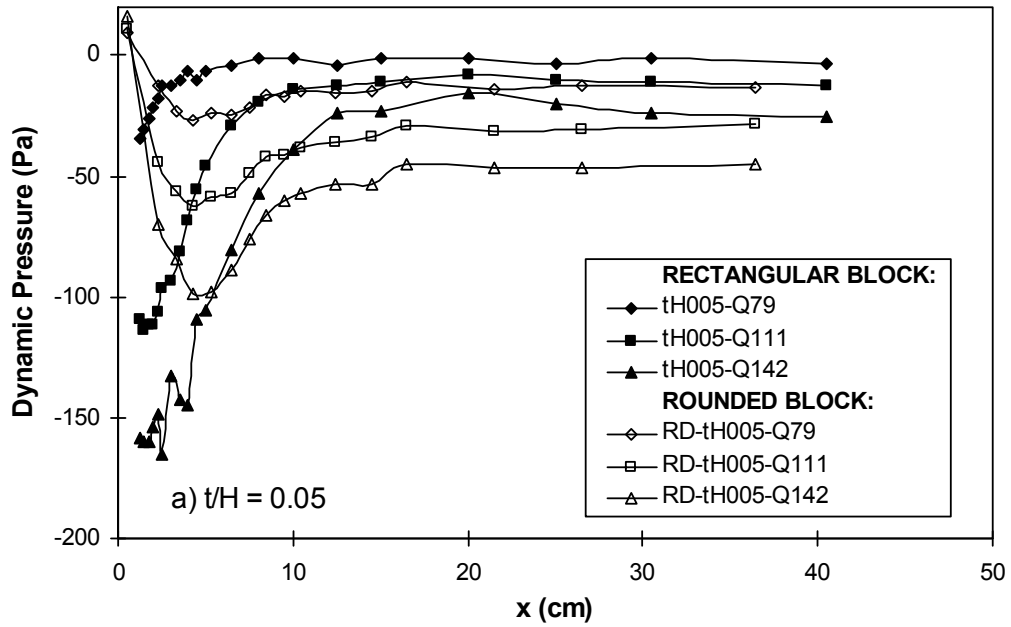


Figure 2-13: Comparison of leading edge effects on the dynamic pressure distribution for various thickness-to-depth ratios.

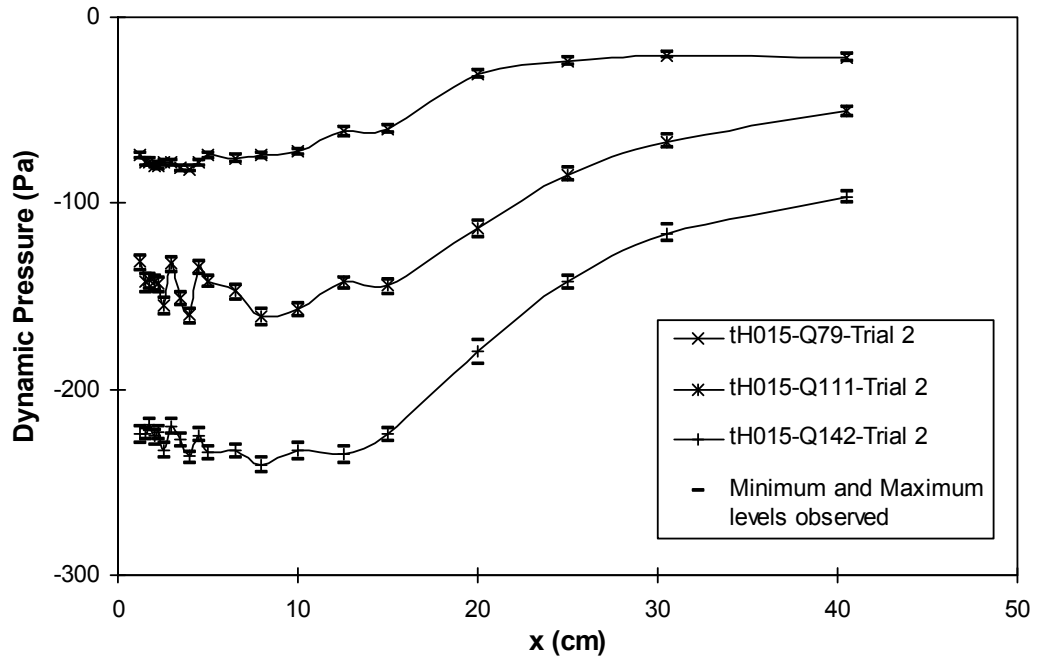


Figure 2-14: Example of the fluctuations observed for a test run in the manometer levels.

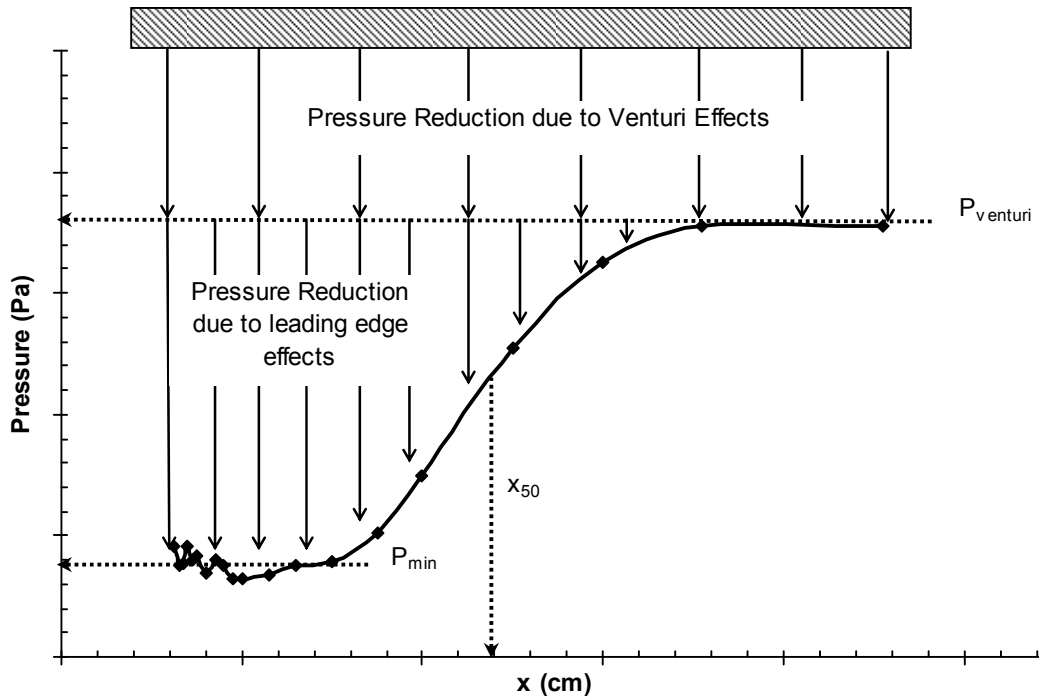


Figure 2-15: Definition of pressure zones and variables used for non-dimensionalization of rectangular block data.

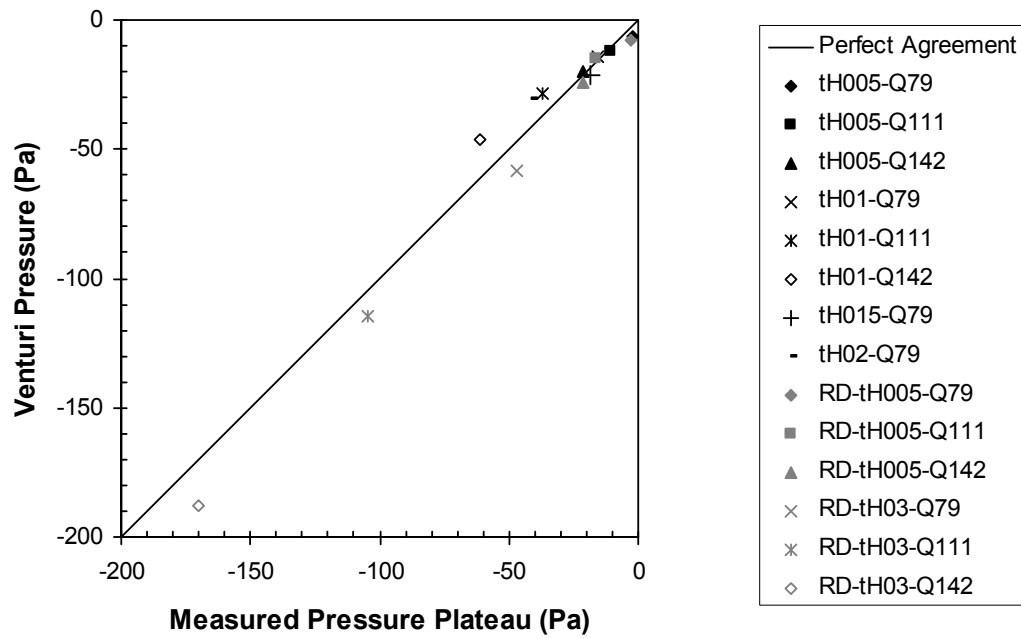
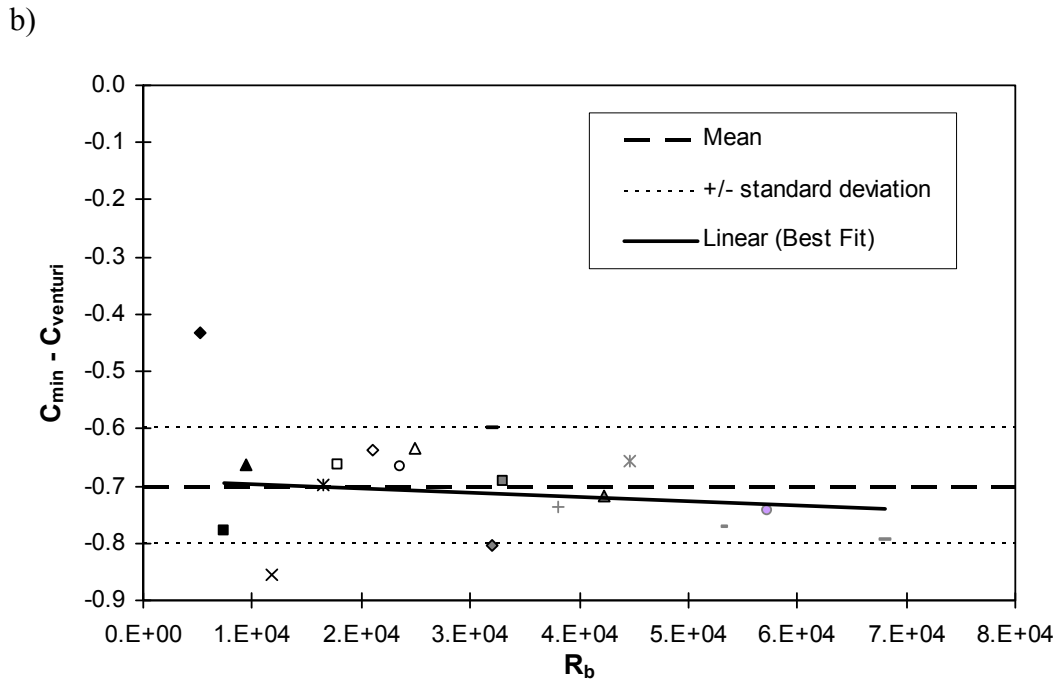
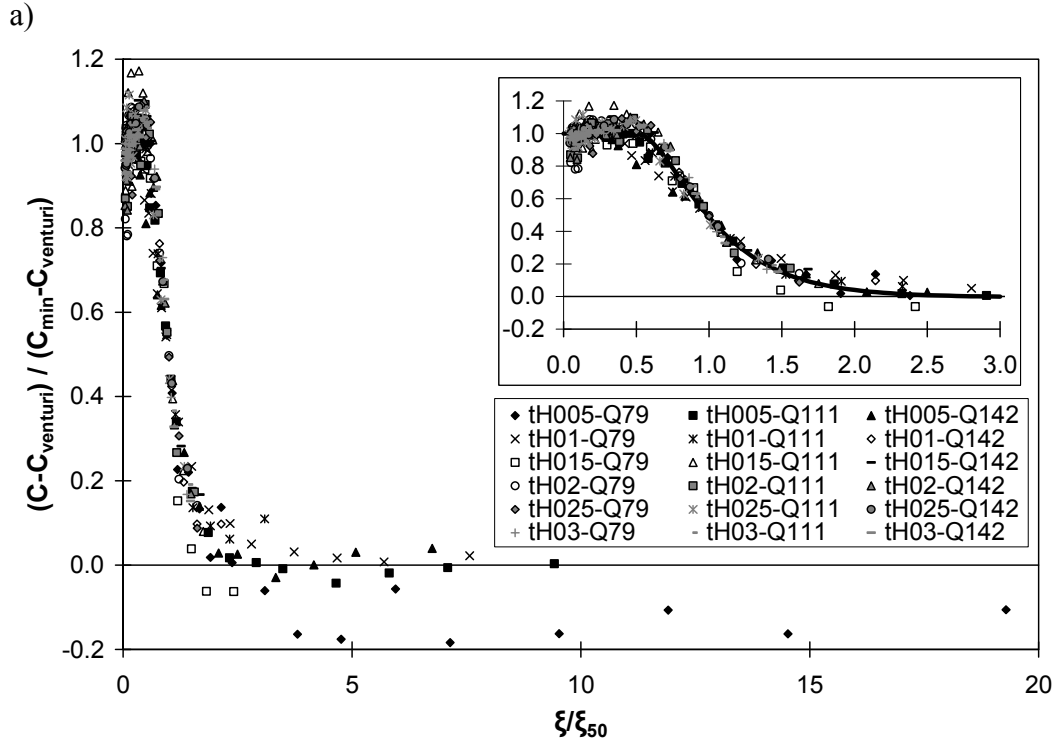


Figure 2-16: Measured pressure plateau compared to the calculated venturi pressure.



c)

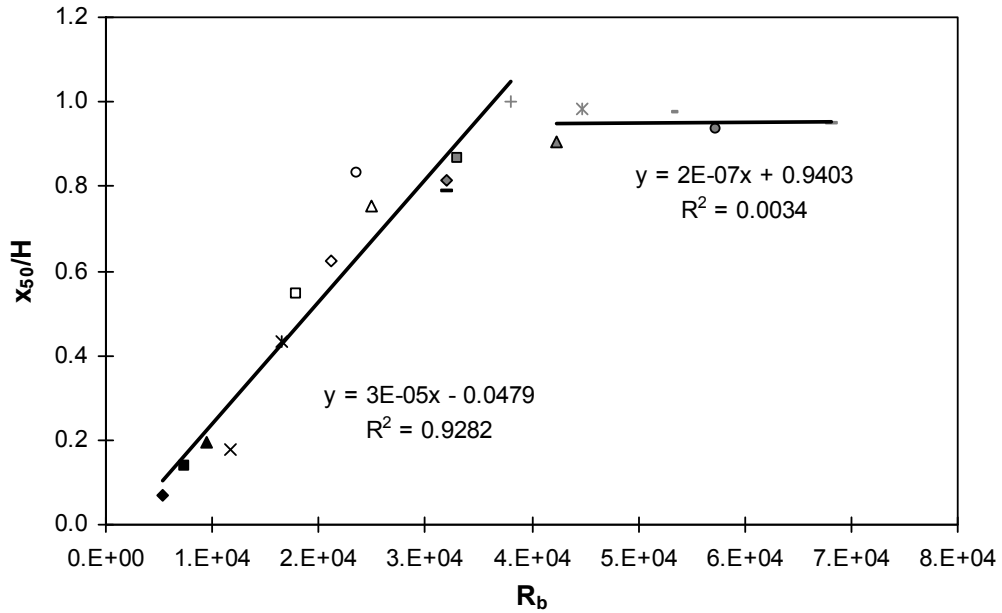
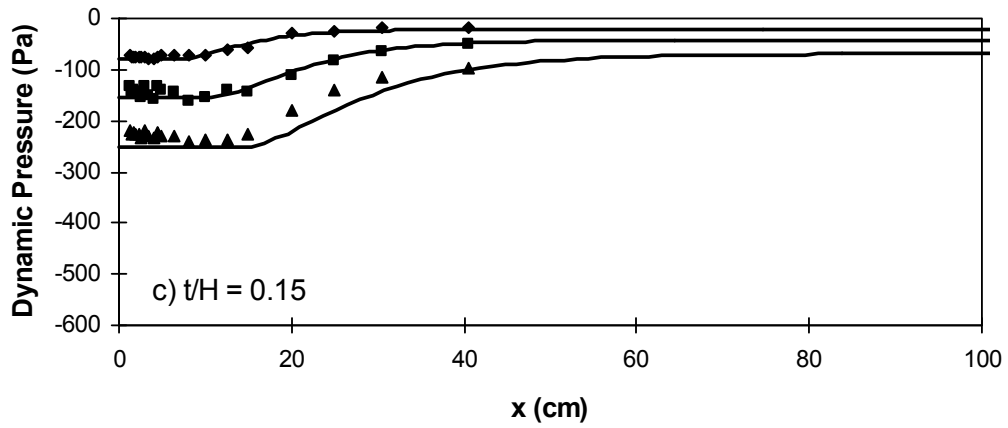
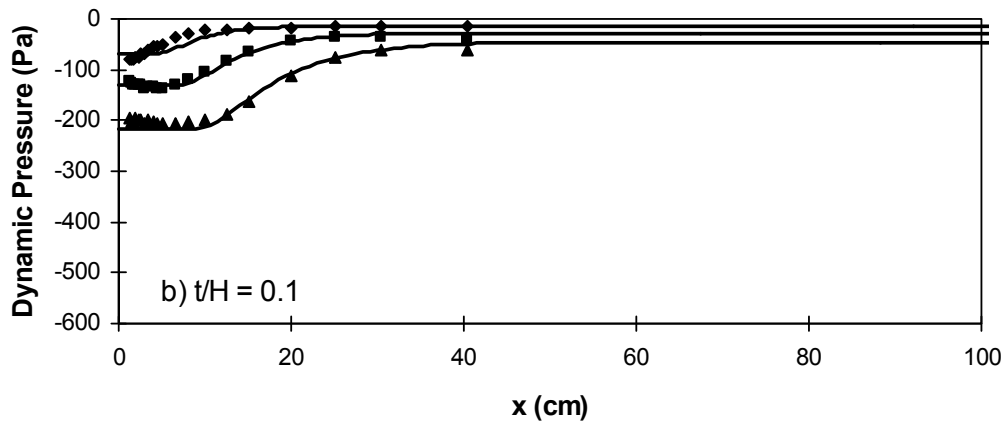
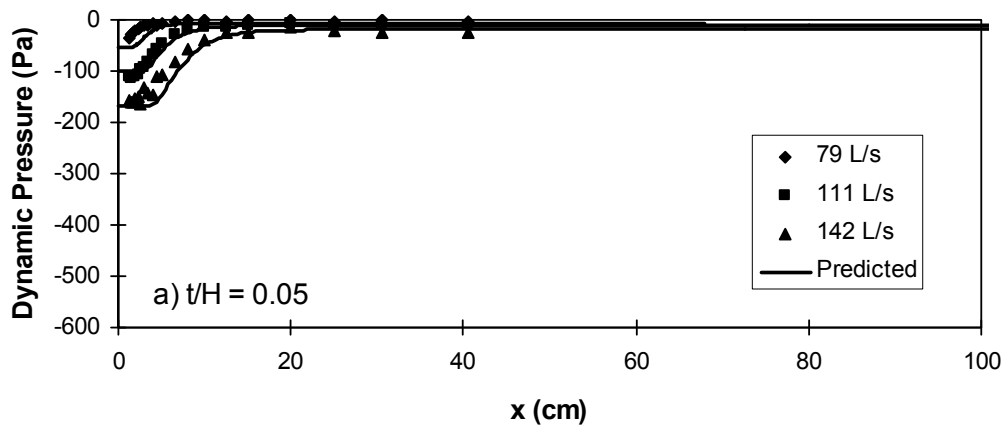


Figure 2-17: a) Non-dimensionalized pressure distribution for all rectangular test cases; b) Non-dimensional relationship to determine the minimum pressure coefficient for a rectangular block; c) Non-dimensional relationship for the location at which the pressure is midway between the initial and final pressure plateau values for a rectangular block measured from the leading edge.



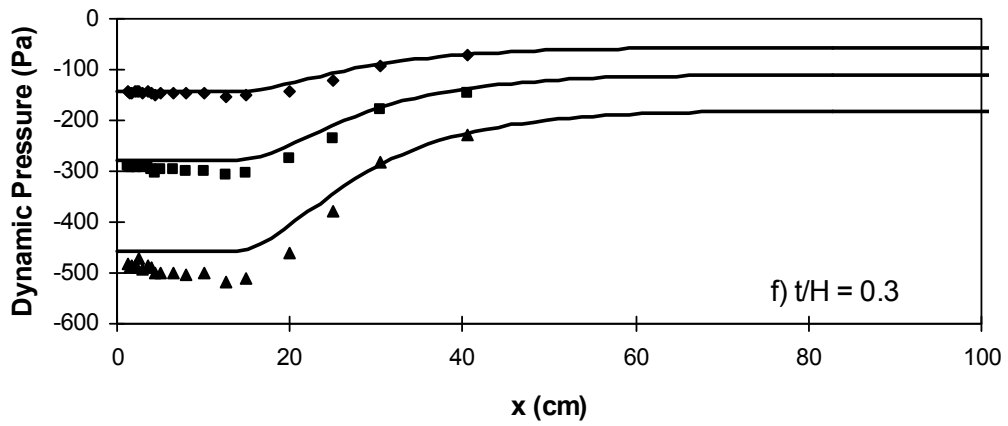
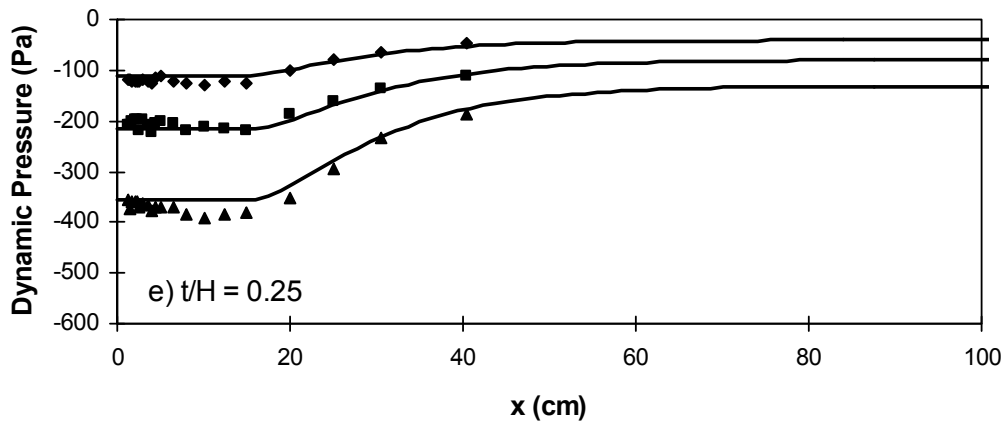
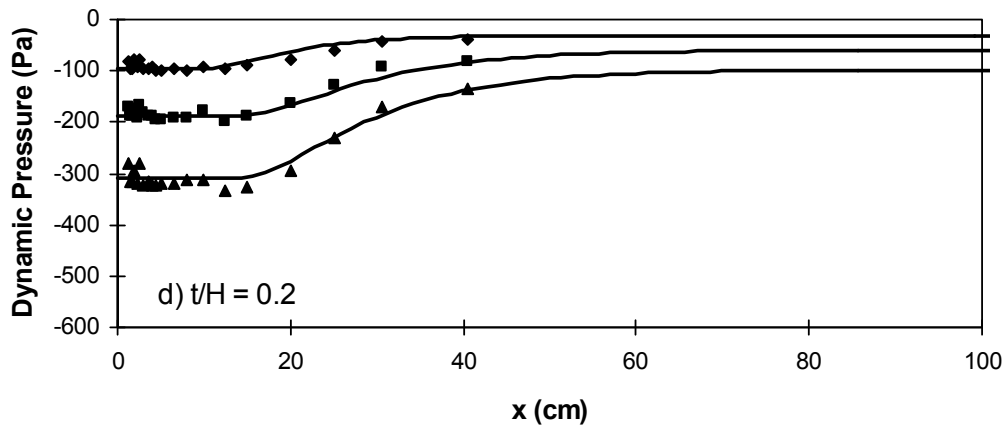


Figure 2-18: Comparing the measured and predicted pressure distributions for various thickness-to-depth ratios.

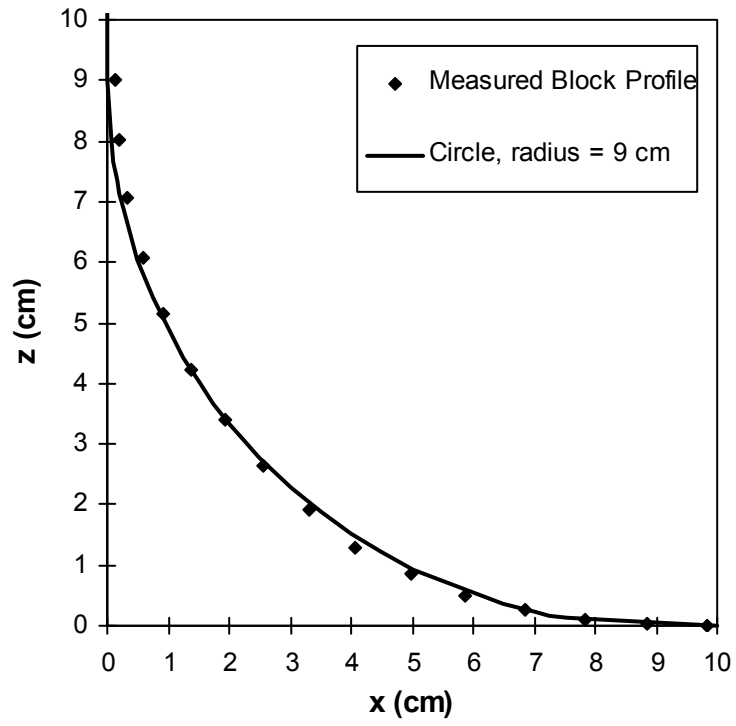


Figure 2-19: Approximate profile of the rounded block using a circle of radius 9 cm.

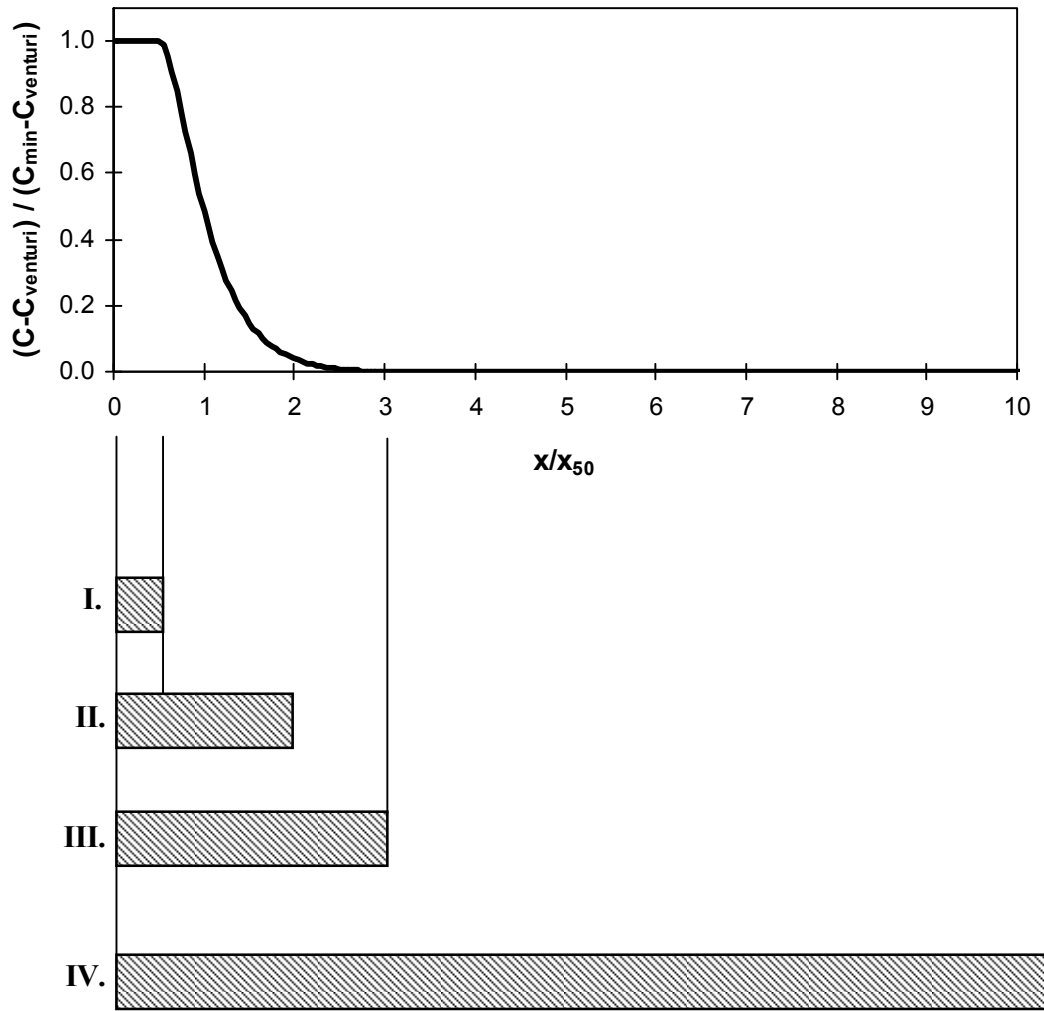


Figure 2-20: Generalized block stability cases: I. Leading edge effects dominated, II. Leading edge partial recovery, III. Leading edge full recovery, and IV. Venturi effects dominated.

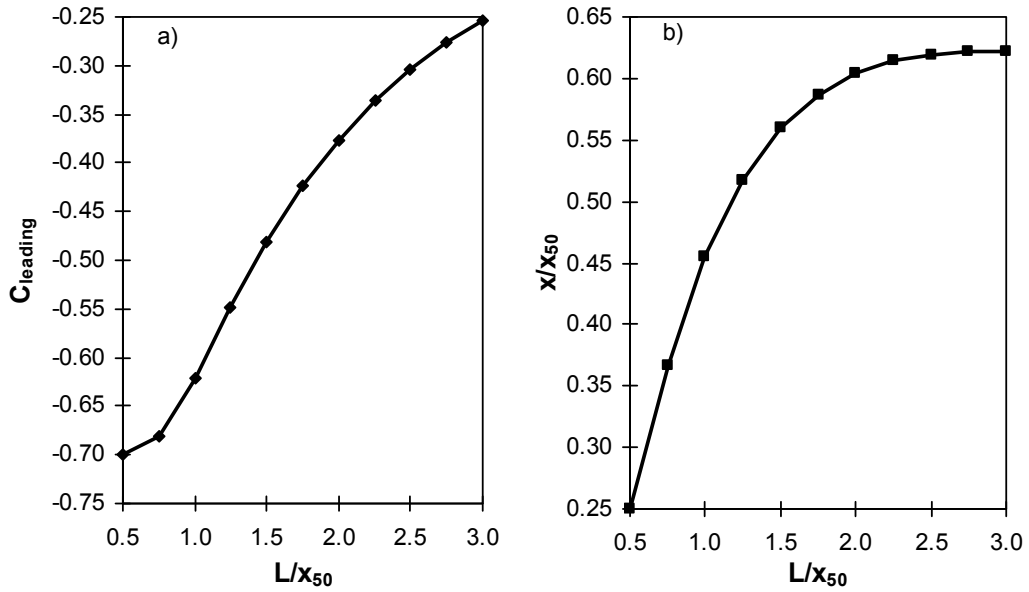


Figure 2-21: a) C_{leading} and b) \bar{x}/x_{50} for a rectangular block of length $0.5x_{50} < L < 3x_{50}$.

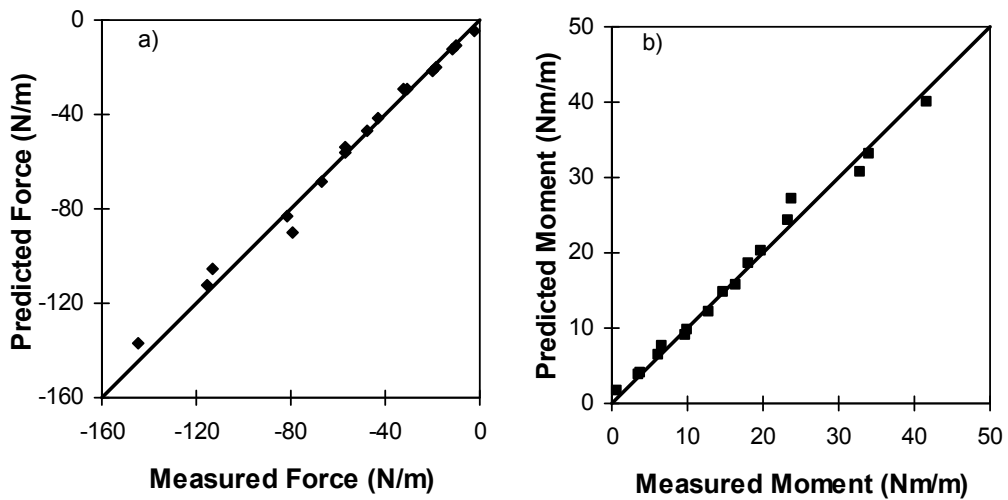


Figure 2-22: Comparison of a) predicted force to measured force and b) predicted moment to measured moment per unit width for the rectangular ice block.

2.8 REFERENCES

- Ashton, G.D., 1974. Froude criterion for ice-block stability. *Journal of Glaciology*, 13(68), pp. 307-313.
- Beltaos, S., 1995. *River Ice Jams*. Water Resources Publications, LLC, Highlands Ranch, Colorado, 372 pp.
- Chee, S.P. and Haggag, M.R.I., 1978. Instability characteristics of ice blocks, *Proceedings, IAHR Symposium on Ice Problems, Lulea, Sweden, August 7-9, 1978, Vol. II*, pp. 375-388.
- Coutermarsh, B. & McGilvary, W.R., 1991. Pressure distribution of an overturning ice floe. *Proc. 6th Workshop on River Ice*, pp. 143-163.
- Coutermarsh, B.A. and McGilvary, W.R., 1993. Static analysis of floating ice block stability. *Journal of Hydraulic Research*, 31(2), pp. 147-160.
- Coutermarsh, B and McGilvary, R., 1994. Analyzing the stability of floating ice floes. *CRREL Report 94-13*, 19 pp.
- Daly, S.F. and Axelson, K.D., 1990. Stability of floating and submerged blocks. *Journal of Hydraulic Research*, 28(6), pp. 737-752.
- Hara, F., Kawai, T., Hanada, M., Nishihata, A., and Saeki, H., 1996. Movement of ice blocks under an ice cover. *Proceedings of IAHR Ice Symposium, Beijing*, pp. 769-778.
- Healy, D. and Hicks, F., 2001. "Experimental Study of Ice Jam Shoving" *Proc. 11th Workshop on River Ice, Ottawa, May*, pp. 126-144.
- Jasek, M., 2003. Ice jam release and break-up front propagation. *Proceedings of the 12th workshop on the hydraulics of ice covered rivers, The CGU HS Committee on River Ice Processes and the Environment. June 19-20, 2003, Edmonton, AB*, pp. 348-368.
- Kawai, T., Hara, F., Masaki, S., Nishihata, A., and Saeki, H., 1997. Experimental study on the process of ice jam development. *Proceedings of 9th CRIPE*, pp. 245-256.

- Kivisild, H.R., 1959. Hanging ice dams, Proceedings of the 8th Congress of the International Association for Hydraulic Research, Vol. 2, paper 23-F, p. 1-30.
- Larsen, P., 1975. Notes on the stability of floating ice blocks. Proceedings of the IAHR third international symposium on ice problems. Hanover, NH, IAHR, pp. 305-313.
- Michel, B., 1971. Winter regime of rivers and lakes, U.S. Army Cold Regions Research and Engineering Laboratory, Cold Regions Science and Engineering Monograph, Pt. III, Sec. Bla., pp. 65-71.
- Pariset, E. and Hausser, R., 1961. Formation and evolution of ice covers on rivers. Transactions of the Engineering Institute of Canada, 5(1), pp. 41-49.
- Uzuner, M.S. and Kennedy, J.F., 1972. Stability of floating ice blocks. Journal of the Hydraulics Division, 98 (HY12), pp. 2117-2133.

CHAPTER 3: ANALYSIS OF THE STABILITY OF FLOATING ICE BLOCKS

3.1 INTRODUCTION

Ice floes approaching an intact ice cover will either come to rest extending the length of the ice cover or become entrained. Once entrained, these floes can be deposited contributing to the thickening of the ice cover, potentially leading to the formation of an ice jam. Beltaos (1995) discussed this current theory suggesting that the leading edge of an ice jam accumulation behaves as a ‘narrow jam’, with floe entrainment or juxtapositioning being the dominant local processes. Healy and Hicks (2001) observed this tendency near the leading edge of ice jams forming in a laboratory flume. The transport of ice is also of relevance in the context of ice jam release as entrained ice floes have the potential to crack and weaken the restraining ice cover (Jasek, 2003). Because of the devastating nature of ice jam formation and ice jam release events, much effort has been put into the development of numerical models that would be able to predict their occurrences. If these models are to predict these phenomena successfully, determining the conditions under which an approaching ice floe becomes entrained is a fundamental component of any model.

This paper has been submitted to the Journal of Hydraulic Engineering and is currently under review.

There have been some studies examining the stability of a floating ice block, however due to the inherent logistical difficulties and safety issues which arise when trying to measure dynamic ice processes in the field, much of our knowledge of these processes is relatively qualitative. This is particularly difficult for ice floe transport under ice jams. Early investigations of this phenomenon focused on defining the critical approach velocity or critical densimetric Froude number (based on approach flow velocity and block thickness) at which floating ice blocks at the leading edges of intact ice covers are submerged (Pariset and Hausser, 1961; Ashton, 1974; Uzuner and Kennedy, 1972; Larsen, 1975). Daly and Axelson (1990) examined the problem analytically and identified that instability was reached when the overturning moment exceeded the righting moment. More recently, Hara *et al.* (1996) and Kawai *et al.* (1997) conducted a series of experiments investigating the movement of ice floes at the leading edge of an ice cover characterizing the movement and the critical densimetric Froude number at movement. They focused on the shape of the edge of the ice cover and the thickness of the ice block.

With recent advances in numerical and experimental technology that allow for better flow visualization and determination, more information about the mechanics of the problem can now be obtained. In the first phase of this study, the pressure distribution beneath a floating ice block was measured to increase the knowledge of the hydrodynamic forces that act upon them and the resulting stability behaviour of the ice blocks (Dow-Ambtman *et al.*, 2009). Using the measured pressure distributions, proposed equations were developed to estimate the submerging forces and overturning moments acting on a floating ice block. In light of this new knowledge, this paper seeks to develop a rigorous method for determining the stability of a floating ice block through a force-moment analysis rather than the conventional empirical estimation based on Froude number only. The proposed equations developed through a force-moment analysis are compared to previously published observations on the critical submergence velocity or densimetric Froude number at block instability.

3.2 BACKGROUND ON ICE BLOCK STABILITY

Consider a right parallelepiped, floating ice block of width b , length L , and thickness t , that is being carried by a uniform flow in a uniform channel as shown in Figure 3-1. In this figure, an ice block has come to rest against an intact floating ice cover of the same specific gravity and thickness as the ice block. Here, V refers to the average velocity of the approach flow, H the approach flow depth, V_u the average velocity beneath the ice block, H_u the depth of flow under the block, t_s the submerged thickness of the block and x the distance along the block measured from the leading edge. This block will either come to rest, contributing to the lengthening of the intact ice cover, or will submerge and become entrained in the flow. A dimensional analysis of this problem (Pariset and Hausser (1961), Uzuner and Kennedy (1972) and Chee and Haggag (1978)) suggests that for solid blocks of rectangular shape, the critical submergence velocity is a function of:

$$\frac{V_{us}}{\sqrt{gH}} = f\left(\frac{t}{H}, \frac{t}{L}, \frac{L}{b}, s_i\right) \quad [3-1]$$

where s_i refers to the specific gravity of ice (i.e. ρ_i/ρ_w).

Previous investigators (Uzuner and Kennedy (1972), Ashton (1974), Larsen (1975), Daly and Axelson (1990), and Coutermarsh and McGilvary (1994)) have surmised that block instability is caused by a pressure reduction beneath the block due to flow acceleration and separation. Investigators examining ice floe entrainment have observed two principal methods of block entrainment. The first method has been termed vertical submergence or “sinking” as pictured in Figure 3-2. Submergence by sinking has been observed by researchers (Uzuner and Kennedy (1972) and Larsen (1975)) for short, thick blocks and long, thin blocks.

A block at rest against a floating obstacle is in perfect force balance, as shown in Figure 3-2a, with the weight of the block balanced by the buoyancy force of the displaced water. Once a flow is introduced, as shown in Figure 3-2b, a resultant submerging force is introduced from the pressure reduction beneath the block due to flow acceleration. This submerging force is located at, or close to, the center of gravity of the block and will cause the block to sink until it reaches another force balance or until it becomes submerged. As the block sinks, the submerging force will increase and the buoyancy force will increase. Once the block becomes submerged, as seen in Figure 3-2d, it will be subjected to additional forces from the surrounding fluid and will likely become entrained by the flow.

The second method has been termed submergence by “underturning” and involves the block rotating about its downstream corner as pictured in Figure 3-3. In this method of submergence, it is the moments that the forces create that lead to instability. The block is initially subjected to the same force-moment balance as described above shown in Figure 3-3a. Again when a flow is introduced the fluid acceleration around the block creates a pressure reduction beneath the block; however, for this case the pressure reduction is not uniform along the block with a greater pressure reduction at the leading edge from the flow separation. The resultant submerging force is therefore located closer to the leading edge of the block, as shown in Figure 3-3b, which causes an underturning moment causing the block to begin rotation about its lower downstream corner. As the block rotates until the point at which the top upstream corner reaches the water surface, as shown in Figure 3-3c, the moment caused by the dynamic pressure changes as well as the moment resisting rotation. Once the top upstream corner becomes submerged the block is subjected to additional forces from the surrounding flow, as shown in Figure 3-3d.

Early investigators examined the problem by attempting to define a critical densimetric Froude number or critical approach velocity at which instability was reached (Uzuner and Kennedy (1972) and Larsen (1975)). Pariset and Hauser

(1961) introduced the concept of the “no-spill” condition which suggested that instability is reached when the top upstream corner of the block becomes submerged and was used by Uzuner and Kennedy (1972), Ashton (1974) and Larsen (1975). Daly and Axelson (1990) examined the problem through a moment analysis reasoning that block instability occurs when the overturning moment exceeds the hydrostatic righting moment. They performed a detailed analysis of the hydrostatic righting moment and discounted the previous “no-spill” condition as they found the maximum hydrostatic righting moment to occur at an angle of rotation greater than the “no-spill” angle. Most recently Kawai et al. (1997) and Hara et al. (1996) examined the movement of ice floes at the leading edge of an ice cover recording the densimetric Froude number at which they submerged and classifying the movement as none, overturning, half turning in which the block began rotation about its downstream corner but was entrained in the flow as pictured in Figure 3-3d without completing the rotation, sliding in which the block was entrained by sinking vertically and pile up in which the block was pushed up on top of the intact ice cover (which was scarcely observed).

Observations of video evidence taken during an experimental study of ice jam formation dynamics (Healy, 2006) suggested that ice floes approaching the intact ice cover either juxtaposed with the intact ice cover or became entrained in the flow by overturning. Entrained blocks were frequently observed to continue “flipping” along the bottom of the intact ice cover before coming to rest some distance from the leading edge of the intact cover. No ice blocks were observed begin the rotation only to stall and become stable. No ice blocks were observed to become fully entrained and carried by the flow a significant distance.

Jasek (2003) noted that when large ice floes are transported downstream under an ice jam past its toe, then it is likely that these floes will be propelled upwards, impacting the underside of the intact solid ice cover. He suggests that such occurrences have the potential to crack and weaken the restraining ice cover, initiating the open leads which are believed to play an important role in the

occurrence of ice jam release. Observations of video evidence from breakup on the Athabasca River at Fort McMurray capturing an incoming ice run approaching an intact ice cover support Jasek's theories. An open lead was initiated downstream of the leading edge of the intact ice cover from the incoming ice run with ice blocks observed to surface within the open lead then disappear again at the end. Observers of breakup have previously described hearing a loud "rumbling" noise while standing on the river bank looking at an intact ice cover. This supports the experimental observations that ice floes once entrained will continue to bump along beneath the intact ice cover until they come to rest. A third method of submergence was commonly observed in the field as shown in Figure 3-4. This is similar to overturning; however, most of the rotation occurs out of the water. Likely this process begins by rotation about the block's lower downstream corner, but the force of the flow is so great that the block does not have time to complete the rotation before the flow begins to push the block downstream causing the downstream end of the block to breach the water surface.

Analysis of Submergence

Based on previous researchers' observations and on video evidence, there appears to be two critical submergence scenarios to examine the force or moment balance: just before the block sinks and just before the block begins to overturn. From these positions the block can take a number of paths to become entrained.

I. Sinking

The critical force balance for vertical submergence occurs just prior to the block submergence, when the top of the block is at the water surface, as shown in Figure 3-2c, where the block is subjected to the maximum submerging force and maximum buoyancy force. The submerging force can be estimated by integrating the pressure reduction beneath the block as:

$$F_s = \int_A P(x, y) dA \quad [3-2]$$

where $P(x, y)$ is the pressure differential from hydrostatic, A is the ice block plane area, x is measured from the block's leading edge along the block, and y is measured across the block. The resisting force is created by the net buoyancy of the ice block, the maximum of which would occur once the entire block becomes submerged. This can be calculated as:

$$F_b = (\rho_w - \rho_i)gtbL \quad [3-3]$$

The ice block can be considered unstable when the submerging force exceeds the buoyancy force as:

$$\frac{|F_s|}{|F_b|} > 1 \quad [3-4]$$

II. Underturning

Previous researchers (Pariset and Hausser (1961), Uzuner and Kennedy (1972), and Ashton (1974)) have discussed the “no-spill” limit which suggested that once water spilled onto the surface of the block, the block would be unstable. Other researchers (Daly and Axelson (1990) and Coutermarsh and McGilvary (1994)) have suggested that this point could not be the limit of stability as the maximum resisting moment occurs at an angle of rotation significantly larger than the “no-spill” limit. Daly and Axelson (1990) performed a detailed analysis of the hydrostatic righting moment that resists the block's rotation. From their analysis, the following equations were developed. The angle of rotation at which the upstream corner of the block reaches the water surface as pictured in Figure 3-3c can be calculated as:

$$\theta_1 = \sin^{-1} \left[\frac{-\frac{\rho_i}{\rho_w} \frac{L}{t} + \sqrt{\left(\frac{L}{t}\right)^2 + 1 - \left(\frac{\rho_i}{\rho_w}\right)^2}}{\left(\frac{L}{t}\right)^2 + 1} \right] \quad [3-5]$$

and the hydrostatic righting moment, R , for an angle of rotation, $0 \leq \theta \leq \theta_1$, can be calculated as:

$$R = \frac{1}{2} \rho_w g t B L \left[\begin{array}{l} \left[t_s \sin \theta \left(\frac{\rho_i}{\rho_w} - 1 \right) \right] + \frac{\rho_i}{\rho_w} (\sec \theta - 1) \\ \left[t_s \tan \theta + (t_s - L \tan \theta) \sin \theta + L \sec \theta \right] \\ + \frac{L}{t} \tan^2 \theta \left(t_s + \frac{2}{3} L \csc \theta - \frac{1}{3} L \sin \theta \right) \end{array} \right] \quad [3-6]$$

The angle at which the downstream upper corner of the block reaches the water surface, as pictured in Figure 3-3d, can be calculated as:

$$\theta_2 = \cos^{-1} \left[\frac{\rho_i}{\rho_w} \right] \quad [3-7]$$

and the hydrostatic righting moment for an angle of rotation $\theta_1 \leq \theta \leq \theta_2$ can be calculated as:

$$R = \frac{1}{2} \rho_w t B L \left[\begin{array}{l} \left(L \cos \theta + t \sin \theta \right) \left(1 - \frac{\rho_i}{\rho_w} \right) - \frac{t}{L} \left(1 - \frac{\rho_i}{\rho_w} \sec \theta \right)^2 \\ \left[t_s + \frac{1}{3} (t \cos \theta - t_s) (\csc^2 \theta + 1) \right] \end{array} \right] \quad [3-8]$$

Finally, for an angle of rotation $\theta_2 \leq \theta \leq \pi/2$, the hydrostatic righting moment can be calculated as:

$$R = \frac{1}{2}(\rho_w - \rho_i)gtBL[L \cos \theta + t \sin \theta] \quad [3-9]$$

Figure 3-5 examines the variation of the hydrostatic righting moment with the block's angle of rotation calculated using the experimental data in Table 3-1. Initially, the hydrostatic righting moment increases rapidly to θ_1 through a linear relationship. At this point there is a slope change and a further increase to a maximum hydrostatic righting moment at some angle of rotation between θ_1 and θ_2 but closer to θ_1 . The hydrostatic righting moment then decreases gradually to θ_2 , then continues to decrease at an increasing rate to $\pi/2$. Coutermarsh and McGilvary (1994) suggested that the maximum righting moment could be estimated as:

$$R_{\max} = \left(1 - \frac{\rho_i}{\rho_w}\right) \rho_w g t B L \left(\frac{L}{2}\right) \quad [3-10]$$

and that the angle of maximum hydrostatic righting moment could be approximated for lengths greater than 2.5 thicknesses as:

$$\theta_{\max} = \tan^{-1}\left(\frac{t}{L}\right) \quad [3-11]$$

as shown in Figure 3-5. Examining this figure, the critical point for overturning will occur at some angle of rotation between 0 and θ_{\max} . If the angle of rotation exceeds θ_{\max} the hydrostatic righting moment begins to decline so a block that reached this angle of rotation will likely continue the rotation to complete entrainment. The critical stability point will depend on how the overturning moment changes with the angle of rotation. The overturning moment can be calculated from the resulting pressure distribution as:

$$M_u = \int_A P(x, y)(L - x)dA \quad [3-12]$$

The location of the resultant submerging force, measured from the leading edge of the block, can be calculated as:

$$\bar{x} = L - \frac{M_u}{F_s} \quad [3-13]$$

The block's rotational stability can be checked by comparing the overturning moment to the hydrostatic righting moment at the critical angle of rotation. Instability will be reached when:

$$\frac{|M_u|}{|R|} > 1 \quad [3-14]$$

3.3 EXPERIMENTAL SETUP AND RESULTS

It is known that once the ice block begins to overturn, or rotate about its downstream corner, the pressure distribution beneath the ice block will change. What is not known is whether this change in the pressure distribution will maintain the instability of the block or whether this new pressure distribution would tend to stabilize the block. The work presented herein is a direct extension of previous investigations on pressure measurements beneath a floating ice block (Dow-Ambtman et al., 2009), and employed the same apparatus and many of the same measurement techniques.

One of the cases from the previous investigation was selected to investigate the effect of block rotation on the pressure distribution beneath the block ($t/H = 0.1$). Figure 3-6 represents a schematic of the experimental apparatus used in this

investigation. The experiments were carried out in a 7.5 m (metre) long recirculating flume located in the T. Blench Hydraulics Lab at the University of Alberta. This rectangular flume has 0.45 m high side walls and a width of 0.75 m. The flume bed and walls are made of glass to facilitate modern optical measurement techniques, such as particle image velocimetry (which was employed in Phase 3 of this study). The pump is controlled by a variable frequency drive and has a maximum discharge of 150 L/s. Flow rates are measured with a magnetic flow meter.

The same hollow rectangular Plexiglas block 50 cm long, 75 cm wide and total thickness of 10.1 cm was used for these experiments. The block was positioned in the flume with the leading edge at $X = 4$ m. The block was held in position by four threaded rods that allowed for height adjustment to enable the simulation of various thicknesses of floating ice. The effective thickness of the “ice” was determined based upon assuming a typical specific gravity of ice of 0.92. In order to measure the pressure distribution beneath the block, the block was outfitted with 20 pressure taps along the centerline shown in Figure 3-7. Each pressure tap was connected to a manometer board using $\frac{1}{4}$ ” O.D. Tygon tubing. De-mineralized water was de-aired for use in the manometer tubing to minimize the occurrence of air bubbles which would compromise the pressure reading and in each test, the manometer board was tilted to 30° to allow for more accurate readings.

The test configuration and procedure were the same as described in Dow-Ambtman et al. (2009). The block was first held flat and the pressure was measured for two different flow rates using the procedure described in Dow-Ambtman et al. (2009). The block was then tilted by holding the downstream corner in place and tilting the block until the upstream corner reached the water surface elevation. This produced an angle of rotation of approximately 0.3° . The same two flow rates were tested and the experimental data is summarized in Table 3-1. In this table F_a refers to the Froude number of the approach flow and R_a is

the Reynolds number of the approach flow. The run numbers are labelled “FL” for flat and “TL” for tilted. Note that the under block velocity reported for the tilted case is an average over the block length. The block was not tilted to further angles of rotation past the point where the upstream corner of the block becomes submerged as the experimental setup, specifically the hollow block, would not properly simulate the flow pattern that would be produced.

Figure 3-8 shows the dynamic pressure measured for each of the tilted block tests and the corresponding flat block cases for comparison. Comparing the pressure distribution of the flat block (solid symbols) to the pressure distribution of the tilted block (open symbols) it is apparent that the magnitude of the initial minimum pressure at the leading edge remains the same. However, the length of the initial pressure plateau is extended when the block is tilted, which shifts the recovery of the pressure further along the block. The magnitude of the second pressure plateau in the tilted case appears to be slightly higher than that for the flat case, likely due to the fact that the under block velocity would be slightly higher in magnitude once the block begins to rotate as there is a greater flow constriction. For a detailed discussion on the accuracy and variability of the pressure measurements, the reader should see Dow-Ambtman et al., 2009.

The results from the previous study suggested that the pressure beneath the block could be non-dimensionalized by breaking the pressure reduction into two effects: a pressure reduction due to leading edge effects which is affected by localized flow behaviour and a pressure reduction due to venturi effects which is affected by the flow constriction from the block. Figures 3-9 show a reproduction of the non-dimensionalized plots produced in Dow-Ambtman et al. (2009). In these figures C is a pressure coefficient, C_{\min} is the minimum value of the sink coefficient, C , calculated for each test case and C_{venturi} is the value of C at the final pressure plateau, ξ is a non-dimensional length scale, x_{50} is the location at which the pressure is midway between the initial and final pressure plateau values

and R_b is a Reynolds number calculated using the submerged block thickness and under block velocity.

Examining the non-dimensionalized plots, tilting the block has little effect on the non-dimensional plot shown in Figure 3-9a, as the manner with which the pressure was non-dimensionalized takes into effect the lower venturi pressure observed as well as the extended initial pressure plateau. There would be a small change in the $C_{\min} - C_{venturi}$ relationship shown in Figure 3-9b due to the reduction in the venturi pressure as the block tilts; however, this change would be within the scatter of the data presented. The most significant effect of the block rotation, in terms of the non-dimensional plots, can be seen in Figure 3-9c. The x_{50} value for the tilted case is greater than that for the flat case, as shown in Table 3-2, which would shift the data points upwards in the plot. This means that the initial pressure plateau extends further along the block, or the recovery to the venturi pressure is delayed, which increases the submerging force acting on the block.

Previous transverse pressure measurements suggested that the block width could be neglected in any force or moment calculation as the pressure was found to be uniform across the block (Dow-Ambtman et al., 2009). The total submerging force per unit width, the overturning moment per unit width and the location at which the submerging force acts were calculated using Equations [3-2] and [3-12] slightly modified to neglect the width of the block and are summarized in Table 3-3. As the block begins to rotate, the submerging force increases from -7 N/m to -10 N/m for the lower flowrate (~ 40 %) and increases from -37.1 N/m to -42 N/m for the higher flowrate (~10 %). Similarly the overturning moment increases as the block begins to tilt, increasing from 2.4 to 3.3 N·m/m for the lower flowrate (~ 40 %) and 11.9 to 13.1 N·m/m for the higher flowrate (~10 %). The location of the resultant force is also shifted along the block as the block is tilted. This indicates that as the block begins to rotate the submerging forces and overturning moments acting on the block increase which will continue to destabilize the block likely leading to its entrainment in the flow.

3.4 ANALYSIS OF BLOCK STABILITY

Detailed pressure measurements beneath a floating block by Dow-Ambtman et al. (2009) suggested that the results could be broken into four scenarios: I) leading edge effects dominated, II) leading edge partial recovery, III) leading edge full recovery and IV) venturi effects dominated. Within each of these scenarios, equations were presented that could be used to estimate the submerging force and overturning moment that would be created by the resulting pressure reduction from the flow around the block. It was also speculated that in the case of the leading edge effects dominated and venturi effects dominated scenarios, the block would be more likely to sink as the pressure distribution beneath these blocks would be uniform.

I. Sinking

For the leading edge effects dominated case, the block is short enough that it will only observe the minimum pressure plateau which can be estimated as:

$$P_{\min} = \frac{1}{2}\rho V^2 - 0.85\rho V_u^2 \quad [3-15]$$

which was derived in Chapter 2. For this case the length of the block is less than or equal to $0.5x_{50}$. The resisting force will be the maximum buoyancy force which occurs when the block has become fully submerged. Since both the resisting and sinking forces are uniformly distributed across and along the block this can be expressed per unit area as:

$$P_{\text{buoyancy}} = \rho_w g t - \rho_i g t \quad [3-16]$$

The block will be at the limit of stability when:

$$P_{\min} = P_{\text{buoyancy}} \quad [3-17]$$

The venturi effects dominated case is so long that $F_{\text{venturi}} \gg F_{\text{leading}}$. The venturi pressure is uniformly distributed along the bottom of the block and can be estimated as:

$$P_{\text{venturi}} = \frac{1}{2} \rho_w V^2 - \frac{1}{2} \rho_w V_u^2 \quad [3-18]$$

The venturi pressure should be calculated by assuming the submerged block thickness is equal to the total thickness of the block and the resisting force can be calculated using Equation [3-16]. The limit of stability is reached when:

$$P_{\text{venturi}} = P_{\text{buoyancy}} \quad [3-19]$$

Previous researchers (Uzuner and Kennedy (1972), Larsen (1975), Ashton (1974), and Daly and Axelson (1990)) have all examined block stability in terms of a critical Froude number or densimetric Froude number recording the point at which the block became unstable. In order to compare these results to those of other researchers, the relationships presented were rearranged to express in terms of a critical densimetric Froude number. The limit of stability equation for the leading edge effects dominated case can be rearranged in the form of a critical densimetric Froude number as:

$$F_{D_{CR-LEADING}} = \sqrt{\frac{1}{\frac{1}{2} - 0.85 \left(\frac{1}{1 - \frac{t}{H}} \right)^2}} \quad [3-20]$$

The limit of stability for the venturi effects dominated case can be rearranged in the form of a critical densimetric Froude number as:

$$F_{D_{CR-VENTURI}} = \sqrt{\frac{2}{\left|1 - \left(\frac{1}{1 - \frac{t}{H}}\right)^2\right|}} \quad [3-21]$$

Figure 3-10 shows a plot of the critical densimetric Froude numbers for the leading edge effects dominated case and the venturi effects dominated case. For the leading edge effects dominated case, the length of the block must be less than or equal $0.5x_{50}$. If the densimetric Froude number calculated for a block of this length falls below the line, the block can be considered stable; if it falls above the line the block will be unstable and will sink. For the venturi effects dominated case, the block must be long enough so that the venturi pressure dominates. If the calculated densimetric Froude number falls below the line, the block will be stable; if it falls above the line the block will be unstable and will sink. To the authors' knowledge, there was no data in literature that fall into either of these two categories to confirm these relationships.

II. Underturning

To determine the critical stability point, the calculated underturning moments are plotted with the hydrostatic righting moment in Figure 3-11 to examine how the change in underturning moment compares to the change in hydrostatic righting moment. Examining the slopes of the moments, it is evident from this figure that the slopes of the underturning moments are less than the slope of hydrostatic righting moment between 0 and θ_1 , but are greater than the slope of the hydrostatic righting moment for an angle of rotation slightly larger than θ_1 . This suggests that for this case the critical angle of rotational stability would occur at an angle of rotation of θ_1 . If the slope of the underturning moment was less than

the slope of the hydrostatic righting moment for an angle slightly larger than θ_1 then the critical angle of rotational stability would occur at some angle between θ_1 and θ_{\max} . If the slope of the overturning moment was greater than the slope of the hydrostatic righting moment between 0 and θ_1 , then the block would be considered unstable at every point.

A generalized method was derived in Dow-Ambtman et al. (2009) for predicting the overturning moment based on pressure measurements in which the submerging force and overturning moment could be calculated as:

$$F_{venturi} = P_{venturi} L \quad [3-22]$$

$$\bar{x}_{venturi} = L/2 \quad [3-23]$$

$$M_{venturi} = P_{venturi} L \left(\frac{L}{2} \right) \quad [3-24]$$

$$F_{leading} = \bar{C}_{leading} \left(\frac{1}{2} \rho V_u^2 \right) (L) \quad [3-25]$$

$$M_{leading} = F_{leading} \left(L - \bar{x}_{leading} \right) \quad [3-26]$$

$$F_s = F_{leading} + F_{venturi} \quad [3-27]$$

$$M_u = M_{leading} + M_{venturi} \quad [3-28]$$

The relationships above were derived based on pressure measurements taken when the block was flat. As the block begins to rotate, the submerging force and overturning moment increase as was shown in Table 3-3. Since there are only two points it is difficult to determine a trend so the increases were simply

averaged, assuming that if the block rotates to the point where the upstream top corner is at water level, the submerging force and overturning moment will increase by approximately 25% so that:

$$M_{u1} = 1.25(M_u) \quad [3-29]$$

Stability can then be checked using Equation [3-14]. In order to compare to previous researchers data, the densimetric Froude number can be calculated for the point at which:

$$M_{u1} = R_{\theta_1} \quad [3-30]$$

3.5 DISCUSSION

Uzuner and Kennedy (1972) had the most detailed analysis of block stability examining a broad range of t/H , t/L and specific gravity ratios. They conducted a series of experiments in which they floated blocks increasing the flow velocity until instability was observed, recording the instability as a critical approach Froude number. These values were converted into a densimetric Froude number as:

$$F_{D_{CR}} = F_2 \times \frac{\sqrt{2}}{\sqrt{\frac{t}{H}(1-s_i)}} \quad [3-31]$$

where $F_2 = \frac{V}{\sqrt{2gH}}$. Figures 3-12 a-e compare the data of Uzuner and Kennedy to the densimetric Froude numbers at the point at which equation [3-30] is satisfied for different t/L ratios.

For the ratio $t/L = 0.096$, shown in Figure 3-12a, the moment analysis predicts a slightly lower critical densimetric Froude number than observed by Uzuner and Kennedy. This suggests that either the overturning moment is being overestimated by equation [3-29] or the resisting moment is being underestimated for this t/L ratio. This figure also examines the effect of using a 10% or 40% increase in overturning moment rather than the assumed 25% increase on the predicted critical densimetric Froude number. The bands show that although the increase in overturning moment with rotation is important in determining the critical angle of rotational stability, the predicted critical densimetric Froude number appears to be insensitive to the actual quantity of the increase suggesting that the assumed 25% increase is acceptable. It is interesting to note that the data of Uzuner and Kennedy for this particular t/L ratio does not collapse when plotted as a densimetric Froude number, as expected. They stated that they observed thin, long blocks would sink rather than overturn for $t/L < 0.1$. It is difficult to ascertain from their paper whether this data presented is for sinking blocks or overturning blocks. It is possible that some of these blocks became entrained by sinking, as Ashton (1974) suggested would occur at a higher critical Froude number than entrainment by overturning.

For the ratio of $t/L = 0.192$ shown in Figure 3-12b the moment analysis fits the observations of Uzuner and Kennedy (1972) better than in the previous case, but the moment analysis seems to estimate a slightly higher densimetric Froude number for t/H ratios less than about 0.2 than what was observed by Uzuner and Kennedy. This suggests that either the overturning moment is being underestimated by equation [3-29] or the righting moment overestimated for these cases. It could be that the 25% increase in the overturning moment is too small for lower t/H ratios.

For the mid-range thickness to length ratios of $t/L = 0.254$ shown in Figure 3-12c and $t/L = 0.5$ shown in Figure 3-12d the moment analysis fits the observed data of Uzuner and Kennedy well. This suggests for this range of thickness to length ratios the overturning moment and resisting moment are being estimated correctly and that there are no additional forces or moments that need to be considered in the stability analysis.

For the ratio of $t/L = 0.773$ shown in Figure 3-12e, the moment analysis underestimates the critical densimetric Froude number compared to the observed data of Uzuner and Kennedy. This observed data is also at a higher critical densimetric Froude number than that observed for the t/L ratio of 0.5 which suggests that there are additional forces acting on this block that must be considered. For this t/L ratio, the block is approaching a cube shape and it is likely that the forces acting on the face of the block can no longer be ignored.

Larsen (1975) also published data on the observed densimetric Froude numbers at instability from a series of experiments using paraffin blocks. However, he did not specify the t/L ratio of his data points, they were all plotted together. His block thickness was either 1.05 or 2.85 cm and block length ranged from 7.5 to 15 cm for a t/L range of 0.07 to 0.38. Figure 3-13 shows Larsen's data with the critical densimetric Froude numbers calculated through the moment analysis for t/L of 0.07 and t/L of 0.38. The moment analysis appears to follow the shape of Larsen's data well. The moment analysis for t/L of 0.07 seems to overestimate the critical densimetric Froude number while the moment analysis for t/L of 0.38 fits the data quite well. As stated before it is not known which of Larsen's data

points correspond to which t/L ratios and whether he tested the t/L ratios equally. It was shown in this analysis that the t/L is important in examining block stability.

Ashton (1974) published a relationship that was based on the experimental results of Uzuner and Kennedy (1972) by performing a simplified moment analysis to develop a densimetric Froude criterion. His relationship has been widely used as it is simple in its application. He suggested that the critical densimetric Froude number can be calculated as:

$$F_D = \frac{2\left(1 - \frac{t}{H}\right)}{\sqrt{5 - 3\left(1 - \frac{t}{H}\right)^2}} \quad [3-32]$$

Figure 3-14 shows a comparison of the moment analysis to his relationship. The moment analysis matches Ashton's relationship well for $t/L = 0.5$ but predicts a higher critical densimetric Froude number for t/L ratios less than this. It is important to note that Ashton's relationship neglects to account for the length of the block, which from this analysis has been shown to be an important factor in determining stability.

Daly and Axelson (1990) published a relationship that was based on the data of Uzuner and Kennedy (1972) and Larsen (1975). They suggested the densimetric Froude number could be calculated as:

$$F_D = \sqrt{\frac{2Z}{a}} e^{\frac{b t}{2H}} \quad [3-33]$$

where Z is a nondimensional function which describes the maximum hydrostatic righting moment which is a function of the specific gravity and t/L , a and b are regression coefficients. Figure 3-15 shows a comparison of the moment analysis to their relationship for a t/L ratio of 0.1 and 0.5. Both relationships show similar dependence on the t/L ratio. For small t/H ratios, the moment analysis appears to predict a higher critical densimetric Froude number than the Daly-Axelson relationship and for higher t/H ratios the moment analysis predicts a lower densimetric Froude number.

Figure 3-16 shows the results of the force-moment analysis all together. In this figure, the sinking limits from the leading edge effects case of equation [3-20] and venturi effects dominated case of equation [3-21] are presented as the thicker lines along with the overturning limits of $t/L = 0.096$ and $t/L = 0.5$ from the moment analysis are presented as thinner lines. In this figure, the symbols represent the critical densimetric Froude numbers calculated for the cases tested in determining the pressure distribution beneath the floating ice block. It is interesting to note that the results generally correspond with Ashton's observation that overturning instability occurs at a lower critical velocity than required for vertical submergence. However, this does not mean that a block will overturn before it will sink. The length of the block must be checked and x_{50} calculated to determine if the block falls into the leading edge effects dominated case or the venturi effects dominated case. It is noted that the data point for $t/H = 0.05$ appears to be high. In the previous paper, the data from the $t/H = 0.05$ case was subject to the highest error in the prediction of the forces and moments due to the small magnitude of the pressures in the measured pressure distributions. This could have contributed to the overestimation of the critical densimetric Froude number in Figure 3-12b.

3.6 CONCLUSIONS AND RECOMMENDATIONS

Ice block stability was evaluated through a force-moment analysis using experimental results that measured the dynamic pressures beneath a floating ice block under various thickness-to-depth ratios and flow velocities at the T. Blench Hydraulics Laboratory at the University of Alberta. These results increase the understanding of the hydrodynamic forces that act on a floating ice block, which is an essential component to any model that attempts to predict ice floe entrainment and movement. Until this time, much of the knowledge of these processes was necessarily qualitative.

The effect of block rotation on the resulting pressure distribution was examined through four test cases on a rectangular block. As the block began to rotate, the magnitude of the minimum pressure at the leading edge of the block remained the same; however, this minimum pressure plateau extended further along the block. The magnitude of the venturi pressure plateau decreased as the block began to rotate, likely due to the increase in mean velocity.

A stability analysis was performed through a force-moment balance and was broken into two methods of entrainment: sinking and overturning by rotation about the downstream corner of the block. The critical position for sinking was assumed to be just prior to complete submergence. The critical position for overturning was found to be at an angle of rotation at which the upstream upper corner of the block reached the water surface. A generalized force-moment analysis was previously developed based on dynamic pressure measurements beneath a floating ice block. This method was used to determine the submerging forces and overturning moments acting on an ice block. The submerging force and overturning moment were found to increase as the block rotated to the critical angle of rotation by approximately 25%. These were compared to the resisting buoyancy force and hydrostatic righting moment at the critical positions.

The results of the force-moment stability analysis were presented as a critical densimetric Froude number in order to compare to previously published observations of block instability and were found to match the observations quite well. As the block approaches more of a cube-like shape ($t/L > 0.5$), it appears the additional forces on the face of the block can no longer be neglected in the analysis. Although previous researchers have neglected the block length, it is an important variable when considering block stability and should not be neglected. Equations for the critical densimetric Froude number for vertical submergence were developed for blocks that are leading edge effects dominated or venturi effects dominated. The critical densimetric Froude number for vertical submergence was found to be higher than that for overturning instability.

It was shown that once the block begins to become entrained the pressure distribution will change. Future work could examine the pressure distribution on all block faces as the block becomes entrained. The force-moment analysis could then be extended to more cube shaped blocks. The question still remains: once the ice floe becomes entrained what happens? Further studies examining ice floe entrainment and deposition should be conducted.

Table 3-1: Summary of experimental variables.

Run #	t (cm)	H (cm)	t/H	Q (L/s)	V (cm/s)	V_u (cm/s)	F_a	R_a
FL-tH01-Q79	3.08	30.19	0.10	80	35.2	38.9	0.2	1.06E+05
FL-tH01-Q142	3.08	30.19	0.10	143	63.2	69.7	0.4	1.91E+05
TL- tH01-Q79	3.28	30.38	0.11	80	34.9	39.0	0.2	1.06E+05
TL-tH01-Q142	3.28	30.38	0.11	143	62.7	70.0	0.4	1.91E+05

Table 3-2: Summary of data used for non-dimensionalization.

Run #	x_{50} (cm)	R_b
FL-tH01-Q79	5.25	1.10E+04
FL-tH01-Q142	17.35	1.97E+04
TL- tH01-Q79	10	1.10E+04
TL-tH01-Q142	19.75	1.97E+04

Table 3-3: Summary of calculated submerging forces and overturning moments.

Run #	F_s (N / m)	M_u (N-m/m)	\bar{x} (cm)
FL-tH01-Q79	-9.3	3.2	15.8
FL-tH01-Q142	-49.5	15.9	17.8
TL- tH01-Q79	-13.3	4.4	16.6
TL-tH01-Q142	-56.0	17.5	18.9

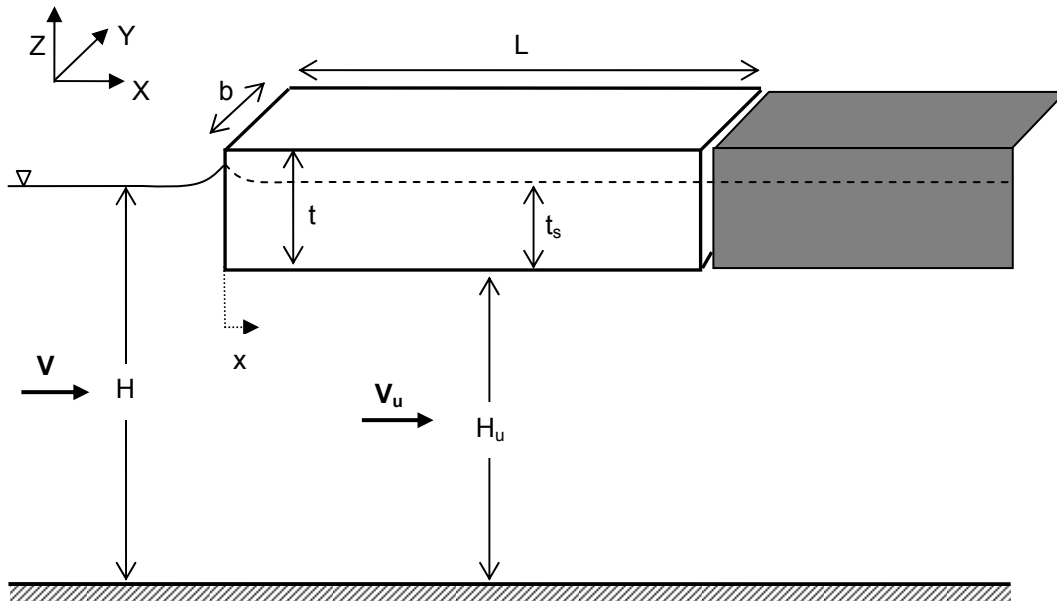


Figure 3-1: Problem definition sketch.

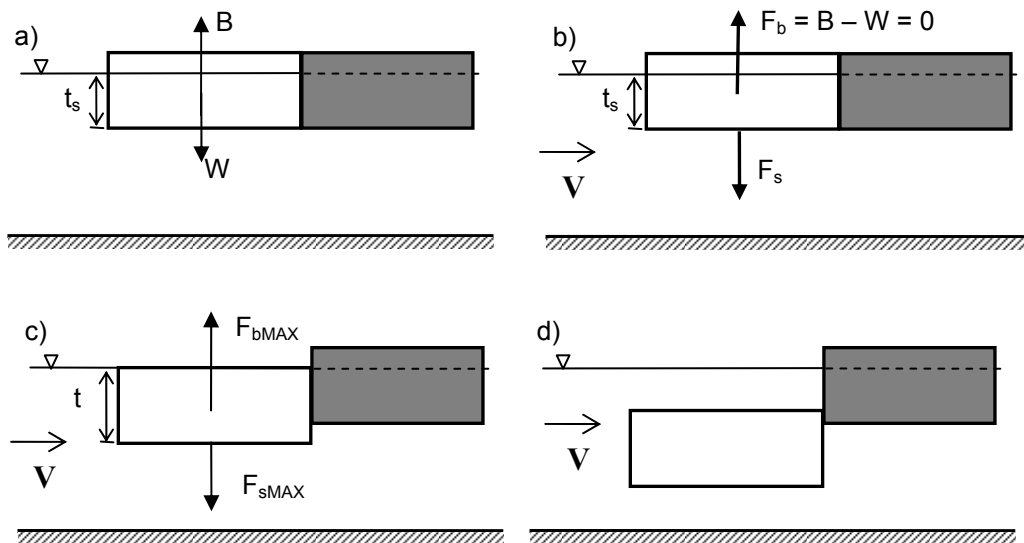


Figure 3-2: Progression of sinking instability: a) Block at rest, forces are in perfect balance; b) Flow is introduced, a submerging force due to pressure reduction is created which will pull the block down; c) The critical position where the net buoyancy force and the submerging force are at a maximum; d) Block entrained in the flow is subjected to additional forces.

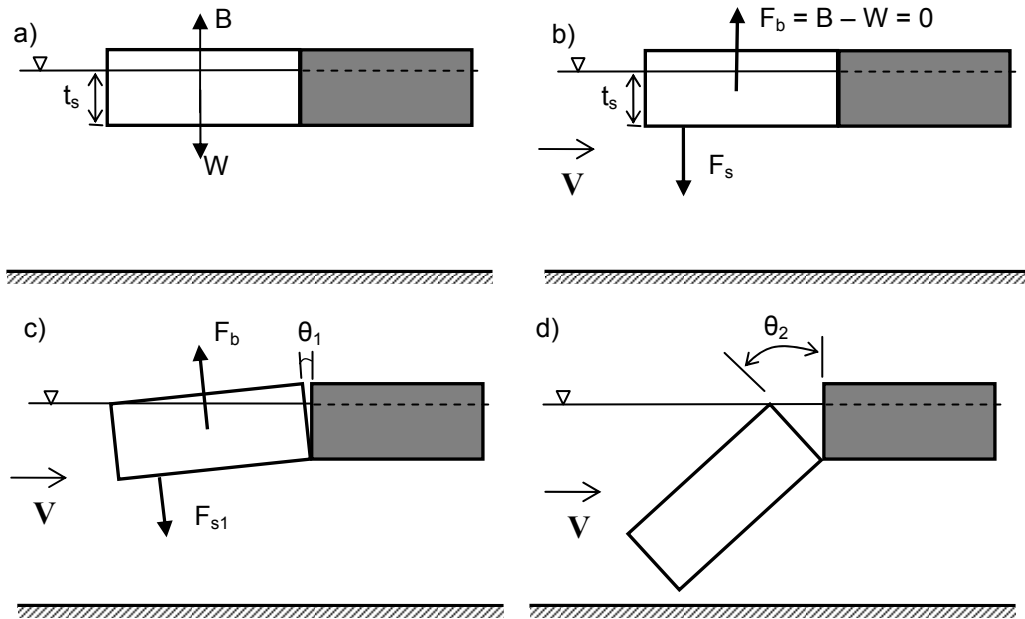


Figure 3-3: Progression of overturning instability: a) Block at rest, moments are in perfect balance; b) Flow is introduced, a resultant submerging force creates overturning moment which will cause block to rotate; c) The critical position for entrainment; d) Block entrained in the flow, is subjected to additional forces.

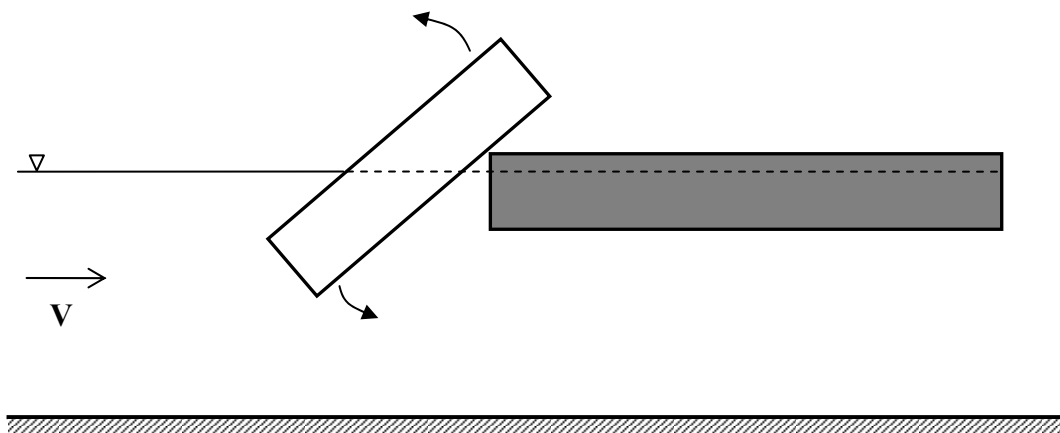


Figure 3-4: Instability observed in field video of breakup on the Athabasca River at Fort McMurray.

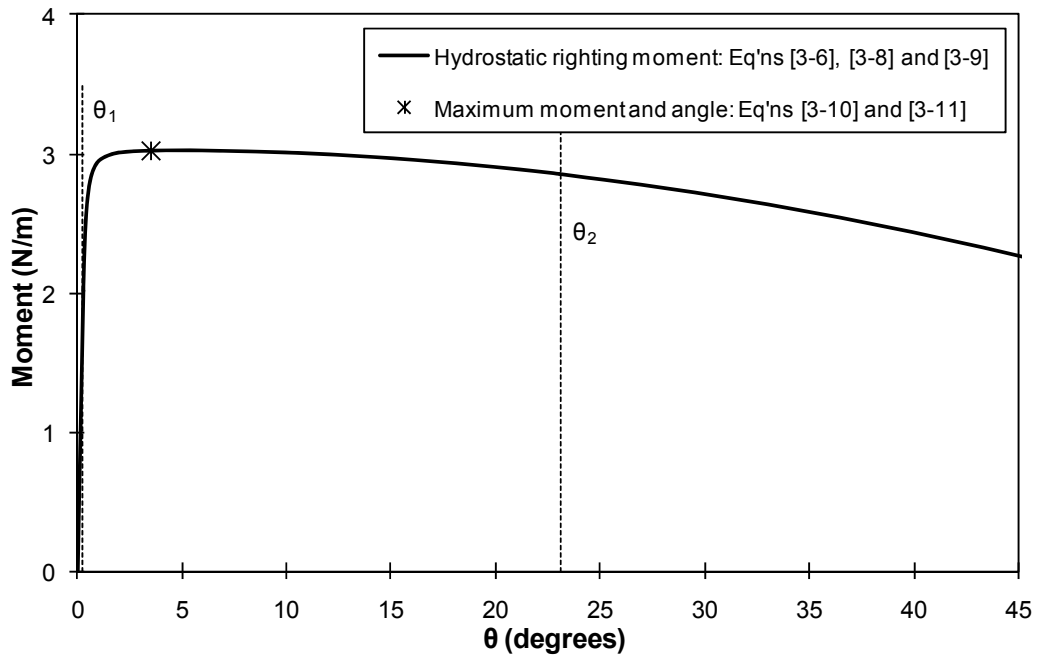


Figure 3-5: Variation of hydrostatic righting moment with block angle of rotation calculated using the experimental data of Table 3-1.

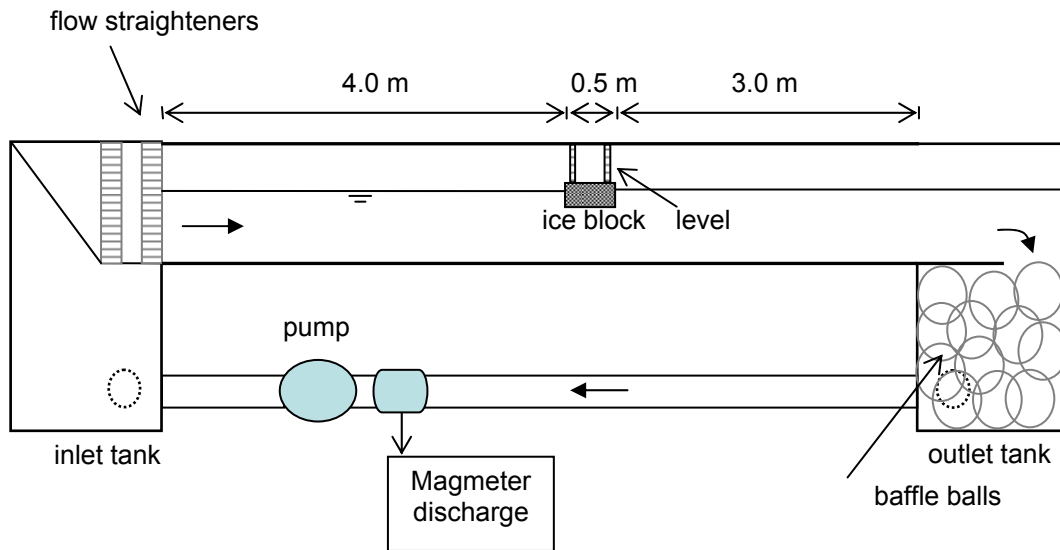


Figure 3-6: Schematic of experimental setup (Dow-Ambtman et al., 2009)

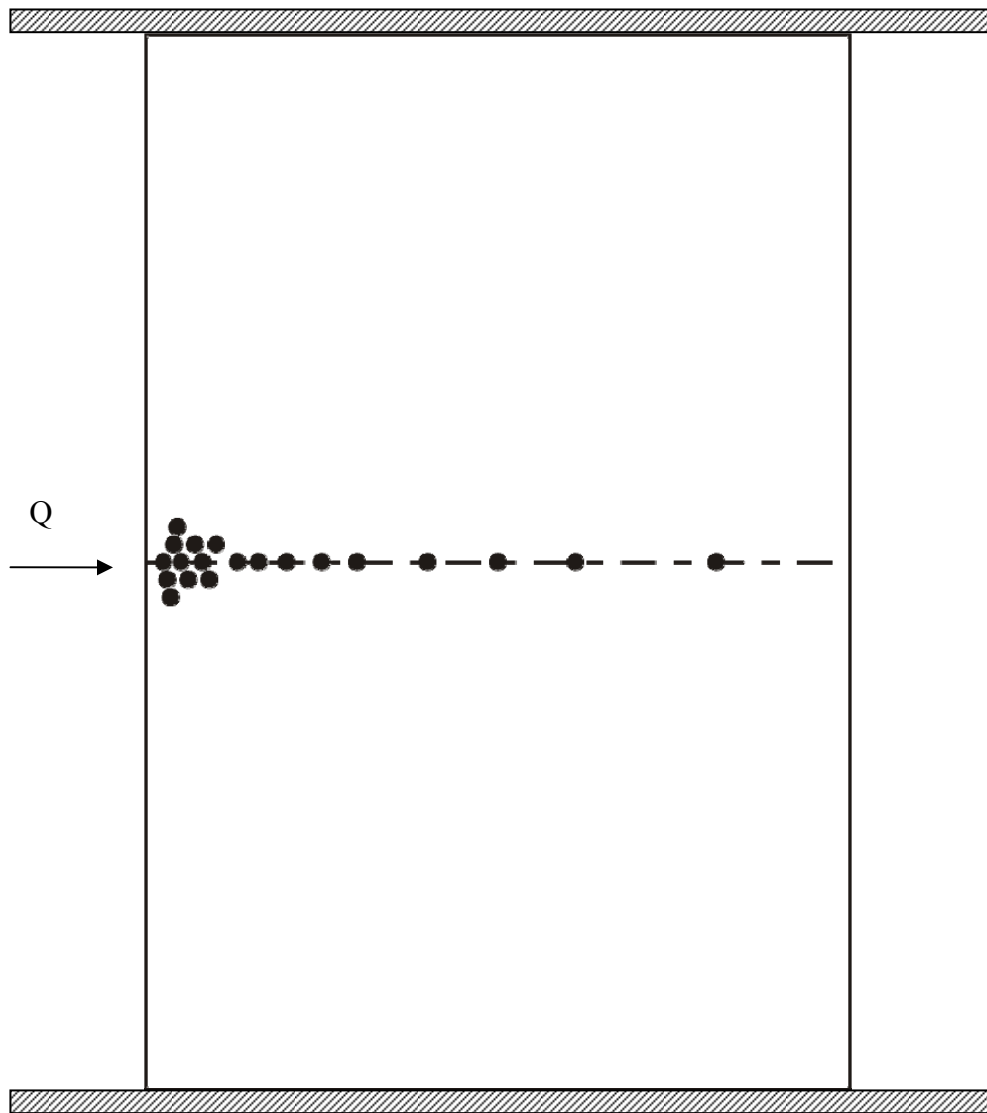


Figure 3-7: Rectangular block pressure tap locations, as seen from below.

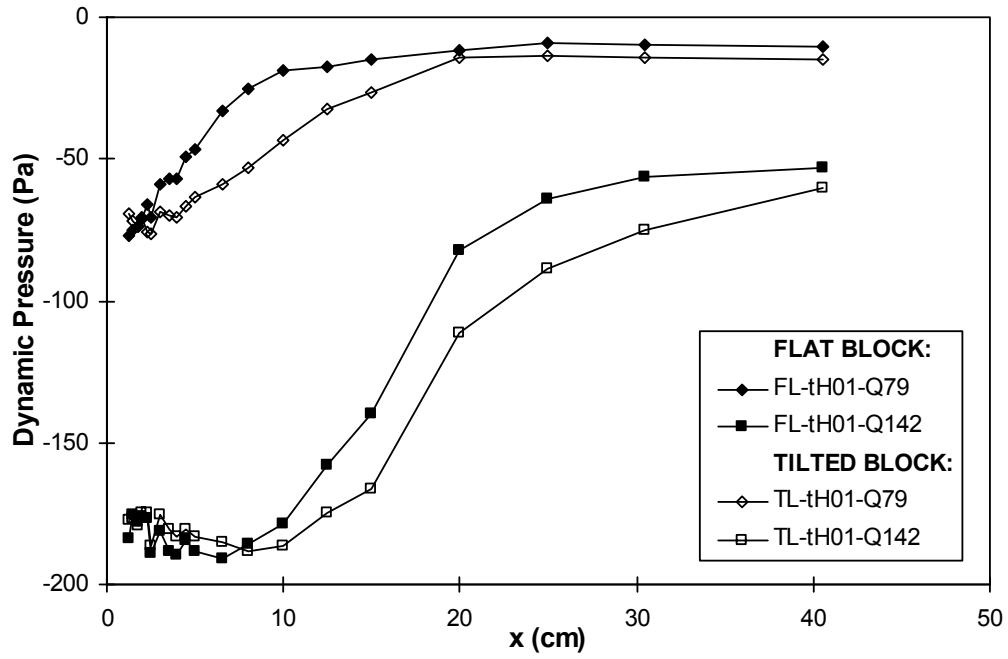
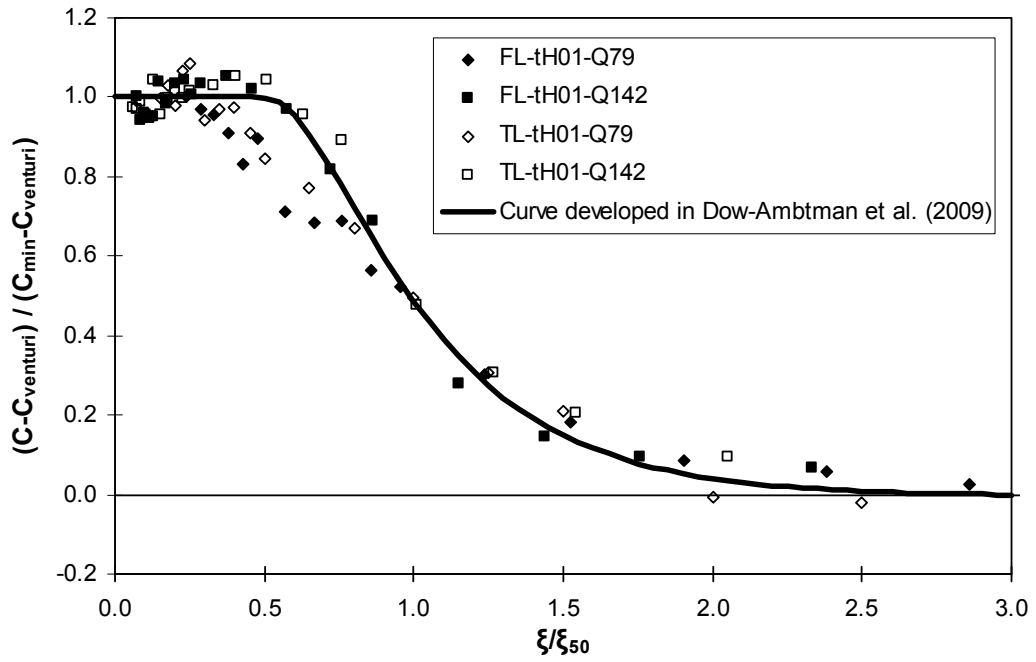
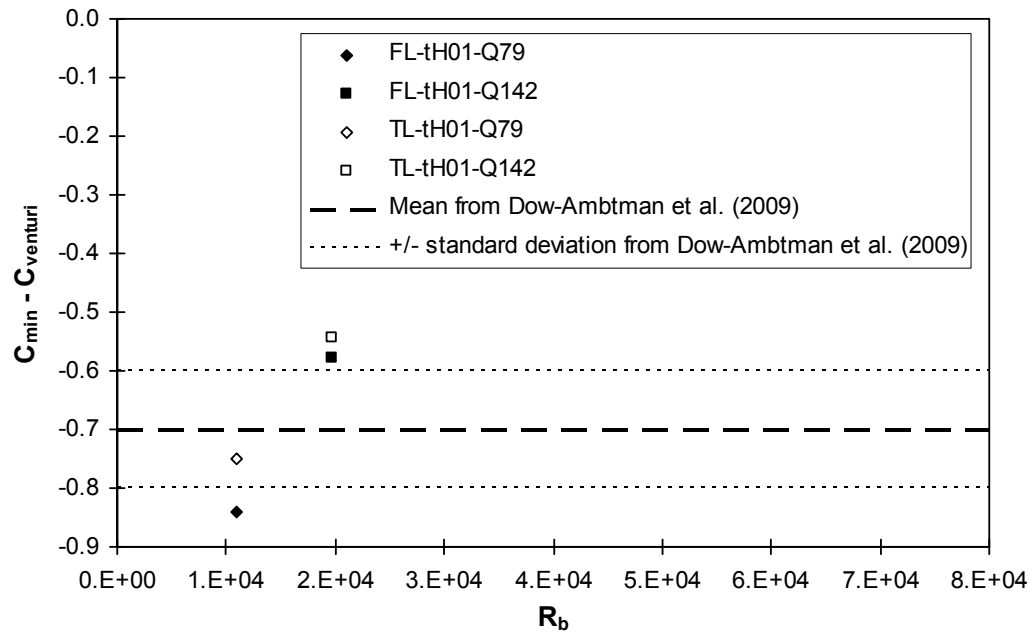


Figure 3-8: Dynamic pressures measured for the tilted block cases.

a)



b)



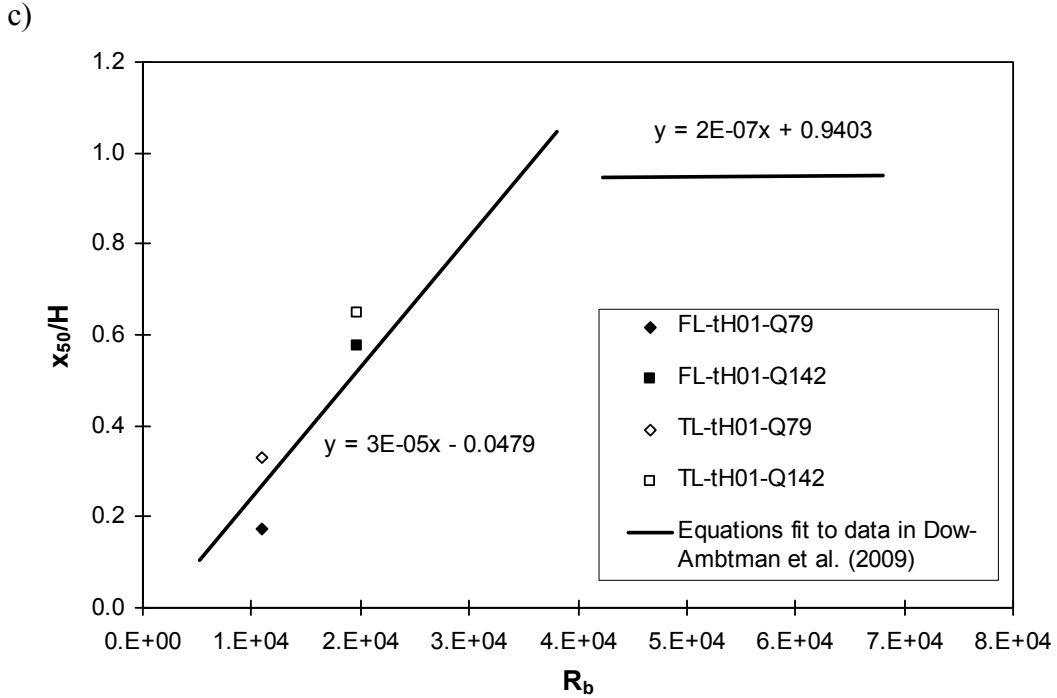


Figure 3-9: a) Non-dimensionalized pressure distribution from Dow-Ambtman et al. (2009) with flat and tilted block data; b) Non-dimensional relationship to determine the minimum pressure coefficient for a rectangular block; c) Non-dimensional relationship for the location at which the pressure is midway between the initial and final pressure plateau values for a rectangular block measured from the leading edge.

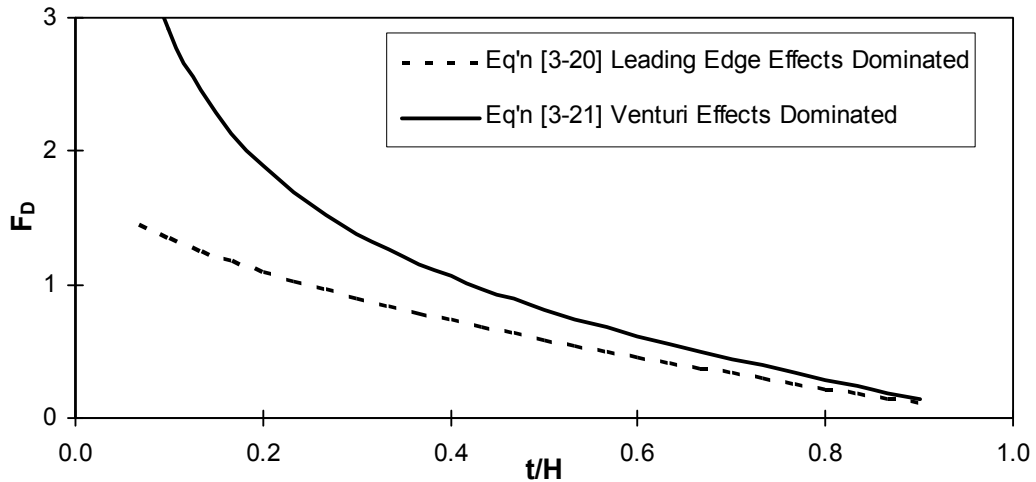


Figure 3-10: Critical densimetric Froude numbers for sinking cases.

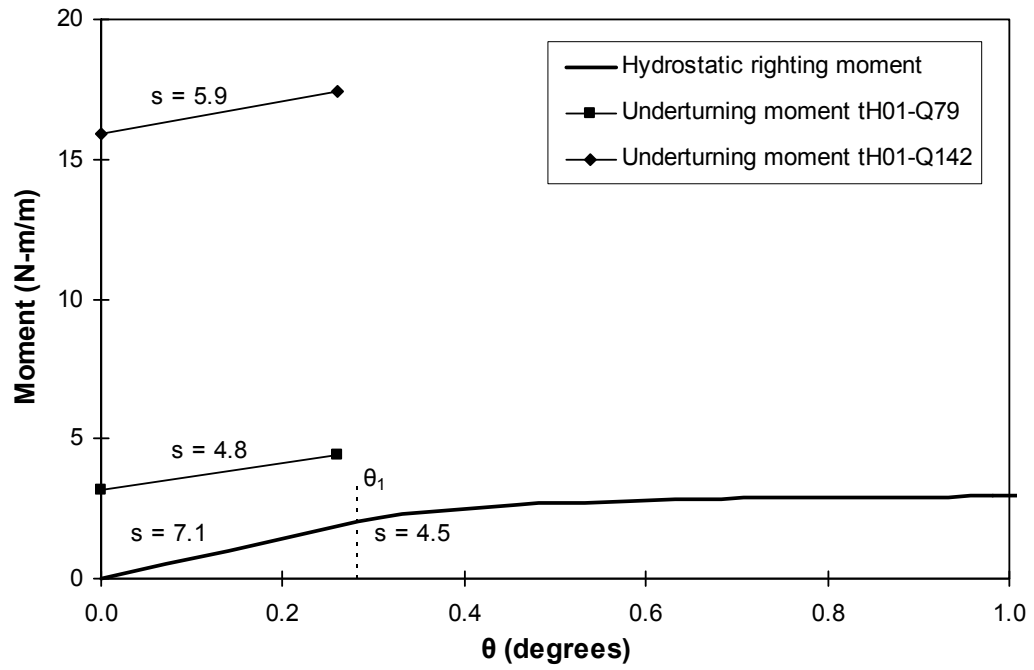
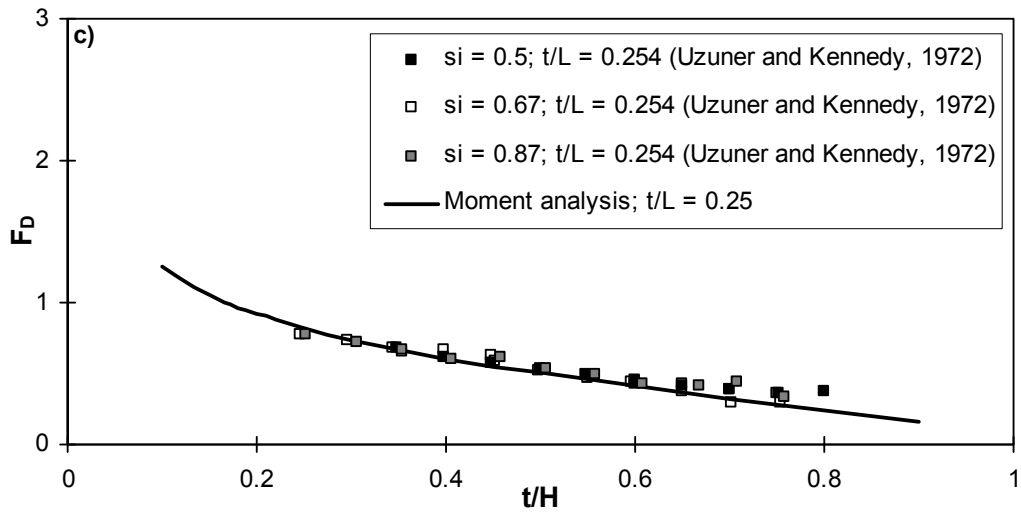
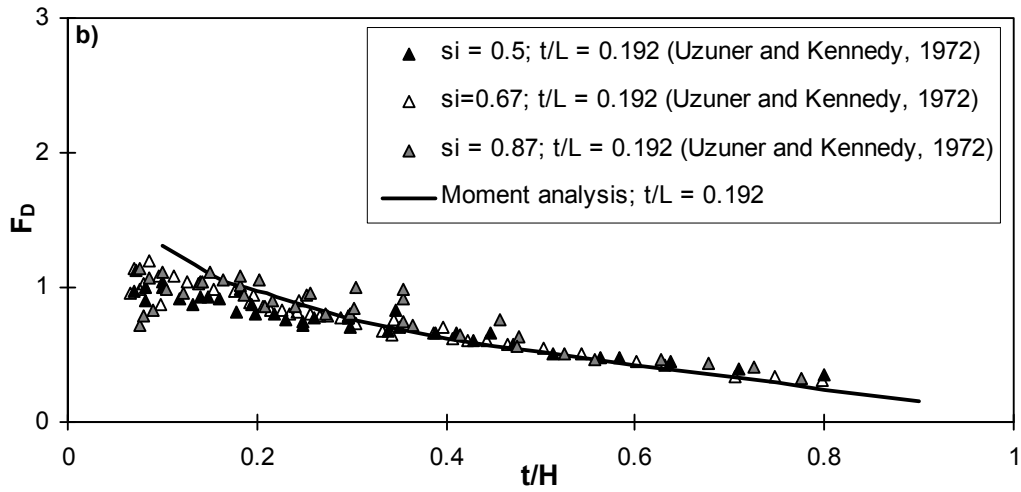
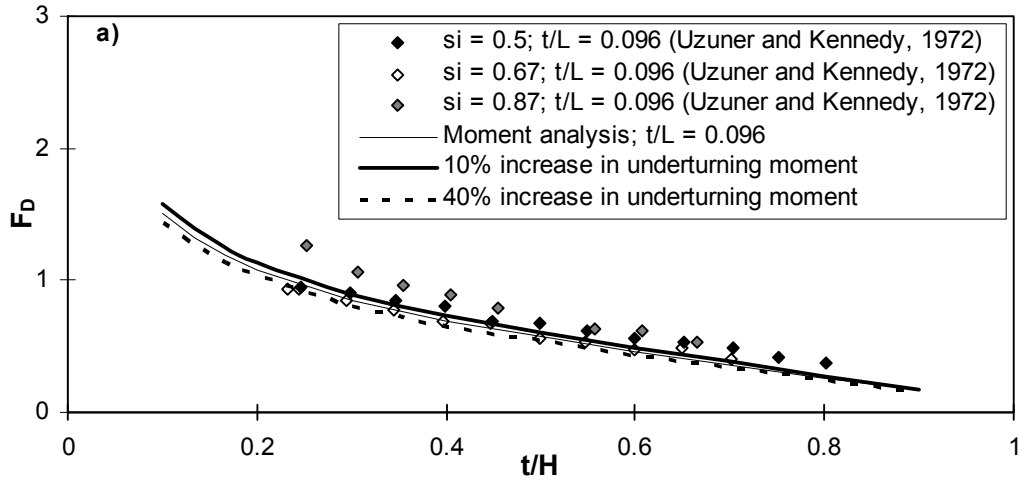


Figure 3-11: Comparison of hydrostatic righting moment to overturning moment.



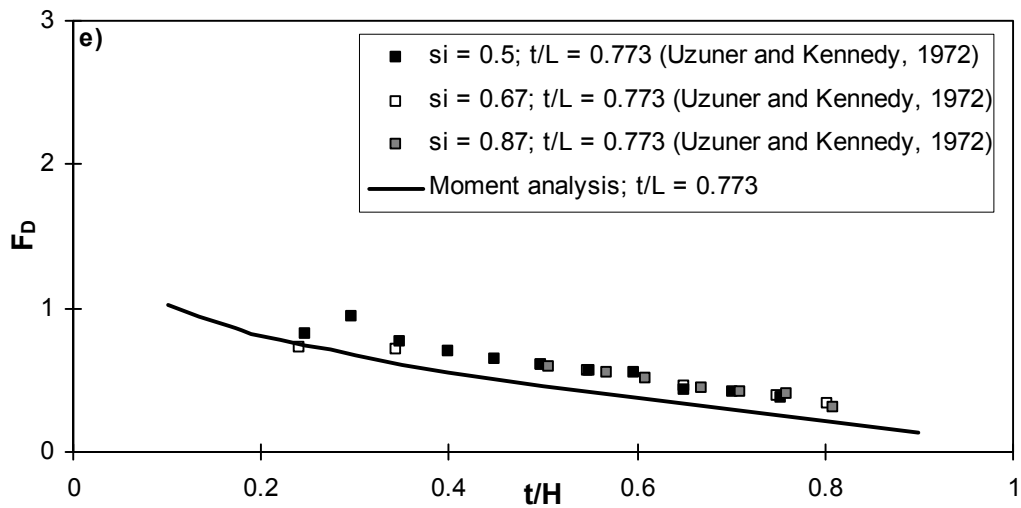
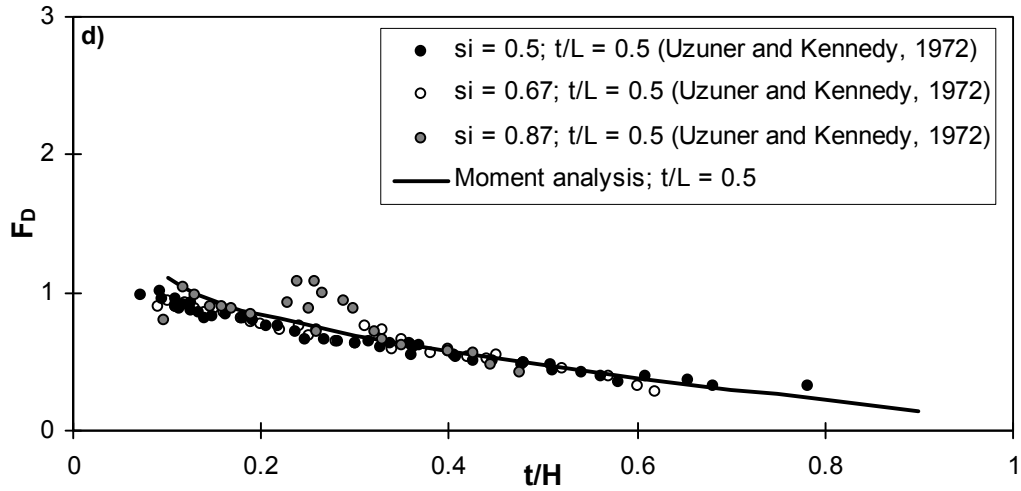


Figure 3-12: Comparison of moment analysis to Uzuner and Kennedy (1972) observations.

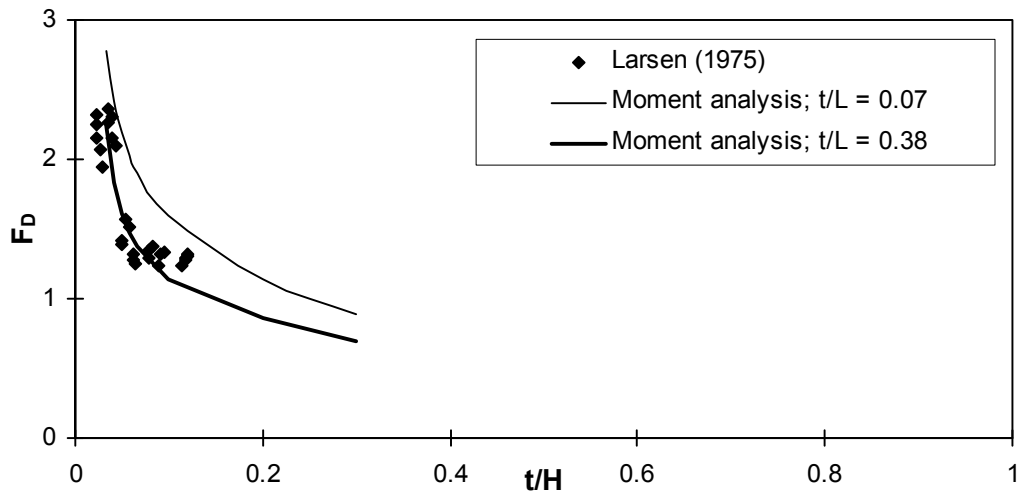


Figure 3-13: Comparison of moment analysis to Larsen (1975) observations.

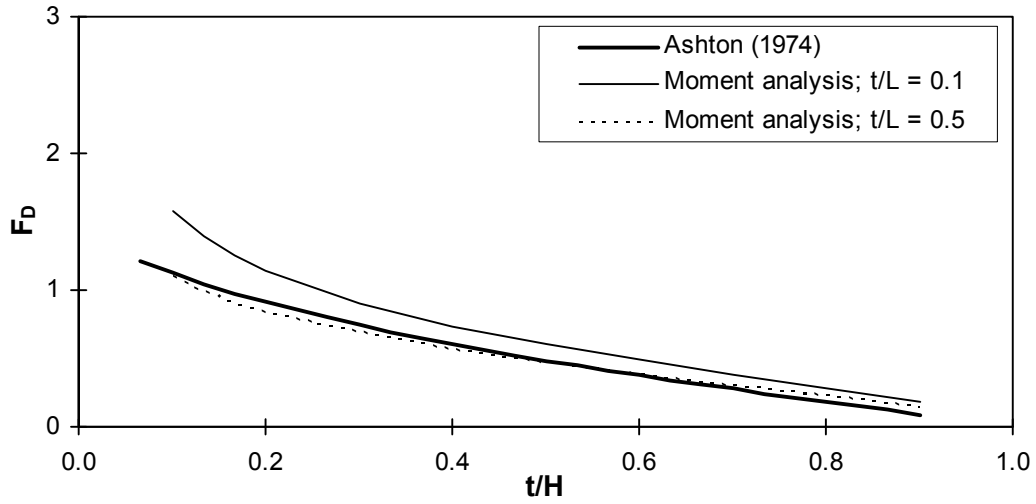


Figure 3-14: Comparison of moment analysis to Ashton (1974) relationship.

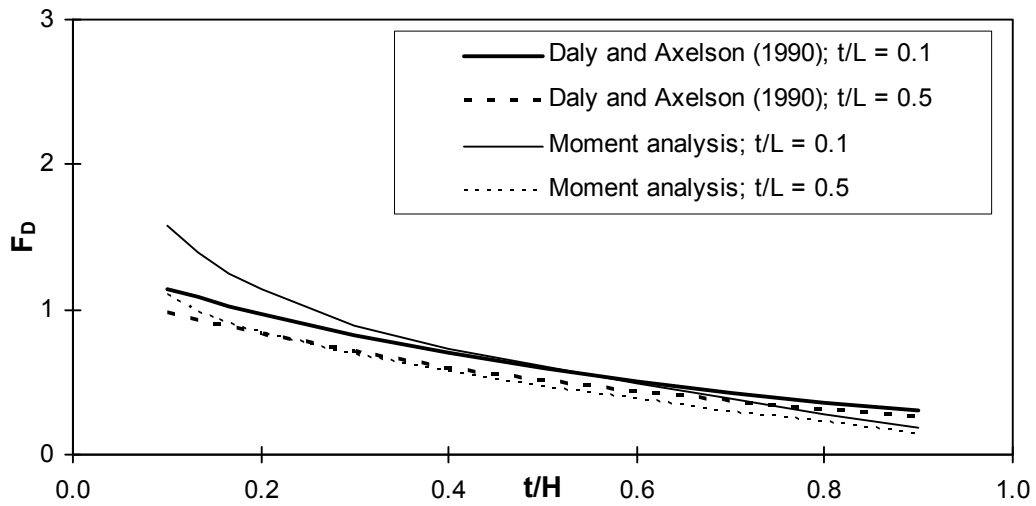


Figure 3-15: Comparison of moment analysis to Daly and Axelson (1990) relationship.

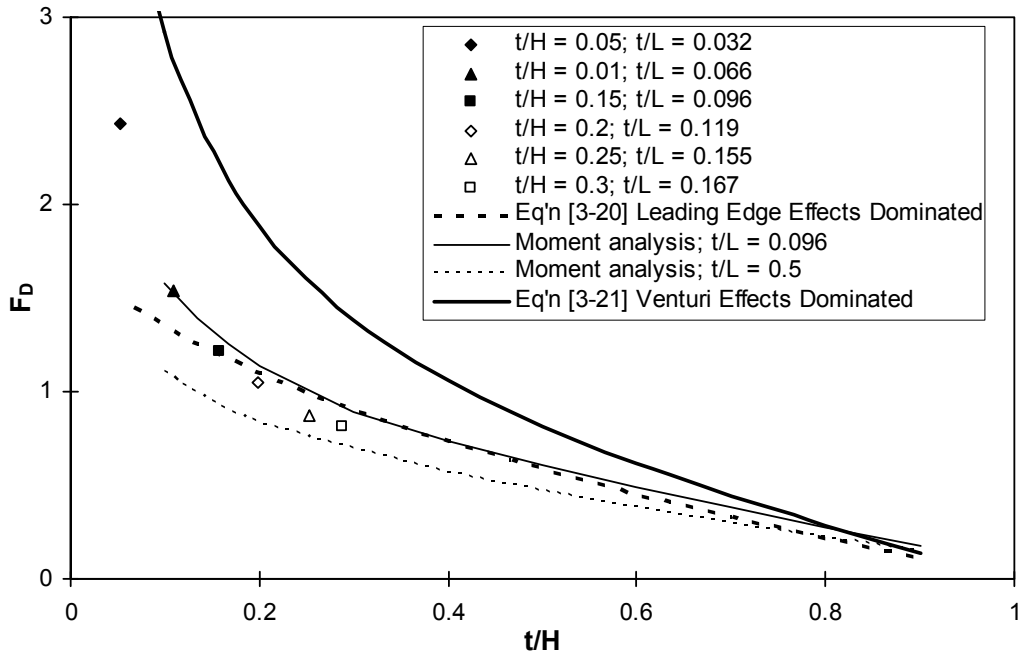


Figure 3-16: Critical densimetric Froude numbers from force-moment analysis.

3.7 REFERENCES

- Ashton, G.D., 1974. Froude criterion for ice-block stability. *Journal of Glaciology*, 13(68), pp. 307-313.
- Beltaos, S., 1995. *River Ice Jams*. Water Resources Publications, LLC, Highlands Ranch, Colorado, 372 pp.
- Chee, S.P. and Haggag, M.R.I., 1978. Instability characteristics of ice blocks, *Proceedings, IAHR Symposium on Ice Problems, Lulea, Sweden, August 7-9, 1978, Vol. II*, pp. 375-388.
- Coutermarsh, B. & McGilvary, W.R., 1991. Pressure distribution of an overturning ice floe. *Proc. 6th Workshop on River Ice*, pp. 143-163.
- Coutermarsh, B.A. and McGilvary, W.R., 1993. Static analysis of floating ice block stability. *Journal of Hydraulic Research*, 31(2), pp. 147-160.
- Coutermarsh, B and McGilvary, R., 1994. Analyzing the stability of floating ice floes. *CRREL Report 94-13*, 19 pp.
- Daly, S.F. and Axelson, K.D., 1990. Stability of floating and submerged blocks. *Journal of Hydraulic Research*, 28(6), pp. 737-752.
- Dow-Ambtman, K.E., Hicks, F.E., and Steffler, P.M., 2009. Experimental investigation of the pressure distribution beneath a floating ice block. *Journal of Hydraulic Research*, submitted.
- Hara, F., Kawai, T., Hanada, M., Nishihata, A., and Saeki, H., 1996. Movement of ice blocks under an ice cover. *Proceedings of IAHR Ice Symposium, Beijing*, pp. 769-778.
- Healy, D. and Hicks, F., 2001. Experimental Study of Ice Jam Shoving. *Proc. 11th Workshop on River Ice, Ottawa, May*, pp. 126-144.
- Healy, D., 2006. Experimental observations on river ice accumulations. Ph.D. Thesis, Department of Civil and Environmental Engineering, University of Alberta, Edmonton, AB, 380 pp
- Jasek, M., 2003. Ice jam release and break-up front propagation. *Proceedings of the 12th workshop on the hydraulics of ice covered rivers, The CGU HS*

- Committee on River Ice Processes and the Environment. June 19-20, 2003, Edmonton, AB, pp. 348-368.
- Kawai, T., Hara, F., Masaki, S., Nishihata, A., and Saeki, H., 1997. Experimental study on the process of ice jam development. Proceedings of 9th CRIPE, pp. 245-256.
- Larsen, P., 1975. Notes on the stability of floating ice blocks. Proceedings of the IAHR third international symposium on ice problems. Hanover, NH, IAHR, pp. 305-313.
- Pariset, E. and Hausser, R., 1961. Formation and evolution of ice covers on rivers. Transactions of the Engineering Institute of Canada, 5(1), pp. 41-49.
- Uzuner, M.S. and Kennedy, J.F., 1972. Stability of floating ice blocks. Journal of the Hydraulics Division, 98 (HY12), pp. 2117-2133.

CHAPTER 4: DPIV INVESTIGATION OF THE FLOW FIELD BENEATH A FLOATING ICE BLOCK

4.1 INTRODUCTION

The phenomenon of ice cover development and potential ice jamming is of major concern to many communities in Canada and the USA. Ice jams can be destructive to both lives and property as they can cause flooding and can release quickly creating dynamic waves of water and ice. Much effort has been put into the development numerical models that predict the frontal progression of ice covers and the formation of ice jams in one or two dimensions. Since it is difficult to directly observe what is happening under an ice cover in the field, experimental and numerical work must be relied upon to understand and predict these ice processes. With advent of sophisticated experimental techniques and instruments, more details of the hydrodynamics surrounding an individual ice floe can now be measured.

A version of this chapter will be submitted to the Journal of Hydraulic Engineering.

It is known that an ice floe approaching an intact ice cover will either come to rest, contributing to the lengthening of the ice cover, or become entrained and deposited beneath the ice cover, potentially leading to the formation of an ice jam. It is known that a floating ice block's instability arises from a pressure reduction beneath the block which is caused by flow acceleration and separation. However, currently numerical ice process models rely on an empirical Froude number criterion, such as the determined by Uzuner and Kennedy (1972), Ashton (1974) and Larsen (1975), to determine ice block stability. Daly and Axelson (1990) attempted to define block stability through a force-moment analysis but had to rely on the data of those previous researchers for the analysis. Coutermarsh and McGilvary (1994) attempted to measure the pressure distribution beneath a floating ice block and found both positive (stabilizing) and negative (destabilizing) pressures acted on the block, with a characteristic saddle shape in the pressure distribution.

In order to model ice cover development processes effectively, specific knowledge of the hydrodynamic forces that act on an individual ice floe must be known. Dow-Ambtman et al. (2009) examined the pressure distribution beneath a floating ice block and developed a method for the prediction of the submerging forces and moments acting on a block. Because this pressure reduction is caused by flow acceleration and separation, it is important to understand how the velocity field beneath the floating ice block relates to the corresponding pressure reduction. Furthermore, it is possible that the unsteady flow characteristics due to vortex shedding at the leading edge of the block may contribute to its instability. If this is the case, the submerging forces and overturning moments developed from the mean pressure distribution may not be sufficient for determining block stability, and time varying properties would need to be considered. The purpose of this study was to explore this question.

Digital Particle Image Velocimetry (DPIV) is a relatively new technique which uses optical imaging techniques to measure fluid velocity vectors at thousands of

points in a flow field simultaneously. It is a non-intrusive technique that can be used to measure the two or three dimensional instantaneous velocity field of a fluid. Other flow properties, such as vorticity, turbulent velocities, and turbulent kinetic energy, can be computed from the measured velocity field. DPIV requires the water to be seeded with tracer particles, a light source to illuminate the particles and a high speed video camera to capture images spaced a certain time apart. The images are then analyzed to determine the displacements of the particles from one image to the next and from this the instantaneous velocity field can be calculated.

With recent advancements in the DPIV technique, investigators have begun to examine flow separation under various conditions. For example, it has been applied successfully by Huang and Fiedler (1997) to investigate the behavior of the starting flow downstream of a backward-facing step, by Higuchi et al (2006) to investigate axial flow over a blunt circular cylinder, by Burgmann and Schroder (2008) to investigate the separation bubble on the suction side of an SD7003 airfoil, and by Agelinchabb and Tachie (2008) to investigate separated flow over two dimensional transverse blocks of square, rectangular and semi-circular cross sections. All of these studies employed the DPIV technique to investigate the flow development and flow separation around these objects. This study will employ a similar methodology to examine the flow separation and development at the leading edge of a floating ice block.

For this study, three cases were selected to examine the effect of changing the block thickness and the shape of the leading edge of the block on the velocity field beneath a floating ice block. The mean velocity field results were compared to the corresponding measured dynamic pressure distributions from Dow-Ambtman et al. (2009). The mean velocity patterns were examined and compared to the time-varying behaviour of the velocity field to determine if the methods developed in Dow-Ambtman et al. (2009) could be considered representative, or if unsteady vortex behaviours should be considered. Ultimately, the results of this

study will be used to validate a 3-D numerical model which can then be used to investigate a broad range of scenarios.

4.2 EXPERIMENTAL METHODS

Three scenarios were tested to measure the instantaneous velocity fields beneath the leading edge of a floating ice block using DPIV technique. Table 4-1 summarizes the experimental variables of these tests. In this table, t refers to the thickness of the block, H the approach flow depth, Q the flow rate, V the average approach flow velocity, V_u the average under block velocity, F_a the Froude number of the approach flow and R_a is the Reynolds number of the approach flow. Case 1, tH005, examined the velocity beneath a rectangular block of block thickness-to-approach flow depth ratio of 0.05; Case 2, tH01, increased the block thickness of the rectangular block for a block thickness-to-approach flow depth ratio of 0.1; and Case 3, tH005Round, examined the velocity beneath a block with a rounded leading edge of block thickness-to-approach flow depth ratio of 0.05. All cases were tested at the same flow rate. The cases were chosen to examine the effects of both increasing the block thickness and rounding of the block's leading edge.

The experiments were carried out in a 7.5 m (metre) long re-circulating flume located in the T. Blench Hydraulics Lab at the University of Alberta. This rectangular flume, shown in Figure 4-1, has 0.45 m high side walls and a width of 0.75 m. The flume bed and walls are made of glass to facilitate modern optical measurement techniques, such as particle image velocimetry. The pump is controlled by a variable frequency drive and has a maximum discharge of 150 L/s. Flow rates are measured with a magnetic flow meter.

A hollow rectangular block 50 cm long, 75 cm wide and total thickness of 10.1 cm was constructed of Plexiglas. A second hollow Plexiglas block was constructed with a rounded leading edge as shown in Figure 4-2. This block was

51.45 cm long, 75 cm wide, and a total thickness of 14.2 cm. To enable the simulation of various thicknesses of floating ice, the block was held in position by four threaded rods that allowed for height adjustment. Both the rectangular and rounded blocks were painted black in order to minimize reflections of the laser sheet. The block was positioned in the flume with the leading edge at $X = 4$ m to ensure the flow was fully developed before reaching the block, and to ensure it would not be affected by the outlet. The block was positioned vertically by adjusting the threaded rods to the desired elevation and using a digital level to ensure the block was level. The effective thickness of the “ice” was determined based upon assuming a typical specific gravity of ice of 0.92. The water depth and block height were measured using a point gauge.

A compact, dual head Nd-YAG laser system was used (Gemini PIV 90-30 Nd:YAG laser system, New Wave Research Inc., Fremont, CA, USA). This laser system has a maximum energy output of 90 mJ per 3 – 5 ns pulse, operating at a wavelength of 532 nm with a maximum 30 Hz repetition rate. The laser head was mounted on a frame and was positioned approximately 1.5 m from the edge of the flume. In order to produce the desired laser sheet, a double optical lens combination was used, as shown in Figure 4-3. The laser beam first passed through a spherical lens (focal length of 1 m) positioned 13 cm from the laser head, which reduced the beam diameter in all directions, then passed through a plano-cylindrical lens (focal length of -19.0 mm) positioned 20.5 cm from the laser head, which expanded the beam into a laser sheet. A mirror tilted to 45° was placed beneath the flume to reflect the laser sheet up into the flow, creating a laser sheet thickness in the area of interest of approximately 2.25 mm. To avoid reflections off of pressure tap holes drilled into the block (see Dow-Ambtman, 2009), the laser head was positioned so that it was 1.1 cm off the flume centerline. There was a slight discrepancy in the thickness and alignment of the two laser heads, but this was confirmed to have negligible effect on the PIV results.

A monochrome, 2 megapixel (1600 x 1200 pixels) CCD camera was used to capture the DPIV images (Dalsa 2M30-SA, model DS-21-02M30, Waterloo, ON, Canada). The camera was mounted on the frame directly above the laser head and was positioned approximately 1.3 m from the flume edge. The camera was outfitted with a 75 mm Fujinon optical lens (Fuji photo optical co 613974 1:18/75) and was tilted down 1° in order to avoid reflections of the laser sheet off the block bottom and water surface. Images were acquired at a rate of 30 Hz through a Pentium-III personal computer equipped with a DVR Express® camera interface (IO Industries, Inc., Canada) and digital video recording software, Video Savant® Basic 4.0 (IO Industries, Inc.), running under Microsoft Windows XP. The images were streamed to a striped array of SCSI drives and ultimately stored as 8-bit gray scale TIFF images on an external hard disk.

The field of view of the camera was 25 by 18.75 cm, for a resolution of 0.15625 mm per pixel and was positioned at the leading edge of the block, approximately 5 cm upstream of the block edge. Figure 4-4 shows an example of the field of view for Case 2: tH01. For the rectangular block cases, the corner of the block closest to the camera obstructs the field of view immediately upstream of the block's leading edge, as shown in Figure 4-5. The true leading edge of the block at the block centerline for the rectangular cases is located at pixel 280 or $x_{FOV} = 4.375$ cm.

The camera and the laser were synchronized through a four channel digital delay generator (BNC 500, Berkeley Nucleonics Corporation, San Rafael, California) to generate a time spacing between the laser pulses of 2.52 ms. A discussion on the timing sequence can be found in Appendix A of Dow-Ambtman (2009). The water was seeded with Conduct-O-Fil® silver coated hollow glass spheres (Potters Industries, Valley Forge, PA, USA). A combination of two types of spheres were used: SH230S33 which has an average particle diameter of 44 μm and density of 0.5 g / cc and SH400S20 which has an average particle diameter of 13 μm and density of 1.6 g / cc. Sufficient seed particles were added in order to

achieve a good seed density; an example is shown in Figure 4-6. The laser was operated at 95% power for 10 minutes, collecting 18000 images for each test case.

4.3 DATA PROCESSING

The images were processed using a workspace developed for use with Heurisko Runtime V.4.0.8 (AEON Verlag and Studio, Germany). This iterative-multigrid DPIV algorithm was applied to the images to obtain the instantaneous 2-D velocity fields. This algorithm was developed using Heurisko® software in C language by Marxen (1998) and is a cross-correlation based DPIV algorithm similar to Willert and Gharib (1991). M. Mukto developed the third version of the workspace, applying improvements to the algorithm as part of his doctoral research. He adopted an iterative-multigrid algorithm similar to Scarano and Riethmuller (2000), applied the Gaussian digital masking technique (Gui et al, 2001) to reduce the uncertainty of the estimation, and applied the universal outlier detection algorithm of Westerweel and Scarano (2005) for the detection of spurious vectors. Table 4-2 summarizes the workspace parameters used in this analysis. Figure 4-7 illustrates the profiles applied for each case, shown as the white line. In this workspace, a grid distance refers to the distance between grid points which is half of the resolution due to the 50% overlap in search windows.

A subset of 100 images was processed for each run to determine the most appropriate grid resolution for the full analyses. Grid distances of 32, 16 and 8 pixels were considered and, in general, it was found that as the grid distance was decreased, more detail in the velocity field could be seen; however, the volume of data produced increased significantly. The three grid distances were quantitatively compared based on the number of spurious vectors detected, the average pixel displacements, average velocity contours and vectors and maximum, minimum and mean velocity in each column (Dow-Ambtman, 2009). For a grid distance of 16 pixels the average number of spurious vectors detected over the 50 image pairs for was 0.3% for Case tH005, 1.1% for Case tH01 and 0.2% for Case

tH005Round. The average raw pixel displacement in the x-direction for a grid distance of 16 was 8.1 pixels for Case tH005, 8.4 pixels for Case tH01 and 8.3 pixels for Case tH005Round. For the mean velocity properties, it was also found that a grid distance of 16 pixels was sufficient for all three test cases. However, in order to see sufficient detail within the recirculation zone for Case tH005, a grid distance of 8 pixels was necessary.

4.4 EXPERIMENTAL RESULTS

In the following, the results of 2D time resolved PIV measurements are presented. The results were analyzed from the 18000 processed images using a grid distance of 16 pixels unless otherwise specified. At this resolution the closest vector to the bottom surface of the block would be 16 pixels, assuming that reflections at the block surface were minimized and that the block profile was accurately defined.

4.4.1 Flow Development

The mean velocity field beneath the block was analyzed for the three cases. The mean velocity contours and vectors are shown in Figures 4-8 through 4-13. For all three cases, the block causes the water to slow at the water surface as the flow approaches the block. It is evident from these figures that the sharp edge of the rectangular block causes the flow to separate at the leading edge forming a recirculation zone that is shown clearly in Figures 4-9 and 4-11. The separation zone created by the thicker block extends further along the block and penetrates further into the flow area. Beneath the separation zone, the flow accelerates; the greater magnitudes of the velocities reached in the thicker block case are largely due to the greater flow constriction. As the shear layer reattaches, the flow begins to reach steady state conditions and the velocity contours level out following the block profile. In contrast, as seen in Figure 4-13, the flow beneath the rounded block follows the block profile with no separation or recirculation observed. The velocity beneath the rounded block remains relatively uniform, as shown in the velocity contours of Figure 4-12. This can also be seen in the mean streamlines

for the three cases in Figure 4-14. Higuchi et al (2006) observed a similar streamline pattern to that presented here for their flow over a blunt cylinder.

The flow development beneath the block at five profile locations is examined in Figures 4-15 to 4-17. The profiles are compared: just before the block ($x_{FOV} = 2.49$ cm), at the leading edge of the block ($x_{FOV} = 4.49$ cm), within the recirculation zone ($x_{FOV} = 6.99$ cm), at middle of the block ($x_{FOV} = 12.5$ cm) and near the end of the block ($x_{FOV} = 20.24$ cm). All three cases show a deceleration of the flow at the water surface just before the block. For the rectangular block cases this effect extends further into the flow and shows a velocity of zero at the water surface or even a slightly negative velocity for the thicker rectangular block case indicating a small recirculation zone. The mean approach velocity is consistent between the three cases. At the leading edge of the blocks, the velocity profiles are constant with some deceleration near the block surface. At $x_{FOV} = 6.99$ cm, flow beneath the rectangle blocks is in the recirculation zone with the thicker rectangular block case showing a larger recirculation. Flow beneath the rounded block shows consistent velocity profiles for the remainder of the block and has therefore reached steady state conditions at this point. At $x_{FOV} = 12.5$ cm, the separation zone for Case1: tH005 has reattached while the separation zone for Case2: tH01 has grown in thickness. The final velocity profile shows the flow beneath the rectangular block cases approaching uniform flow with a larger magnitude of velocity beneath the thicker block due to the greater block thickness.

Examining the velocity pattern in greater detail and comparing the three cases, Figure 4-18 through 4-20 shows the mean, minimum and maximum velocities beneath the block, respectively, plotted as a function of distance from the leading edge of the block. As the flow approaches the block, the thinner block cases have the same mean approach velocity while the thickest block case has a lower mean approach velocity, likely from a greater backwater effect. This is also evident from the minimum velocities as the thickest block has the smallest minimum

velocity approaching the block. The rectangular block cases show comparable velocity patterns. There appears to be a jump in the mean velocity, but this is artificial, due to the obstruction of the view of the slower velocities from the block corner. As the fluid accelerates around the rectangular block, the velocity increases to a maximum then decreases gradually to a constant value; however, the thicker block stays at a maximum longer due to the longer separation zone. The minimum velocity appears to peak at the leading edge of the block, which indicates that the velocity gradients are high at this location so the grid resolution is too large to resolve the slow velocity near the block. Through the separation zone, the minimum velocity remains near zero then increases as the flow begins to stabilize to a normal velocity profile. The magnitude does not reflect the actual minimum velocity but rather the resolution of the PIV near the block surface. In contrast, the velocity under the rounded block increases steadily as the flow accelerates to adjust to the reduced flow area before coming to a plateau. Again there appears to be a sharp increase in the minimum velocities at the leading edge reflecting the resolution of the PIV. Comparing the final mean velocities to the expected under block values tabulated in Table 4-1 the final mean velocity reached for Case 2: tH01 was slightly lower than what was expected at 52.9 cm/s, while Case 3: tH005Round was very close to the expected at 51.8 cm/s and Case 1: tH005 at 50.7 cm/s.

Examining the location of the maximum and minimum velocities relative to the bottom of the block surface in Figures 4-21 and 4-22, respectively, the rectangular block cases show a similar pattern. The maximum velocity moves sharply towards the block surface as the flow accelerates around the block, gradually moving away from the block, then moves sharply away from the block before becoming steady. The minimum velocity stays at the block surface moving away from the block through the recirculation zone. For the rounded block case, the maximum velocity also moves towards the block bottom as the flow accelerates around the block then drops suddenly and plateaus where the flow reaches steady conditions. The maximum velocity is located at a point that is approximately half the depth of the

flow. The shifting of the minimum velocity for the rounded block case is an artifact of the PIV resolution, as the minimum velocity would be at the block surface.

4.4.2 Length of Separation Zone (rectangular block cases)

For this study, the separation zone length was defined using the method of Agelinchabb and Tachie (2008), in which the end of the separation zone is defined as the point at which the mean, U , velocity at the first grid point beneath the block switches from negative to positive, or when the mean velocity at the first grid point beneath the block reaches zero. Figure 4-23 shows the mean longitudinal, U , velocity beneath the block for Case 1: tH005 plotted as a function of distance from the leading edge of the block. From this figure it is evident that the length of the separation zone is 4.46 cm and the recirculation zone begins 1.74 cm from the leading edge. In comparison, Figure 4-24 displays the mean longitudinal, U , velocity beneath the block for Case 2: tH01. For this case the separation zone extends 12.71 cm from the leading edge of the block with the recirculation zone beginning 1.05 cm from the leading edge.

As was observed by other researchers (Higuchi et al., 2006), the separation zone appeared well defined when averaged over the 18000 images; however, when examined through the instantaneous velocity fields, the separation zone length varied considerably, often composed of several separate vortices. When the instantaneous velocity fields were analyzed, the mean longitudinal velocity, U , beneath the block was found to change from negative to positive several times. The mean number of velocity changes beneath the block detected for Case 1: tH005 was 2.4 as shown in the histogram of Figure 4-25. In comparison, the mean number of velocity changes beneath the block detected for Case 2: tH01 was 2.2 as shown in the histogram of Figure 4-26. This can be seen clearly when examining the instantaneous velocity and vorticity fields in Figures 4-27 and 4-28 which are shown for four consecutive image pairs.

4.4.3 Reynolds Stresses

The Reynolds stresses were calculated for the two rectangular block cases and non-dimensionalized with the average approach velocity as:

$$\text{Re} = -\frac{\overline{uv}}{V^2} \quad [4-1]$$

where u and v are the instantaneous turbulent velocities in the x and y directions, respectively. The Reynolds stress is an indication of the shear stress of the separation zone. Figures 4-29 and 4-30 shows the contours of the Reynolds stresses for the rectangular block cases, both calculated using a grid distance of 8 pixels, as well as plots of the maximum Reynolds stress beneath the block. As can be seen in the figures, the two cases have a similar pattern with the Reynolds stress both larger in magnitude and shifted further downstream, for the thicker block. Burgmann and Schröder (2008) showed a similar distribution of Reynolds stress within their separation zone over an airfoil, with their plot of maximum Reynolds stress showing a similar shape to that presented here.

4.4.4 Comparison to pressure distribution

The DPIV results were compared to the measured pressure distributions of Dow-Ambtman et al. (2009). Comparing the experimental variables of the DPIV in Table 4-1 to the experimental variables of the pressure measurements from Dow-Ambtman et al. (2009) in Table 4-3 the block thickness for Case 1: tH005 is slightly higher for the DPIV case but the resulting average velocities are comparable, the block thickness for Case 2: tH01 is slightly lower for the DPIV case and likewise for the resulting average velocities, while the rounded block experimental variables are almost identical. Dow-Ambtman et al. (2009) found that the pressure distribution for the rectangular block cases began at a minimum pressure plateau that extended some distance from the leading edge of the block, then recovered to a second pressure plateau which they found could be estimated as the venturi pressure. They defined x_{50} as the point at which the pressure was

midway between the minimum pressure and venturi pressure and used this to non-dimensionalize the data. They suggested that the pressure reduction beneath a block is affected by two separate effects: a pressure reduction due to leading edge effects and a pressure reduction due to venturi effects.

Comparing the mean, maximum and minimum velocities to the measured pressure distributions in Figures 4-31 through 4-33, it is apparent that the minimum pressure corresponds with the peak maximum velocity for all three cases. The peak maximum velocity observed for each of the cases occurs at the minimum pressure. The peak maximum velocity observed for Case 1: tH005, Case 2: tH01 and Case 3: tH005Round were 62.6, 67.1, and 54.4 cm/s respectively. The minimum pressures observed were -112, -132 and -49 Pa respectively. If the pressure difference is calculated following the Bernoulli equation, using the approach mean velocity and the peak maximum velocity the estimated pressure difference is -89, -131, and -39 Pa, respectively. These correspond to the observed minimum pressures, suggesting that it is the localized flow behaviour that causes the initial pressure reduction at the leading edge. For the thinner rectangular block (Case 1), the pressure begins to recover as the maximum velocity decreases. For the thicker rectangular block (Case 2), the maximum velocity peaks around the minimum pressure then decreases only slightly through the initial pressure plateau. The pressure begins to recover as the maximum velocity stabilizes. In all three cases the pressure stabilizes to $P_{venturi}$ as the flow reaches steady state.

Comparing the length of the separation zone for the rectangular block cases with the pressure distribution in Figures 4-34 and 4-35, the position of the mid pressure of x_{50} corresponds well with the end of the separation zone for both cases. For the thinner block, x_{50} occurs at 4.3 cm while the separation zone ends at 4.46 cm and for the thicker block, x_{50} occurs at 13.1 cm while the separation zone ends at 12.7 cm. The length of the initial minimum pressure plateau extends for approximately half the length of the separation zone before beginning to recover to the venturi

pressure, which is consistent with the findings in Dow-Ambtman et al. (2009) that suggested the value of x_{50} is twice the length of the minimum pressure plateau. This supports the theory that the pressure reduction is due to two separate effects, initially being affected by localized flow behaviour due to flow separation and acceleration, then stabilizing to the mean under block velocity due to the flow constriction of the block.

In terms of unsteady flow behaviour, it is unlikely that that vortex shedding at the leading edge could cause the block to destabilize and become entrained. The minimum leading edge pressure reduction appears to be correlated with the fluid acceleration around the block for all three cases and the extent of the pressure reduction appears to be correlated with the size of the main separation zone for the rectangular block cases. There will be some fluctuation in the peak maximum velocity under the block and some fluctuation in the strength of the separation zone, but qualitatively it is unlikely that these fluctuations would be sufficient to destabilize the block to cause entrainment. Thus, the mean flow properties and mean pressure reduction should be adequate for analyzing ice block stability.

4.5 CONCLUSIONS AND RECOMMENDATIONS

DPIV was employed to investigate the velocity field beneath the leading edge of a floating ice block for three cases of varying ice thickness and leading edge shape. These results provide valuable information about the velocity development beneath a floating ice block. The velocity field beneath a rectangular block was found to separate at the leading edge creating a recirculation zone that extends some distance from the leading edge. The separation was found to extend further along the block and penetrate further into the flow as the thickness of the block increased. In contrast the rounded block did not produce any flow separation; the flow followed the block profile as it accelerated under the block. The separation zone beneath the rectangular blocks appeared well defined when examining the mean velocity field averaged over the 18000 images; however, when examined

instantaneously, the separation zone length varied considerably and was often composed of several separate vortices. The Reynolds stress beneath the rectangular blocks was found to increase to a maximum, with the maximum peak shifted further along the block for the thicker block.

The DPIV results were compared with previously measured dynamic pressure distributions. The location of the peak maximum velocity was found to correlate well with the measured minimum pressure for all three cases. For the rectangular block cases, the extent of the initial pressure plateau was found to correlate with the middle of the separation zone and the position of the mid-pressure, x_{50} , was found to correlate well with the end of the separation zone. For the thicker block case, both the velocity distribution and pressure distribution were observed to have a different shape than that of the thinner block. The pressure at the leading edge of the block appears to be affected by localized flow patterns and stabilizes as the flow reaches the mean under block velocity. The unsteady flow behaviour was examined and was found that the mean flow properties and mean pressure measurements are adequate for analyzing the block stability.

This study will provide valuable validation data for a 3-D numerical model which will be used to examine a broad range of scenarios. Future work in this area could use DPIV to examine the velocity field beneath a rough ice cover or ice jam. It could be used to track a block's entrainment beneath an intact ice cover to see how the velocity field changes and to track the entrained block's trajectory. It would be useful for determining under what conditions an entrained block come to rest beneath an intact ice cover.

Table 4-1: Summary of experimental data.

Run #	t (cm)	H (cm)	t/H	Q (L/s)	V (cm/s)	V_u (cm/s)	F_a	R_a
tH005	1.63	30.61	0.053	110.4	48.1	50.6	0.28	1.47E+05
tH01	3.01	30.32	0.10	110.3	48.5	53.4	0.28	1.47E+05
tH005Round	1.89	30.49	0.062	110.4	48.3	51.2	0.28	1.47E+05

Table 4-2: Summary of variables used to process the images.

Variable	Setting
Number of iterations	3
Number of pixels - x	1600
Number of pixels - y	1200
Origin of first pixel	0.5
Window shift type	Cardinal Sync Interpolation Function
Apply Gaussian Mask?	Yes
Subtract local mean intensity from windows?	No
Surface profile?	Yes
Test type for detection of spurious PIV data	Universal Outlier Detection
Initial threshold values	2.0; 0.5
Correct for background image?	No
Image preprocessing parameters	{3.0, 0.0, 200.0, 32.0, 1.2}
CMAREAS	5.0
Stencil	3.0
RESETVAL	1.0
Initial particle image pattern size	64
Search particle image pattern size	128
Distance between grid points	32
Peak threshold	2

Table 4-3: Summary of experimental variables from pressure measurements in Dow-Ambtman et al. (2009).

Run #	t (cm)	H (cm)	t/H	Q (L/s)	V (cm/s)	V_u (cm/s)	F_a	R_a
tH005-Q111	1.59	30.64	0.05	111	48.2	50.6	0.28	1.48E+05
tH01-Q111	3.29	30.20	0.11	111	49.0	54.4	0.28	1.48E+05
RD-tH005-Q111	1.89	30.45	0.06	111	48.7	51.4	0.3	1.48E+05

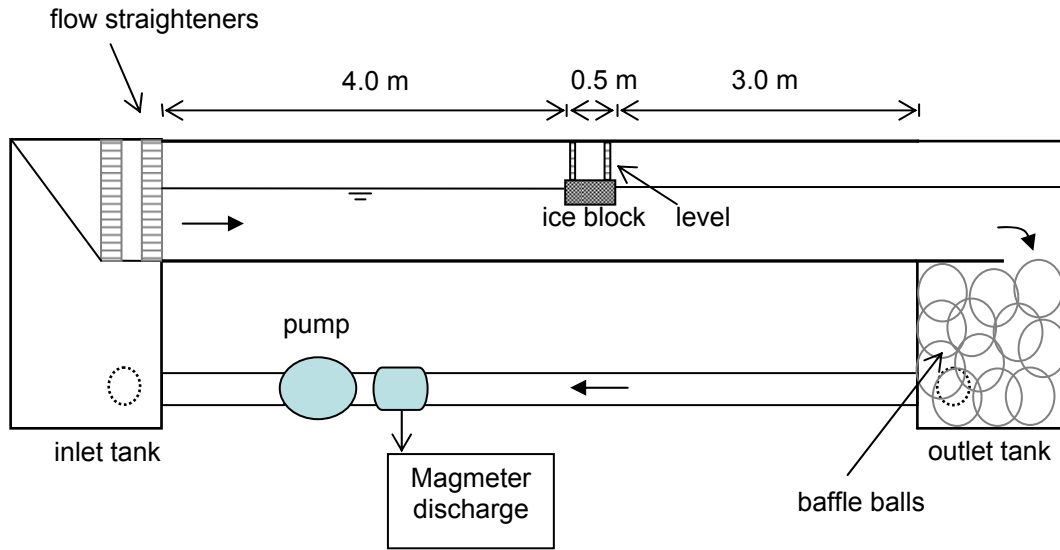


Figure 4-1: Schematic of experimental setup.

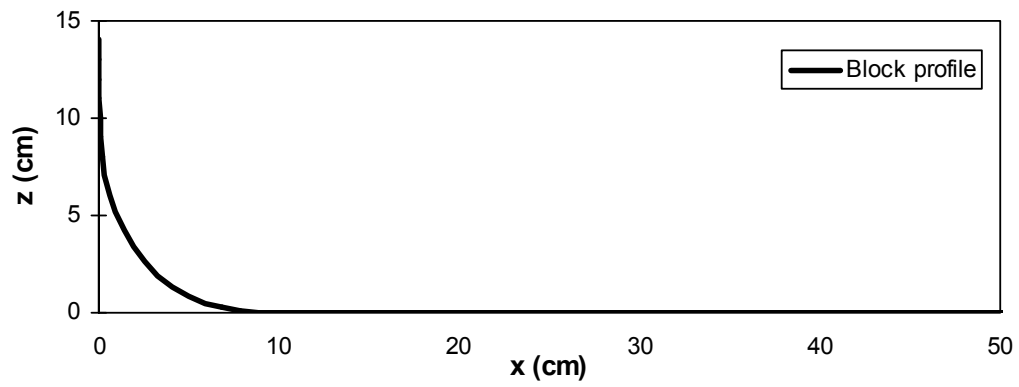


Figure 4-2: Rounded block profile.

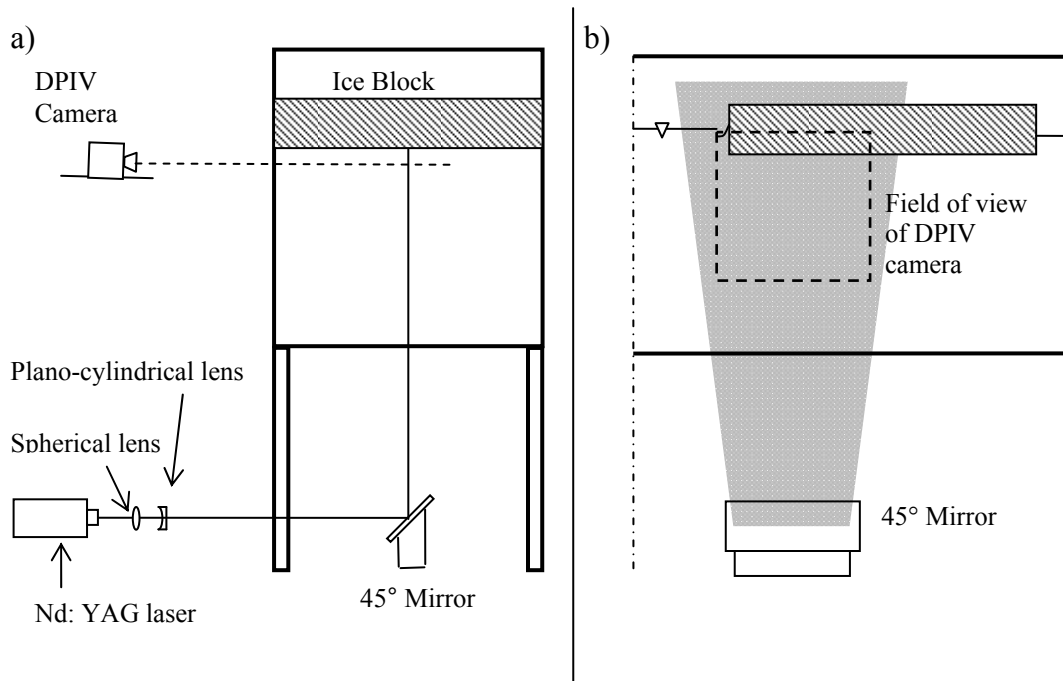


Figure 4-3: Schematic of laser system setup: a) in profile; b) in plan.

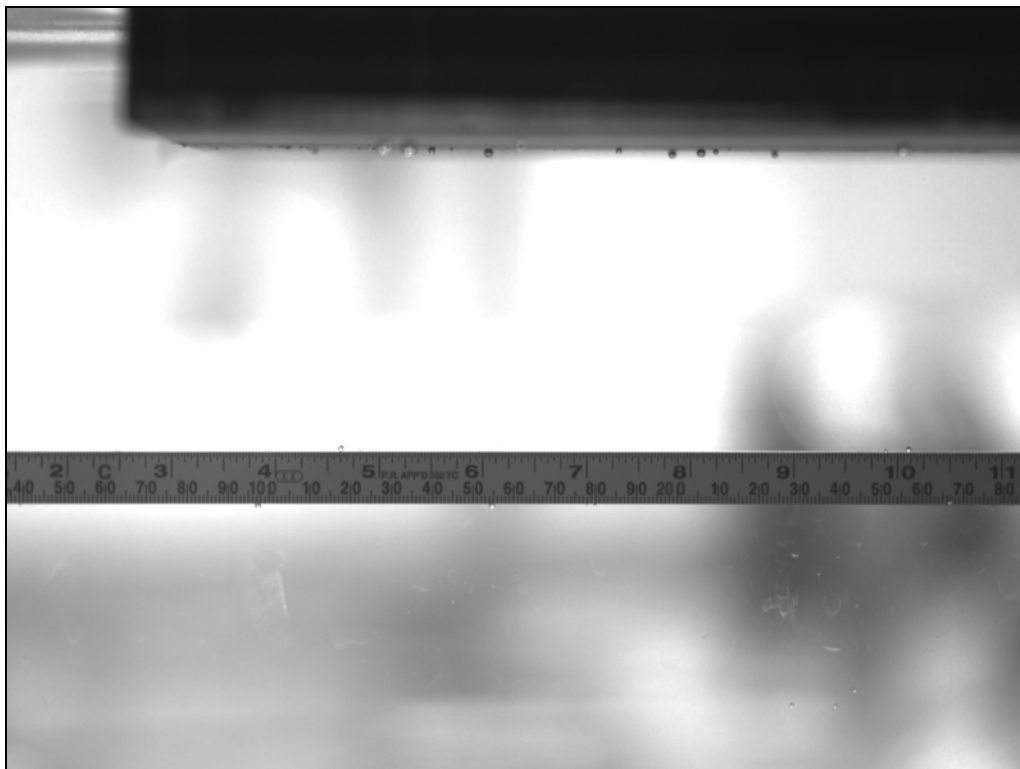


Figure 4-4: Field of view for Case 2: tH01.

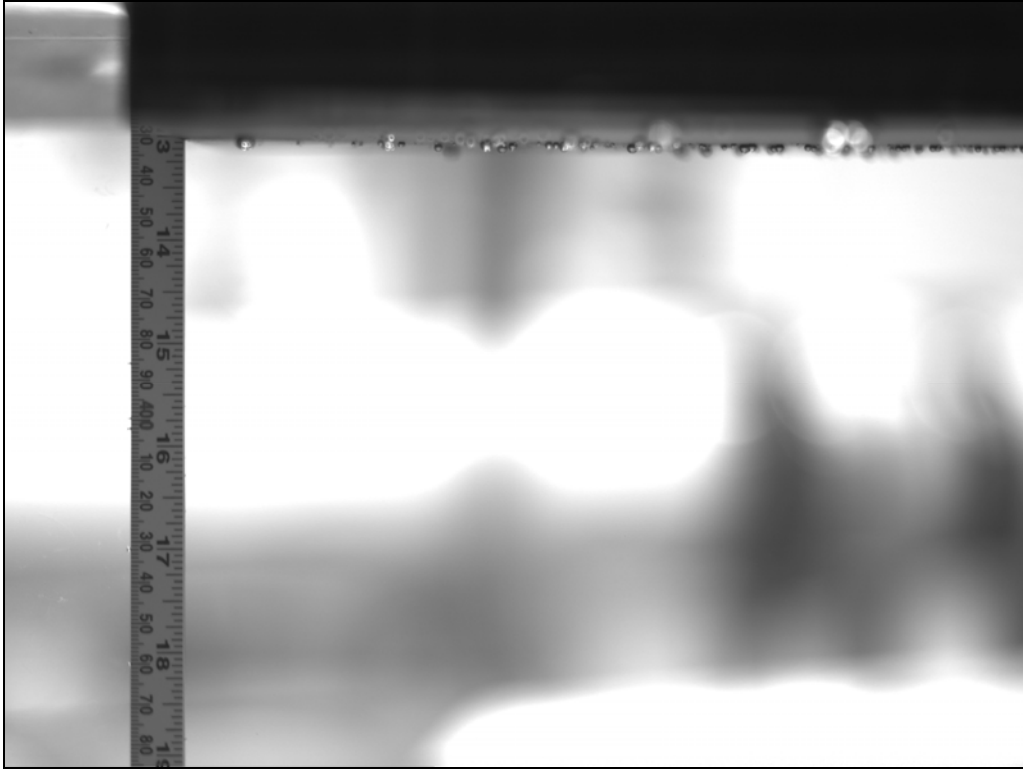


Figure 4-5: Location of leading edge for the rectangular block cases.

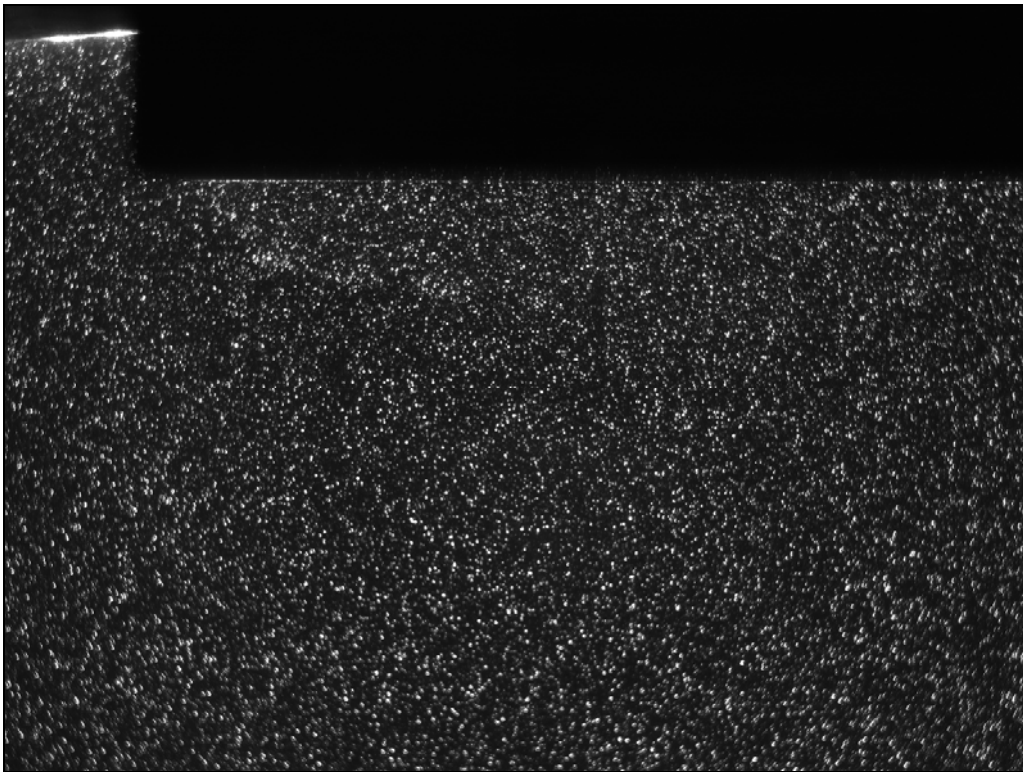
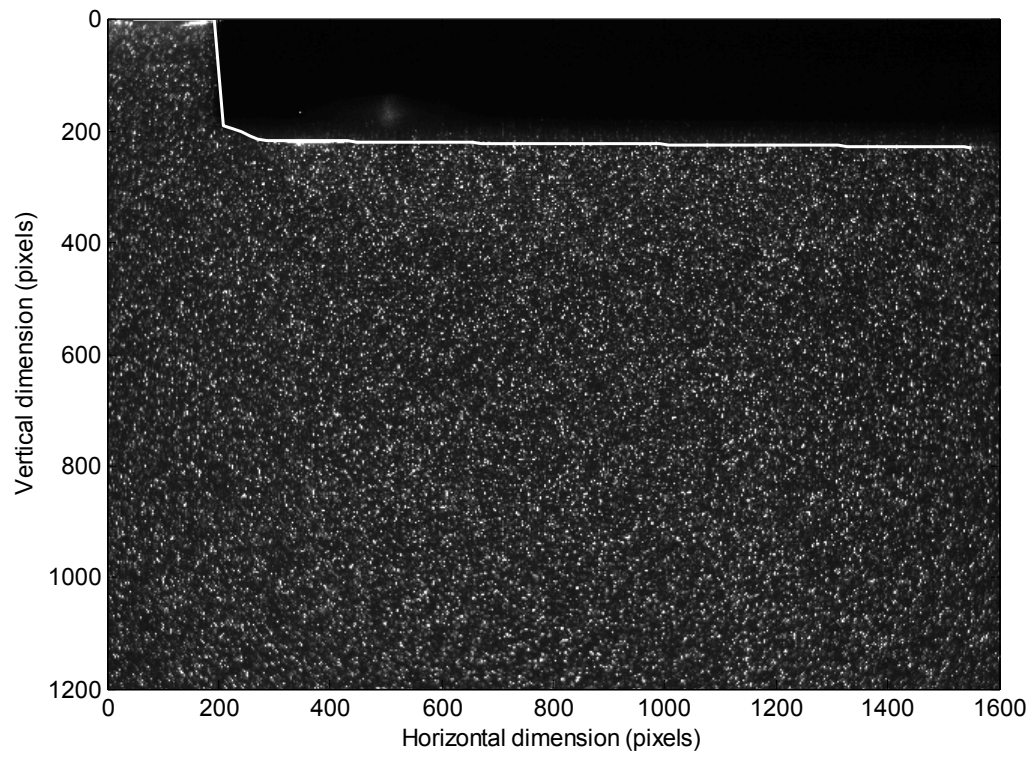
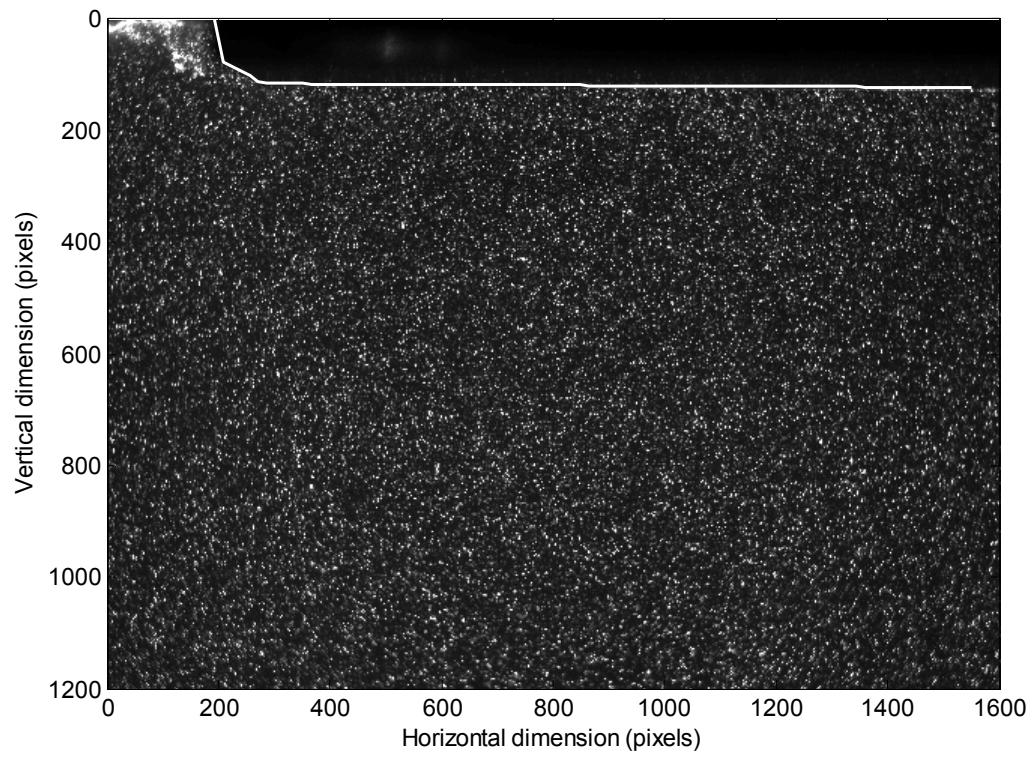


Figure 4-6: Example of typical seed density achieved in a DPIV image.



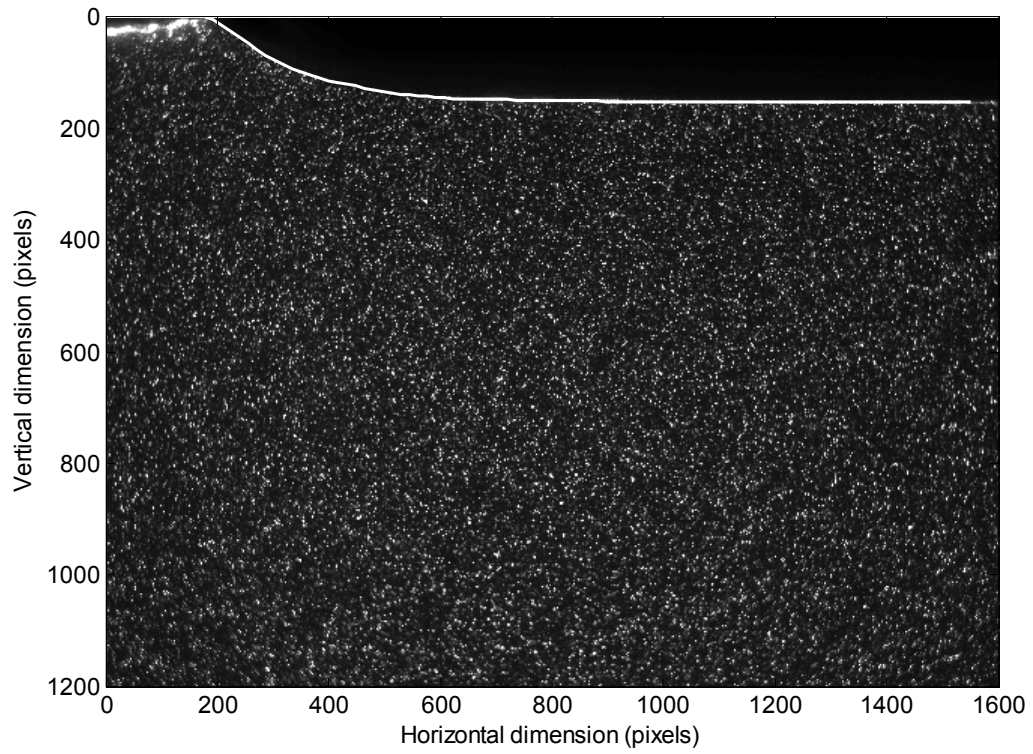


Figure 4-7: Profiles used in image processing.

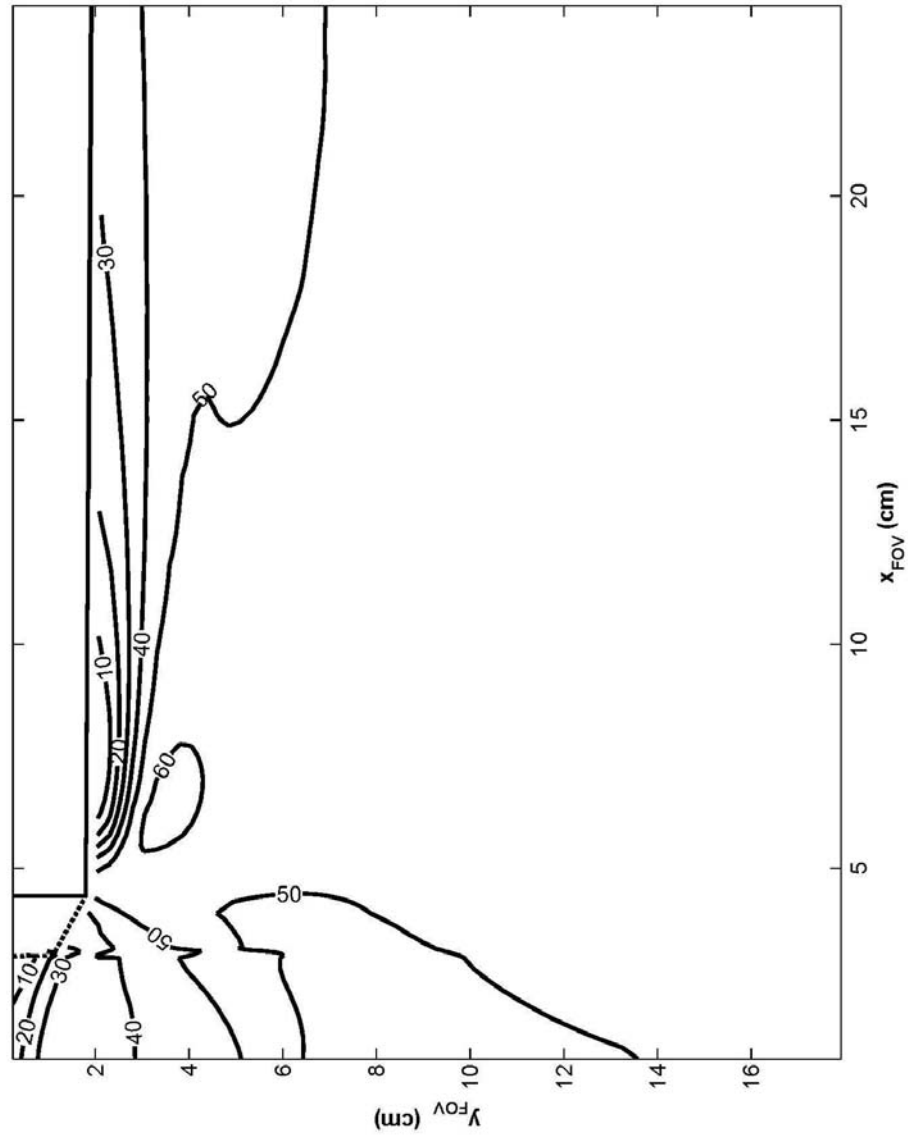


Figure 4-8: Mean velocity contours for Case 1: tH005 using a grid distance of 16 with the profile used for processing shown as the dashed line.

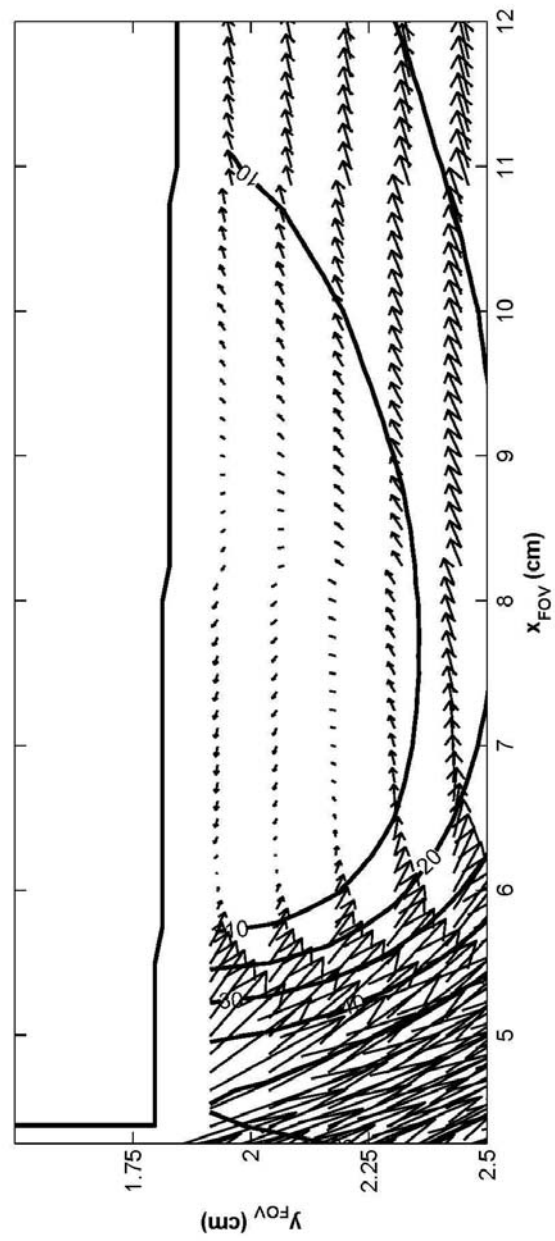


Figure 4-9: Mean velocity vectors and contours near the leading edge for Case 1: tH005.

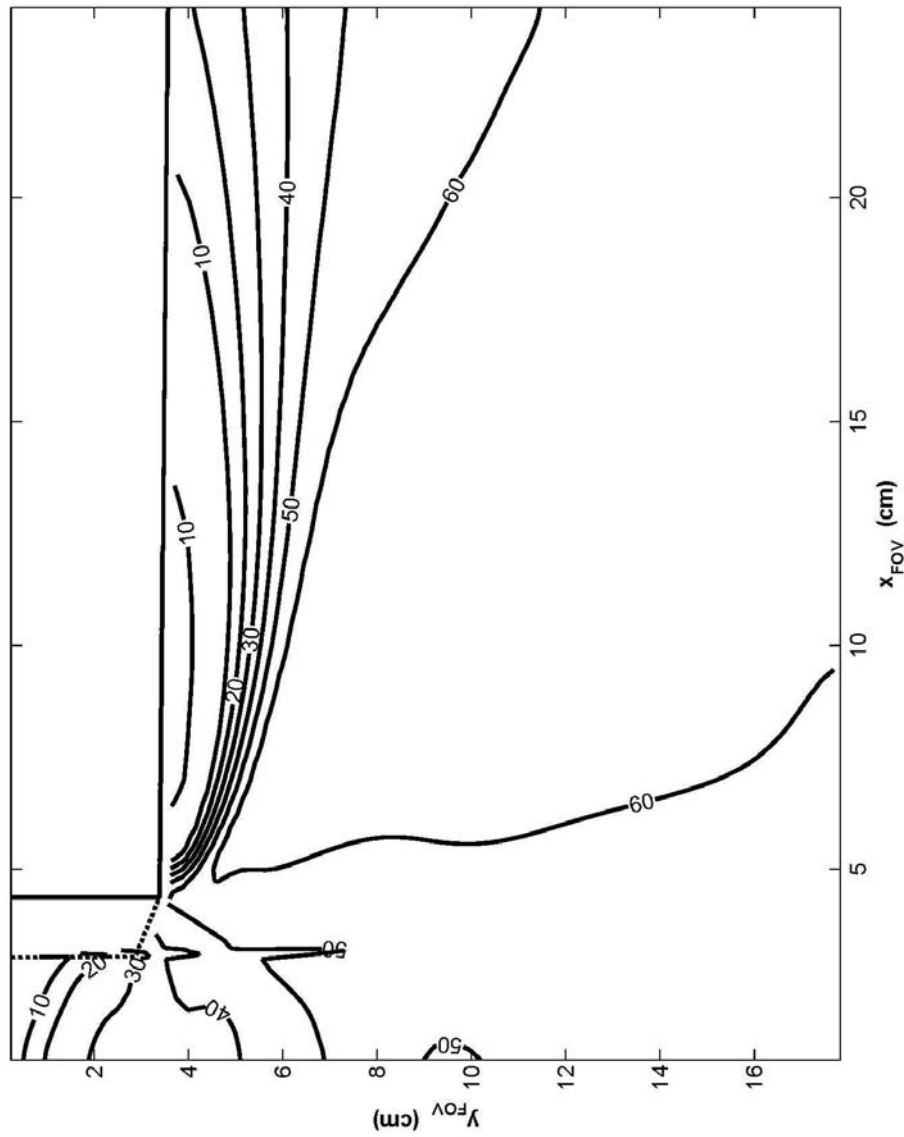


Figure 4-10: Mean velocity contours for Case 2: tH01.

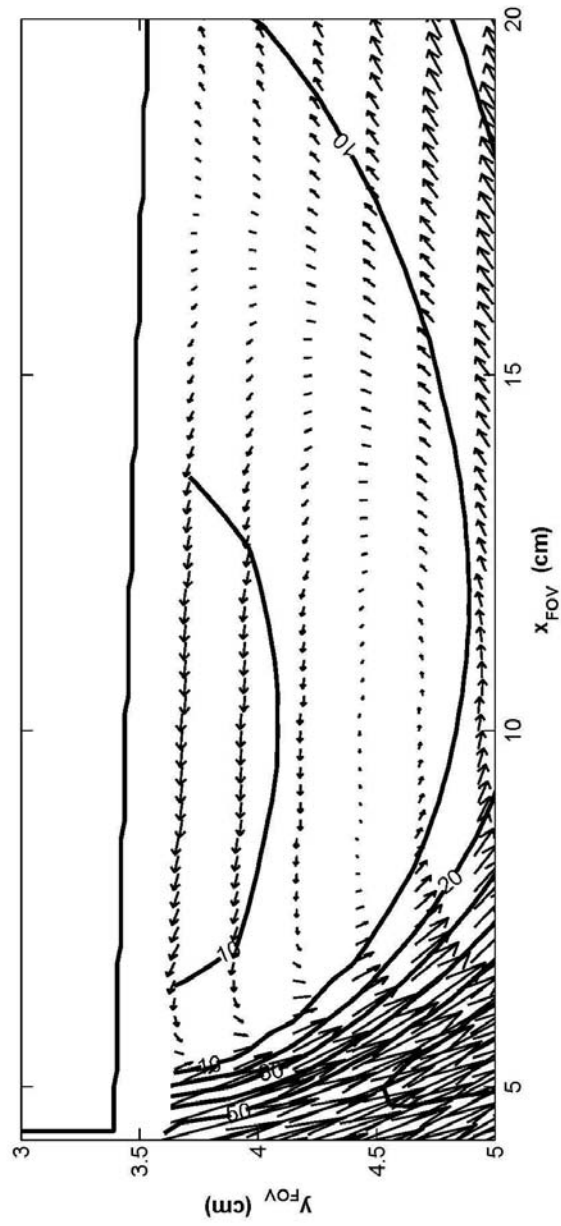


Figure 4-11: Mean velocity vectors and contours for Case 2: tH01 near the leading edge of the block.

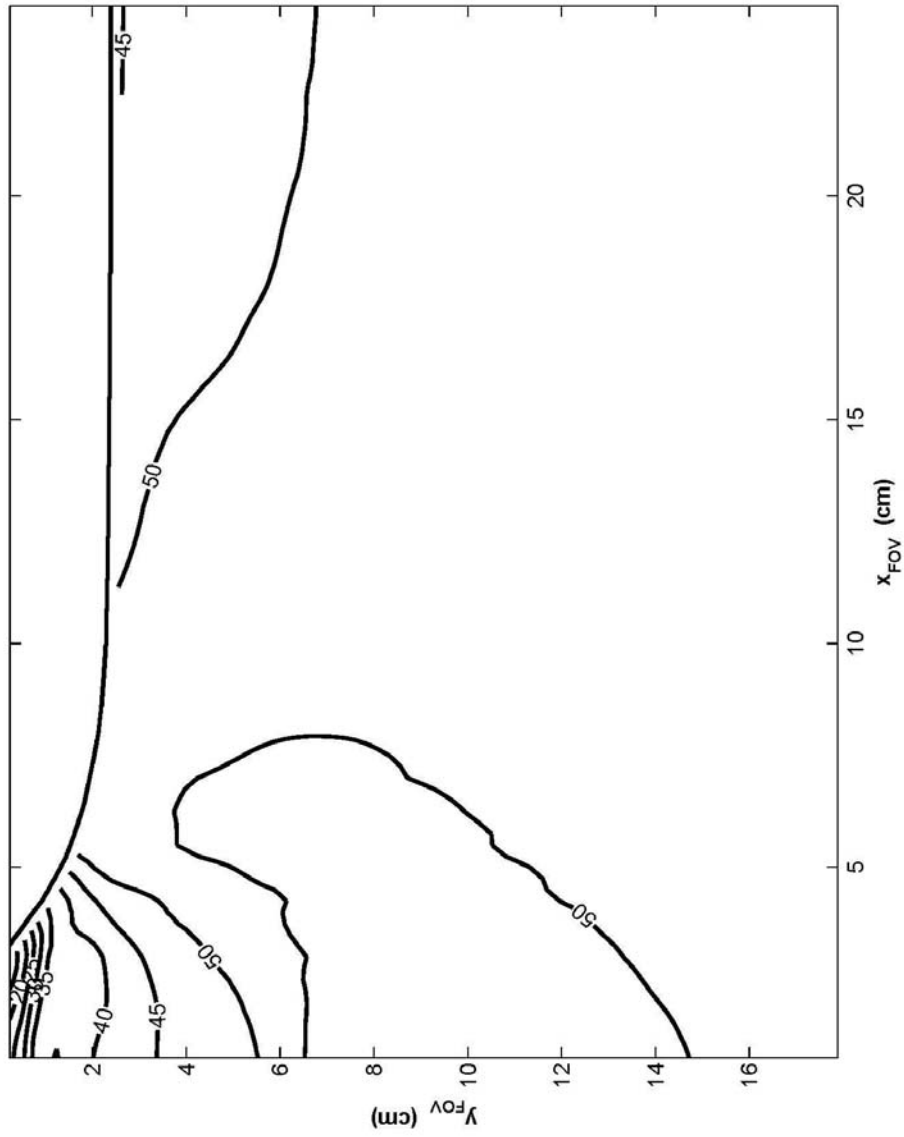


Figure 4-12: Mean velocity contours for Case 3: tH005Round.

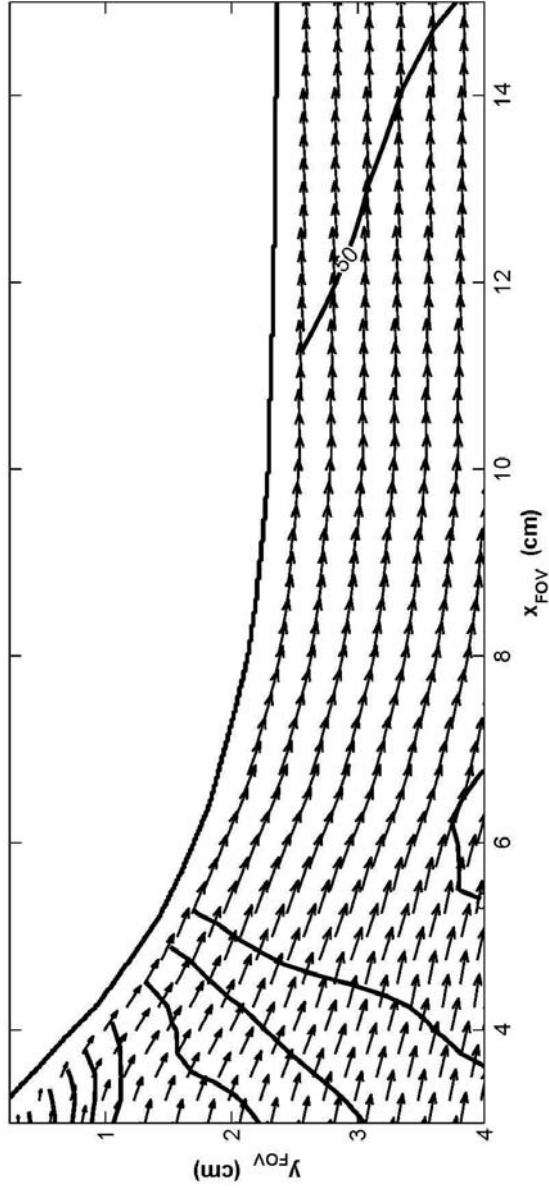
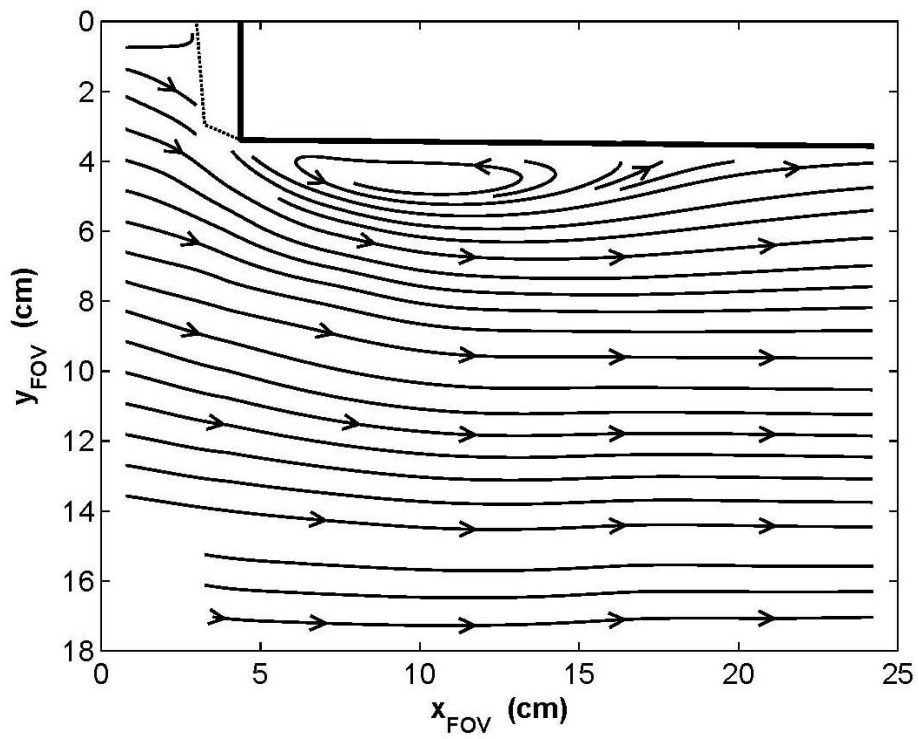
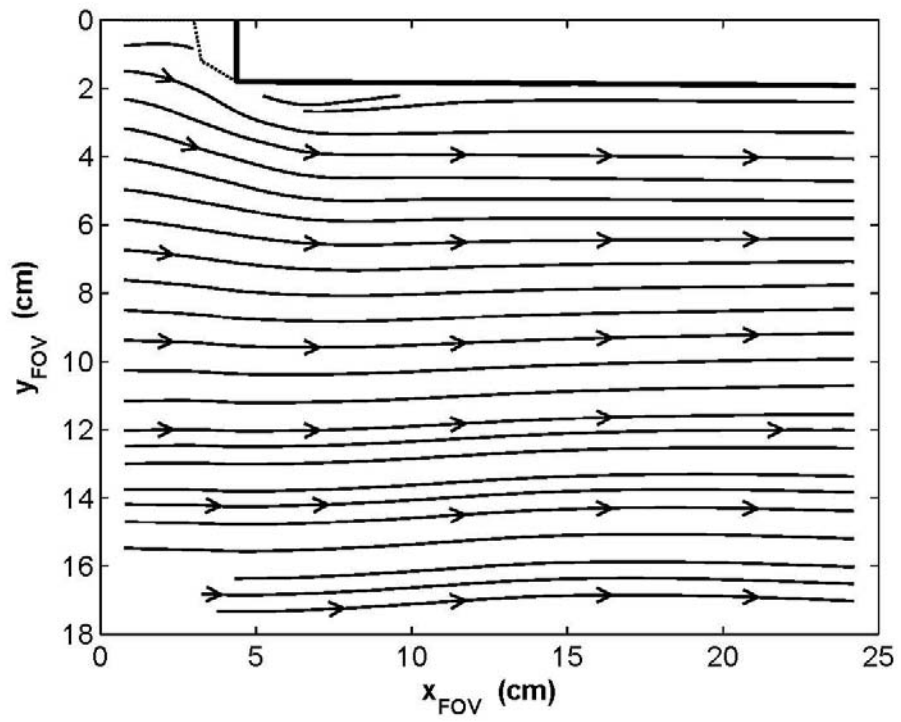


Figure 4-13: Mean velocity vectors and contours near the leading edge for Case 3: tH005Round.



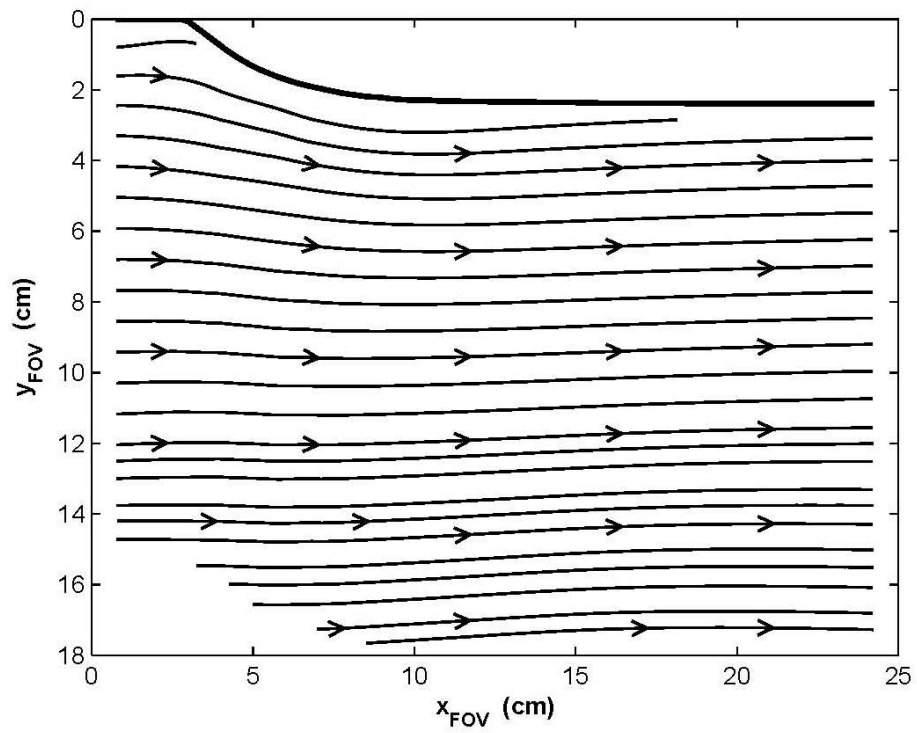


Figure 4-14: Streamlines for the three cases.

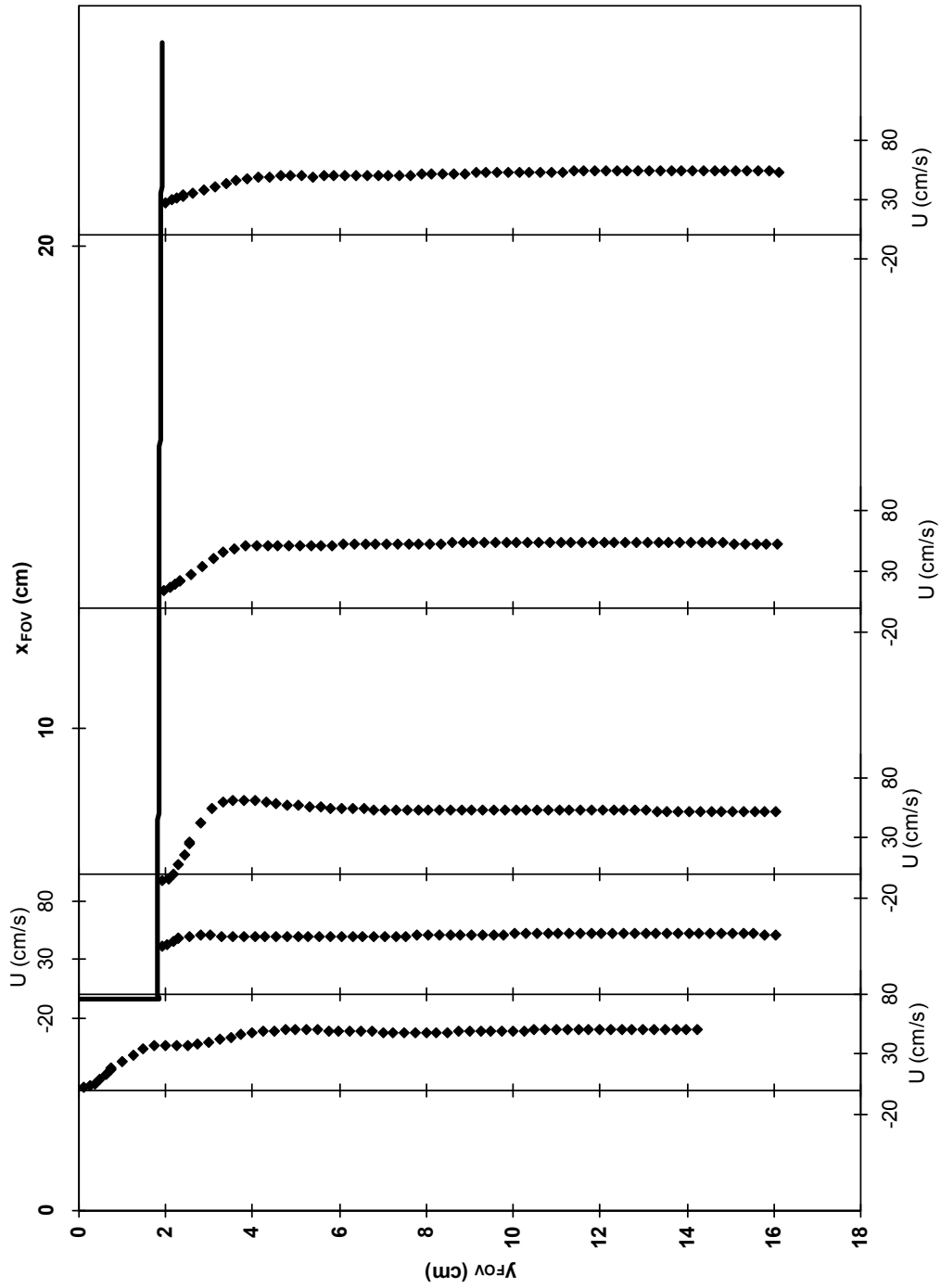


Figure 4-15: Mean velocity profile development beneath the block for Case 1:tH005.

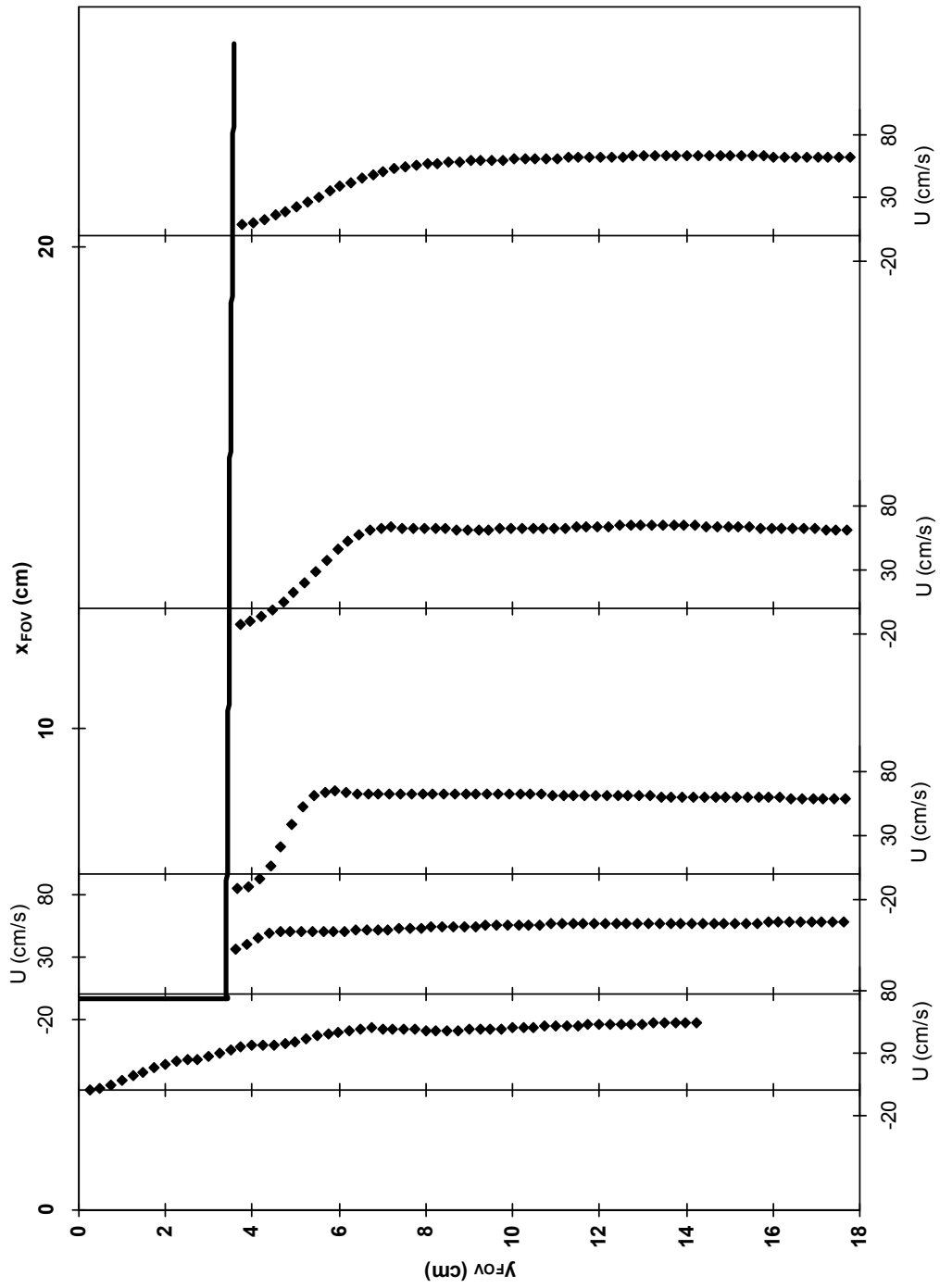


Figure 4-16: Mean velocity profile development beneath the block for Case 2: tH01.

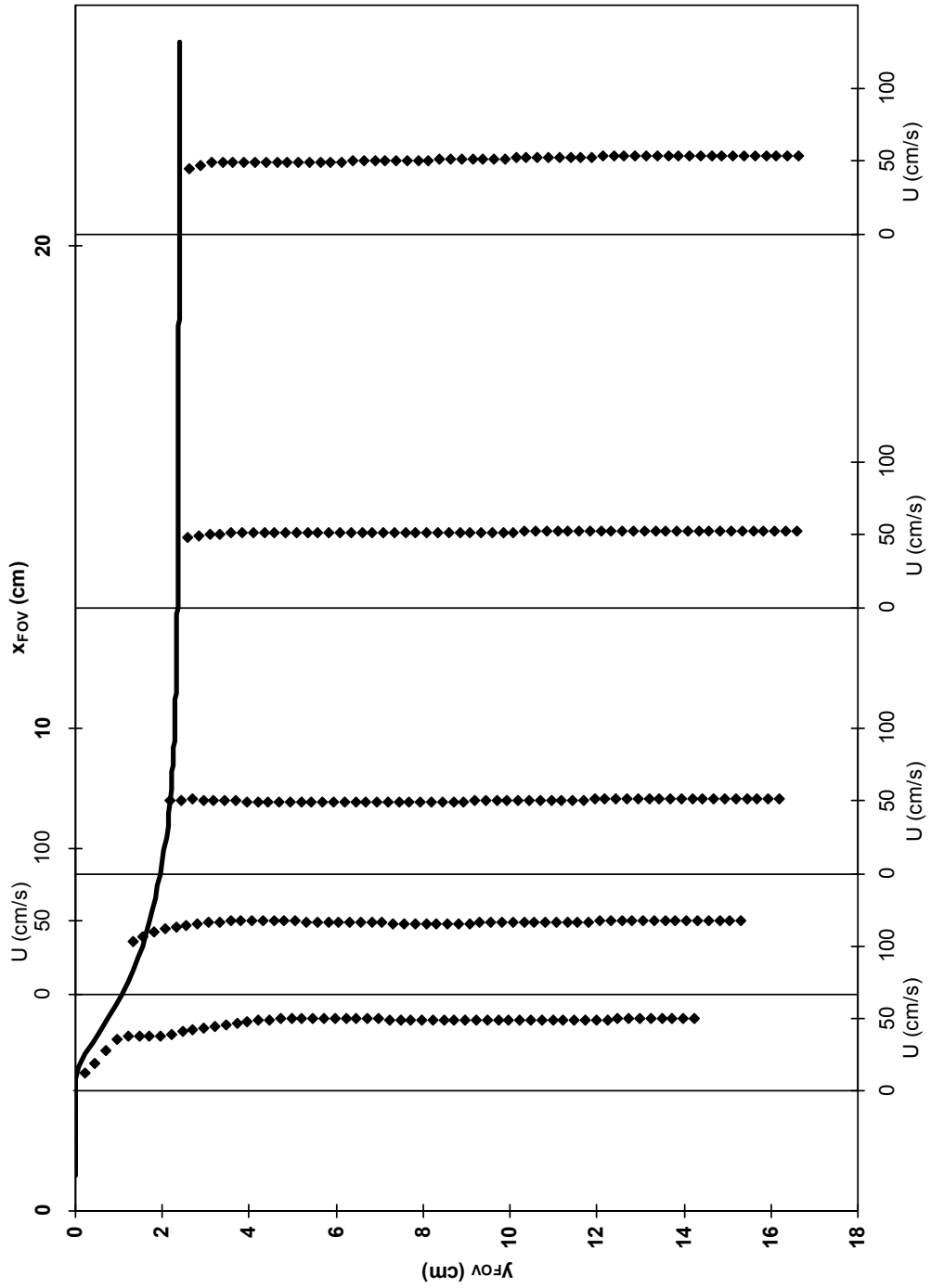


Figure 4-17: Mean velocity profile development beneath the block for Case 3: tH005Round.

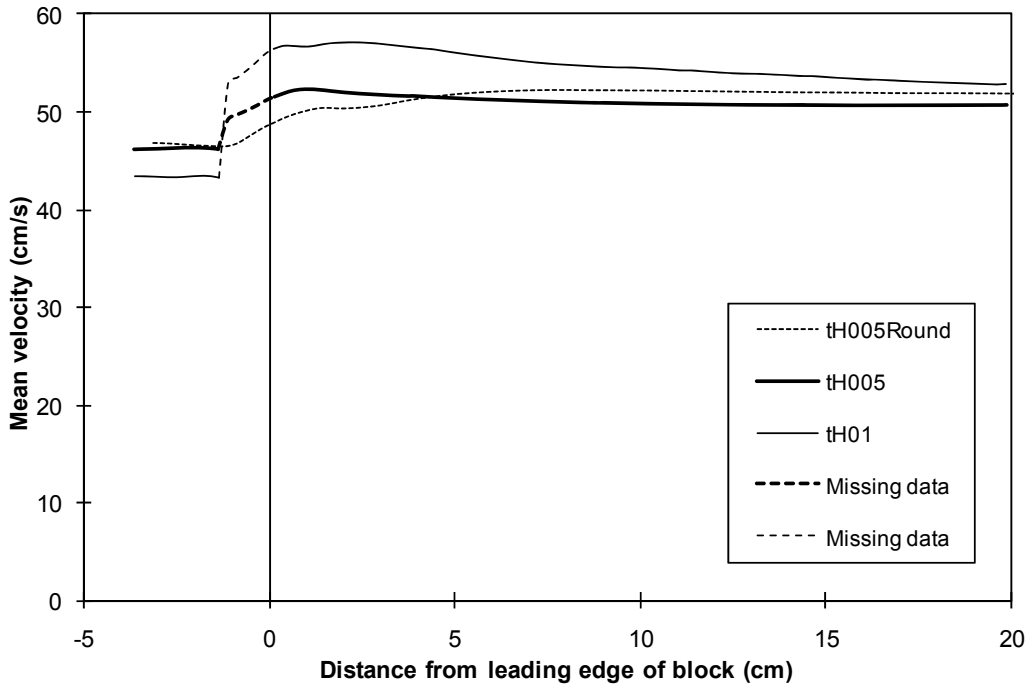


Figure 4-18: Comparison of mean velocity for the three cases.

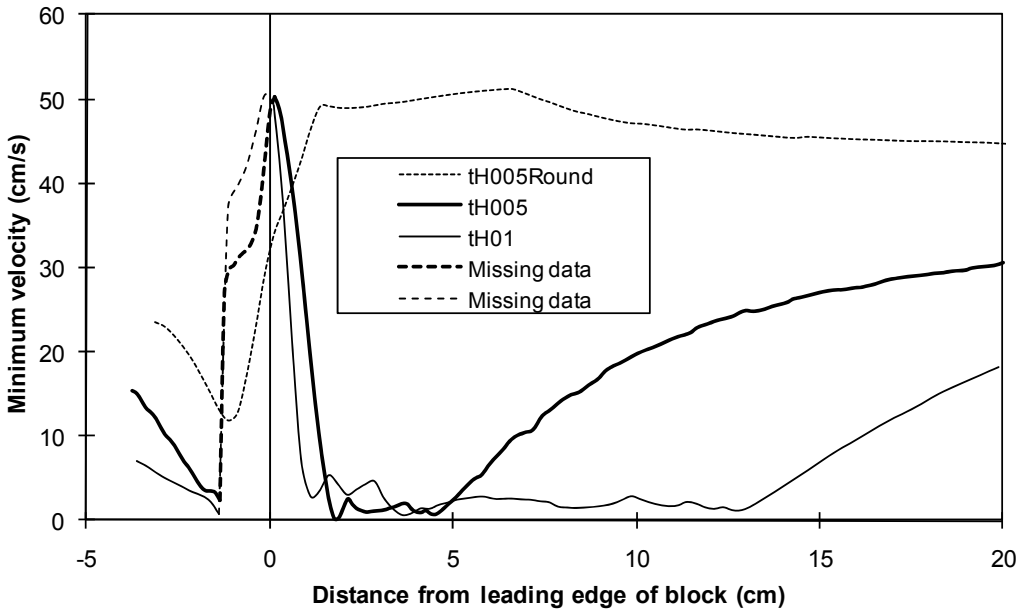


Figure 4-19: Comparison of minimum velocity for the three cases.

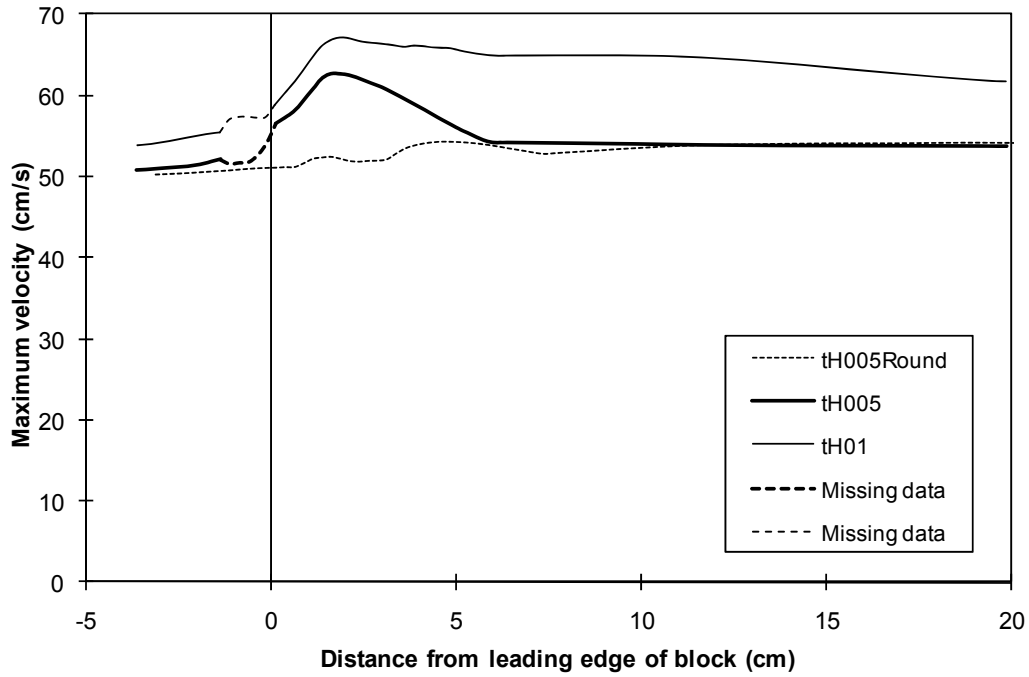


Figure 4-20: Comparison of maximum velocity for the three cases.

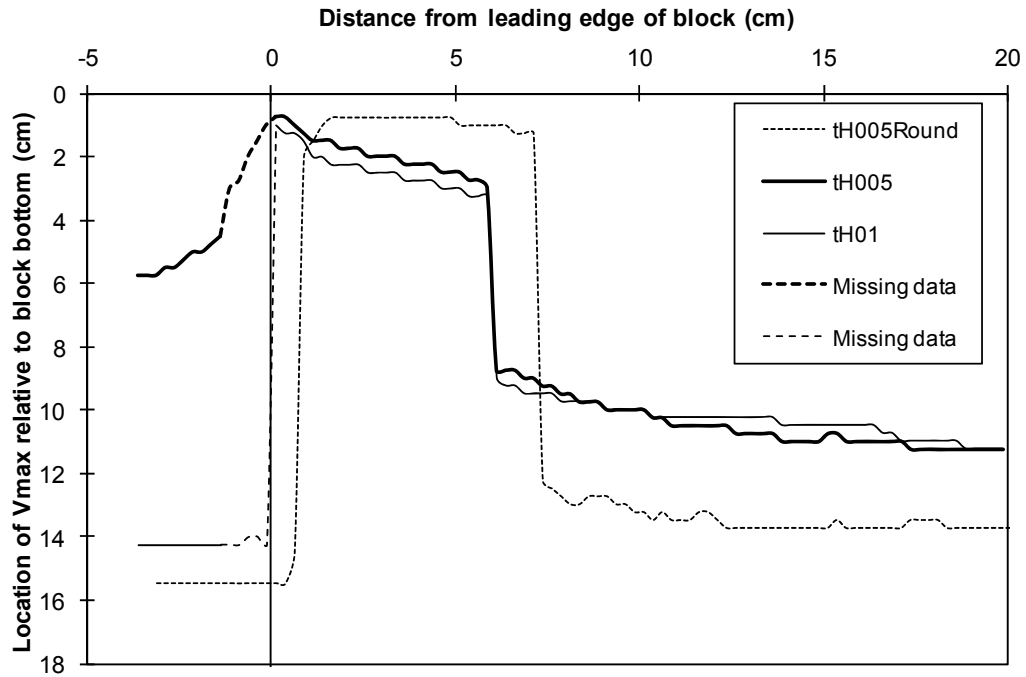


Figure 4-21: Comparison of the location of the maximum velocity relative to the bottom of the block.

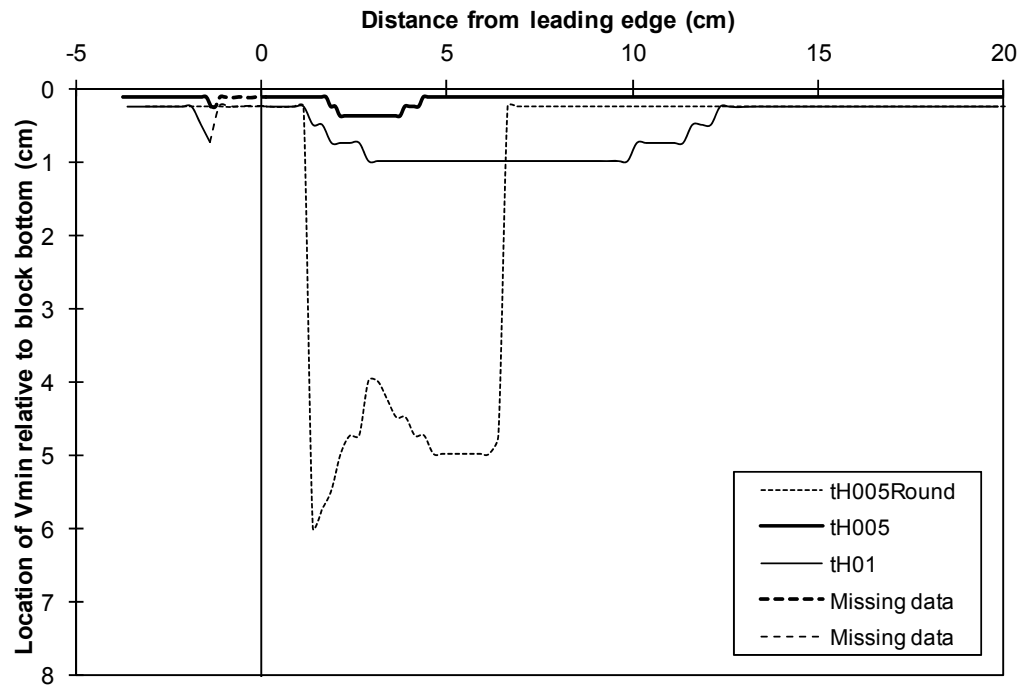


Figure 4-22: Comparison of the location of the minimum velocity relative to the bottom of the block.

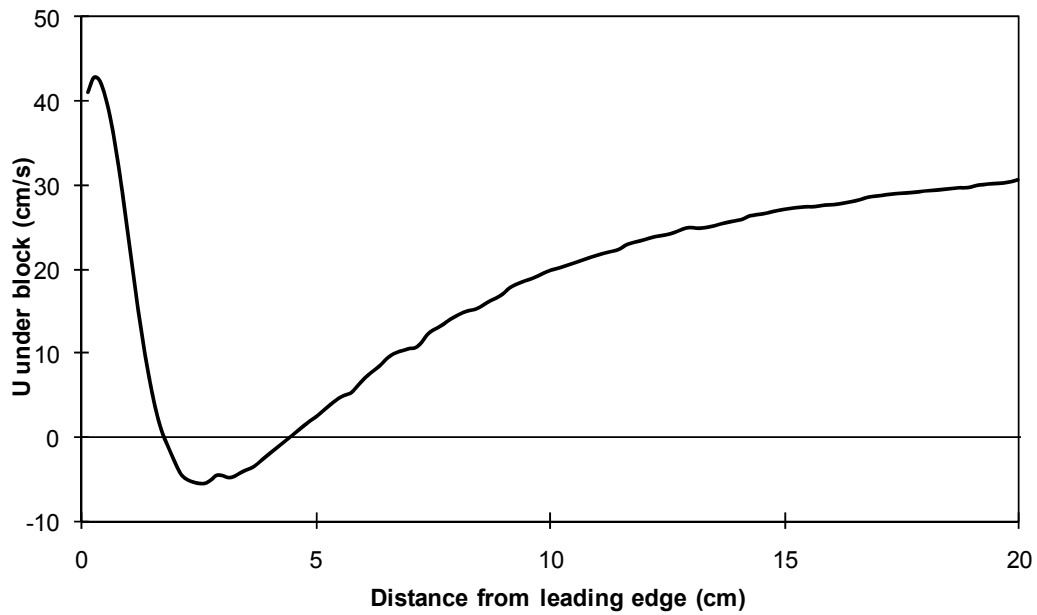


Figure 4-23: Mean U velocity at the first grid point beneath the block for Case 1: tH005.

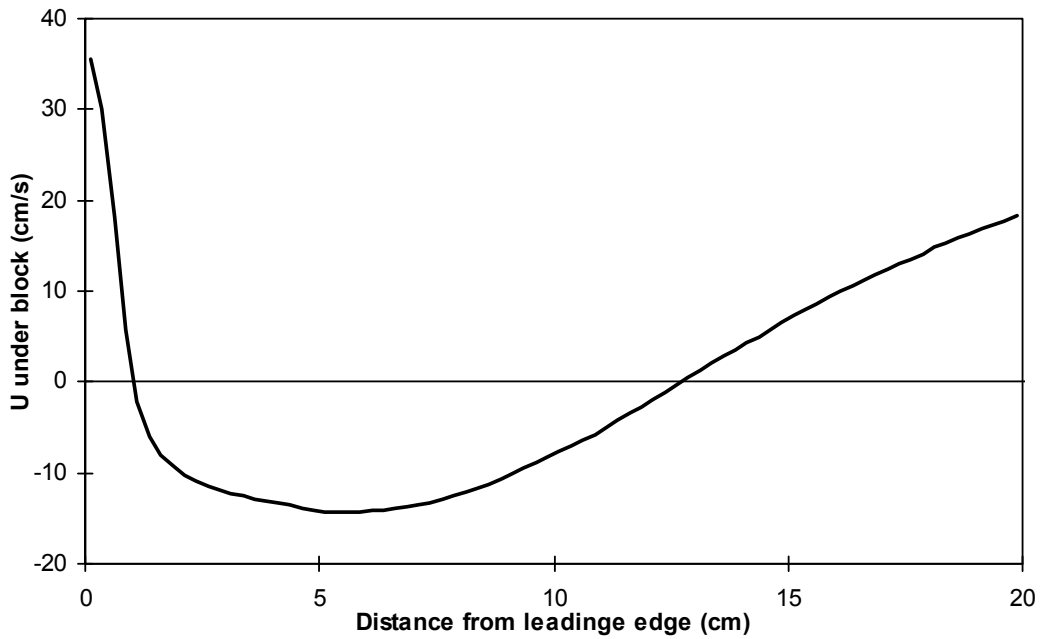


Figure 4-24: Mean U velocity at the first grid point beneath the block for Case 2: tH01.

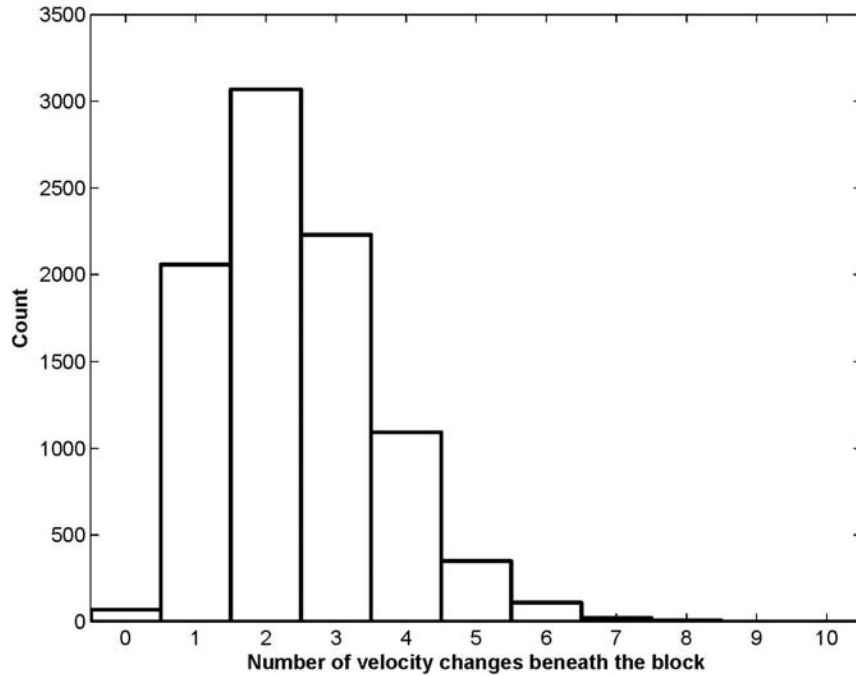


Figure 4-25: Number of velocity changes beneath the block detected for Case 1: tH005 with a mean of 2.4.

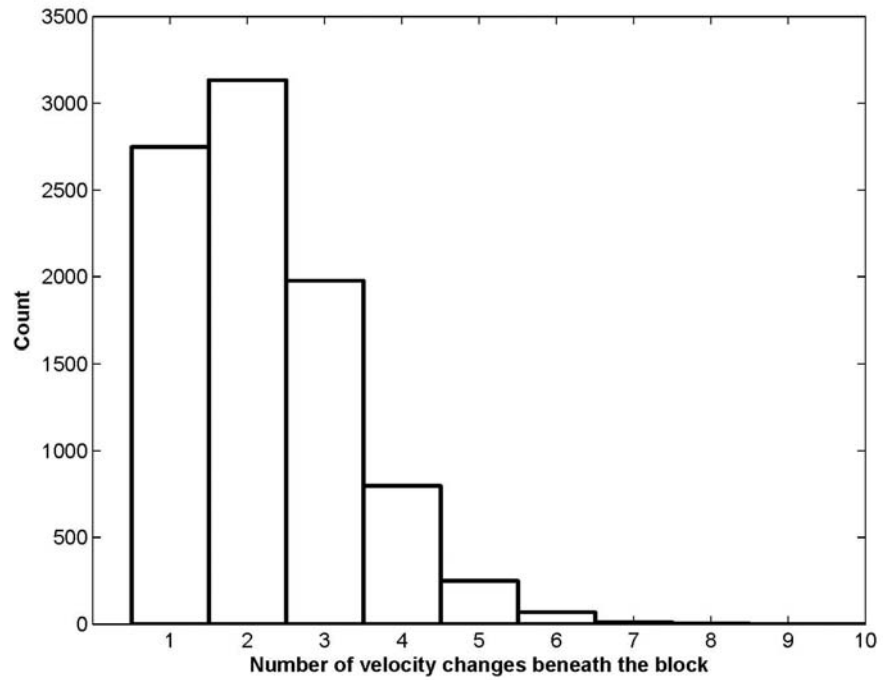
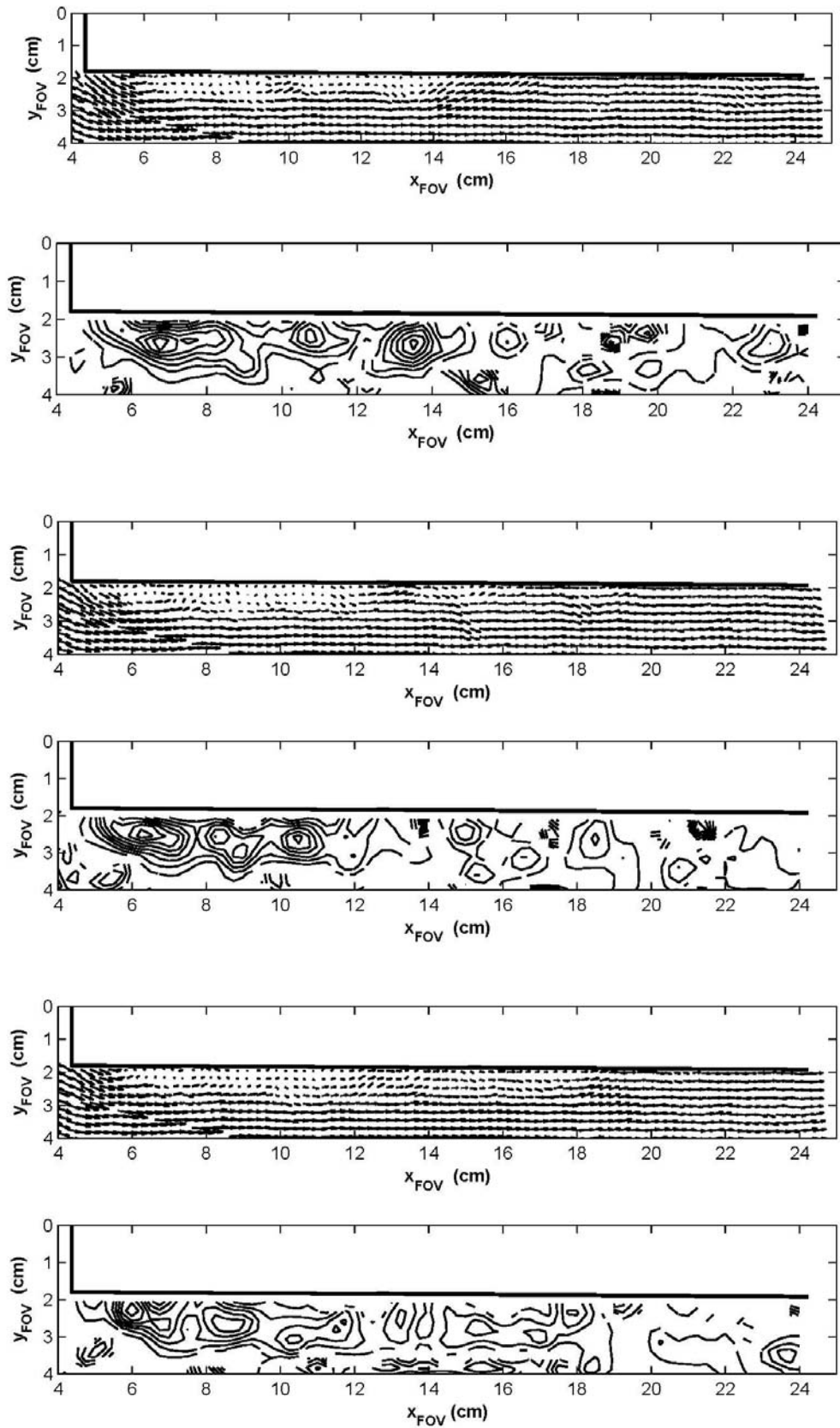


Figure 4-26: Number of velocity changes beneath the block detected for Case 2: tH01 with a mean of 2.2.



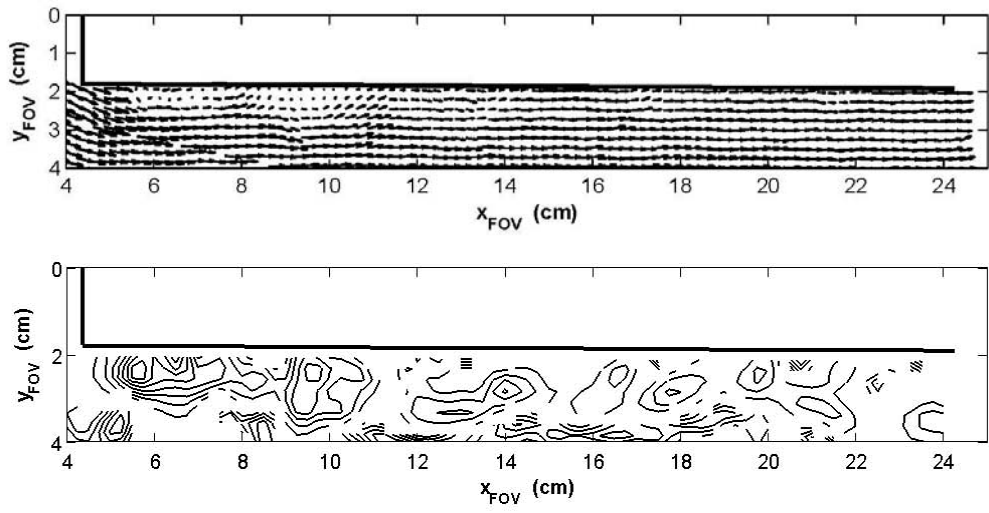
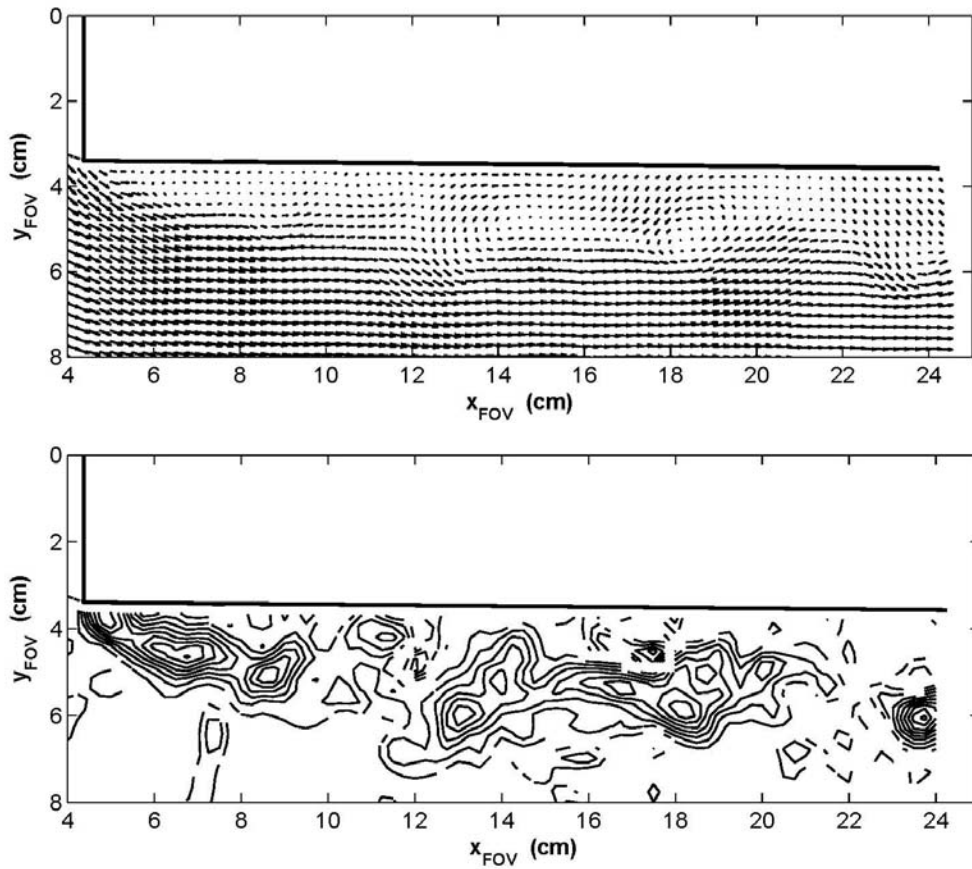
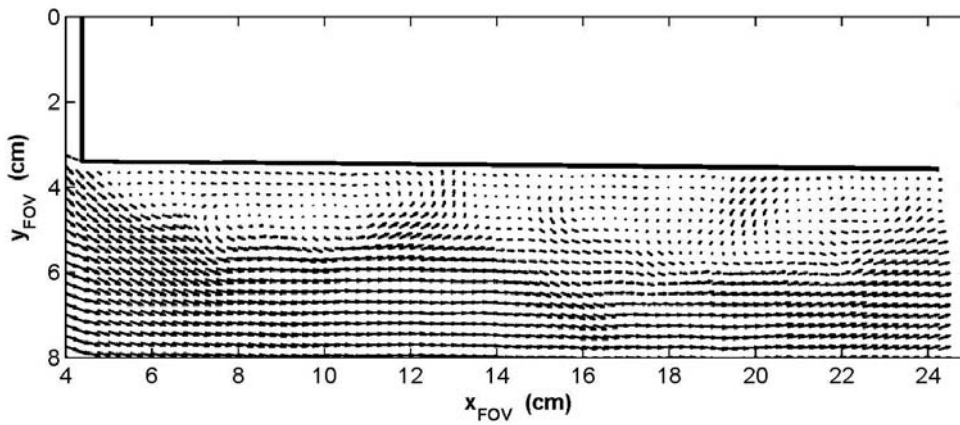
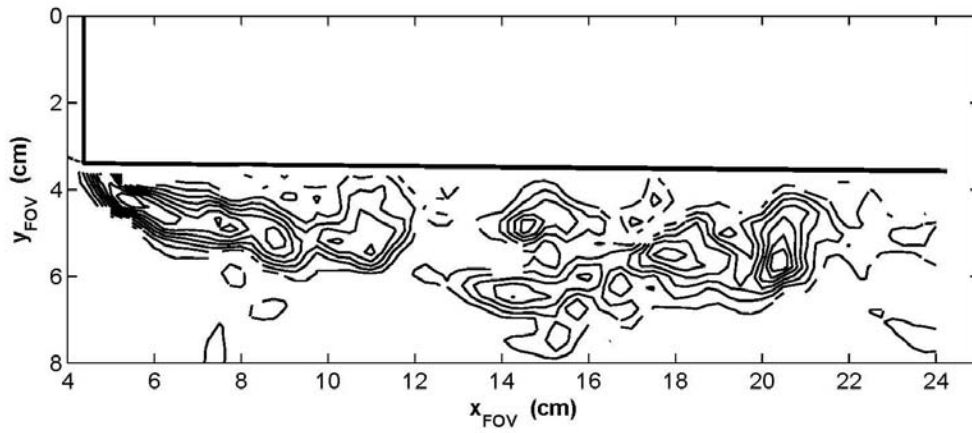
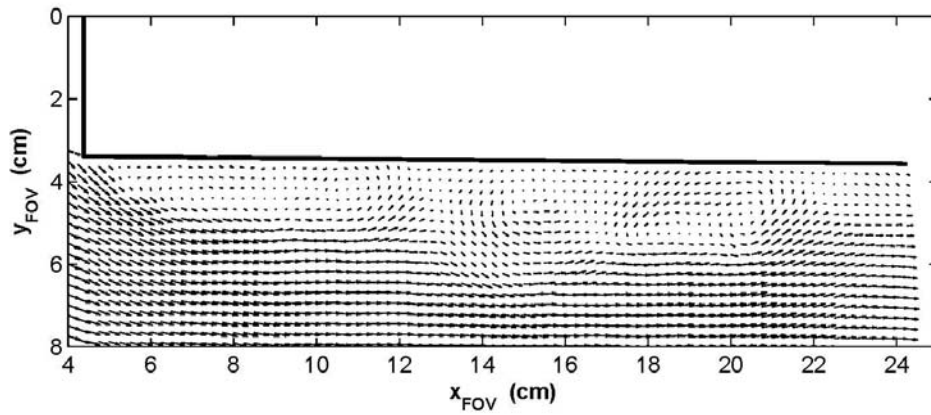


Figure 4-27: Instantaneous velocity vectors and vorticity for four consecutive image pairs for Case 1: tH005.





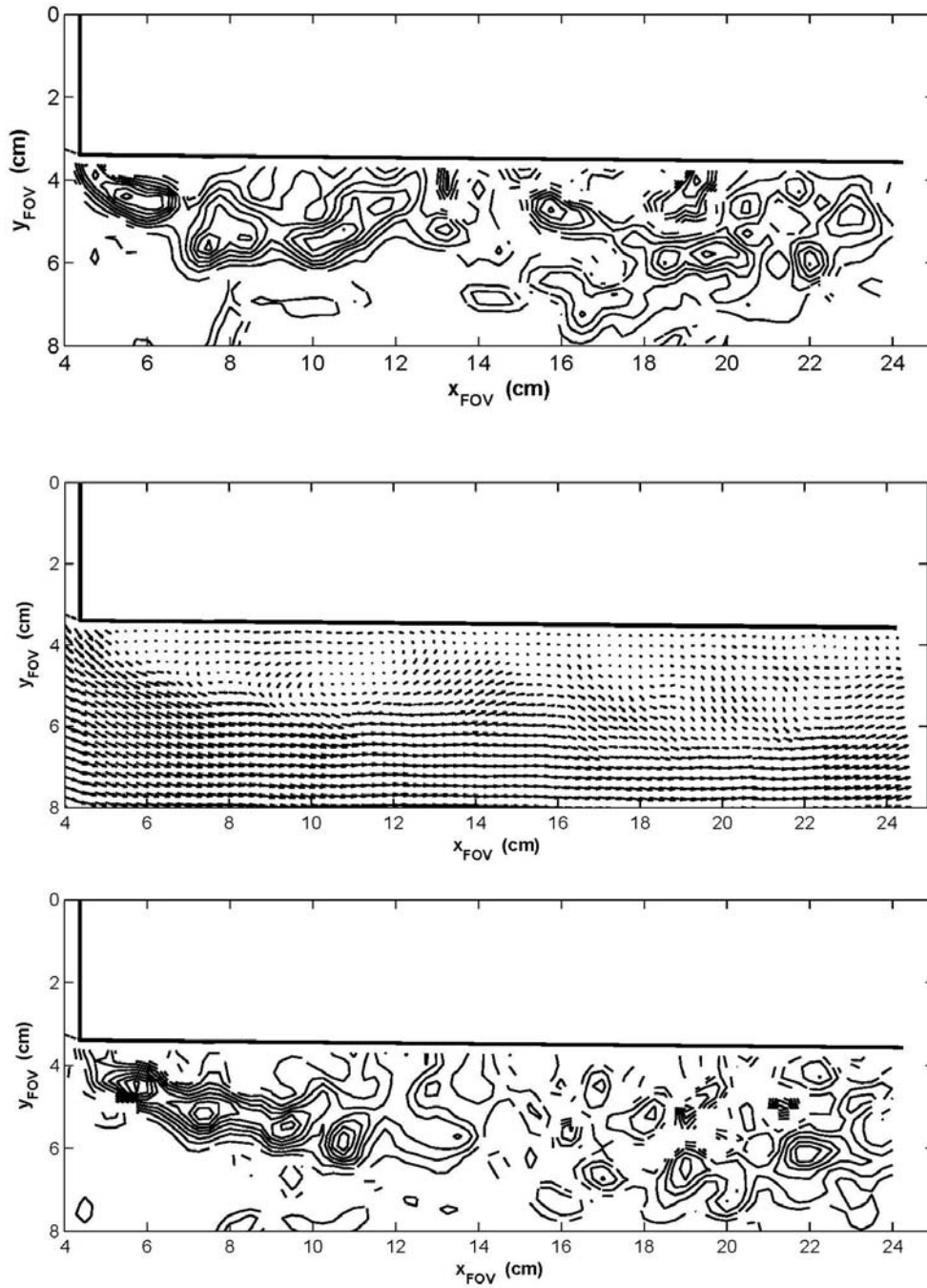
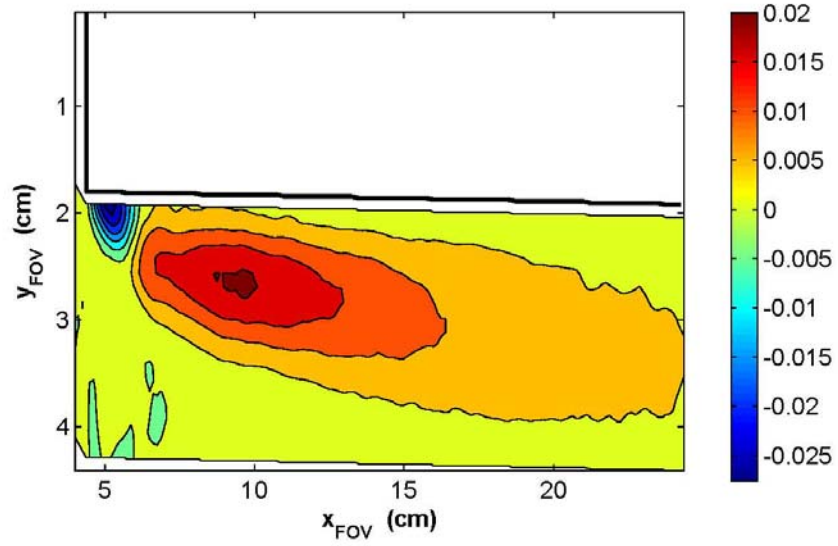


Figure 4-28: Instantaneous velocity vectors and vorticity for four consecutive image pairs for Case 2: tH01.

a)



b)

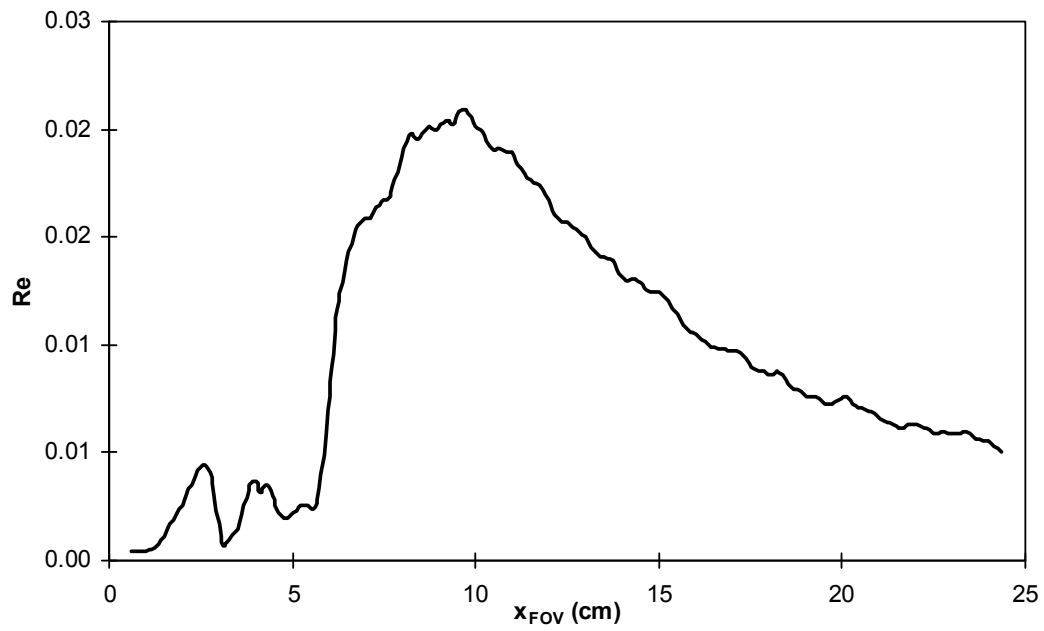
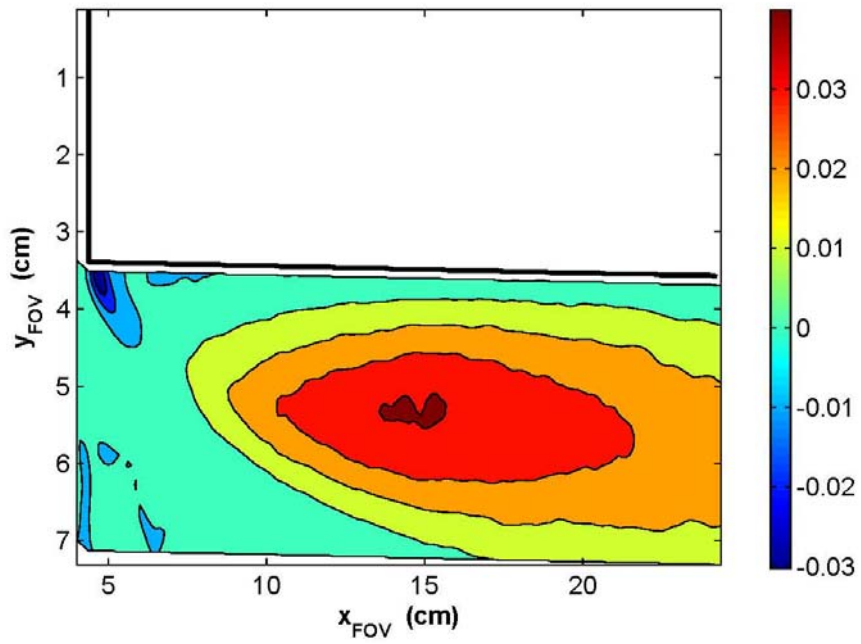


Figure 4-29: Reynolds stress for Case 1: tH005: a) contour of stresses; b) maximum Reynolds stress with distance.

a)



b)

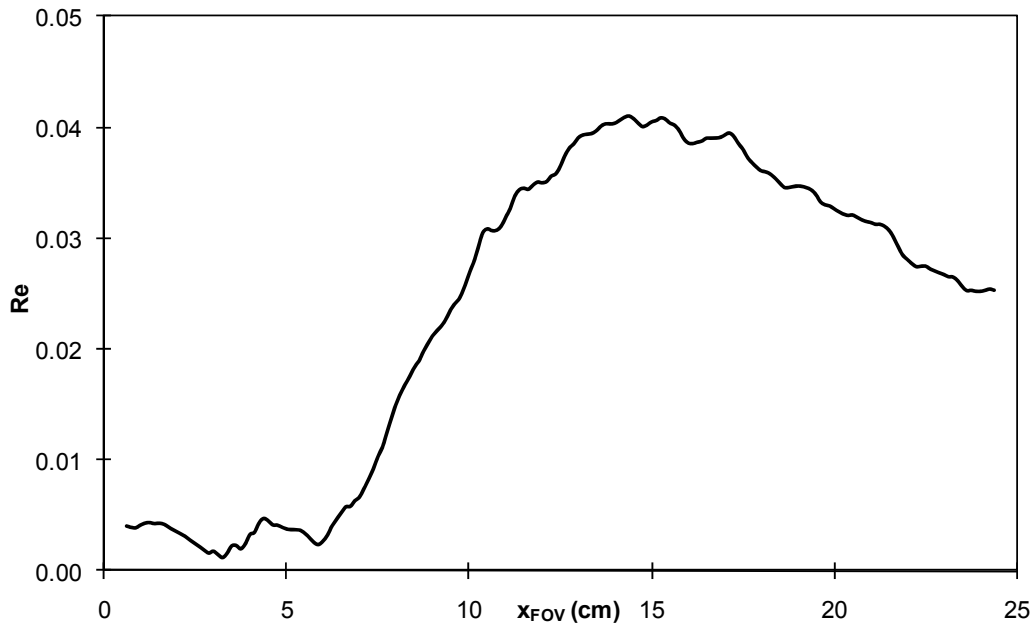


Figure 4-30: Reynolds stress for Case 2: tH01: a) a) contour of stresses; b) maximum Reynolds stress with distance.

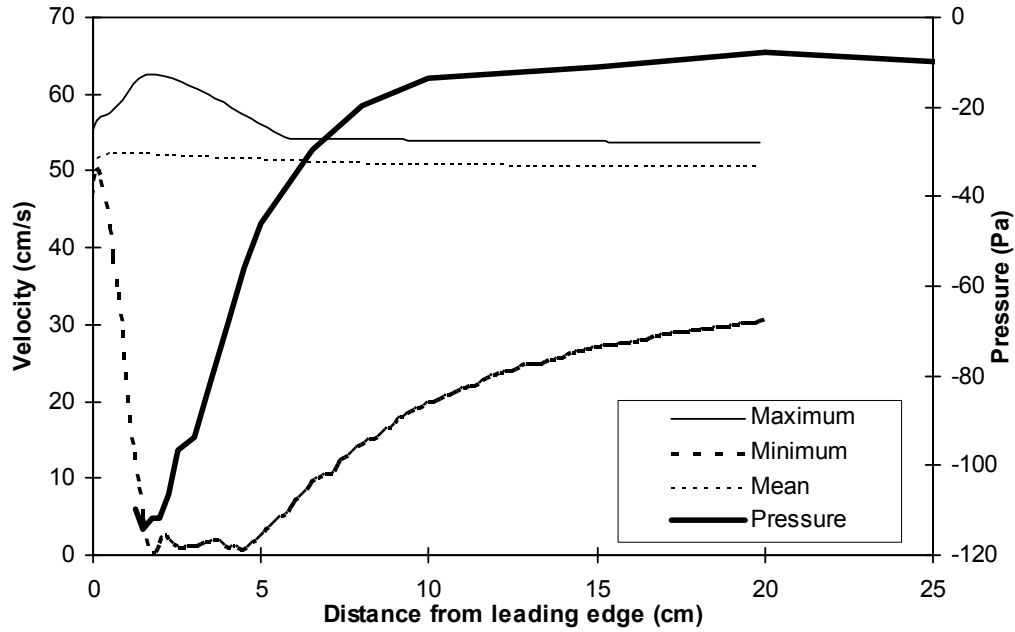


Figure 4-31: Compare dynamic pressure to maximum, minimum and mean velocity for Case 1: tH005.

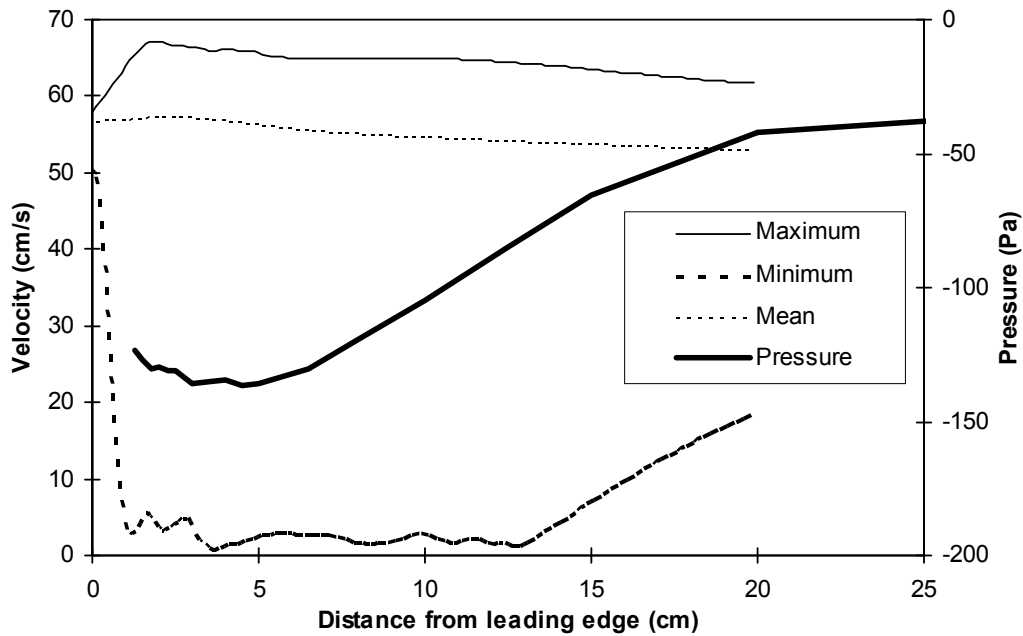


Figure 4-32: Compare dynamic pressure to maximum, minimum and mean velocity for Case 2: tH01.

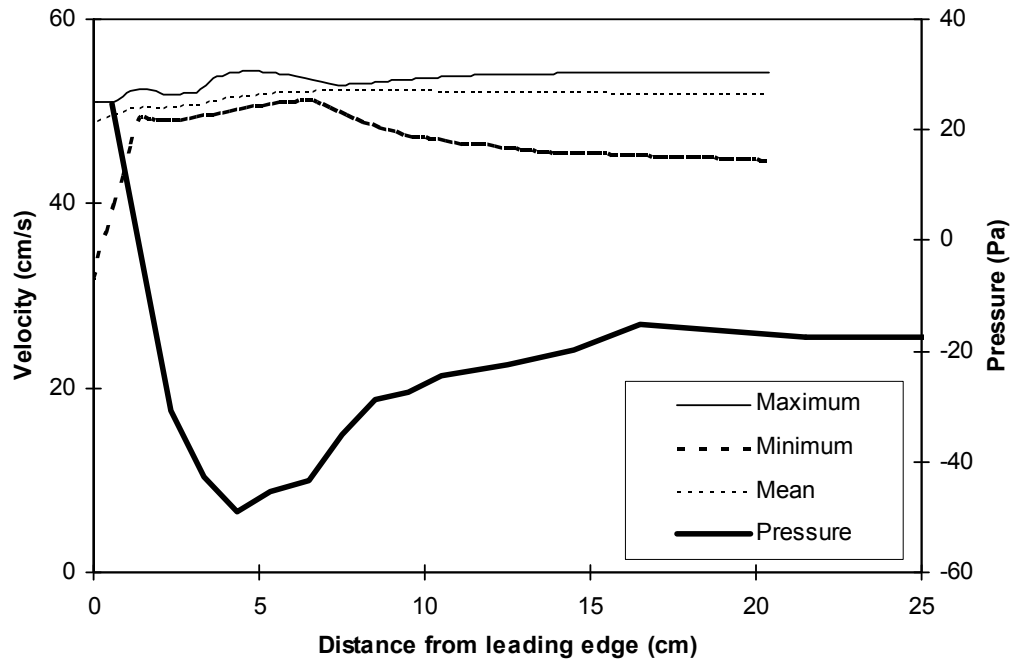


Figure 4-33: Comparison of dynamic pressure to maximum, minimum and mean velocity for Case 3: tH005Round.

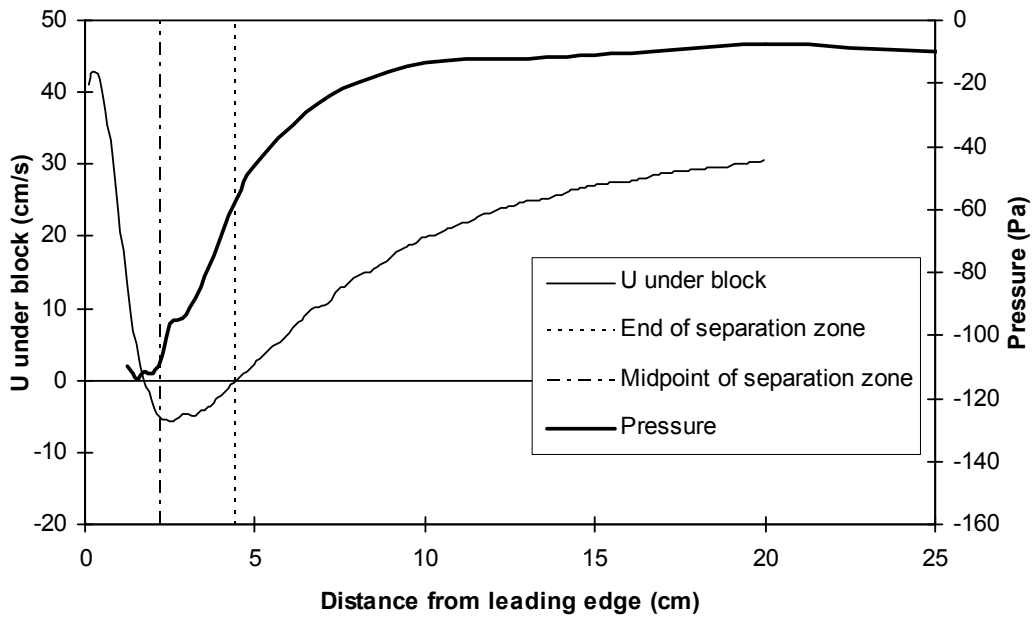


Figure 4-34: Comparison of separation zone length to pressure distribution for Case 1: tH005.

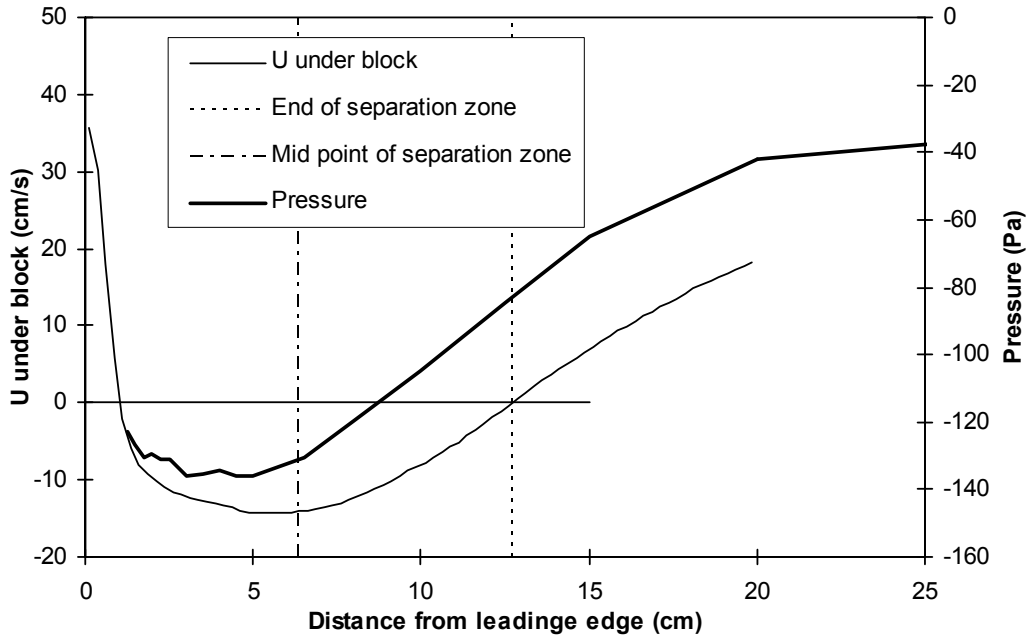


Figure 4-35: Comparison of separation zone length to pressure distribution for Case 2: tH01.

4.6 REFERENCES

- Agelinchabb, M. and Tachie, M.F., 2008. PIV study of separated and reattached open channel flow over surface mounted blocks. *Journal of Fluids Engineering*, 130(6), 9 pp.
- Ashton, G.D., 1974. Froude criterion for ice-block stability. *Journal of Glaciology*, 13(68), pp. 307-313.
- Burgmann, S. and Schröder, W., 2008. Investigation of the vortex induced unsteadiness of a separation bubble via time-resolved and scanning PIV measurements. *Experiments in Fluids*, 45(4), pp. 675-691.
- Coutermarsh, B and McGilvary, R., 1994. Analyzing the stability of floating ice floes. CRREL Report 94-13, 19 pp.
- Daly, S.F. and Axelson, K.D., 1990. Stability of floating and submerged blocks. *Journal of Hydraulic Research*, 28(6), pp. 737-752.
- Dow-Ambtman, K.E., 2009. Experimental investigation of ice-floe stability. Ph.D. Thesis, Department of Civil and Environmental Engineering, University of Alberta, Edmonton, Alberta.
- Dow-Ambtman, K.E., Hicks, F.E., and Steffler, P.M., 2009. Experimental investigation of the pressure distribution beneath a floating ice block. Submitted to *Journal of Hydraulic Engineering*.
- Gui, L., Longo, J., and Stern, F., 2001. Biases of PIV measurement of turbulent flow and the masked correlation-based interrogation algorithm. *Experiments in Fluids*, 30(1), pp. 27-35.
- Higuchi, H., van Langen, P., Sawada, H., and Tinney, C.E., 2006. Axial flow over a blunt circular cylinder with and without shear layer reattachment. *Journal of Fluids and Structures*, 22(7), pp. 949-959.
- Huang, H.T. and Fiedler, H.E., 1997. A DPIV study of a starting flow downstream of a backward-facing step. *Experiments in Fluids*, 23(5), pp. 395-404.

- Larsen, P., 1975. Notes on the stability of floating ice blocks. Proceedings of the IAHR third international symposium on ice problems. Hanover, NH, IAHR, pp. 305-313.
- Marsen, M., 1998. Particle image velocimetry in stromungen mit starken geschwindigkeitsgradienten. Ph.D. Thesis, Ruprecht – Karls - Universitat Heidelberg, Heidelberg, Germany.
- Mukto, M., to be published. Ph.D. Thesis, Department of Civil and Environmental Engineering, University of Alberta, Edmonton, Alberta.
- Scarano, F. and Riethmuller, M.L., 2000. Advances in iterative multigrid PIV image processing. Experiments in Fluids, 29(S1), pp. S051-S060.
- Uzuner, M.S. and Kennedy, J.F., 1972. Stability of floating ice blocks. Journal of the Hydraulics Division, 98 (HY12), pp. 2117-2133.
- Westerweel, J. and Scarano, F., 2005. Universal outlier detection for PIV data. Experiments in Fluids, 39(6), pp. 1096 – 1100.
- Willert, C.E. and Gharib, M., 1991. Digital particle image velocimetry. Experiments in Fluids, 10(4), 181-193.

CHAPTER 5: CONCLUSIONS AND RECOMMENDATIONS

This research sought to further understand the physics of flow under a floating ice block, and the hydrodynamic forces that act on it, through a series of experiments. It is known that an ice floe approaching an intact ice cover will either come to rest, extending the length of the cover, or it will become entrained. The two principle methods of block entrainment are submergence by sinking, in which the ice floe sinks vertically, or submergence by overturning, in which the ice floe rotates about its downstream corner. An entrained ice floe can be deposited beneath the intact cover contributing to its thickness, and potentially leading to the formation of an ice jam. The buoyancy of an entrained ice floe can also cause it to impact the underside of the intact ice cover, causing it to crack and weaken. This could, in turn, lead to an ice jam release event if the intact cover is restraining an ice jam. Current ice floe stability theory is based on an empirical Froude number criterion and is being used in numerical models which attempt to predict ice transport and deposition.

The objectives of this research were: to increase the knowledge of the physical behaviour of ice pieces in water; to quantify the hydrodynamic forces and moments that act on a floating ice block; to develop a more rigorous method for determining ice block stability; to characterize the velocity field beneath a floating ice block to correlate the velocity field to the resulting pressure reduction beneath a floating ice block; and to determine if unsteady flow behaviour at the leading edge of a floating ice block should be considered in analyzing ice block stability. The research was broken into three separate components, the first examining the pressure distribution beneath a floating ice block, the second analyzing the stability of a floating ice block and the third investigating the velocity field beneath a floating ice block.

5.1 SUMMARY AND KEY FINDINGS

Experiments measuring the pressure distribution beneath a rectangular floating ice block were the first to find it to have a characteristic shape that began at a minimum pressure plateau then recovered to a second pressure plateau. The magnitude of the pressure reduction beneath the block was found to increase with increasing block thickness-to-approach flow depth ratio and increasing velocity. It was found that the pressure distribution could be broken into two separate effects: a pressure reduction due to leading edge effects from localized flow behaviour and a pressure reduction due to venturi effects from the flow constriction of the ice block. This was further supported through experiments measuring the pressure distribution beneath a floating ice block with a rounded leading edge. These experiments found the pressure distribution to have a different shape at the leading edge with the pressure beginning at a positive pressure, decreasing to a smaller minimum pressure than that observed for the rectangular block then recovering immediately to a pressure plateau that could again be defined as the venturi pressure. The results were non-dimensionalized to develop an original method that can be used for predicting the pressure distribution beneath any rectangular floating ice block.

Experiments measuring the transverse pressure distribution showed that the pressure beneath the block was symmetrical about the centerline of the block and could be considered uniform in magnitude across the width of the block. This is an important finding as it means that the width of block can be neglected in any submerging force and moment calculations, and block stability can be considered a two dimensional phenomenon. This suggests that numerical models which attempt to predict block stability can be effectively represented in two dimensions.

The submerging force and overturning moment was found to increase with increasing ice thickness-to-approach flow depth ratio and increasing flow

velocity. Rounding the leading edge of the block significantly decreased the submerging forces and overturning moments, suggesting the importance of localized flow separation and acceleration on the resulting stability of a floating ice block.

A generalized submerging force and moment analysis was developed for rectangular blocks that found the results could be broken into four scenarios: 1. leading edge effects dominated, 2. leading edge effects partial recovery, 3. leading edge effects full recovery, and 4. venturi effects dominated. The scenario under which a block will fall depends on the length of the block. Fundamental equations were developed that can be used to predict the submerging forces and overturning moments for each scenario. The analysis suggested that the leading edge effects dominated and venturi effects dominated cases would tend to become entrained by sinking as the pressure is uniformly distributed across the bottom of the block. The leading edge effects partial recovery and leading edge effects full recovery cases should be analyzed for both sinking and overturning, but are more likely to become entrained by overturning.

The stability of a floating ice block was examined through a force-moment analysis. This study represents the first detailed analysis of the critical stability point for a block being entrained by overturning. Experiments measuring the pressure distribution beneath a block as it begins to rotate about its downstream corner suggested that the overturning moment increased with the angle of rotation. This increase was compared to the increase in the hydrostatic righting moment with block angle of rotation and it was found that the critical stability point for an overturning block would be at the point when the top upstream corner of the block reached the water surface. This is similar to what previous researchers described as the no-spill angle.

The generalized results developed in Chapter 2 were used to estimate the submerging forces and overturning moments for a broad range of scenarios. The

critical stability points were examined and the critical densimetric Froude numbers were calculated at stability to compare to the work of previous researchers. The results were found to match well up to an ice thickness-to-block length ratio of 0.5. However, it was found that as the block approaches a cube-like shape, the forces on the face of the block could no longer be neglected. The block length was found to be an important factor in determining block stability. This represents a more rigorous method for determining the stability of a floating ice block that is based on actual flow physics. The methods presented can be implemented immediately into any frontal progression numerical model.

This thesis presents the first detailed measurements of the velocity field beneath a floating ice block using particle image velocimetry. It was found that the separation zone formed at the leading edge of the rectangular block increased in length and thickness as the thickness of the block increased. Rounding the block's leading edge eliminated the separation zone, as the flow followed the block profile as it accelerated under the block. The velocity distribution results corroborated the findings of the pressure distribution, results suggesting that the pressure reduction at the leading edge is related to localized flow behaviour due to flow separation and acceleration. Similar to previous PIV studies on flow separation, instantaneously the separation zone was found to vary considerably and was often composed of several large vortices. However, the unsteady flow behaviour was examined qualitatively and it was found that the mean flow properties and mean pressure measurements are adequate for analyzing the block stability.

5.2 FUTURE WORK

Future work in this area could investigate the pressure reduction beneath floating ice blocks of different leading edge shapes to develop a general method for the prediction of the submerging forces and overturning moments and a generalized stability analysis as was done herein for rectangular floating ice blocks. It was

shown that the pressure distribution will change as the block becomes entrained and that as the block approaches a cube-like shape the forces on the face of the block can no longer be neglected. A model ice block can be constructed to examine the pressure distribution on all block faces as the block becomes entrained. The force-moment analysis could then be extended to more cube shaped blocks.

Digital particle image velocimetry was shown to be an effective technique for measuring the velocity field beneath a floating ice block. This technique could be used to examine the velocity field beneath a rough ice cover or ice jam. The question still remains: once the ice floe becomes entrained what happens? Further studies examining ice floe entrainment and deposition should be conducted. Particle image velocimetry could be used to track a block's entrainment beneath an intact ice cover to see how the velocity field changes and to track the entrained block's trajectory. The force and moment of the moving ice pieces can be inferred from its measured trajectory and velocity. It would be useful for determining under what conditions an entrained block come to rest beneath an intact ice cover.

This study will provide valuable validation data for a 3-D numerical model which will be used to examine a broad range of scenarios. Commercially available computational fluid dynamics code could be built on to simulate this phenomenon. It is conceivable that the best approach may be to write computational code from scratch. If this is the case, two approaches could be investigated. The first would treat the ice as a superviscous fluid entrained within the water and the system would be treated as two phase flow. The second approach would change the boundary conditions with time as the ice block moves through the water. If this is the case, the computational mesh would have to be generated every time step.

APPENDIX A: DETAILS FOR PIV STUDY

A.1 TIMING SEQUENCE

A schematic is shown in Figure A-1 to illustrate the timing sequence. The computer generated a 30 Hz signal from the camera, this signal was passed through a circuit that divided the signal in half. This 15 Hz signal was then transmitted to a four channel digital delay generator (BNC 500, Berkeley Nucleonics Corporation, San Rafael, California). The delay generator was used to set the timings to trigger a laser to pulse once during each camera frame and at a desired time spacing. The timings were set in order for the first laser to pulse at $t_c - \frac{\Delta t}{2}$ and the second laser to pulse at $t_c + \frac{\Delta t}{2}$ where t_c is the time of one camera frame. The camera operates at 30 Hz so $t_c = 1/30 = 0.03333$ seconds. The delay generator automatically calculates T_2 from T_1 and that there is a fixed time delay from when the laser is triggered to when it actually fires the laser pulse so from Δt the input timings can be calculated as follows:

$$T_1 = t_c - \frac{\Delta t}{2} - Q - A_1 - L - \frac{t_c}{2} \quad [\text{A-1}]$$

$$T_2 = L + A_1 \quad [\text{A-2}]$$

where:

T_1 triggers the lamp on laser 1 to fire

T_2 triggers the Q-switch of laser 1

Q = delay between external Q-switch trigger IN and laser pulse = 180 ns

A_1 = adjustable Q-switch delay for laser 1 = 188 μ s

L = delay between external lamp trigger IN and lamp sync out = 9.25 μ s

Note: $t_c/2$ must be subtracted from the values because the external generator triggers the timings from the falling edge of the 15 Hz signal while the camera initiates an image at the rising edge of the 30 Hz signal.

T_3 triggers the lamp on laser 2 to fire and T_4 triggers the Q-switch of laser 2 and can be calculated as follows:

$$T_3 = t_c + \frac{\Delta t}{2} - Q - A_2 - L - \frac{t_c}{2} \quad [\text{A-3}]$$

$$T_4 = t_c + \frac{\Delta t}{2} - Q - \frac{t_c}{2} \quad [\text{A-4}]$$

where:

A_2 = adjustable Q-switch delay for laser 2 = 194 μs .

The timings were set to generate a time spacing between the two laser pulses of 2.52 ms by using the following settings in the pulse generator: $T_1 = 0.0152092$, $T_2 = 0.0001972$, $T_3 = 0.0177232$, and $T_4 = 0.0179266$. A Tektronix TDS2004 4 channel digital storage oscilloscope was used to check the signals to ensure the camera and laser were synchronized and that the laser pulse timing was correct.

A.2 DATA PROCESSING

This algorithm works using pairs of DPIV images with short exposure times separated by small time spacings. The images are broken into interrogation windows in the first image and search windows in the second image. The displacements are determined by iteratively tracking groups of particles between the interrogation window in the first image and the corresponding search window in the second image, in a multi-grid environment by the locating the cross-correlation peak. First estimate displacements for large interrogation windows (64

by 64 pixels) are considered coarse results and are used as a predictor. The interrogation areas are then halved in both directions to a 32 by 32 pixel window and shifted in the direction of the predictor information to get a better estimate of the displacements. A 50% window overlap is used to increase the spatial resolution to 16 by 16 pixels. The instantaneous velocities are then obtained by dividing the displacement fields with the time interval.

100 images were processed from each run to compare the results from the three iterations to refine the processing parameters. The first iteration uses a 64 by 64 pixel window with a grid distance between displacement vectors of 32 pixels, the second iteration uses a 32 by 32 pixel window with a grid distance between displacement vectors of 16 pixels, and the third iteration uses a 16 by 16 pixel window with a grid distance between displacement vectors of 8 pixels. The three iterations were compared for the number of spurious vectors detected, the average pixel displacements, average velocity contours and vectors and maximum, minimum and mean velocity in each column.

The average number of spurious vectors detected over the 50 image pairs for each of the iterations is summarized in Table A-1. The spurious vectors increase with grid distance but are all within acceptable limits. The locations of the spurious vectors detected for one of the image pairs using a grid distance of 16 is illustrated in Figures A-2 to A-4 where the black grid indicates a location where the vector was designated as a spurious vector. This illustrates that the spurious vector locations were not concentrated in one area of the image.

The raw pixel displacements in each direction for each of the iterations are summarized in Table A-2. Figures A-5 to A-7 shows the displacement histogram for a grid distance of 16 for each case. The appropriateness of the time spacing can be checked by plotting a histogram of the raw displacements from the processed images. The maximum displacement should be less than 50% of the

calculation window size. This is the case for the first two iterations with the third iteration close to the threshold requirement.

Figures A-8 to A-10 compares the overall velocity contours for each of the three iterations. For all three of the cases, a grid distance of 32 produces the smoothest velocity contours because the velocity is being averaged over a greater region and a grid distance of 8 produces the most jagged velocity contours. Examining each case separately, for tH005 the greatest difference is seen under the leading edge of the block where the minimum contour in the 32 grid distance plot is 30 cm/s, in grid distance of 16 there is a 10 cm/s contour and in grid distance 8 this contour extends further along the block. Similarly for tH01 the greatest difference is seen under the leading edge of the block where a grid distance of 32 does not show any recirculation beneath the block and the contours of 10 and 20 cm/s do not extend as far. Little difference is seen between the contours for a grid distance of 16 and 8 for this case. For the rounded block case all three grid distances produce similar velocity contours and indicate the flow beneath the rounded block is rather uniform.

To look at the difference in calculated velocities in detail, the maximum, minimum and mean velocity at each x-location are shown in Figures A-11 to A-13. Similar to the velocity contours, a grid distance of 32 produces a smoother curve with lower peak maximum velocities while a grid distance of 8 produces a jagged curve with more oscillations due to the fact that the velocity is being averaged over a smaller region. For the case tH005, there is little difference between the maximum velocities for a grid distance of 16 and 8. For the minimum velocities, a grid distance of 32 is too coarse to capture the minimum velocity as it smoothes the data too much while a grid distance of 8 captures the minimum velocities the best as it resolves the velocities closer to the block. There is little difference in the mean velocities, though as expected a grid distance of 32 shows the highest mean velocities. Examining the case of tH01, there is little difference between the three grid spacings. A grid distance of 16 and 8 do a better job of

capturing the minimum velocities however there is no significant difference between the two grid spacings. For the rounded block, all three resolutions calculate similar maximum velocities and show little difference between the calculated mean velocities. The biggest difference is seen in the minimum velocity where a grid distance of 32 calculates the largest minimum velocities and a grid distance of 8 calculates the smallest minimum velocities although the difference between 8 and 16 is not much.

A final comparison focuses on the velocity contours and vectors at the leading edge of the block shown in Figures A-14 to A-16. For tH005 a grid distance of 32 shows no recirculation under the block and the minimum contour is 30 cm/s. A grid distance of 16 does not show any recirculation either but captures lower velocities with a minimum contour of 10 cm/s. A grid distance of 8 shows the most detail under the leading edge of the block with some recirculation with a minimum contour of 10 cm/s. The 10 cm/s contour has about the same thickness at that predicted by the grid distance of 16 but extends further along the block. Examining the velocity vectors for tH01, a grid distance of 32 shows some recirculation under the block and shows the separation zone ending around 11 cm. A grid distance of 16 shows more detail within the separation zone and shows the separation zone ending around 15 cm. A grid distance of 8 shows the most detail within the recirculation zone and shows the zone ending around 15.5 cm. For the rounded block, there is no recirculation of the flow at the leading edge of the block and there is little information gained by increasing the resolution.

Taking these comparisons into account, a grid distance of 8 should be used for tH005 in order to estimate the characteristics of the recirculation zone. Within the recirculation zone the velocities are low so even though the mean raw displacements exceed the limit of the grid distance, this will not happen within the recirculation zone due to the smaller displacements. For the mean velocity properties, there was little difference between the calculations using a grid distance of 16 and a grid distance of 8 so a grid distance of 16 is sufficient for

capturing the mean velocity field. For the case of tH01, while a grid distance of 8 captured more detail within the recirculation zone than a grid distance of 16, there was little difference between the size of the separation zone and the mean velocity properties so the smaller resolution does not provide any advantage over the grid distance of 16. Therefore a grid distance of 16 was deemed appropriate for defining the mean velocity field as well as the separation zone characteristics. For the rounded block case there was little difference between a grid distance of 16 or 8, therefore a resolution of a grid distance of 16 was deemed sufficient for analyzing the 18000 images.

Table A-1: Spurious vectors.

Case	Grid distance (pixels)	Spurious vector count	Total vector count	Spurious vectors (%)
tH005	32	6	1457	0.4%
	16	21	6080	0.3%
	8	597	24639	2.4%
tH01	32	13	1316	1.0%
	16	60	5415	1.1%
	8	821	22156	3.7%
tH005Round	32	1	1410	0.0%
	16	11	5890	0.2%
	8	634	23875	2.7%

Table A-2: Raw pixel displacements.

Case	Grid distance (pixels)	x Max dis	x Min dis	x Mean dis	y Max dis	y Min dis	y Mean dis
tH005	32	10	1.1	8.4	4.2	-0.2	0.27
	16	11	-4.2	8.1	6.6	-3.5	0.08
	8	14	-4.2	8.1	7.9	-4.4	0.33
tH01	32	11	-3.8	8.3	6.2	-5.3	0.67
	16	12	-6.3	8.4	8	-7.4	0.57
	8	13	-6.6	8.2	9.2	-9.1	0.67
tH005Round	32	9.5	1.4	8.6	2.9	-0.67	0.32
	16	10	-0.21	8.3	3.8	-1.6	-0.014
	8	11	-1.7	8.4	4.4	-2.5	0.42

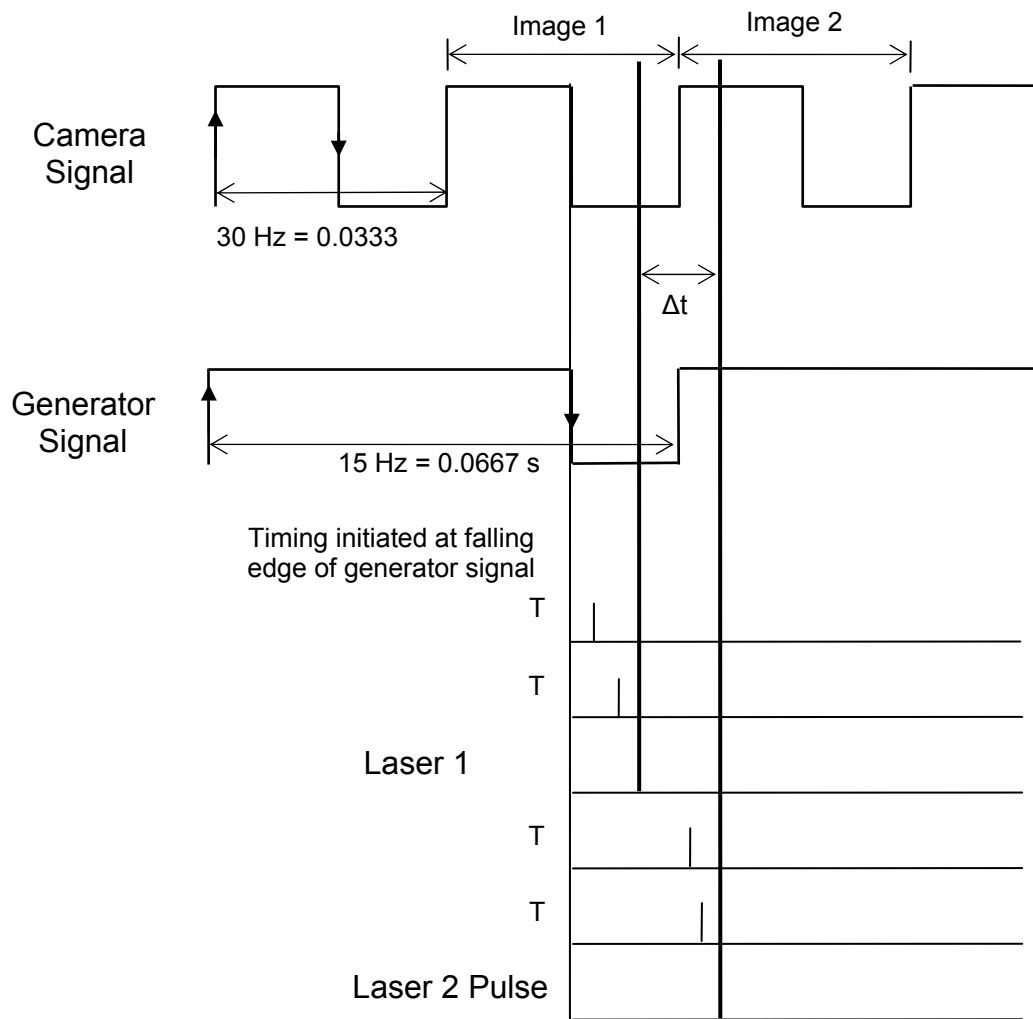


Figure A-1: Schematic of laser pulse timings.

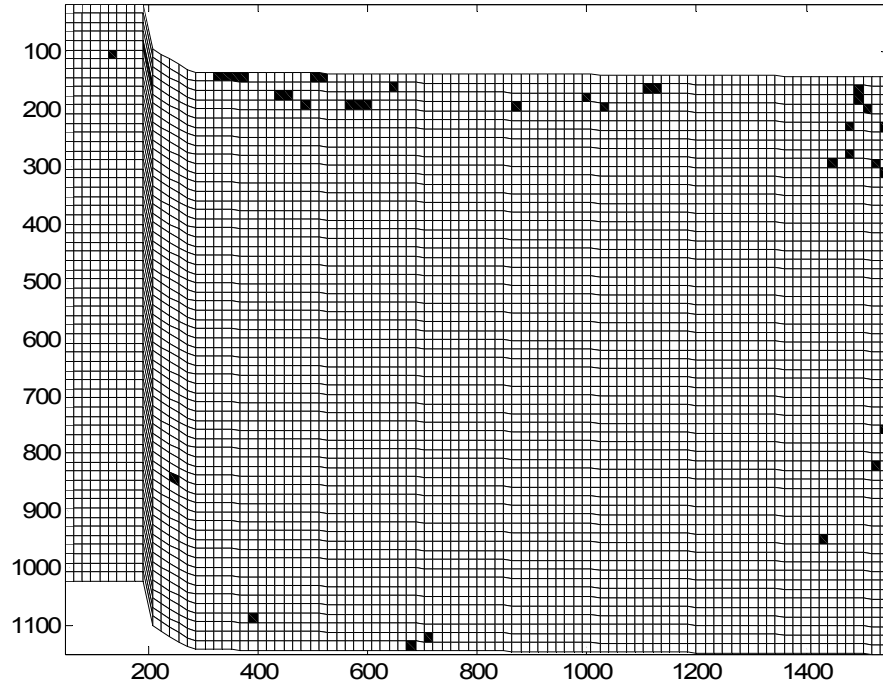


Figure A-2: Spurious vector locations for tH005.

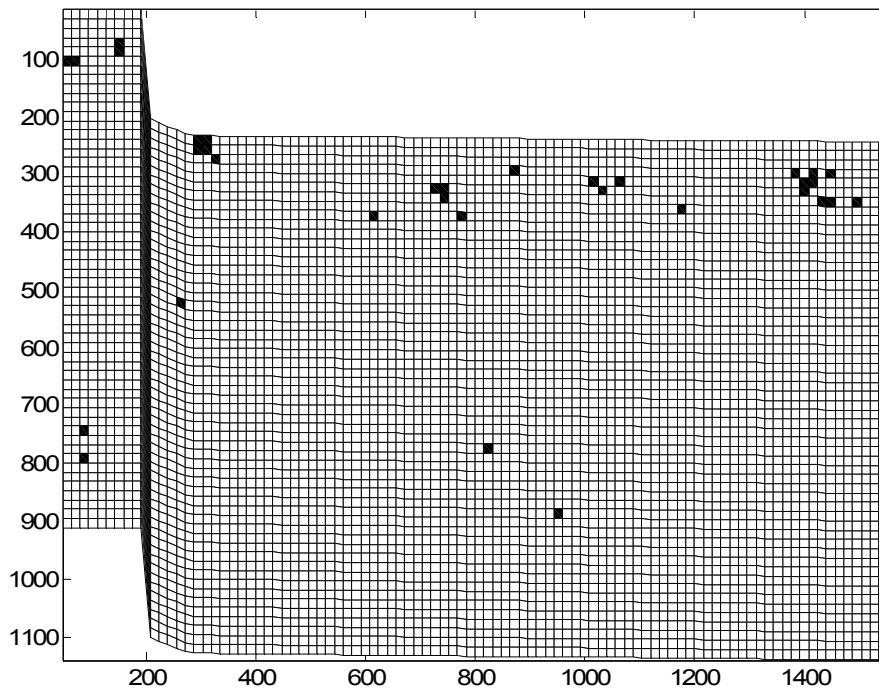


Figure A-3: An example of the spurious vector locations tH01.

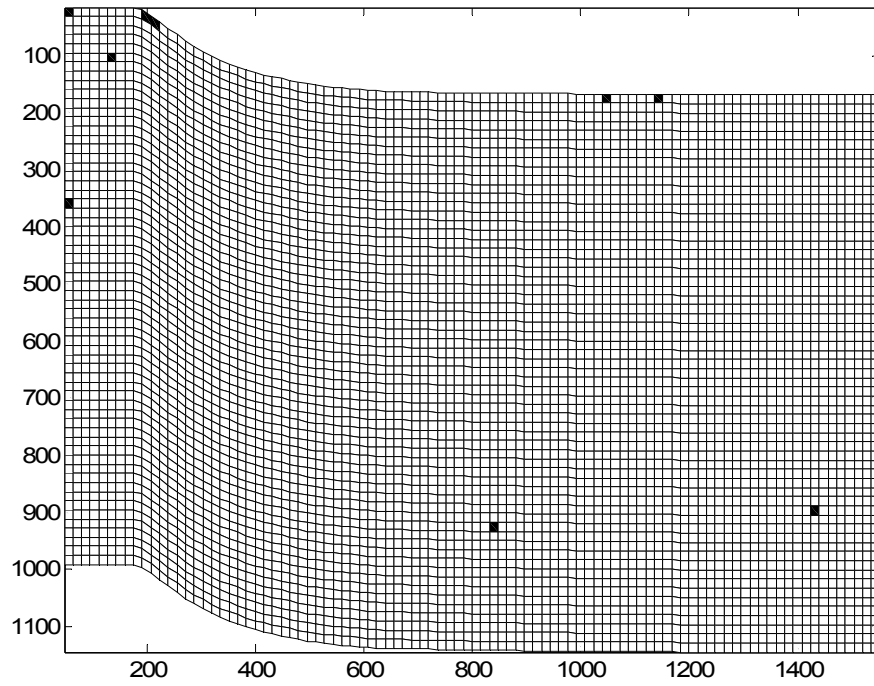


Figure A-4: Example of locations of spurious vectors detected for tH005Round.

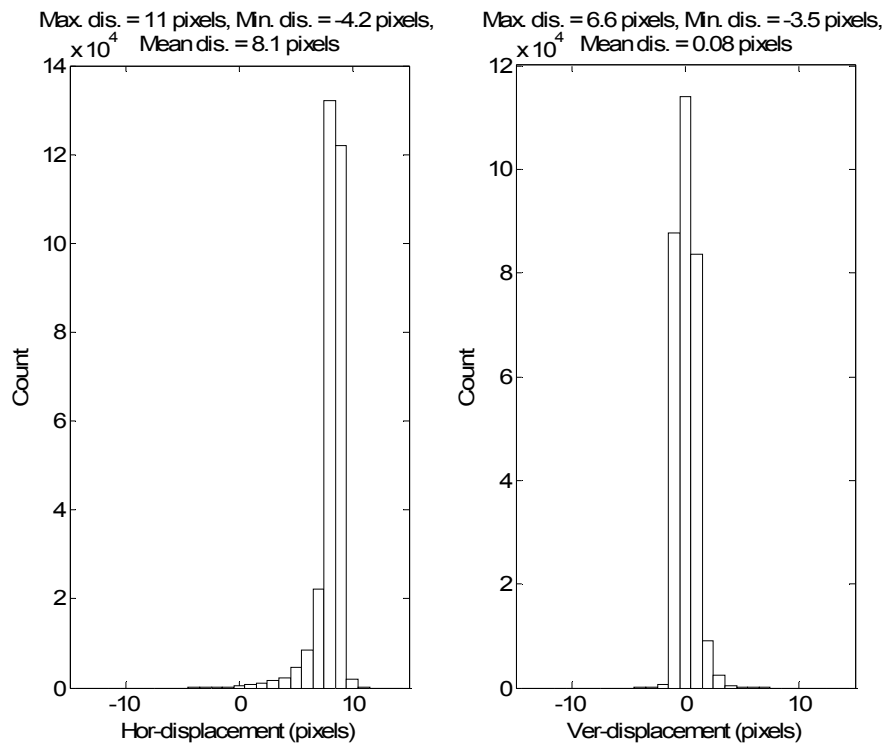


Figure A-5: Raw pixel displacements for tH005, grid distance of 16.

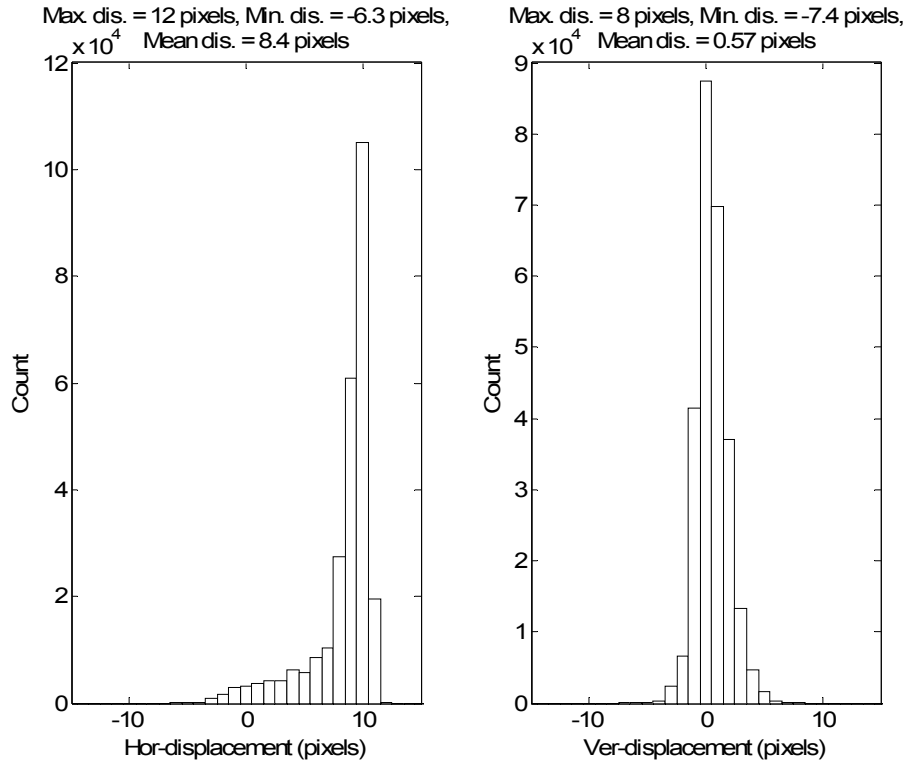


Figure A-6: Raw displacements for tH01.

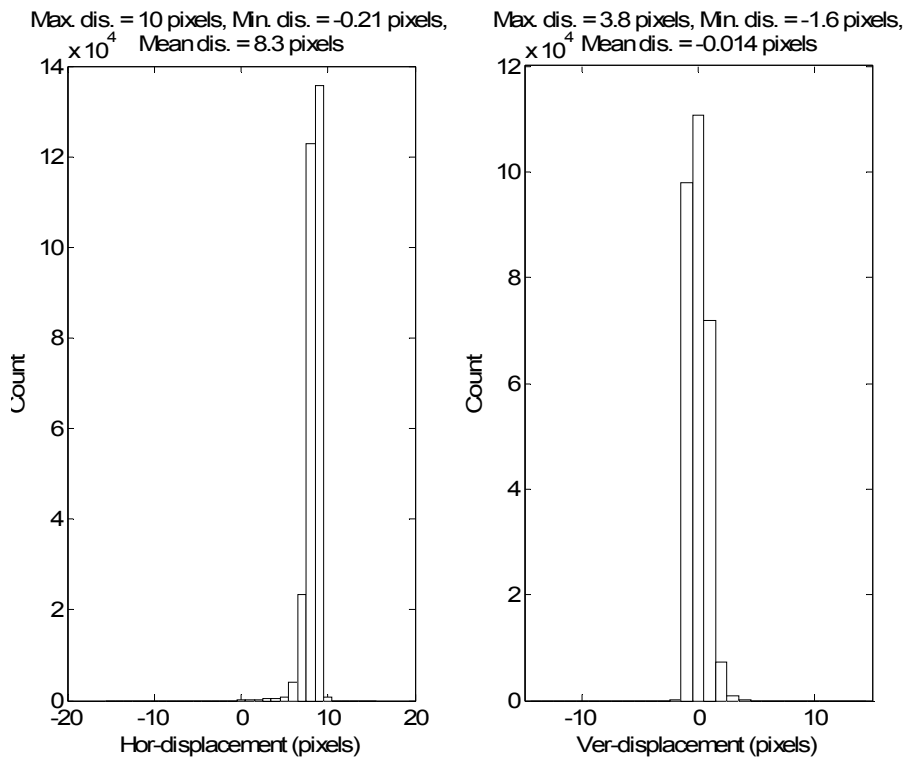


Figure A-7: Raw displacement histogram for tH05Round for a grid distance 16.

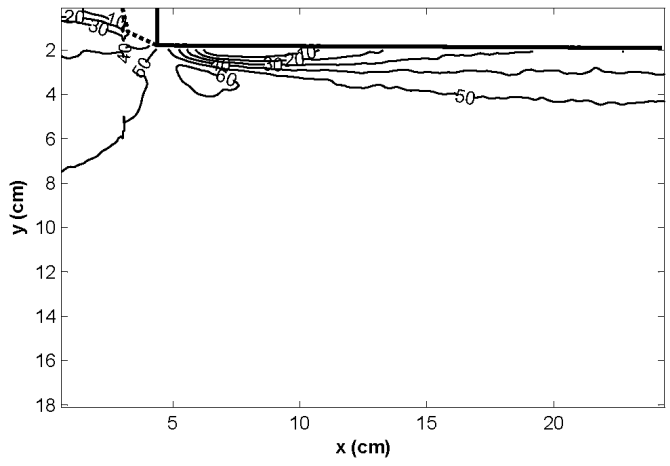
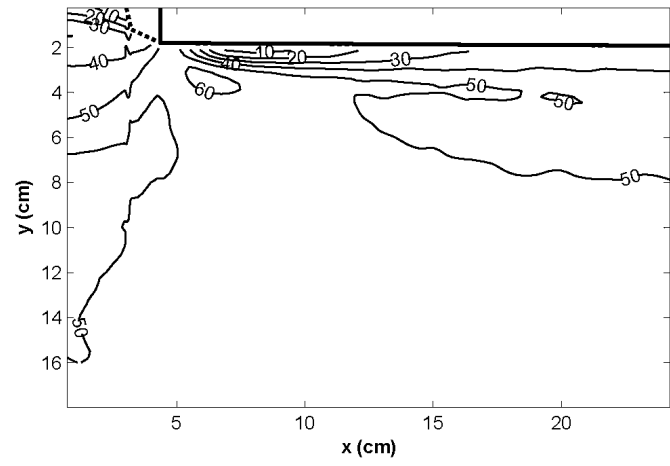
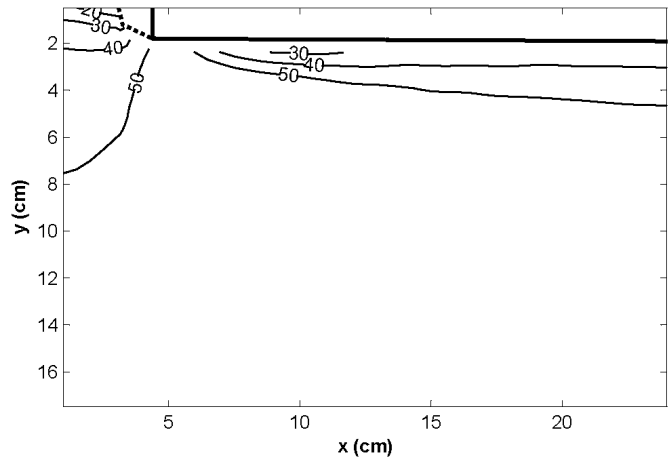


Figure A-8: Velocity contours for tH005 for a grid distance of 32, 16 and 8.

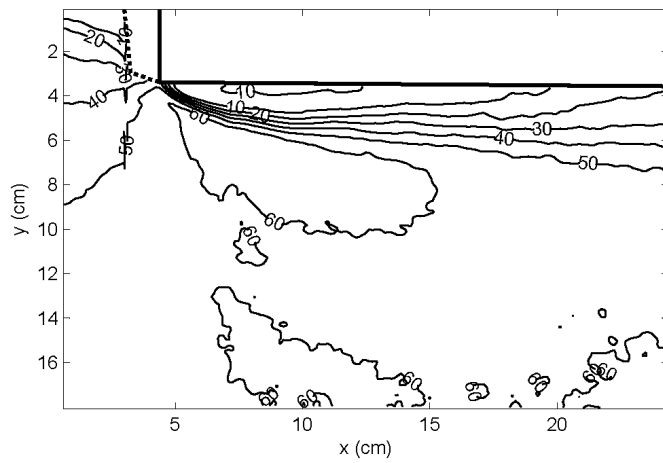
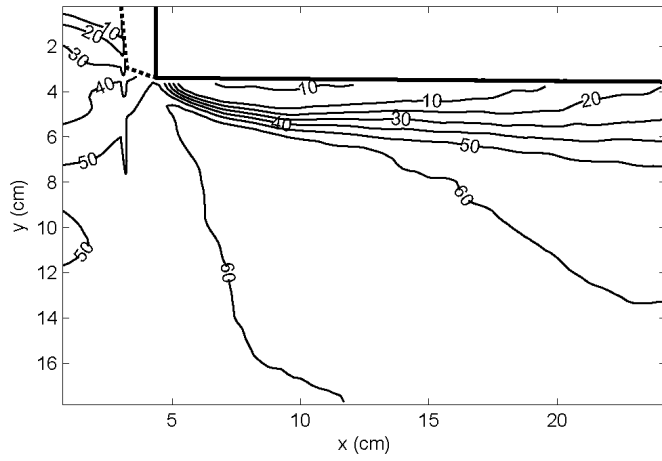
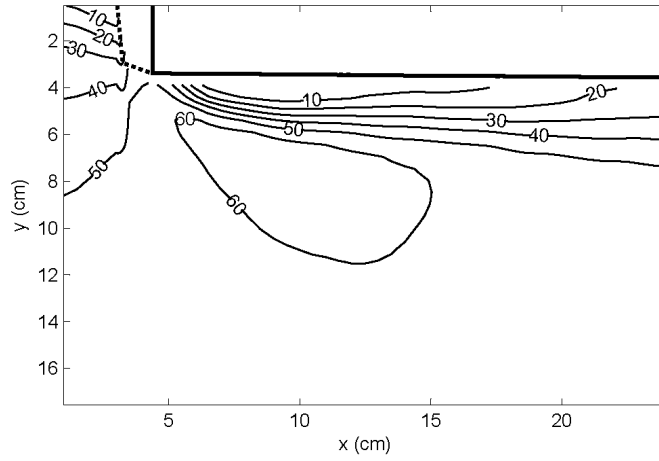


Figure A-9: Mean velocity contours for tH01 averaged over 100 images for a grid distance of 32, 16 and 8.

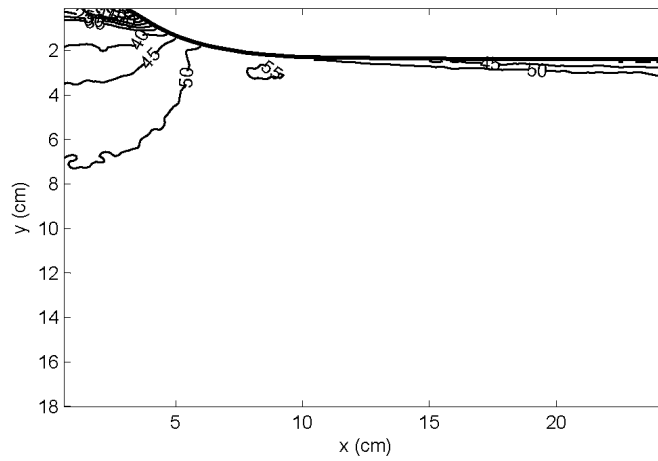
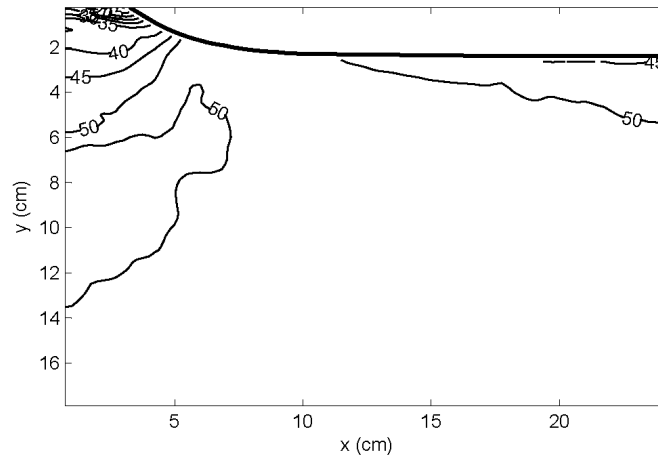
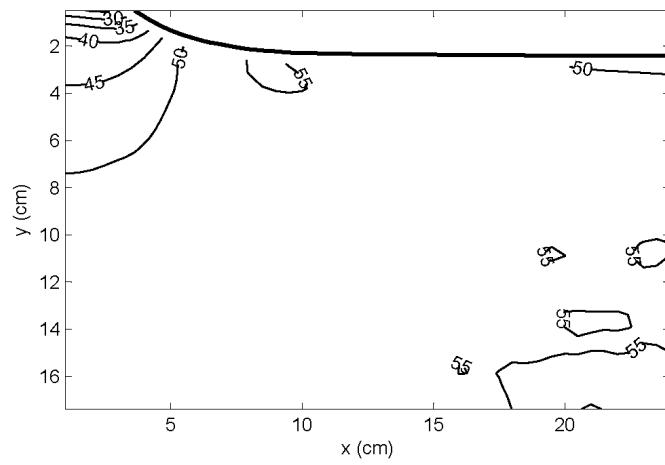


Figure A-10: Mean velocity contours for tH005Round averaged over 100 images for a grid distance of 32, 16 and 8.

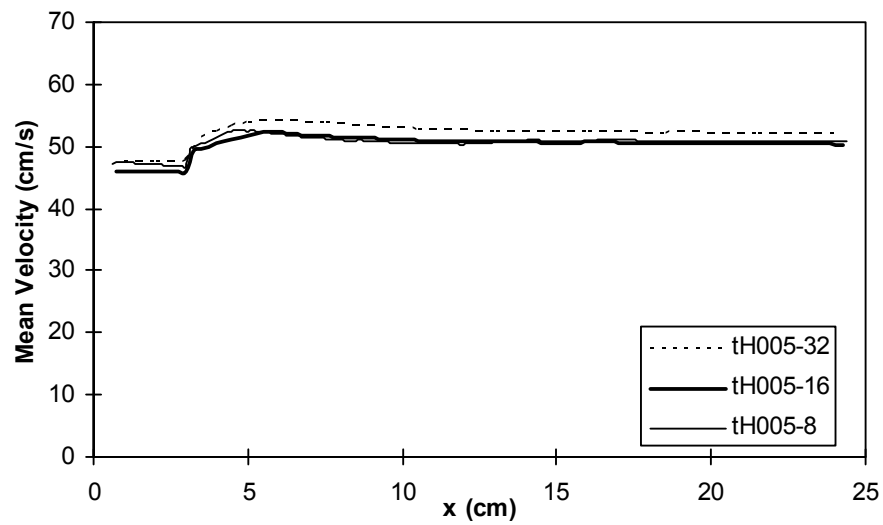
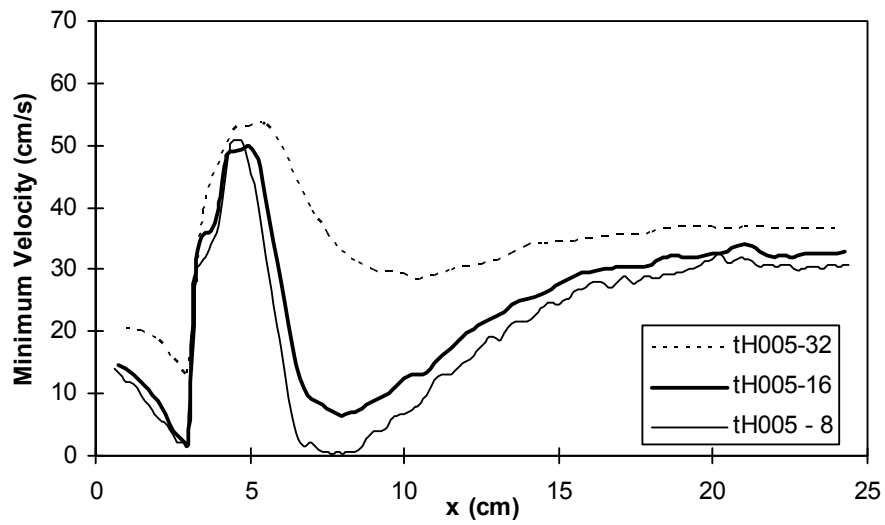
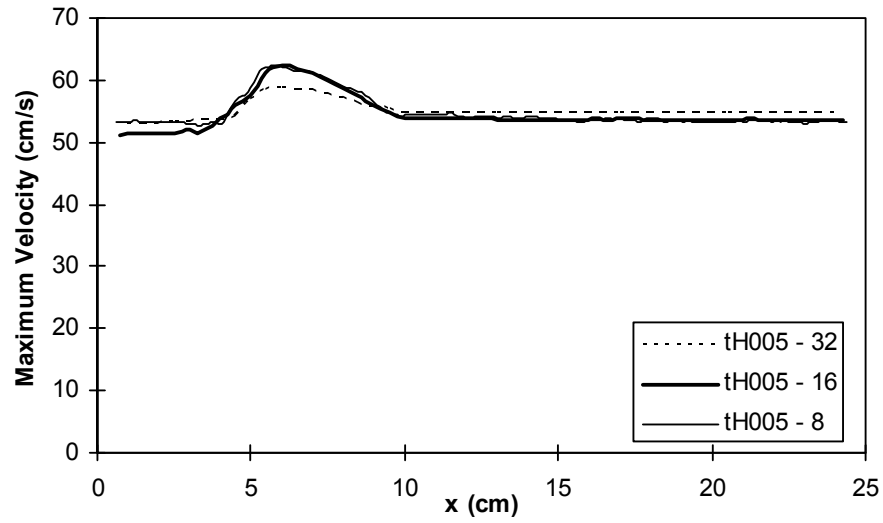


Figure A-11: Compare maximum, minimum, and mean velocity for tH005.

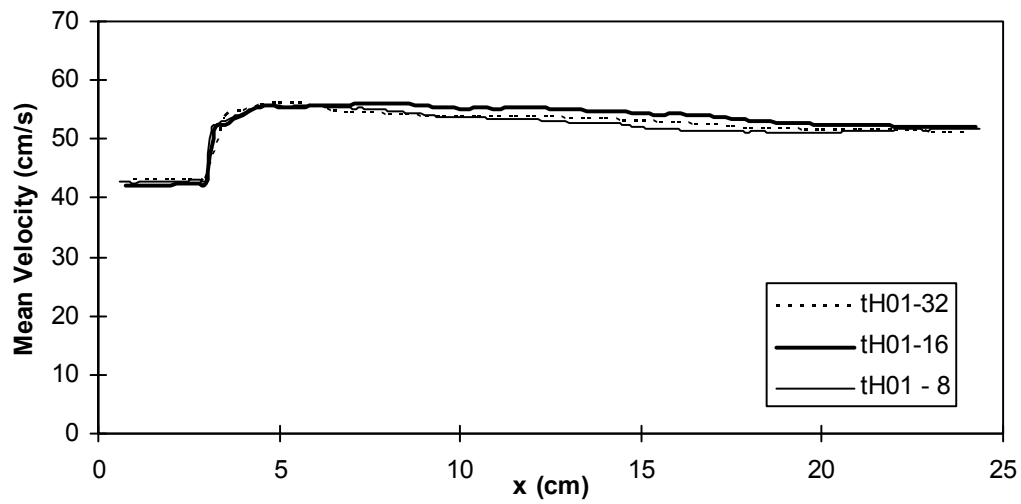
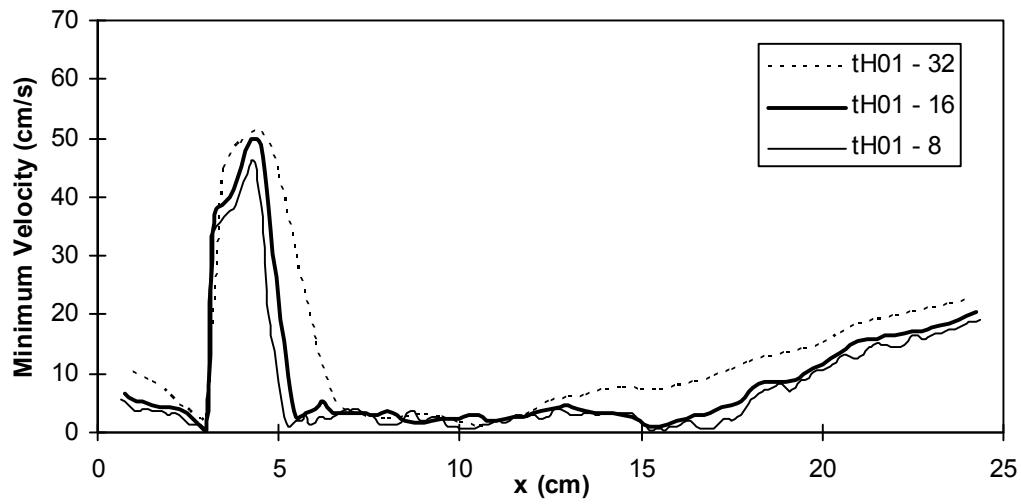
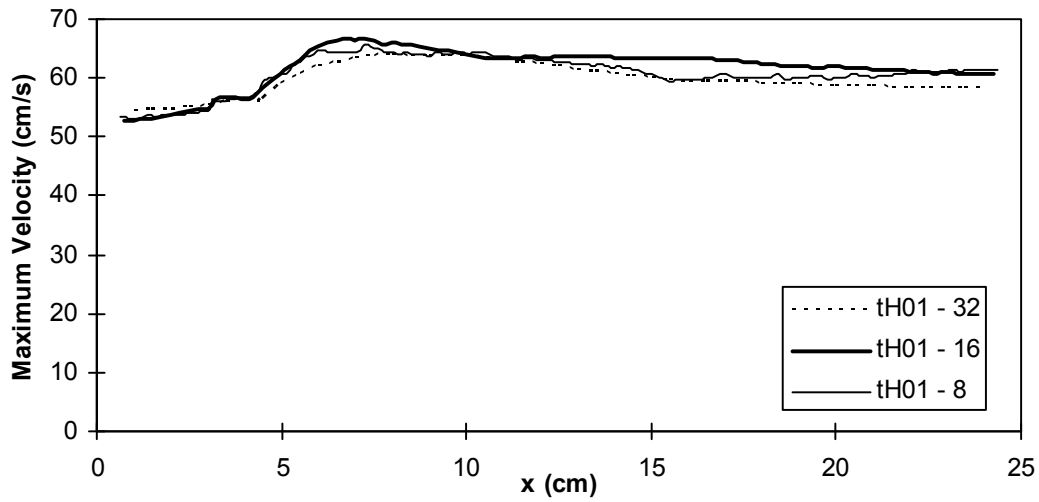


Figure A-12: Maximum, minimum and mean velocity grid size comparison for tH01.

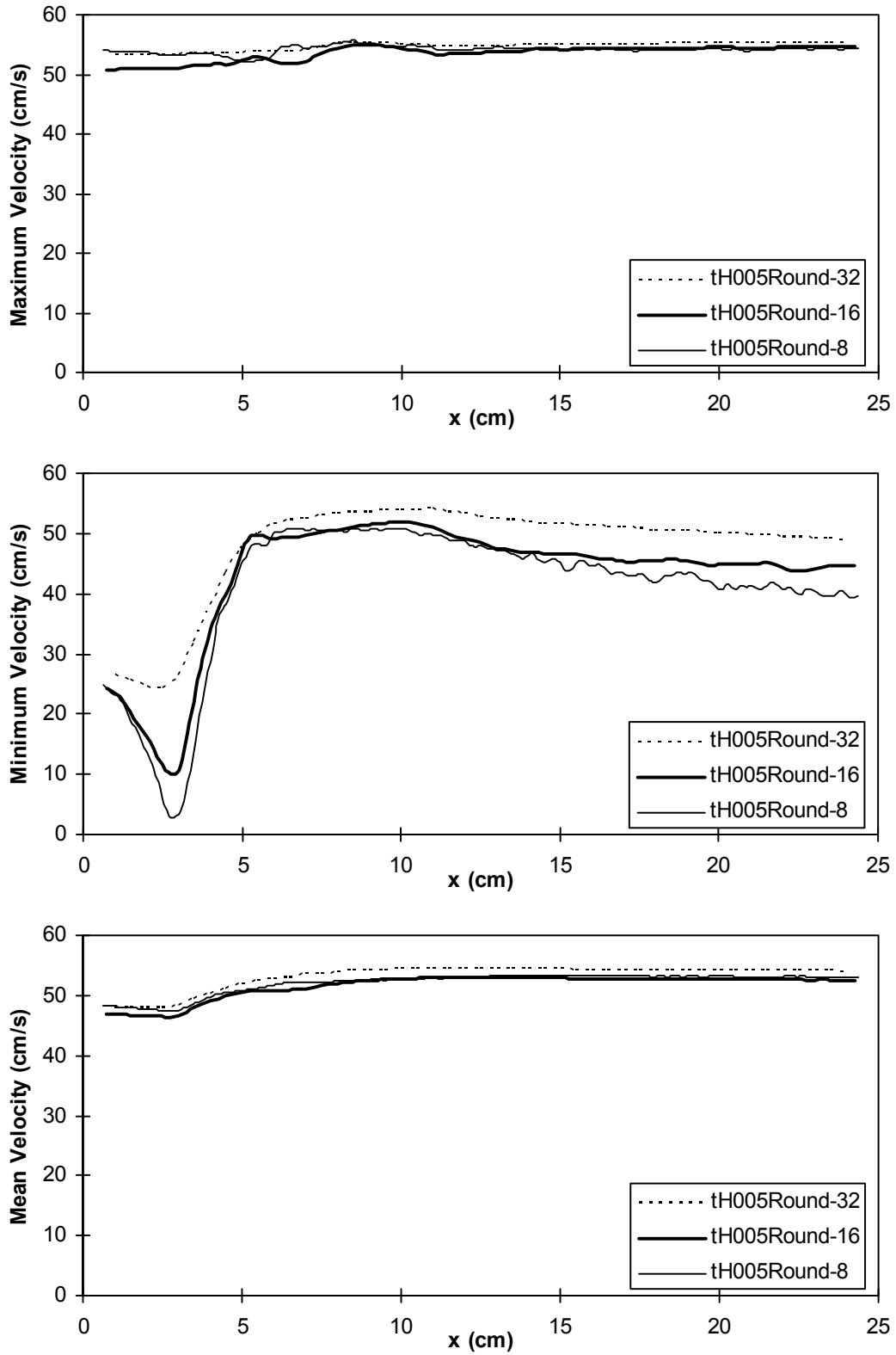


Figure A-13: Comparison of maximum, minimum and mean velocity for tH005Round.

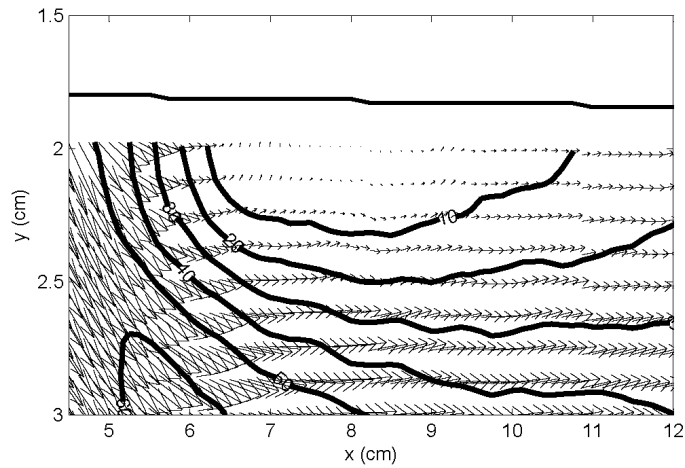
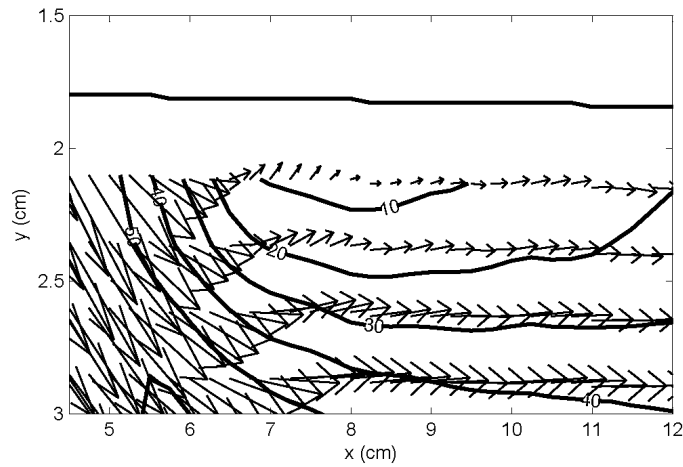
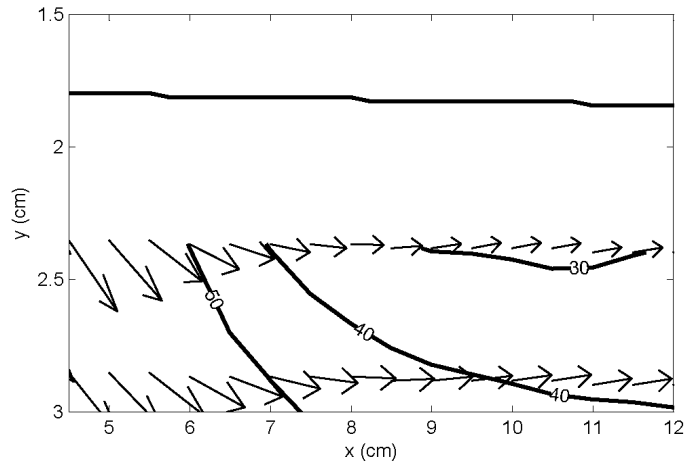


Figure A-14: Velocity vectors at leading edge averaged over 100 images for tH005 at a grid distance of 32, 16 and 8.

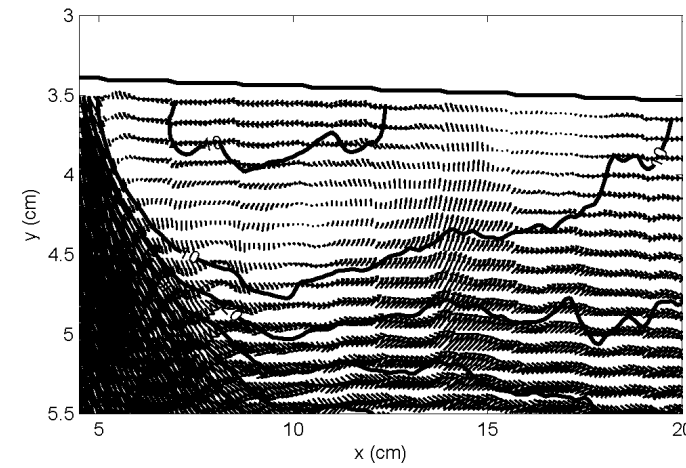
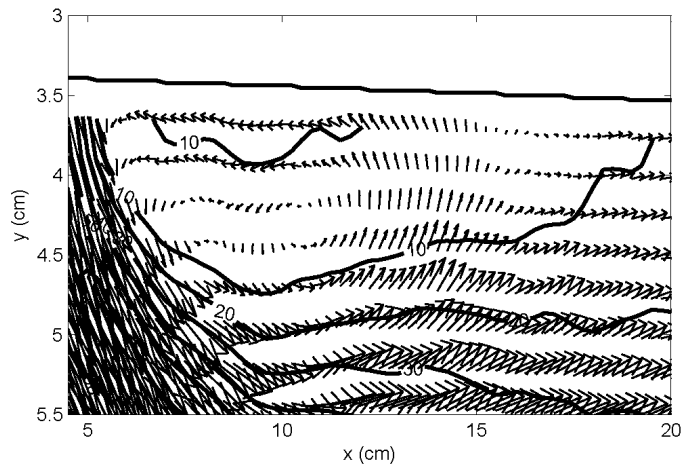
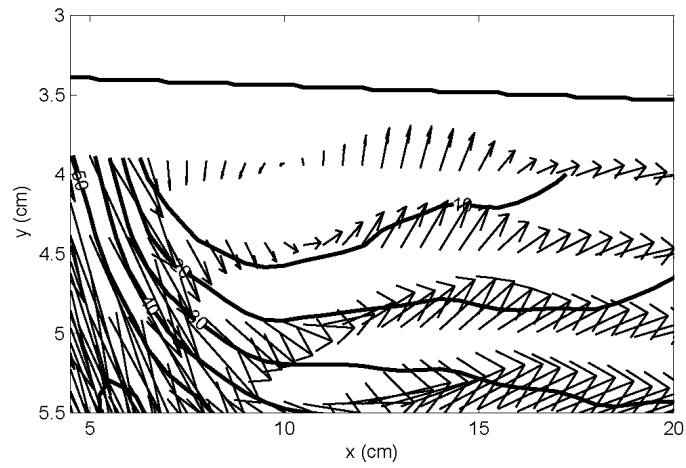


Figure A-15: Mean velocity vectors for tH01 averaged over 100 images for a grid distance of 32, 16, and 8.

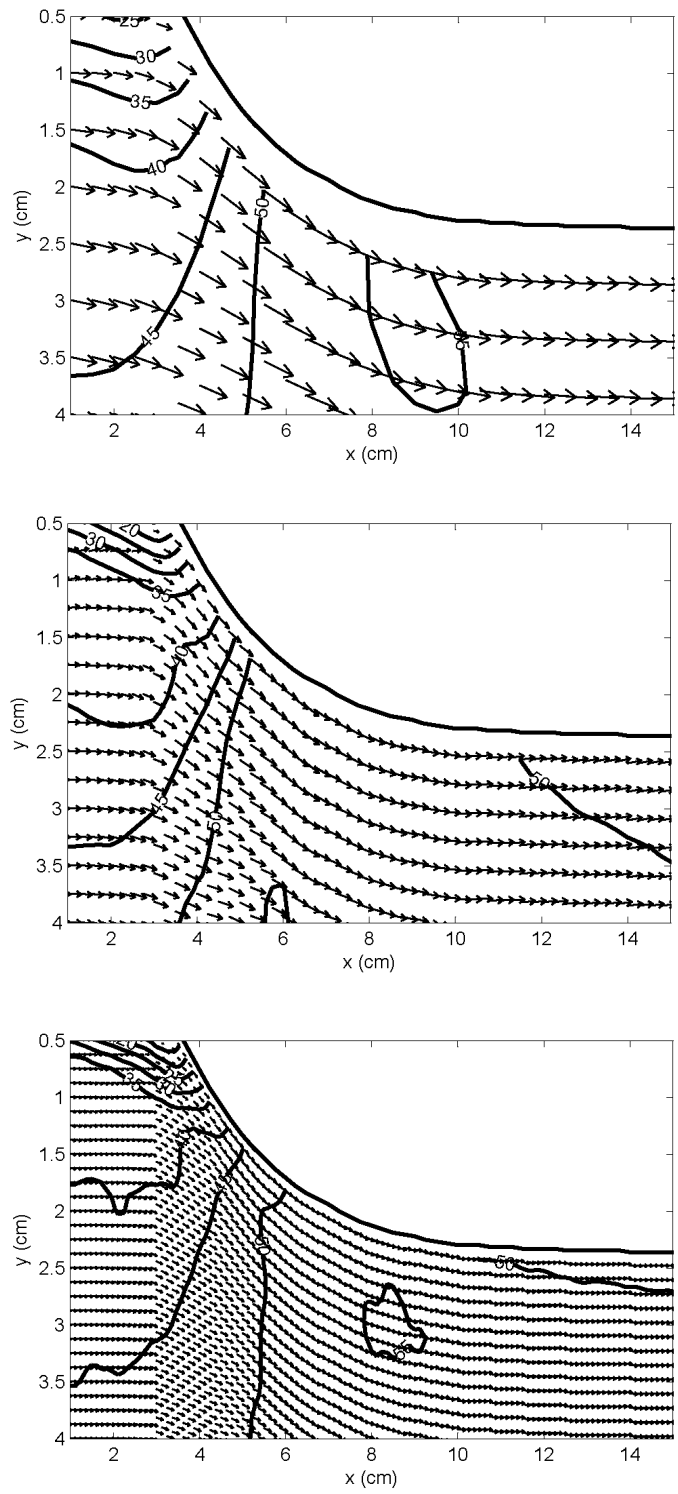


Figure A-16: Mean velocity vectors at leading edge for tH005Round averaged over 100 images for a grid distance of 32, 16, and 8.

APPENDIX B: INVESTIGATION OF ICE BLOCK STABILITY – NUMERICAL MODELING ISSUES

B.1 INTRODUCTION

The transport and accumulation of ice is one of the more complicated problems in river ice hydraulics, because of the complex fluid dynamics surrounding individual ice floes. It is of relevance to the physics of ice cover development and ice jam formation, but is of particular in the context of ice jam release. Jasek (2003) notes that when large ice floes are transported downstream under an ice jam past its toe, then it is likely that these floes will be propelled upwards, impacting the underside of the intact solid ice cover. He suggests that such occurrences have the potential to crack and weaken the restraining ice cover, initiating the open leads which are believed to play an important role in the occurrence of ice jam release (Jasek, 2003). If true, specific knowledge of the hydrodynamic forces acting on individual ice floes will be an important component of any model which attempts to predict the occurrence of ice jam release events.

This paper was presented by the first author at the CGU HS Committee on River Ice Processes and the Environment 13th Workshop on the Hydraulics of Ice Covered Rivers Hanover, NH, September 15-16, 2005 and is published in its proceedings.

In the practical context of this problem, there are a number of component phenomena to consider. For example, the initial question is whether or not discrete ice floes approaching an ice jam accumulation from upstream will contribute to lengthening, or will be entrained in the flow and transported beneath the ice jam. For the latter case, the further question is whether or not the entrained floe will be transported all the way past the ice jam toe, to be in a position to rise under the intact restraining ice cover.

At present, much of our knowledge of these processes is necessarily qualitative, due to the inherent logistical difficulties and safety issues which arise when trying to measure dynamic ice processes in the field. This is particularly difficult for ice floe transport under ice jams. As a consequence, we must rely in large part on experimental and numerical work to further understand the mechanics of ice floe entrainment and transport, and that is the purpose of this investigation. Here we discuss some preliminary results of the first phase of this investigation, in which we focus on the issue of ice floe entrainment at the leading edge. Current theory and observations (e.g. Beltaos, 1995) suggest that the leading edge of an ice jam accumulation behaves as a narrow jam, with floe entrainment or juxtapositioning being the dominant local processes. Healy and Hicks (2001) observed this same tendency near the leading edge of ice jams forming in a laboratory flume.

Numerous studies have already been conducted to examine this problem of ice block stability. Early investigations of this phenomenon focused on defining the critical approach velocity or critical densimetric Froude number (based on approach flow velocity and block thickness) at which floating ice blocks at leading edges of intact ice covers are submerged (Pariset and Hausser, 1961; Ashton, 1974; Uzuner and Kennedy, 1972; Larsen, 1975). Daly and Axelson (1990) examined the problem analytically and determined that instability was reached when the overturning moment exceeded the righting moment. Coutermarsh and McGilvary (1991, 1993, 1994) attempted to measure the two dimensional pressure distribution along the bottom surface of a floating block and

found both positive (stabilizing) and negative (destabilizing) pressures acted on the block, with a characteristic saddle shape in the pressure distribution. They observed that changes in flow velocity had little effect on the pressure distribution but primarily changed the pressure magnitude. More recently Hara *et al.* (1996) and Kawai *et al.* (1997) conducted a series of experiments investigating the movement of ice floes at the edge of an ice cover characterizing the movement and the critical densimetric Froude number at movement. They focused on the shape of the edge of the ice cover and the thickness of the ice block.

With recent advances in numerical and experimental technology that allow for better flow visualization and determination, more information about the mechanics of the problem can now be now realized. The objective of this first phase of our study is to examine the steady state stability of floating ice blocks that have come to rest against an intact ice cover using a three-dimensional (3-D) computational fluid dynamics package. We seek to increase our knowledge of the stability behaviour of floating ice floes and the hydrodynamic forces that act upon them. The results of this study will be used to assist in the design of an experimental study, and will hopefully ultimately prove valuable to the advancement of discrete particle models of river ice. At this stage, preliminary results of the numerical modeling effort are presented with a focus on the effects of the assumed inlet velocity profile and the shape of the leading edge of the ice cover on the pressure distribution under the ice cover.

B.2 DIMENSIONAL ANALYSIS

When an ice floe comes to rest against a floating obstacle, it can remain in place or it can become submerged. Buoyancy is the resisting force against motion, while the submerging forces are due to the pressure reductions under the ice floe caused by flow separation and acceleration. The significant variables in this analysis are (Figure 1):

- the mean flow velocity under the block, V_u ;

- the depth of the approach flow, H ;
- the block length L , block thickness, t ;
- the block width b , block density, ρ' ;
- the fluid density, ρ ; and
- the acceleration due to gravity, g ,

such that,

$$V_u = f(b, t, L, \rho', \rho, g, H) \quad [\text{B-1}]$$

Dimensional analysis leads to the following relationship:

$$\frac{V_u}{\sqrt{gt}} = f\left(\frac{b}{L}, \frac{t}{H}, \frac{\rho'}{\rho}, \frac{t}{L}\right) \quad [\text{B-2}]$$

which is the same result as in Beltaos (1995).

However, most authors have expressed their results in terms of a densimetric Froude number which would be in the form of:

$$F = \frac{V_u}{\sqrt{\left(\frac{\rho - \rho'}{\rho}\right)gt}} = f\left(\frac{b}{L}, \frac{t}{H}, \frac{t}{L}\right) \quad [\text{B-3}]$$

B.3 MODEL IMPLEMENTATION

B.3.1 Modeling Platform

A three dimensional (3-D) computational fluid dynamics package, ANSYS CFX-5, was used to investigate the steady state stability of ice blocks resting against an ice cover. CFX-5 is based on the finite volume technique which solves the Navier Stokes equations in their conservation form. For steady state, inviscid flow the

equations of motion presented in the CFX-5 Solver Theory Manual in differential form reduce to:

$$\nabla \cdot (\rho \vec{U} \otimes \vec{U}) = \nabla \cdot (-\rho \delta) + S_M \quad [\text{B-4}]$$

where:

$$\nabla = \left(\frac{\partial}{\partial x}, \frac{\partial}{\partial y}, \frac{\partial}{\partial z} \right)$$

\vec{U} = velocity vector

ρ = density

\otimes = tensor product

δ = Kronecker delta or identity matrix

S_M = momentum source

Turbulence models are necessary in CFD simulations to enable the effects of turbulence to be predicted without requiring a prohibitively fine mesh and computing power that does not yet exist. There are many turbulence models available in CFX-5 and can be divided into eddy viscosity models, Reynolds stress models, Large Eddy Simulation (LES) and Detached Eddy Simulation (DES). The turbulence models equations presented here are described in the CFX-5 Solver Theory Manual while general description can be found in the CFX-5 Solver Modelling Manual. Within the eddy viscosity models, the k - ε model is considered the industry standard turbulence model as it is good for many engineering flows. The term k is the turbulence kinetic energy and ε is the turbulence eddy dissipation. This model introduces two variables to the system of equations, specifically the effective viscosity μ_{eff} and the modified pressure p' as:

$$\mu_{eff} = \mu + \mu_t \quad [\text{B-5}]$$

$$p' = p + \frac{2}{3} \rho k \quad [\text{B-6}]$$

where μ_t is the turbulence viscosity which in the k - ε model is assumed to be linked to the turbulence kinetic energy and dissipation via the relationship:

$$\mu_t = C_\mu \rho \frac{k^2}{\varepsilon} \quad [\text{B-7}]$$

where C_μ is a constant equal to 0.09 (CFX-5 Solver Theory Manual).

The Large Eddy Simulation model is for transient large scale fluctuating flows. It filters the velocity field so that it contains only the large scale components of the total field as it is the large scale motions that are more energetic and effective transporters. LES filters the equations of movement and decomposes the flow variables into a large scale (resolved) and a small scale (unresolved) parts. The LES model is used primarily for research purposes and is not practical because of the fine grid and time step requirements. It must be run in a transient mode and gives detail on the structure of turbulent flow such as pressure fluctuations that would not be obtained from a Reynolds Averaged Navier Stokes formulation.

Boundary conditions in CFX-5 can be modeled as an inlet, outlet, opening (fluid can simultaneously flow both in and out of the domain), wall, or symmetry plane. The most robust boundary configuration is to specify a velocity / mass flow at an inlet with a static pressure at an outlet (CFX-5 Solver Modelling Manual).

B.3.2 Test Case for Ice Block Stability

A key component of any numerical modeling study is validation data, and at present the most comprehensive validation data found in the literature are the detailed pressure measurements by Coutermarsh and McGilvary (1991,1993,1994). Although at this time, these data are not yet available to us, our

preliminary test cases were modeled after that study in the hope that ultimately a verification comparison might be conducted. Their experiments were conducted in a warm flume with cross section of 0.91 by 0.91 m and length of 7.32 m with a variable pumping capacity of 0.3 m³/s. A hollow Plexiglas square ice floe 61.6 by 61.6 cm and thickness of 7.62 cm with 91 pressure taps on the bottom surface was fastened to the flume to hold the block rigid through the test. The upstream end of the block was fixed with a threaded rod that allowed the block angle of attack to be varied. The t/H ratio was varied by changing the water depth as the thickness of the ice floe remained constant.

For this preliminary study component, simulations were limited to the following test cases:

- angle of attack of 0°,
- t/H of 0.1, and
- approach flow mean velocity, V , of 0.45 m/s.

in order to conduct detailed sensitivity analyses of the following parameters:

- inflow boundary conditions (i.e. assumed velocity profile)
- shape of the leading edge of the ice floe;
- location of outlet boundary
- use of a symmetry plane
- domain setup

B.3.3 Model Implementation

Geometry

Figure 2 illustrates the geometry of the modeled domain, which was created to match that of the apparatus used by Coutermarsh and McGilvary (1994), as discussed earlier. The pressure measurements made by Coutermarsh and McGilvary (1994) verified that the pressure distributions were always symmetrical about the centerline of the ice floe and initial runs of our numerical model also confirmed this. Therefore, a symmetrical boundary condition was

used at the centerline of the flume ($x = 0.455$ m), to minimize computational memory and processing requirements.

The regions of fluid flow and/or heat transfer in CFX-5 are called domains. Fluid domains define regions of fluid flow while solid domains are regions occupied by conducting solids. As there was no need to model thermal heat transfer between the ice and the water and the ice remains stationary, the ice floe and ice cover were modeled as cavities rather than as solid domains. By modeling as a cavity, the physical properties of the ice are not modeled (density, heat transfer, etc.). This saves on computational time as there is no computational mesh over the ice cover. The specific gravity of ice was assumed to be 0.92 and was used to determine the vertical displacement of the ice.

As this simulation was steady state and the ice floe remained stationary there is little advantage to modeling the ice floe and ice cover separately. Rather the ice floe and ice cover were modeled as one continuous piece of 1 meter length. This simplified the meshing procedure and geometry setup and had the advantage of effectively modeling an ice block of infinite length.

Computational Mesh

A key aspect of developing a meaningful 3-D numerical model for this study was the determination of an appropriate computational mesh. Ideally, a fine mesh throughout the computational domain would be best, but this is impractical both in terms of the memory requirements and the length of time required to conduct a 3-D simulation. Consequently, a more practical overall meshing strategy is to have a relatively coarse mesh in areas where the solution does not change rapidly and a finer mesh in areas with large gradients in velocity or pressure. In this context then the computational mesh development is an iterative process which can be automated in the CFX-5 software using a built-in feature known as “*mesh adaptation*”. Figure 3 illustrates an example of a cross section (YZ plane) of the mesh at the edge of the ice block both before and after mesh adaptation.

Normally, for optimal results, the mesh should be refined to a point at which a grid independent solution is reached. In other words, to a point at which the solution no longer changes with further mesh refinement. However, this case provided an interesting situation because of the sharp leading edge on the ice cover. It was found that if the mesh became too refined, the steady state solution would no longer converge, and oscillations would result both in the residuals (solution error) and in the solution itself. Figure 4 illustrates an example of this. It is suspected that this behaviour is evidence of either vortex shedding beneath the ice cover, or pressure oscillations rebounding from the outlet. These possibilities will be investigated further at a later time using transient large eddy simulation (LES). However, at this preliminary stage, the mesh was refined as far as possible with the additional criterion of achieving a converged steady state solution. In addition, the effect of smoothing the leading edge of the ice was examined.

Boundary Conditions

For this preliminary investigation, the flume walls and bed as well as the ice underside were modeled as smooth, no slip, walls while the open water surface was modeled as a free slip surface. The outlet boundary condition was specified as an average static pressure of 0 Pa. This is an average over the whole outlet which is the most commonly used option. The average constraint is applied by comparing the area weighted pressure average over the outlet to the user specified value of 0 Pa. A sensitivity analysis was carried out to ensure that the location of the outlet was not affecting the solution in the region of interest. The length of the ice cover was varied from 1 to 5 m. It was found that an ice cover of 1 m yielded similar results to longer ice covers, which gave confidence that the location of the outlet was not adversely affecting the pressure distribution beneath the ice cover.

The inlet boundary condition was specified as Cartesian velocity components with a medium turbulence intensity of 5%, which is the recommended option if

there is no information available about the inlet turbulence. This preliminary study was primarily focused on conducting a detailed sensitivity analysis examining the effects of the inlet velocity profile shape and inlet boundary location (flow development length) on the pressure distribution and force calculation under the ice floe.

B.4 MODEL RESULTS

B.4.1 Sensitivity Analysis on Inlet Development Length and Inflow

Boundary Condition

A sensitivity analysis was performed on the inlet boundary conditions by systematically changing the location of the inlet and the inlet velocity profile to see the effect on the resulting pressure distribution beneath the ice cover. In order to examine solution sensitivity to the location of the inlet, the distance from the inlet boundary to the upstream edge of the ice cover was varied from 0 to 50 meters holding all other variables constant. The inlet velocity profile was examined by comparing results for uniform, power law, and log-law velocity profile distributions while keeping all other variables constant. A one-seventh power law profile was prescribed as:

$$u = u_{\max} \left(\frac{z}{H} \right)^{1/7} \quad [\text{B-8}]$$

where u_{\max} is the surface velocity.

The log-law velocity profile was prescribed as:

$$u = u_* \left(\frac{1}{\kappa} \ln \frac{zu_*}{\nu} + 5.0 \right) \quad [\text{B-9}]$$

where κ = von Karman's constant (0.41)

u_* = shear velocity

ν = viscosity

Effect of Varying Development Length

In this first series of tests, the inlet velocity profile was set to be a uniform velocity of 0.45 m/s with a medium turbulence intensity of 5%. The distance from the inlet boundary to the upstream edge of the ice cover was varied as 0, 5, 10, 20, 30, 40 or 50 m. The outlet boundary condition was set as 0 Pa, the k - ϵ turbulence modelling option was selected, and all walls were modeled as smooth walls. Figure 5 presents the results of this sensitivity analysis, illustrating the centerline pressure profiles along the ice cover. As the figure illustrates, these tend to have a similar shape regardless of development length. However, as the development length increased the magnitude of the pressure drop increased. This suggests the importance of the surface velocity on the magnitude of the pressure reduction at the leading edge of the ice cover. The velocity profile becomes increasingly developed from the uniform profile as the development length increases. This would lead to a higher surface velocity as the average velocity would be kept constant at 0.45 m/s. So one would expect that the surface velocity with a development length of 50 m to be higher than the surface velocity with a development length of 5 m.

Effect of Varying Inlet Boundary Condition

Three different inlet velocity profiles were tested, specifically: uniform, power law and log-law profiles. In this case, the results were compared based on a 1m development length (chosen to minimize computational requirements). Only the inlet velocity profile was changed, all other variables were kept constant. The outlet boundary condition was set as 0 Pa, the k - ϵ turbulence modelling option was used, all walls were modeled as smooth walls, and a medium intensity turbulence inlet boundary condition was chosen. As the results of the development length sensitivity analysis indicated that the surface velocity was important in the pressure reduction at the leading edge of the ice cover, the

surface velocity of all three profiles was set to 0.45 m/s which gave an average velocity of 0.45 m/s, 0.41 m/s and 0.39 m/s for the uniform, power and log law profiles, respectively.

Figure 6 presents the results of this sensitivity analysis, illustrating the centerline pressure distributions. The figure shows that the greatest pressure reduction is for the uniform velocity profile and the least is for the power law profile. However, the difference between the three profiles is rather small compared to the development length investigation. To further investigate the surface velocity effect a one seventh power law profile with an average velocity of 0.45 m/s (surface velocity of 0.5156 m/s) was tested and is also shown in Figure 6. The pressure reduction is significantly larger for this profile than the other three.

B.4.2 Sensitivity Analysis on Shape of the Leading Edge of the Ice Cover

As discussed earlier, assuming a sharp leading edge on the ice cover creates a strong separation and recirculation zone that is difficult for the numerical model to resolve, particularly in a steady state simulation. To explore this effect further, additional simulations were conducted in which the leading edge of the ice cover was beveled (as illustrated in Figure 7). In this case, results were compared to that for the sharp leading edge, based on a 5 m development length (chosen to minimize computational requirements).

The centerline pressure results are compared in Figure 8, where it is seen that the pressure distribution obtained for the beveled leading edge is significantly different than obtained for a rectangular leading edge. The negative peak pressure near the leading edge is much larger in magnitude, occurs further downstream (just after the edge of the bevel) and recovers more rapidly, as compared to the behaviour for the sharp leading edge case. This increased magnitude of the negative peak pressure actually seems to go against intuition, as one might expect the beveled edge to produce a smaller pressure drop (as the flow separation would not be as strong). The most likely explanation for this is that the results for the

sharp leading edge case are not realistic; in fact, the pressure drop in that case should tend towards negative infinity at the leading edge. Clearly then, this behaviour cannot be resolved properly using this steady state simulation. Further analyses, employing the transient large eddy simulation available in CFX-5 are planned to investigate this further.

This limitation, however, has little effect on the overall force calculation. The peak negative pressure occurs over a small area so it has little effect on the overall force acting on the ice cover. Thus, even though the peak negative pressure for the beveled edge is greater, the magnitude of the calculated vertical force acting on the ice cover for the sharp leading edge is actually larger (-6.13 N) than for the beveled edge(-3.73 N). It is the overall distribution of the pressure which is important.

B.5 SUMMARY AND CONCLUSIONS

Preliminary results of a numerical study on the steady state stability of floating ice blocks that have come to rest against an intact ice cover have been presented. This knowledge of the hydrodynamic forces that act on individual ice floes is crucial to the prediction of ice jam release events as much of the current knowledge of these processes is necessarily qualitative. A 3-D computational fluid dynamics package, ANSYS CFX-5, was used for this study. The logistics of setting up the model were discussed including meshing, boundary conditions, and physical model selection. Sensitivity analyses on the inlet development length and inflow boundary conditions were conducted.

The sensitivity analysis showed that as the development length increased, the velocity profile became more developed and the pressure reduction at the leading edge of the ice cover was increased. This suggested the importance of the surface velocity on the pressure reduction. The inflow boundary condition (velocity profile) sensitivity analysis showed that three different profiles with the same

surface velocity (different average velocities) produced a similar pressure reduction on the ice cover. This is important not just for a numerical study but also for an experimental study in a shorter flume. If the velocity profile is not fully developed before reaching the region of interest the results may not be accurate. Also when modeling experimental results it may be important to use the actual velocity profile from the experiment as an inlet boundary condition rather than assuming a fully developed profile. A good practice would be for experimenters to measure the velocity profile in the flume experiment.

The effect of beveling the leading edge of the ice cover was a reduction in the overall force acting on the ice cover. This suggests, as other researchers have found, that the local pressure reduction caused by the separation zone is important. Most current ice models assume a sharp leading edge on the underside of the ice cover, which may not be realistic in all circumstances. The effect of different leading edge shapes will be investigated further in the next phase of this study.

Plans for further numerical investigations also include switching the simulation to a transient large eddy simulation which will allow for more detailed modeling of the vortex shedding at the leading edge of the ice cover. This can then be used to determine whether it is the instantaneous pressure distribution due to vortex shedding or the overall average pressure acting on the block that is important in determining whether the ice block will overturn. The final step of the numerical modeling will attempt to model the actual block movement under the ice cover. This will involve a transient simulation with moving mesh techniques to track the movement of the block with the appropriate hydrodynamic forces.

In the future, the detailed pressure measurements of Coutermarsh and McGilvary (1994) could provide excellent validation data for these numerical results. From this the model can be used as a testing device to investigate a wider range of variables (such as block geometry and flow characteristics) in much less time than

would be feasible with an experimental model. The results of this testing will be further used to design an experimental program employing particle image velocimetry to obtain detailed velocity field measurements, and digital imaging techniques to track the movement of ice blocks at the leading edge.

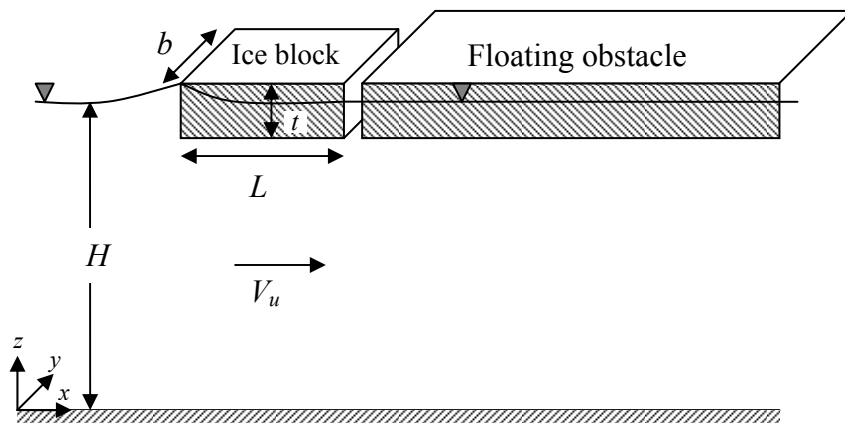


Figure B-1: Defining sketch for ice floe stability problem.

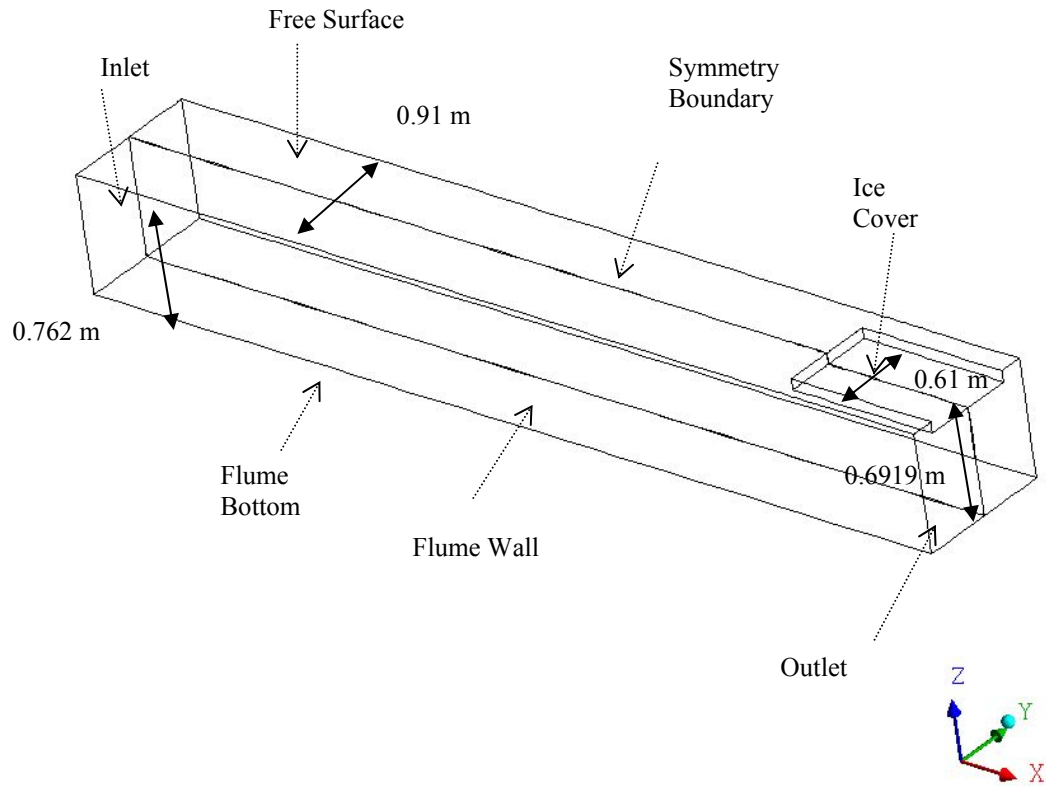
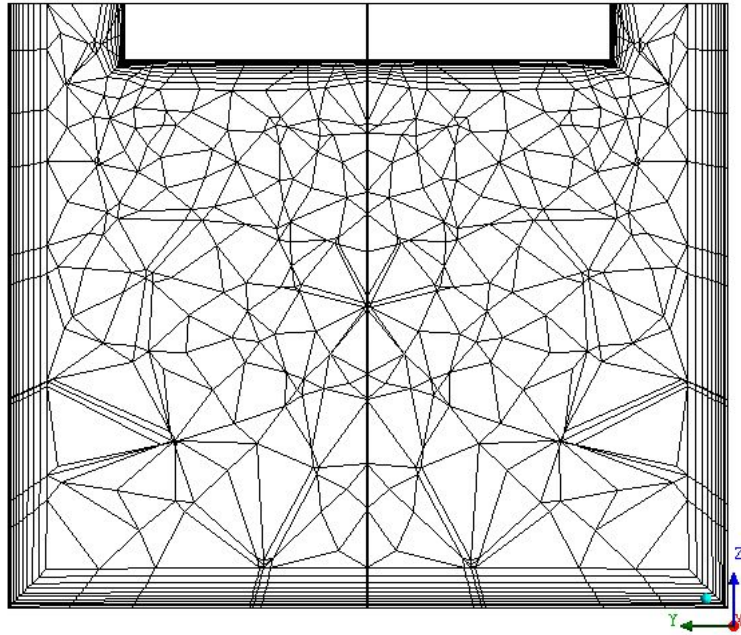


Figure B-2: Model geometry for preliminary simulations.

a)



b)

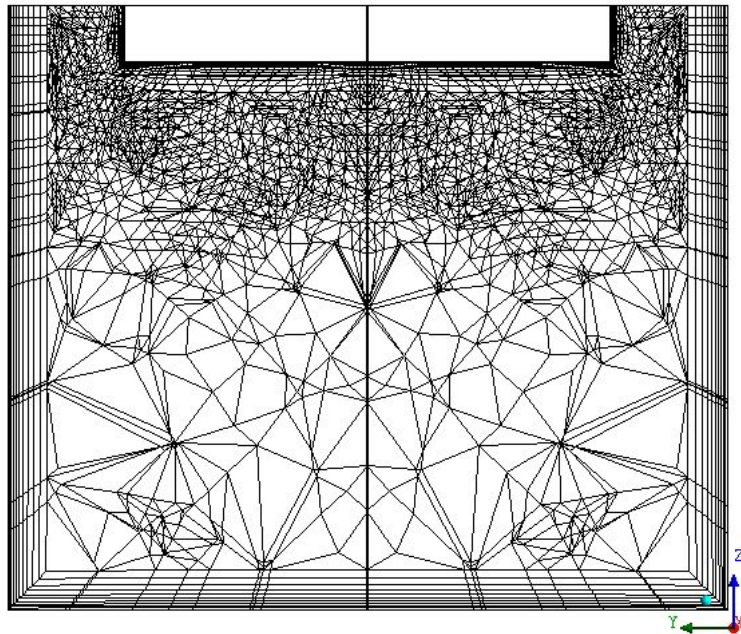


Figure B-3: YZ plane at edge of ice cover a) before mesh adaption, and b) after mesh adaption.

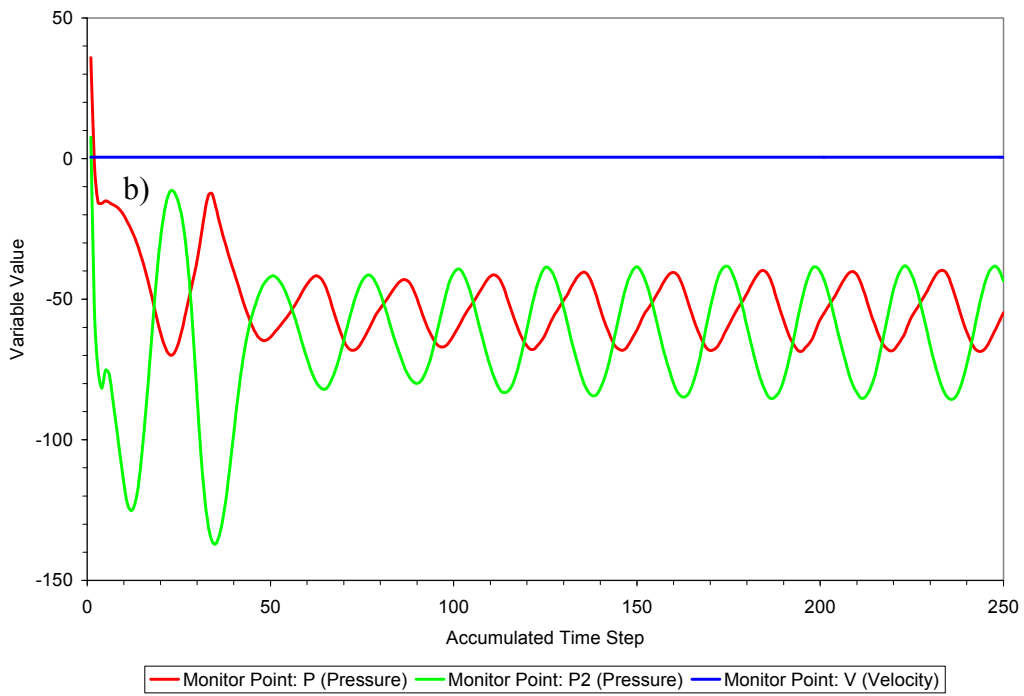
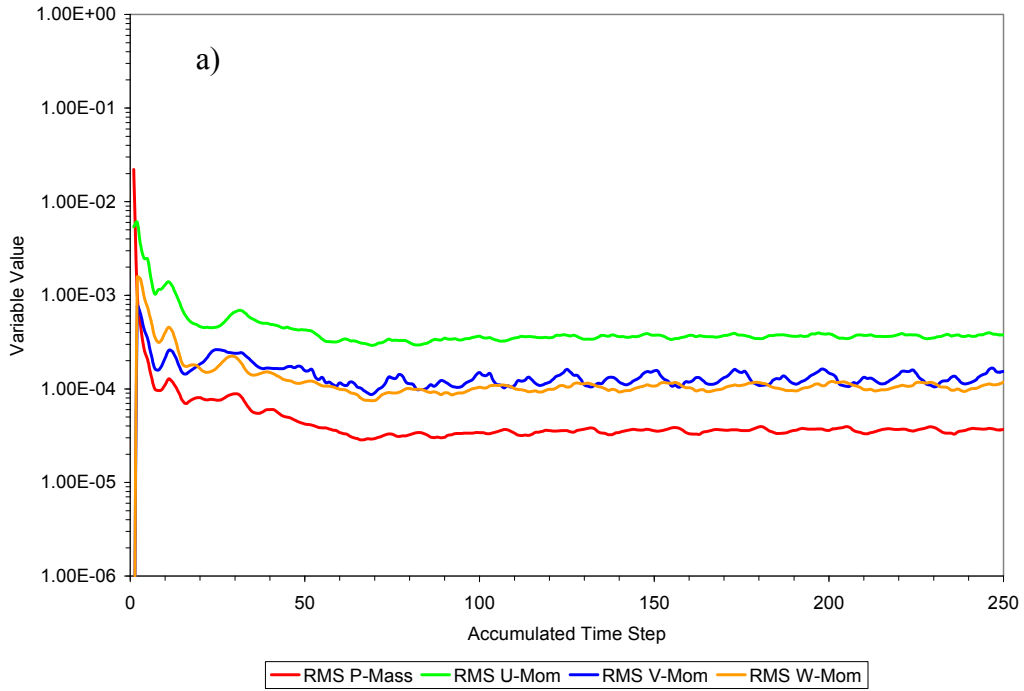


Figure B-4: Refined mesh solution a) residual plot and b) monitor points on ice cover for pressure.

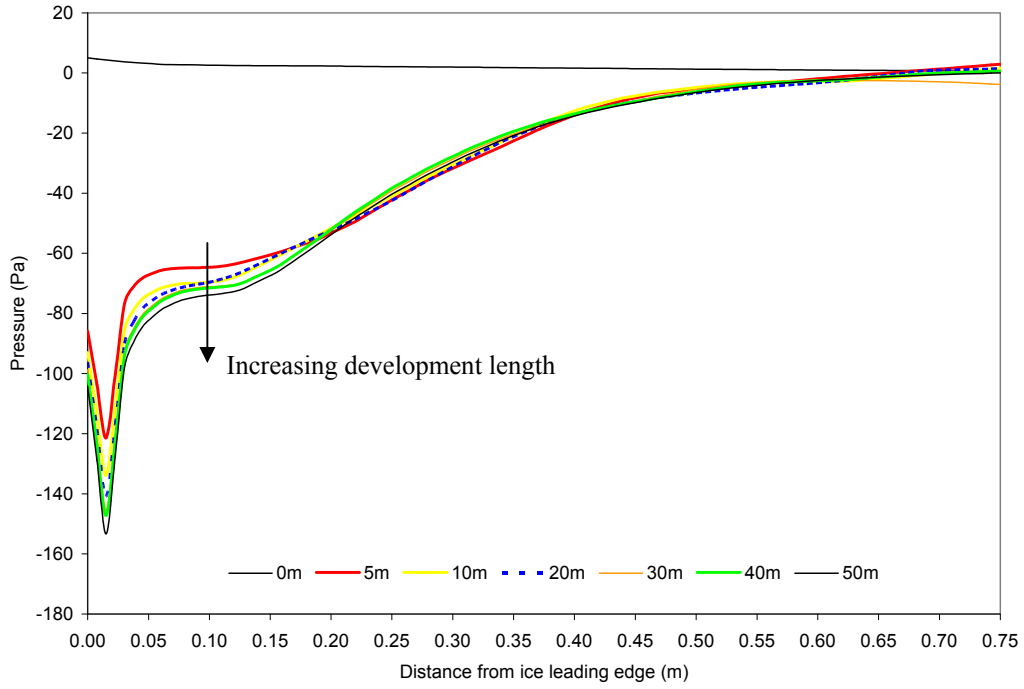


Figure B-5: Sensitivity of model results to variation in flow development length.

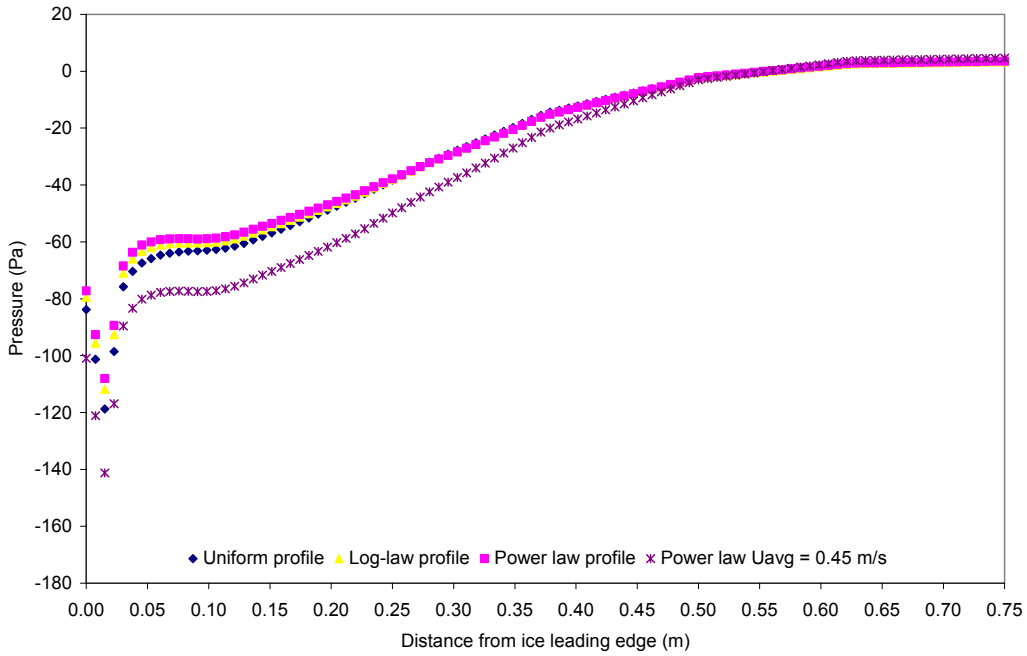


Figure B-6: Sensitivity of model results to variation in inlet velocity profile.

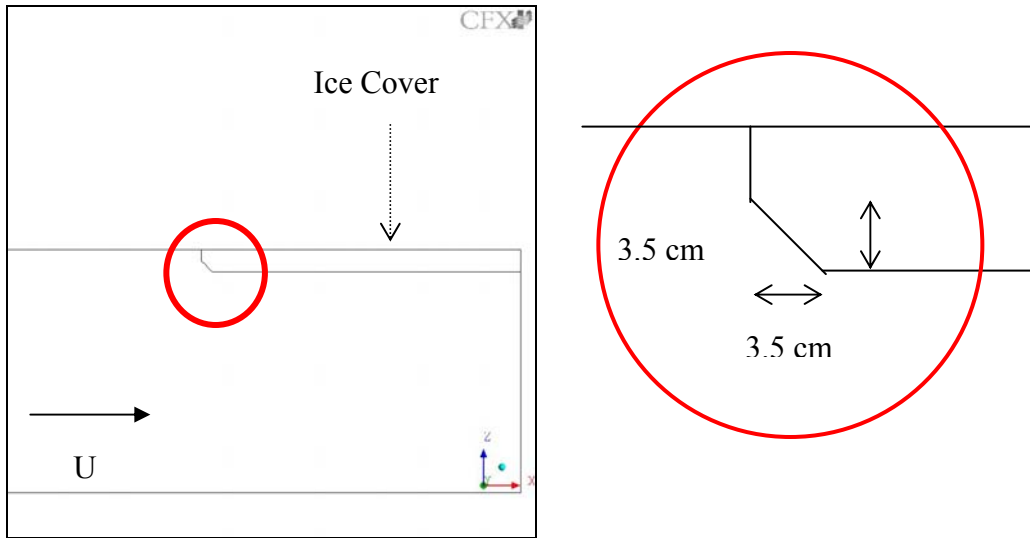


Figure B-7: Model configuration for testing a beveled leading edge on the ice cover.

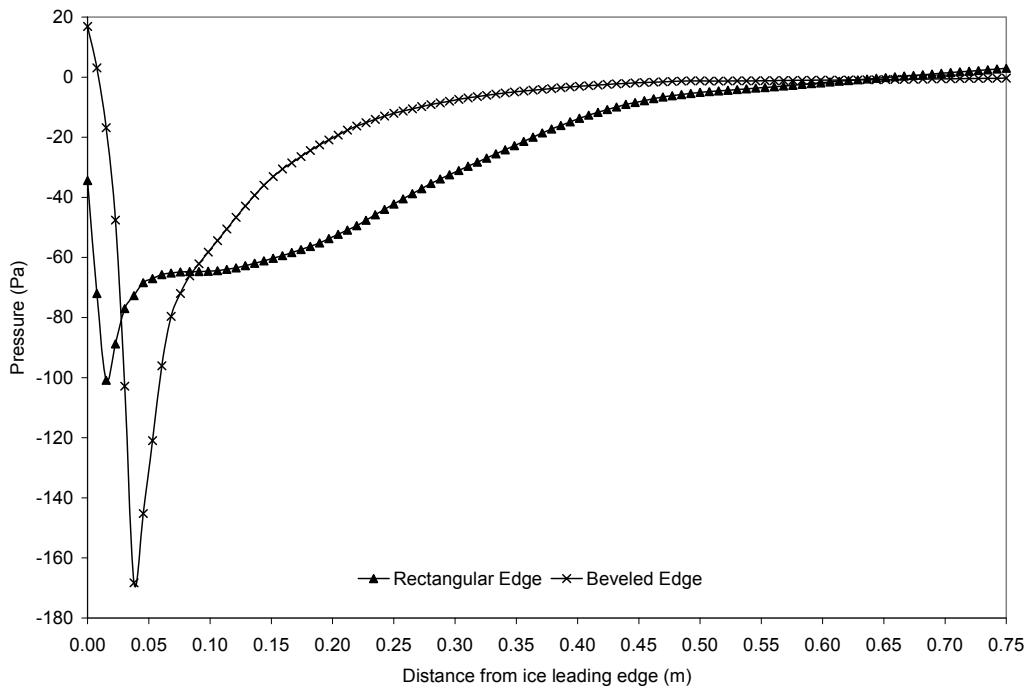


Figure B-8: Effect of ice leading edge shape on computed under ice pressure distribution.

B.6 REFERENCES

- Ashton, G.D., 1974. Froude criterion for ice-block stability. *Journal of Glaciology*, 13(68), pp. 307-313.
- Beltaos, S. (1995). *River Ice Jams*. Water Resources Publications, LLC, Highlands Ranch, Colorado, 372 pp.
- CFX-5 Solver Modelling Manual
- CFX-5 Solver Theory Manual
- Coutermarsh, B. & McGilvary, W.R., 1991. Pressure distribution of an overturning ice floe. *Proc. 6th Workshop on River Ice*, pp. 143-163.
- Coutermarsh, B.A. and McGilvary, W.R., 1993. Static analysis of floating ice block stability. *Journal of Hydraulic Research*, 31(2), pp. 147-160.
- Coutermarsh, B and McGilvary, R., 1994. Analyzing the stability of floating ice floes. *CRREL Report 94-13*, 19 pp.
- Daly, S.F. and Axelson, K.D., 1990. Stability of floating and submerged blocks. *Journal of Hydraulic Research*, 28(6), pp. 737-752.
- Hara, F., Kawai, T., Hanada, M., Nishihata, A., and Saeki, H., 1996. Movement of ice blocks under an ice cover. *Proceedings of IAHR Ice Symposium, Beijing*, pp. 769-778.
- Healy, D. and Hicks, F. (2001) "Experimental Study of Ice Jam Shoving" *Proc. 11th Workshop on River Ice, Ottawa, May*, pp. 126-144.
- Jasek, M., 2003. Ice jam release and break-up front propagation. *Proceedings of the 12th workshop on the hydraulics of ice covered rivers, The CGU HS Committee on River Ice Processes and the Environment. June 19-20, 2003, Edmonton, AB*, pp. 348-368.
- Kawai, T., Hara, F., Masaki, S., Nishihata, A., and Saeki, H., 1997. Experimental study on the process of ice jam development. *Proceedings of 9th CRIPE*, pp. 245-256.
- Larsen, P., 1975. Notes on the stability of floating ice blocks. *Proceedings of the IAHR third international symposium on ice problems. Hanover, NH, IAHR*, pp. 305-313.

- Pariset, E. and Hausser, R., 1961. Formation and evolution of ice covers on rivers. Transactions of the Engineering Institute of Canada, 5(1), pp. 41-49.
- Uzuner, M.S. and Kennedy, J.F., 1972. Stability of floating ice blocks. Journal of the Hydraulics Division, 98 (HY12), pp. 2117-2133.

APPENDIX C: DATA FROM PRESSURE EXPERIMENTS

The following tables and graphs are data that was collected in the pressure experiments of Chapters 2 and 3 following the procedures described in these chapters.

Table C-1: Water Surface Profile for $t/H = 0.05$; Top Block = 52.47 cm; $t = 1.59$ cm; $H = 30.64$ cm.

Q = 79 L/s								
Trial 1								
Before				During				
X (m)	Bottom (cm)	Top Water (cm)	H (cm)	X (m)	Bottom (cm)	Top Water (cm)	H (cm)	Δ (cm)
1	13.1	43.4	30.3	1	13.1	43.32	30.22	-0.08
2	13.1	43.51	30.41	2	13.1	43.44	30.34	-0.07
3	13.17	43.69	30.52	3	13.17	43.66	30.49	-0.03
3.98	13.2	43.92	30.72	3.98	13.19	43.95	30.76	0.04
Trial 2								
Before				During				
X (m)	Bottom (cm)	Top Water (cm)	H (cm)	X (m)	Bottom (cm)	Top Water (cm)	H (cm)	Δ (cm)
1	13.1	43.49	30.39	1	13.1	43.39	30.29	-0.1
2	13.1	43.57	30.47	2	13.1	43.54	30.44	-0.03
3	13.17	43.78	30.61	3	13.17	43.62	30.45	-0.16
3.98	13.19	43.98	30.79	3.98	13.19	44.06	30.87	0.08
Q = 111 L/s								
Trial 1								
Before				During				
X (m)	Bottom (cm)	Top Water (cm)	H (cm)	X (m)	Bottom (cm)	Top Water (cm)	H (cm)	Δ (cm)
1	13.1	43.33	30.23	1	13.1	43.23	30.13	-0.1
2	13.1	43.4	30.3	2	13.1	43.32	30.22	-0.08
3	13.18	43.64	30.46	3	13.17	43.49	30.32	-0.14
3.98	13.2	43.8	30.6	3.98	13.19	44.25	31.06	0.46
Trial 2								
Before				During				
X (m)	Bottom (cm)	Top Water (cm)	H (cm)	X (m)	Bottom (cm)	Top Water (cm)	H (cm)	Δ (cm)
1	13.1	43.39	30.29	1	13.1	43.23	30.13	-0.16
2	13.1	43.46	30.36	2	13.09	43.35	30.26	-0.1
3	13.17	43.66	30.49	3	13.17	43.52	30.35	-0.14
3.98	13.19	43.86	30.67	3.98	13.19	44.3	31.11	0.44
Q = 142 L/s								
Trial 1								
Before				During				

X (m)	Bottom (cm)	Top Water (cm)	H (cm)	X (m)	Bottom (cm)	Top Water (cm)	H (cm)	Δ (cm)
1	13.09	43.21	30.12	1	13.09	43.09	30	-0.12
2	13.08	43.27	30.19	2	13.09	43.13	30.04	-0.15
3	13.16	43.5	30.34	3	13.16	43.25	30.09	-0.25
3.98	13.19	43.68	30.49	3.98	13.19	44.7	31.51	1.02
Trial 2								
Before				During				
X (m)	Bottom (cm)	Top Water (cm)	H (cm)	X (m)	Bottom (cm)	Top Water (cm)	H (cm)	Δ (cm)
1	13.1	43.29	30.19	1	13.1	43.1	30	-0.19
2	13.1	43.35	30.25	2	13.09	43.26	30.17	-0.08
3	13.17	43.58	30.41	3	13.16	43.32	30.16	-0.25
3.98	13.19	43.75	30.56	3.98	13.19	44.77	31.58	1.02

Table C-2: Water Surface Profile for $t/H = 0.15$; Top Block = 58.25 cm; $t = 4.82$ cm; $H = 30.65$ cm.

Q = 79 L/s								
Trial 1								
Before				During				
X (m)	Bottom (cm)	Top Water (cm)	H (cm)	X (m)	Bottom (cm)	Top Water (cm)	H (cm)	Δ (cm)
1	21.83	52.16	30.33	1	21.83	52.13	30.3	-0.03
2	21.83	52.27	30.44	2	21.84	52.25	30.41	-0.03
3	21.91	52.44	30.53	3	21.91	52.45	30.54	0.01
3.98	21.93	52.65	30.72	3.98	21.93	53.03	31.1	0.38
Trial 2								
Before				During				
X (m)	Bottom (cm)	Top Water (cm)	H (cm)	X (m)	Bottom (cm)	Top Water (cm)	H (cm)	Δ (cm)
1	21.84	52.18	30.34	1	21.84	52.16	30.32	-0.02
2	21.85	52.3	30.45	2	21.85	52.24	30.39	-0.06
3	21.9	52.45	30.55	3	21.91	52.44	30.53	-0.02
3.98	21.93	52.67	30.74	3.98	21.93	52.99	31.06	0.32
Q = 111 L/s								
Trial 1								
Before				During				
X (m)	Bottom (cm)	Top Water (cm)	H (cm)	X (m)	Bottom (cm)	Top Water (cm)	H (cm)	Δ (cm)
1	21.84	52.07	30.23	1	21.84	52.08	30.24	0.01
2	21.82	52.17	30.35	2	21.83	52.13	30.3	-0.05
3	21.89	52.37	30.48	3	21.89	52.29	30.4	-0.08
3.98	21.94	52.55	30.61	3.98	21.93	53.52	31.59	0.98
Trial 2								
Before				During				
X (m)	Bottom (cm)	Top Water (cm)	H (cm)	X (m)	Bottom (cm)	Top Water (cm)	H (cm)	Δ (cm)
1	21.84	52.12	30.28	1	21.84	52.08	30.24	-0.04
2	21.84	52.19	30.35	2	21.84	52.22	30.38	0.03
3	21.89	52.42	30.53	3	21.91	52.36	30.45	-0.08
3.98	21.94	52.58	30.64	3.98	21.93	53.56	31.63	0.99
Q = 142 L/s								
Trial 1								
Before				During				

X (m)	Bottom (cm)	Top Water (cm)	H (cm)	X (m)	Bottom (cm)	Top Water (cm)	H (cm)	Δ (cm)
1	21.83	51.99	30.16	1	21.83	51.96	30.13	-0.03
2	21.83	52.08	30.25	2	21.83	52.05	30.22	-0.03
3	21.89	52.28	30.39	3	21.89	52.2	30.31	-0.08
3.98	21.93	52.48	30.55	3.98	21.93	54.08	32.15	1.6
Trial 2								
Before				During				
X (m)	Bottom (cm)	Top Water (cm)	H (cm)	X (m)	Bottom (cm)	Top Water (cm)	H (cm)	Δ (cm)
1	21.84	52.05	30.21	1	21.84	52.02	30.18	-0.03
2	21.83	52.1	30.27	2	21.84	52.09	30.25	-0.02
3	21.9	52.31	30.41	3	21.92	52.28	30.36	-0.05
3.98	21.93	52.55	30.62	3.98	21.93	54.05	32.12	1.5

Table C-3: Water Surface Profile for $t/H = 0.25$; Top Block = 55.64 cm; $t = 7.76$ cm; $H = 30.74$ cm.

Q = 79 L/s								
Trial 1								
Before				During				
X (m)	Bottom (cm)	Top Water (cm)	H (cm)	X (m)	Bottom (cm)	Top Water (cm)	H (cm)	Δ (cm)
1	21.84	52.25	30.41	1	21.84	52.24	30.4	-0.01
2	21.83	52.33	30.5	2	21.83	52.36	30.53	0.03
3	21.91	52.55	30.64	3	21.89	52.58	30.69	0.05
3.98	21.93	52.76	30.83	3.98	21.94	53.21	31.27	0.44
Trial 2								
Before				During				
X (m)	Bottom (cm)	Top Water (cm)	H (cm)	X (m)	Bottom (cm)	Top Water (cm)	H (cm)	Δ (cm)
1	21.85	52.28	30.43	1	21.85	52.35	30.5	0.07
2	21.83	52.37	30.54	2	21.84	52.42	30.58	0.04
3	21.89	52.58	30.69	3	21.9	52.61	30.71	0.02
3.98	21.94	52.79	30.85	3.98	21.93	53.16	31.23	0.38
Q = 111 L/s								
Trial 1								
Before				During				
X (m)	Bottom (cm)	Top Water (cm)	H (cm)	X (m)	Bottom (cm)	Top Water (cm)	H (cm)	Δ (cm)
1	21.83	52.16	30.33	1	21.83	52.28	30.45	0.12
2	21.83	52.28	30.45	2	21.83	52.33	30.5	0.05
3	21.91	52.48	30.57	3	21.89	52.48	30.59	0.02
3.98	21.94	52.65	30.71	3.98	21.94	53.72	31.78	1.07
Trial 2								
Before				During				
X (m)	Bottom (cm)	Top Water (cm)	H (cm)	X (m)	Bottom (cm)	Top Water (cm)	H (cm)	Δ (cm)
1	21.85	52.2	30.35	1	21.85	52.28	30.43	0.08
2	21.85	52.31	30.46	2	21.83	52.37	30.54	0.08
3	21.9	52.49	30.59	3	21.89	52.52	30.63	0.04
3.98	21.94	52.69	30.75	3.98	21.94	53.71	31.77	1.02
Q = 142 L/s								
Trial 1								
Before				During				

X (m)	Bottom (cm)	Top Water (cm)	H (cm)	X (m)	Bottom (cm)	Top Water (cm)	H (cm)	Δ (cm)
1	21.84	52.06	30.22	1	21.84	52.24	30.4	0.18
2	21.85	52.16	30.31	2	21.85	52.35	30.5	0.19
3	21.9	52.36	30.46	3	21.89	52.62	30.73	0.27
3.98	21.94	52.56	30.62	3.98	21.93	54.41	32.48	1.86
Trial 2								
Before				During				
X (m)	Bottom (cm)	Top Water (cm)	H (cm)	X (m)	Bottom (cm)	Top Water (cm)	H (cm)	Δ (cm)
1	21.84	52.13	30.29	1	21.84	52.33	30.49	0.2
2	21.84	52.21	30.37	2	21.85	52.38	30.53	0.16
3	21.91	52.42	30.51	3	21.91	52.52	30.61	0.1
3.98	21.94	52.63	30.69	3.98	21.94	54.41	32.47	1.78

Table C-4: Water Surface Profile for Transverse $t/H = 0.1$; Top Block = 59.25 cm; $t = 2.67$ cm; $H = 29.67$ cm.

Q = 79 L/s								
Trial 1								
Before				During				
X (m)	Bottom (cm)	Top Water (cm)	H (cm)	X (m)	Bottom (cm)	Top Water (cm)	H (cm)	Δ (cm)
1	21.85	51.08	29.23	1	21.85	51.01	29.16	-0.07
2	21.84	51.18	29.34	2	21.85	51.09	29.24	-0.1
3	21.91	51.41	29.5	3	21.89	51.25	29.36	-0.14
3.98	21.94	51.61	29.67	3.98	21.94	51.79	29.85	0.18
Trial 2								
Before				During				
X (m)	Bottom (cm)	Top Water (cm)	H (cm)	X (m)	Bottom (cm)	Top Water (cm)	H (cm)	Δ (cm)
1	21.85	51.17	29.32	1	21.85	51.15	29.3	-0.02
2	21.86	51.26	29.4	2	21.85	51.16	29.31	-0.09
3	21.91	51.44	29.53	3	21.9	51.31	29.41	-0.12
3.98	21.95	51.66	29.71	3.98	21.95	51.74	29.79	0.08
Q = 142 L/s								
Trial 1								
Before				During				
X (m)	Bottom (cm)	Top Water (cm)	H (cm)	X (m)	Bottom (cm)	Top Water (cm)	H (cm)	Δ (cm)
1	21.85	51.05	29.2	1	21.85	50.96	29.11	-0.09
2	21.86	51.19	29.33	2	21.85	50.99	29.14	-0.19
3	21.89	51.3	29.41	3	21.89	51.16	29.27	-0.14
3.98	21.93	51.54	29.61	3.98	21.94	53.09	31.15	1.54
Trial 2								
Before				During				
X (m)	Bottom (cm)	Top Water (cm)	H (cm)	X (m)	Bottom (cm)	Top Water (cm)	H (cm)	Δ (cm)
1	21.84	51.12	29.28	1	21.84	51.01	29.17	-0.11
2	21.84	51.2	29.36	2	21.85	51.09	29.24	-0.12
3	21.9	51.44	29.54	3	21.9	51.28	29.38	-0.16
3.98	21.93	51.61	29.68	3.98	21.94	53.16	31.22	1.54

Table C-5: Water Surface Profile for Transverse $t/H = 0.3$; Top Block = 54.11 cm;
 $t = 8.13$ cm; $H = 29.56$ cm.

Q = 79 L/s								
Trial 1								
Before				During				
X (m)	Bottom (cm)	Top Water (cm)	H (cm)	X (m)	Bottom (cm)	Top Water (cm)	H (cm)	Δ (cm)
1	21.85	50.95	29.1	1	21.85	50.98	29.13	0.03
2	21.85	51.03	29.18	2	21.84	51.08	29.24	0.06
3	21.89	51.26	29.37	3	21.89	51.25	29.36	-0.01
3.98	21.93	51.34	29.41	3.98	21.93	51.95	30.02	0.61
Trial 2								
Before				During				
X (m)	Bottom (cm)	Top Water (cm)	H (cm)	X (m)	Bottom (cm)	Top Water (cm)	H (cm)	Δ (cm)
1	21.85	50.98	29.13	1	21.85	51.04	29.19	0.06
2	21.85	51.09	29.24	2	21.84	51.15	29.31	0.07
3	21.89	51.29	29.4	3	21.88	51.32	29.44	0.04
3.98	21.92	51.48	29.56	3.98	21.92	52.02	30.1	0.54
Q = 142 L/s								
Trial 1								
Before				During				
X (m)	Bottom (cm)	Top Water (cm)	H (cm)	X (m)	Bottom (cm)	Top Water (cm)	H (cm)	Δ (cm)
1	21.85	51.05	29.2	1	21.85	51.38	29.53	0.33
2	21.84	51.14	29.3	2	21.84	51.46	29.62	0.32
3	21.89	51.34	29.45	3	21.91	51.59	29.68	0.23
3.98	21.94	51.52	29.58	3.98	21.93	53.54	31.61	2.03
Trial 2								
Before				During				
X (m)	Bottom (cm)	Top Water (cm)	H (cm)	X (m)	Bottom (cm)	Top Water (cm)	H (cm)	Δ (cm)
1	21.85	51.09	29.24	1	21.85	51.43	29.58	0.34
2	21.84	51.17	29.33	2	21.85	51.5	29.65	0.32
3	21.89	51.37	29.48	3	21.89	51.65	29.76	0.28
3.98	21.94	51.62	29.68	3.98	21.93	53.62	31.69	2.01

Table C-6: Water Surface Profile for Round $t/H = 0.05$; Top Block = 59.1 cm; $t = 1.89$ cm; $H = 30.45$ cm.

Q = 79 L/s								
Trial 1								
Before				During				
X (m)	Bottom (cm)	Top Water (cm)	H (cm)	X (m)	Bottom (cm)	Top Water (cm)	H (cm)	Δ (cm)
1	16.18	46.25	30.07	1	16.18	46.18	30	-0.07
2	16.04	46.24	30.2	2	16.04	46.14	30.1	-0.1
3	16.18	46.49	30.31	3	16.18	46.43	30.25	-0.06
3.98	16.19	46.69	30.5	3.98	16.19	46.7	30.51	0.01
Trial 2								
Before				During				
X (m)	Bottom (cm)	Top Water (cm)	H (cm)	X (m)	Bottom (cm)	Top Water (cm)	H (cm)	Δ (cm)
1	16.18	46.3	30.12	1	16.18	46.14	29.96	-0.16
2	16.04	46.29	30.25	2	16.04	46.18	30.14	-0.11
3	16.18	46.55	30.37	3	16.18	46.46	30.28	-0.09
3.98	16.19	46.72	30.53	3.98	16.19	46.66	30.47	-0.06
Q = 111 L/s								
Trial 1								
Before				During				
X (m)	Bottom (cm)	Top Water (cm)	H (cm)	X (m)	Bottom (cm)	Top Water (cm)	H (cm)	Δ (cm)
1	16.18	46.21	30.03	1	16.18	46.08	29.9	-0.13
2	16.04	46.18	30.14	2	16.04	46.05	30.01	-0.13
3	16.18	46.44	30.26	3	16.18	46.29	30.11	-0.15
3.98	16.19	46.62	30.43	3.98	16.19	46.65	30.46	0.03
Trial 2								
Before				During				
X (m)	Bottom (cm)	Top Water (cm)	H (cm)	X (m)	Bottom (cm)	Top Water (cm)	H (cm)	Δ (cm)
1	16.18	46.23	30.05	1	16.18	46.14	29.96	-0.09
2	16.04	46.22	30.18	2	16.04	46.05	30.01	-0.17
3	16.18	46.46	30.28	3	16.18	46.3	30.12	-0.16
3.98	16.19	46.64	30.45	3.98	16.19	46.65	30.46	0.01
Q = 142 L/s								
Trial 1								
Before				During				

X (m)	Bottom (cm)	Top Water (cm)	H (cm)	X (m)	Bottom (cm)	Top Water (cm)	H (cm)	Δ (cm)
1	16.18	46.18	30	1	16.18	45.98	29.8	-0.2
2	16.04	46.15	30.11	2	16.04	45.9	29.86	-0.25
3	16.18	46.4	30.22	3	16.18	46.14	29.96	-0.26
3.98	16.19	46.58	30.39	3.98	16.19	46.54	30.35	-0.04
Trial 2								
Before				During				
X (m)	Bottom (cm)	Top Water (cm)	H (cm)	X (m)	Bottom (cm)	Top Water (cm)	H (cm)	Δ (cm)
1	16.18	46.2	30.02	1	16.18	45.97	29.79	-0.23
2	16.04	46.18	30.14	2	16.04	45.9	29.86	-0.28
3	16.18	46.42	30.24	3	16.18	46.17	29.99	-0.25
3.98	16.19	46.6	30.41	3.98	16.19	46.68	30.49	0.08

Table C-7: Water Surface Profile for Round $t/H = 0.3$; Top Block = 56.18 cm; $t = 9.51$ cm; $H = 30.43$ cm.

Q = 79 L/s								
Trial 1								
Before				During				
X (m)	Bottom (cm)	Top Water (cm)	H (cm)	X (m)	Bottom (cm)	Top Water (cm)	H (cm)	Δ (cm)
1	20.28	50.34	30.06	1	20.28	50.3	30.02	-0.04
2	20.15	50.31	30.16	2	20.15	50.29	30.14	-0.02
3	20.27	50.55	30.28	3	20.27	50.5	30.23	-0.05
3.98	20.3	50.73	30.43	3.98	20.3	51.13	30.83	0.4
Trial 2								
Before				During				
X (m)	Bottom (cm)	Top Water (cm)	H (cm)	X (m)	Bottom (cm)	Top Water (cm)	H (cm)	Δ (cm)
1	20.28	50.34	30.06	1	20.28	50.33	30.05	-0.01
2	20.15	50.31	30.16	2	20.15	50.33	30.18	0.02
3	20.27	50.58	30.31	3	20.27	50.58	30.31	0
3.98	20.3	50.74	30.44	3.98	20.3	51.09	30.79	0.35
Q = 111 L/s								
Trial 1								
Before				During				
X (m)	Bottom (cm)	Top Water (cm)	H (cm)	X (m)	Bottom (cm)	Top Water (cm)	H (cm)	Δ (cm)
1	20.28	50.27	29.99	1	20.28	50.26	29.98	-0.01
2	20.16	50.23	30.07	2	20.15	50.18	30.03	-0.04
3	20.28	50.46	30.18	3	20.27	50.43	30.16	-0.02
3.98	20.3	50.66	30.36	3.98	20.3	51.59	31.29	0.93
Trial 2								
Before				During				
X (m)	Bottom (cm)	Top Water (cm)	H (cm)	X (m)	Bottom (cm)	Top Water (cm)	H (cm)	Δ (cm)
1	20.28	50.29	30.01	1	20.28	50.26	29.98	-0.03
2	20.15	50.27	30.12	2	20.15	50.29	30.14	0.02
3	20.28	50.53	30.25	3	20.28	50.46	30.18	-0.07
3.98	20.3	50.69	30.39	3.98	20.3	51.71	31.41	1.02
Q = 142 L/s								
Trial 1								
Before				During				

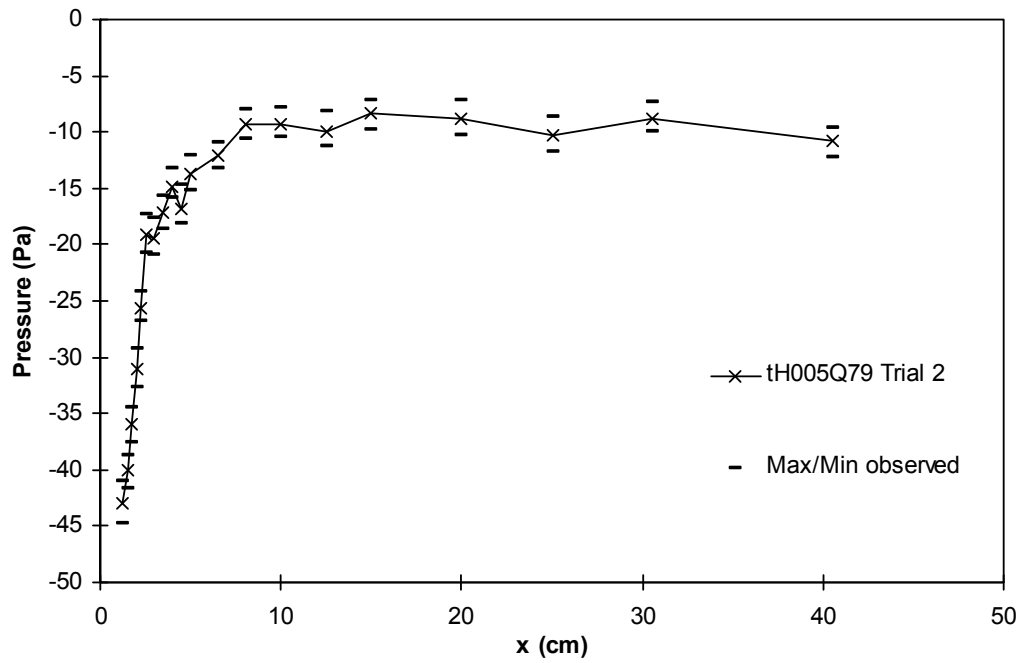
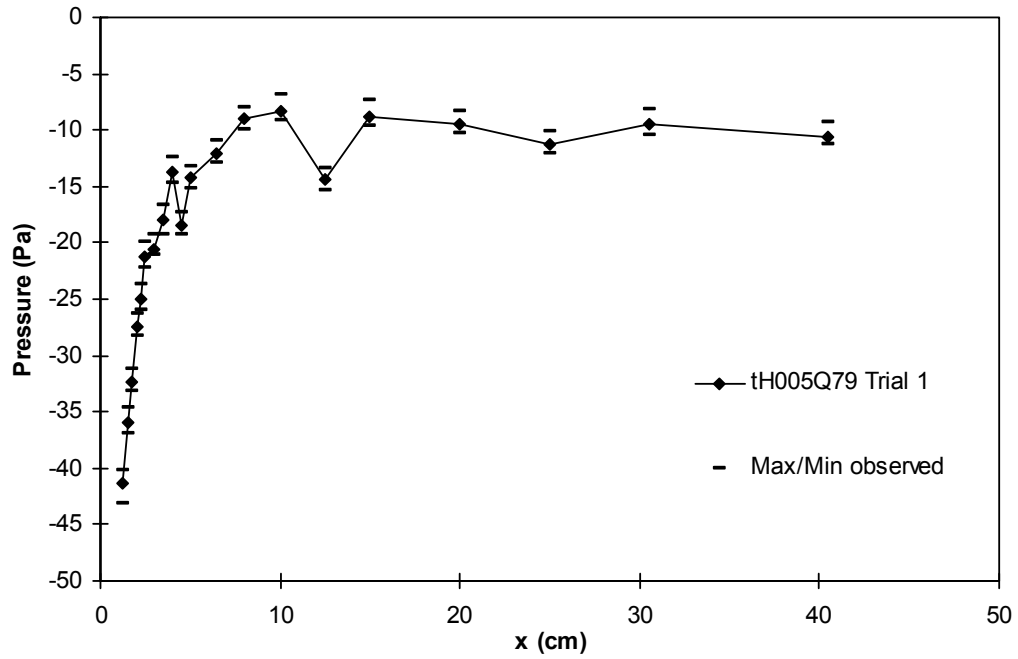
X (m)	Bottom (cm)	Top Water (cm)	H (cm)	X (m)	Bottom (cm)	Top Water (cm)	H (cm)	Δ (cm)
1	20.28	50.32	30.04	1	20.28	50.36	30.08	0.04
2	20.15	50.32	30.17	2	20.15	50.33	30.18	0.01
3	20.28	50.58	30.3	3	20.28	50.51	30.23	-0.07
3.98	20.3	50.79	30.49	3.98	20.3	52.28	31.98	1.49
Trial 2								
Before				During				
X (m)	Bottom (cm)	Top Water (cm)	H (cm)	X (m)	Bottom (cm)	Top Water (cm)	H (cm)	Δ (cm)
1	20.28	50.35	30.07	1	20.28	50.38	30.1	0.03
2	20.15	50.31	30.16	2	20.15	50.37	30.22	0.06
3	20.28	50.57	30.29	3	20.28	50.56	30.28	-0.01
3.98	20.3	50.76	30.46	3.98	20.3	52.34	32.04	1.58

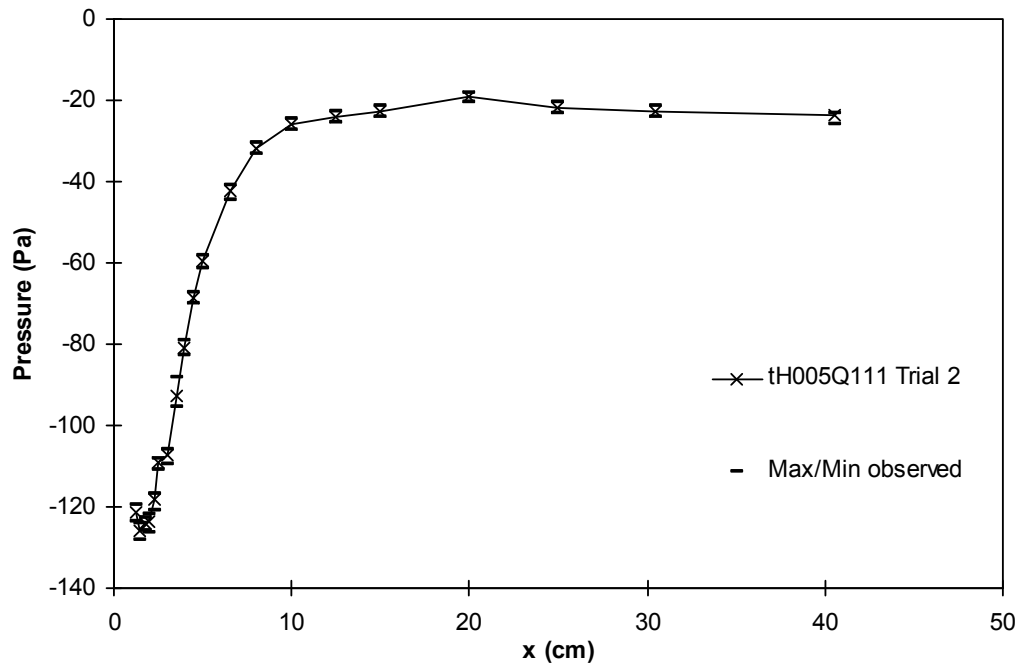
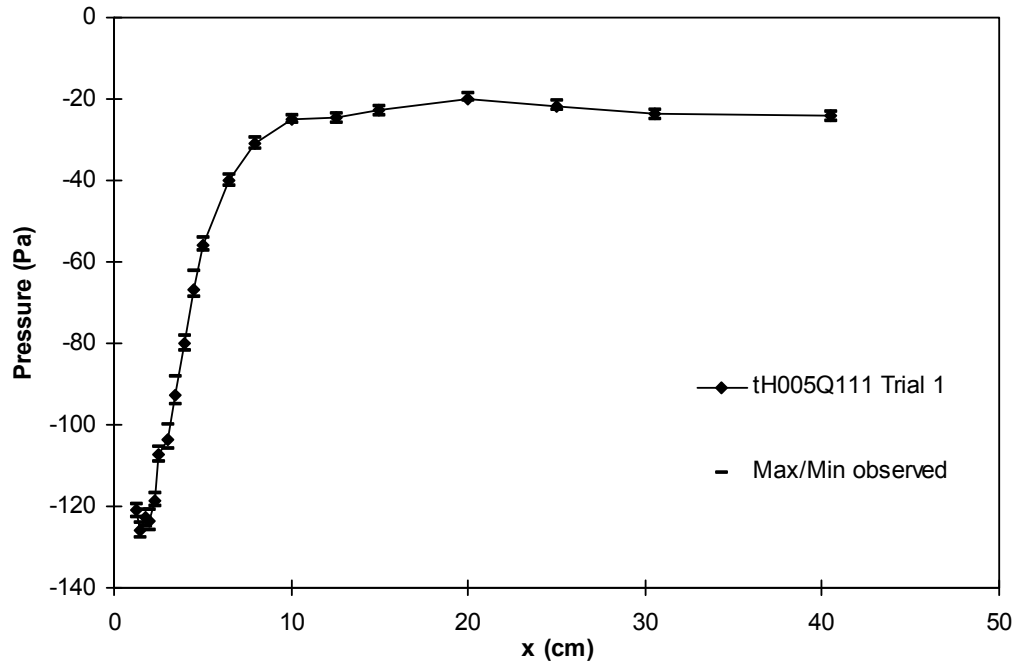
Table C-8: Water Surface Profile for Flat $t/H = 0.1$; Top Block = 48.65 cm; $t = 3.08$ cm; $H = 30.19$ cm.

Q = 79 L/s								
Trial 1								
Before				During				
X (m)	Bottom (cm)	Top Water (cm)	H (cm)	X (m)	Bottom (cm)	Top Water (cm)	H (cm)	Δ (cm)
1	11.15	40.87	29.72	1	11.15	40.85	29.7	-0.02
2	11.02	40.84	29.82	2	11.02	40.79	29.77	-0.05
3	11.14	41.09	29.95	3	11.14	41.05	29.91	-0.04
3.98	11.19	41.32	30.13	3.98	11.19	41.55	30.36	0.23
Trial 2								
Before				During				
X (m)	Bottom (cm)	Top Water (cm)	H (cm)	X (m)	Bottom (cm)	Top Water (cm)	H (cm)	Δ (cm)
1	11.15	40.91	29.76	1	11.15	40.9	29.75	-0.01
2	11.02	40.9	29.88	2	11.02	40.82	29.8	-0.08
3	11.14	41.15	30.01	3	11.14	41.08	29.94	-0.07
3.98	11.19	41.35	30.16	3.98	11.19	41.58	30.39	0.23
Q = 142 L/s								
Trial 1								
Before				During				
X (m)	Bottom (cm)	Top Water (cm)	H (cm)	X (m)	Bottom (cm)	Top Water (cm)	H (cm)	Δ (cm)
1	11.15	40.99	29.84	1	11.15	40.89	29.74	-0.1
2	11.02	40.96	29.94	2	11.02	40.84	29.82	-0.12
3	11.14	41.18	30.04	3	11.14	41.09	29.95	-0.09
3.98	11.19	41.39	30.2	3.98	11.19	42.98	31.79	1.59
Trial 2								
Before				During				
X (m)	Bottom (cm)	Top Water (cm)	H (cm)	X (m)	Bottom (cm)	Top Water (cm)	H (cm)	Δ (cm)
1	11.15	41	29.85	1	11.15	41.01	29.86	0.01
2	11.02	41	29.98	2	11.02	40.88	29.86	-0.12
3	11.14	41.24	30.1	3	11.14	41.07	29.93	-0.17
3.98	11.19	41.46	30.27	3.98	11.19	43.05	31.86	1.59

Table C-9: Water Surface Profile for Tilt $t/H = 0.1$; Top Block = 48.42 cm; $t = 3.53$ cm; $H = 30.38$ cm.

Q = 79 L/s								
Trial 1								
Before				During				
X (m)	Bottom (cm)	Top Water (cm)	H (cm)	X (m)	Bottom (cm)	Top Water (cm)	H (cm)	Δ (cm)
1	11.15	41.05	29.9	1	11.15	41.04	29.89	-0.01
2	11.02	41.03	30.01	2	11.02	40.98	29.96	-0.05
3	11.14	41.27	30.13	3	11.14	41.18	30.04	-0.09
3.98	11.19	41.49	30.3	3.98	11.19	41.82	30.63	0.33
Trial 2								
Before				During				
X (m)	Bottom (cm)	Top Water (cm)	H (cm)	X (m)	Bottom (cm)	Top Water (cm)	H (cm)	Δ (cm)
1	11.15	41.1	29.95	1	11.15	41.11	29.96	0.01
2	11.02	41.08	30.06	2	11.02	41.02	30	-0.06
3	11.14	41.28	30.14	3	11.14	41.25	30.11	-0.03
3.98	11.19	41.53	30.34	3.98	11.19	41.92	30.73	0.39
Q = 142 L/s								
Trial 1								
Before				During				
X (m)	Bottom (cm)	Top Water (cm)	H (cm)	X (m)	Bottom (cm)	Top Water (cm)	H (cm)	Δ (cm)
1	11.15	41.16	30.01	1	11.15	41.09	29.94	-0.07
2	11.02	41.14	30.12	2	11.02	41.06	30.04	-0.08
3	11.14	41.38	30.24	3	11.14	41.23	30.09	-0.15
3.98	11.19	41.61	30.42	3.98	11.19	43.18	31.99	1.57
Trial 2								
Before				During				
X (m)	Bottom (cm)	Top Water (cm)	H (cm)	X (m)	Bottom (cm)	Top Water (cm)	H (cm)	Δ (cm)
1	11.15	41.19	30.04	1	11.15	41.09	29.94	-0.1
2	11.02	41.18	30.16	2	11.02	41.04	30.02	-0.14
3	11.14	41.42	30.28	3	11.14	41.3	30.16	-0.12
3.98	11.19	41.64	30.45	3.98	11.19	43.33	32.14	1.69





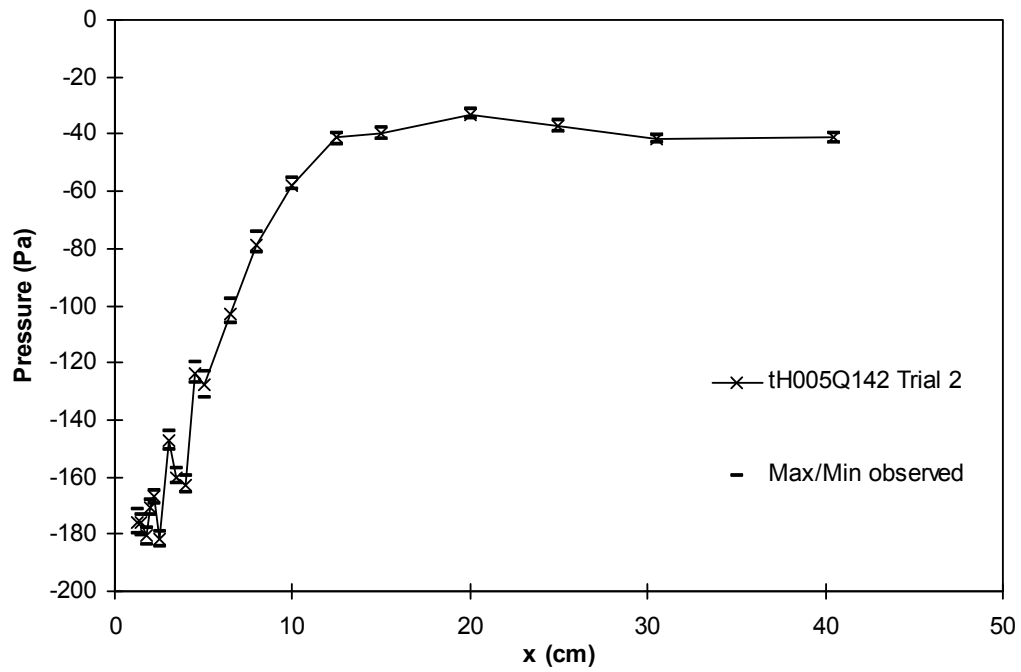
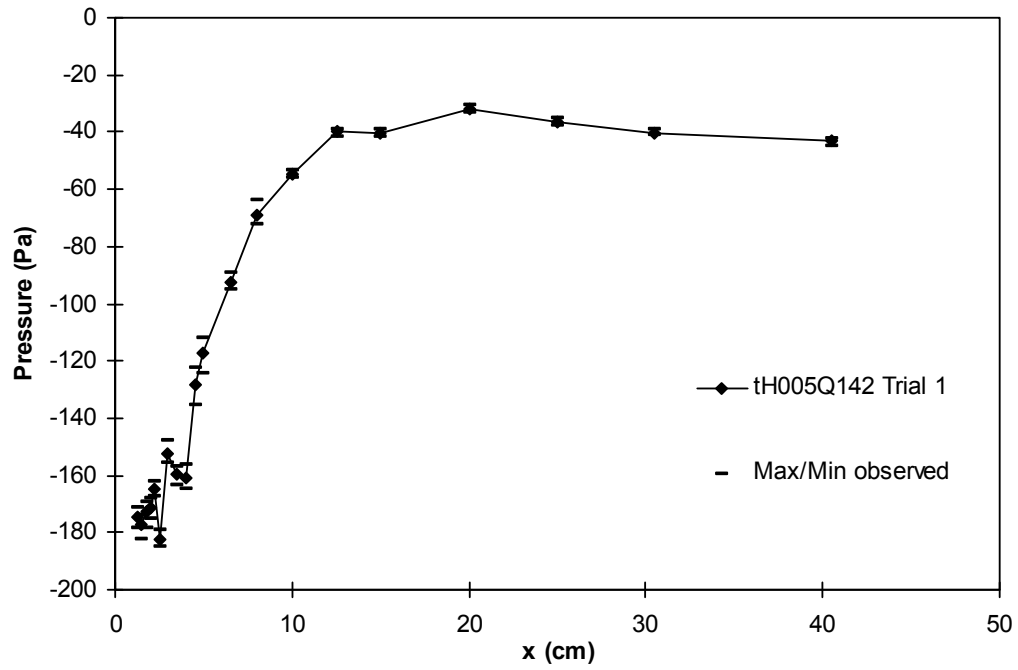
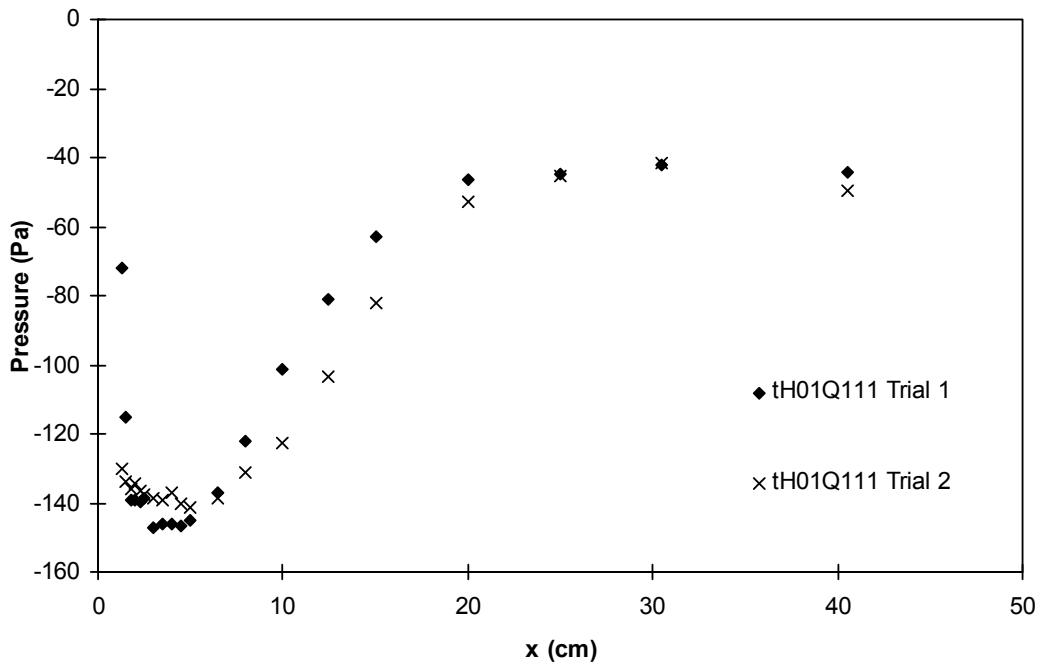
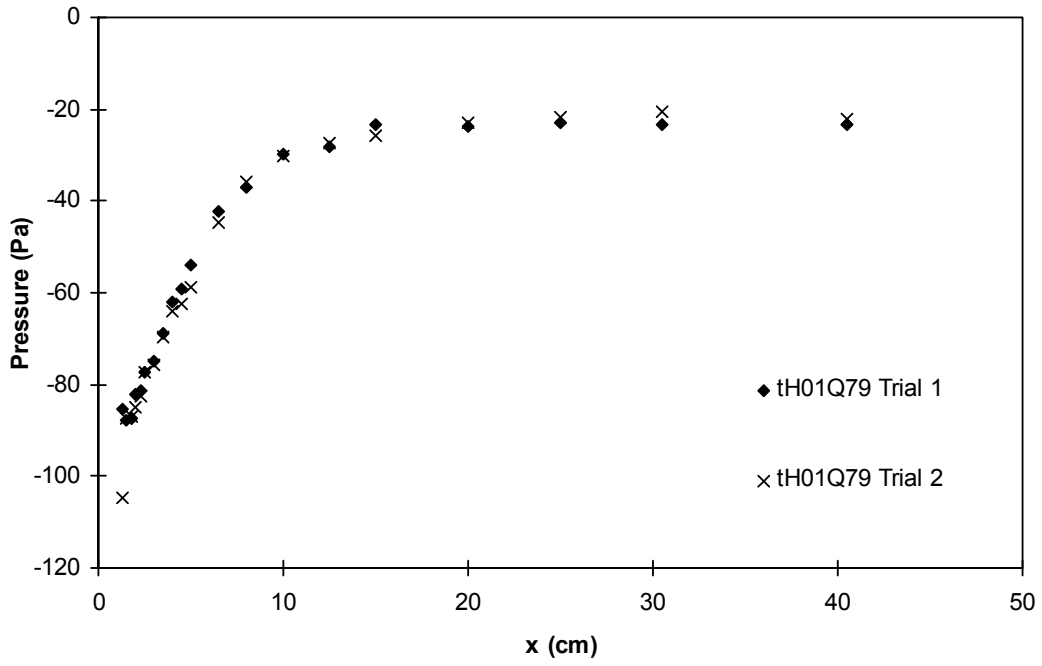


Figure C-1: Pressure measurements for $t/H = 0.05$.



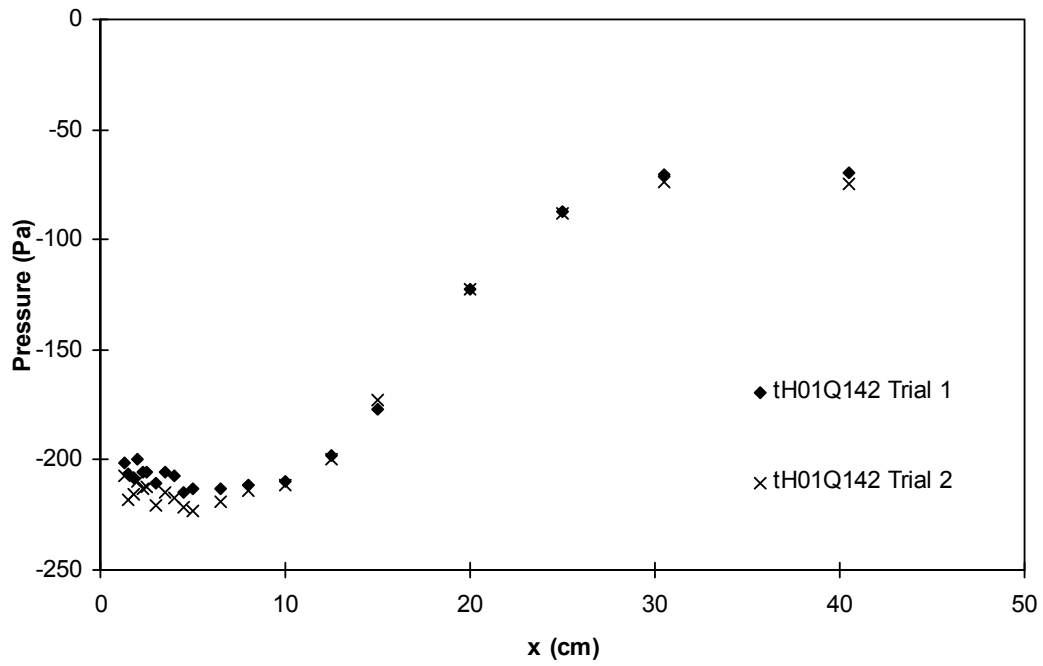
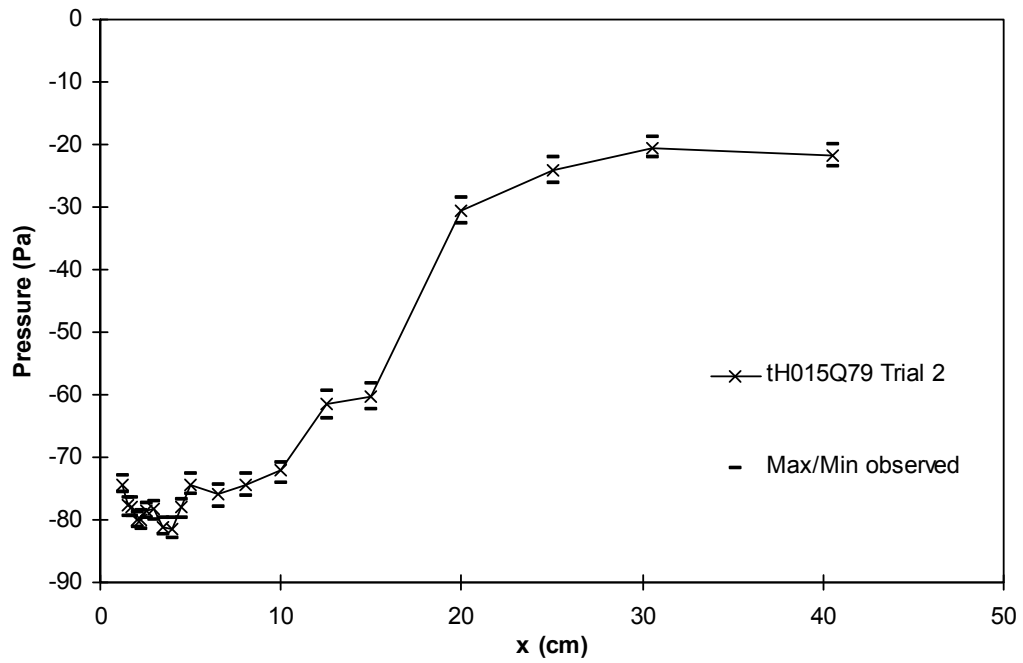
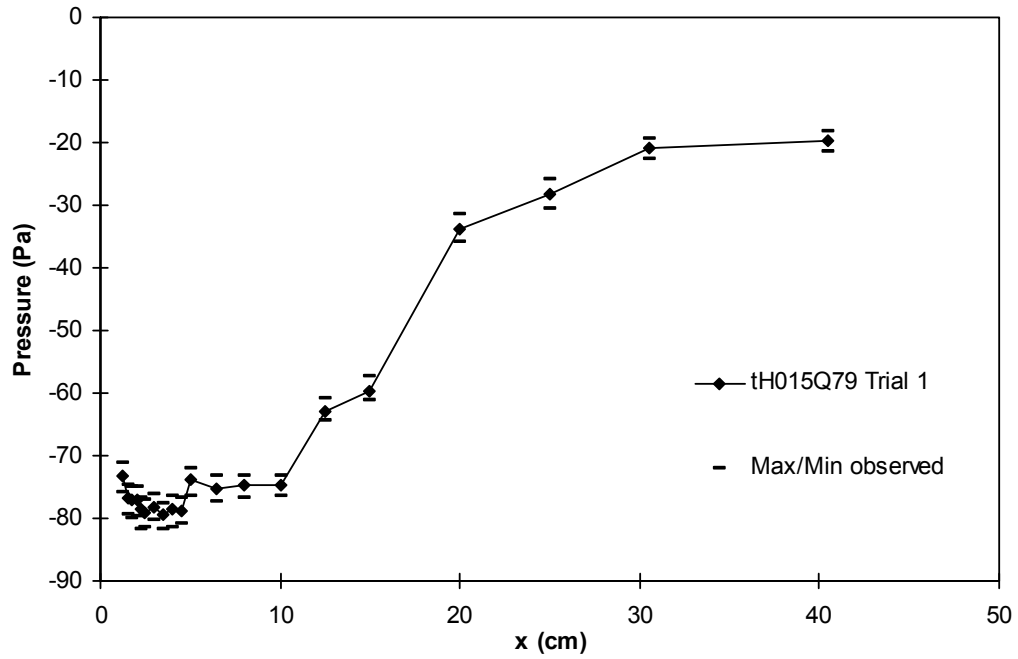
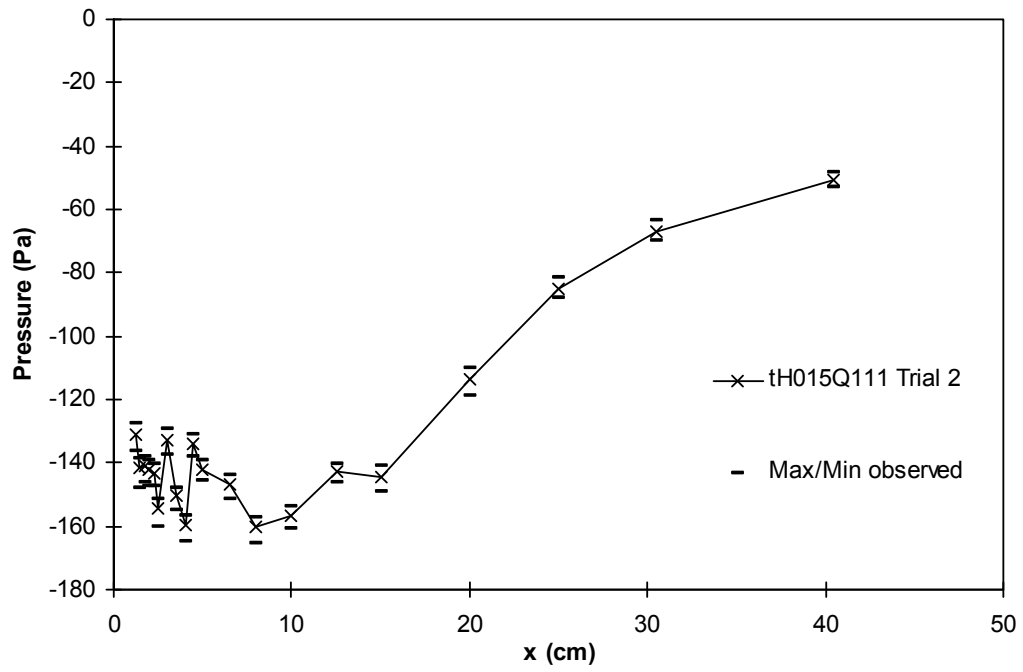
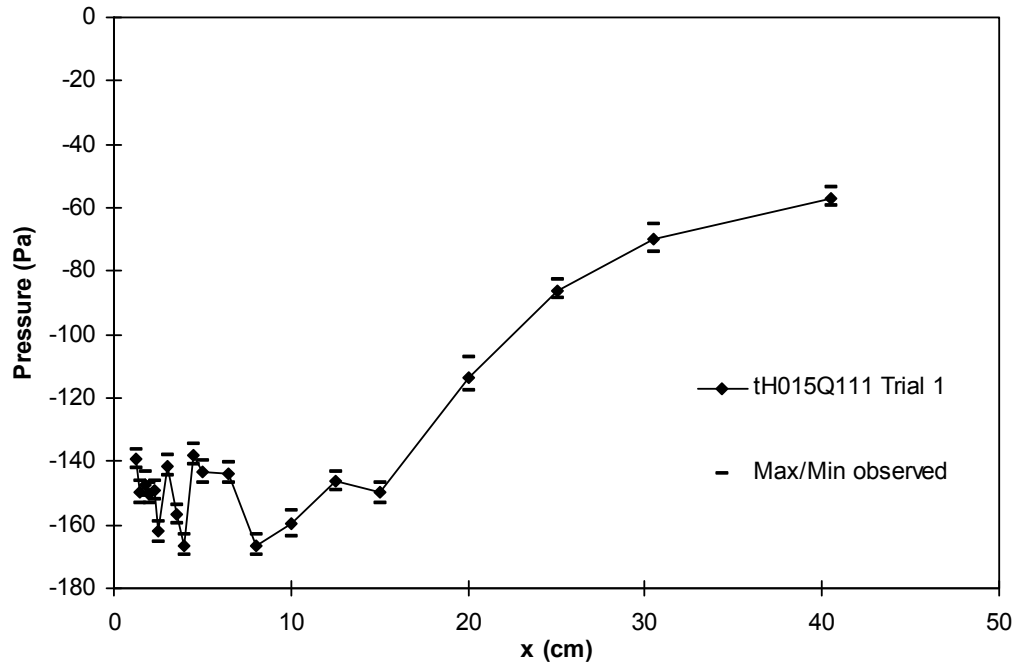


Figure C-2: Pressure measurements for $t/H = 0.1$.





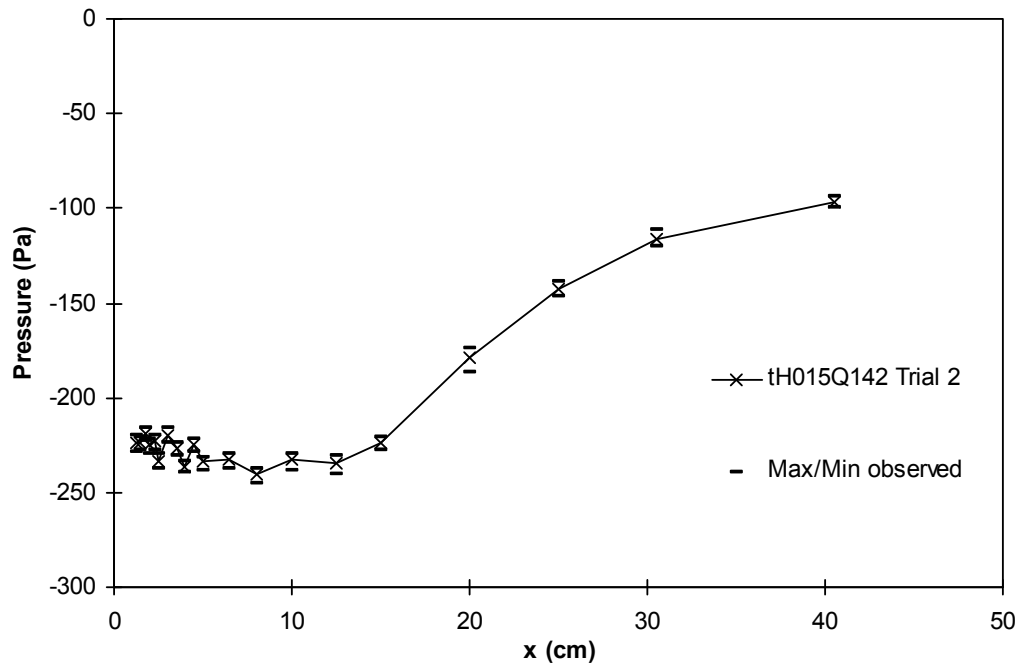
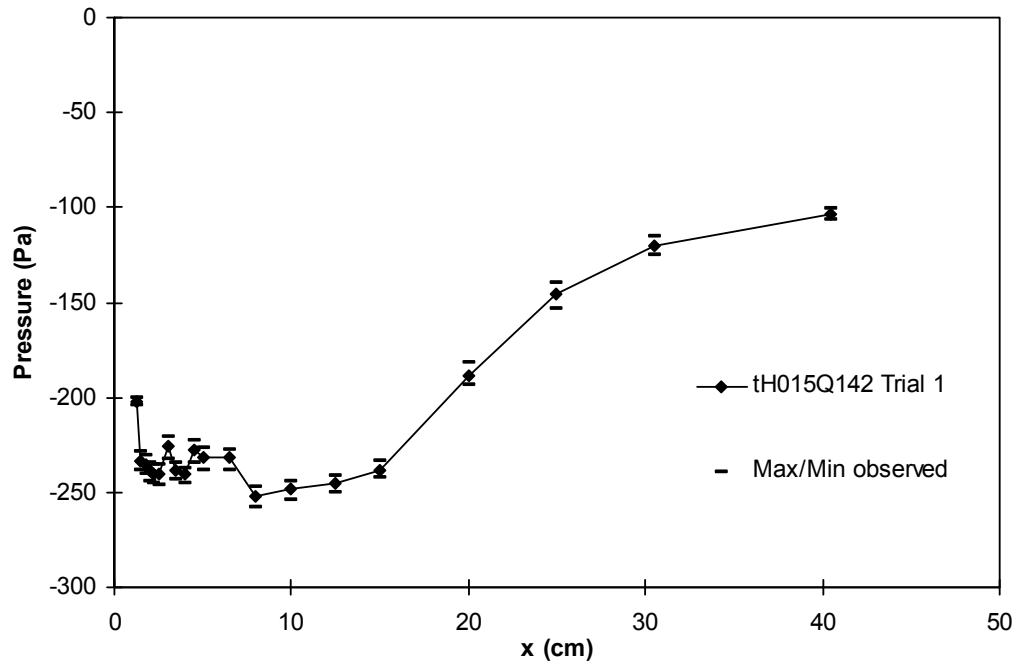
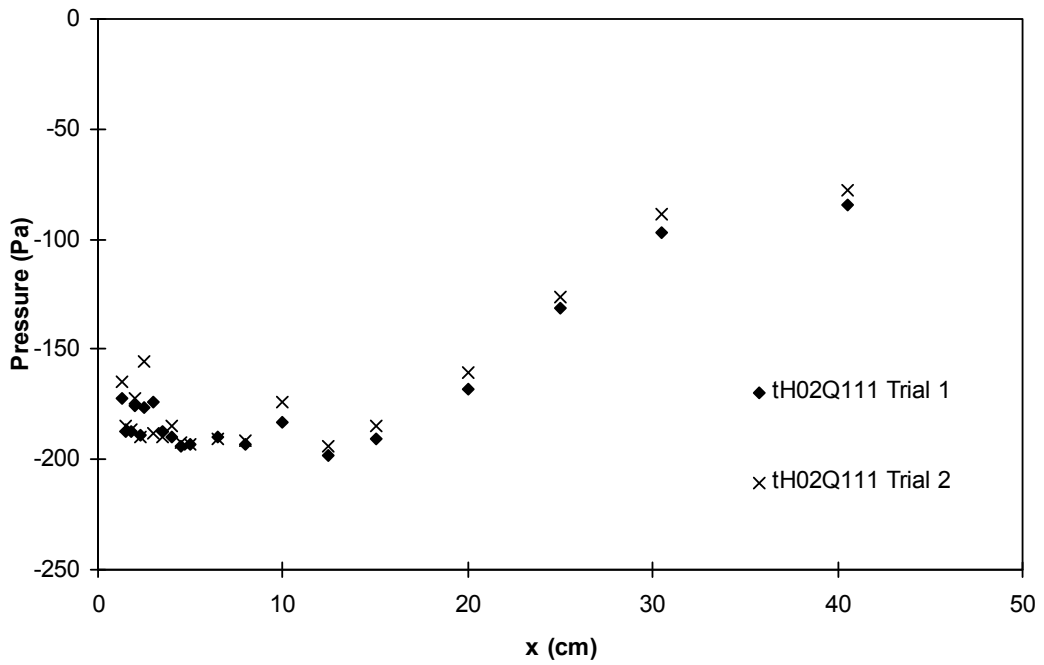
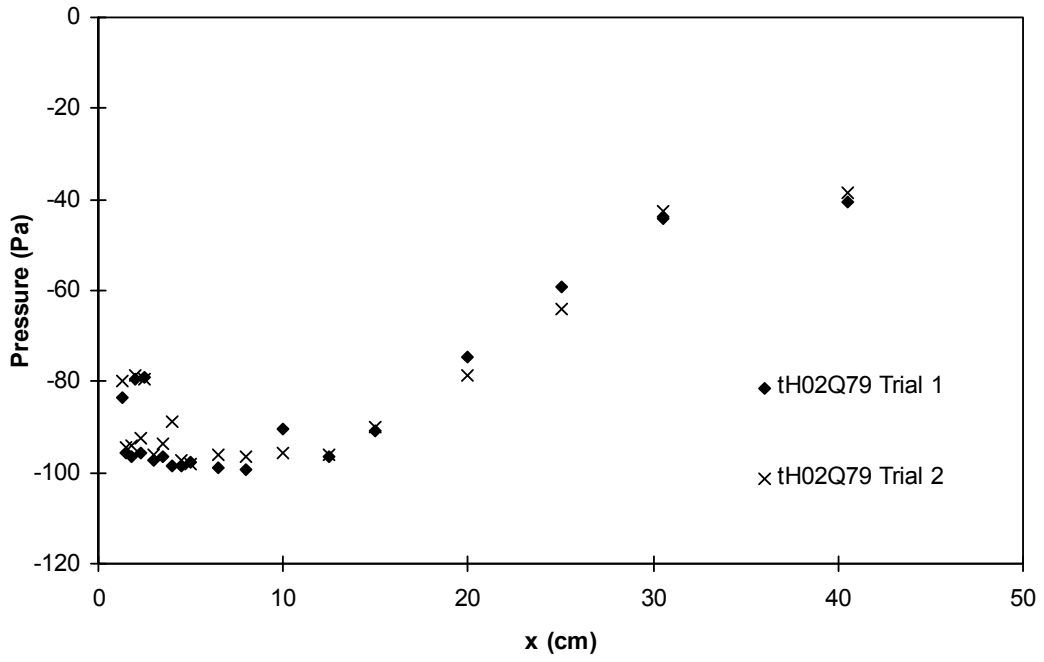


Figure C-3: Pressure measurements for $t/H = 0.15$.



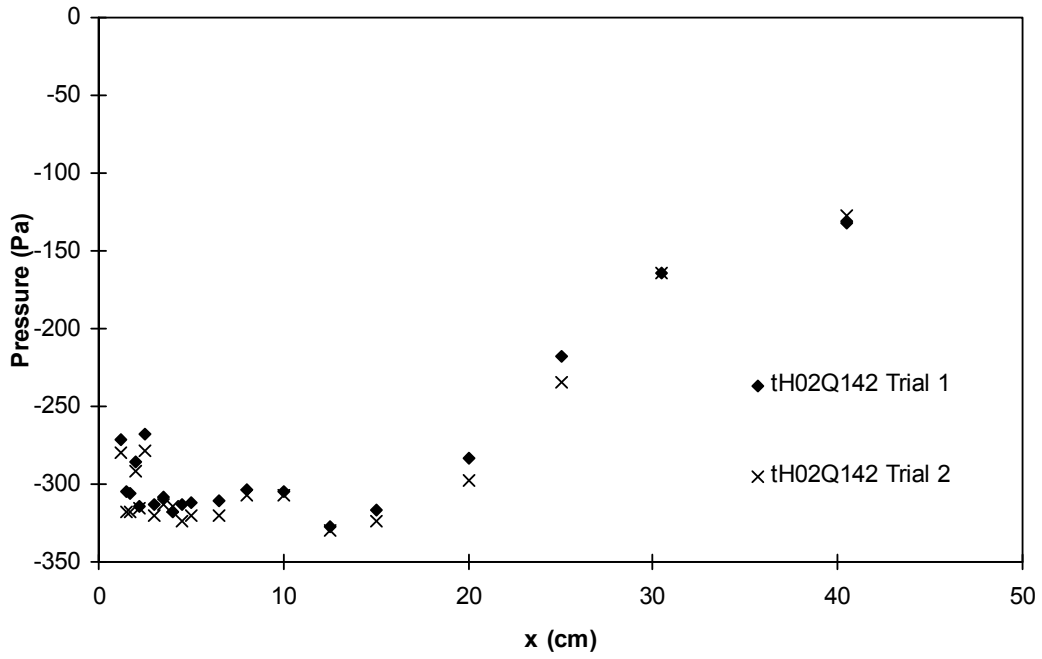
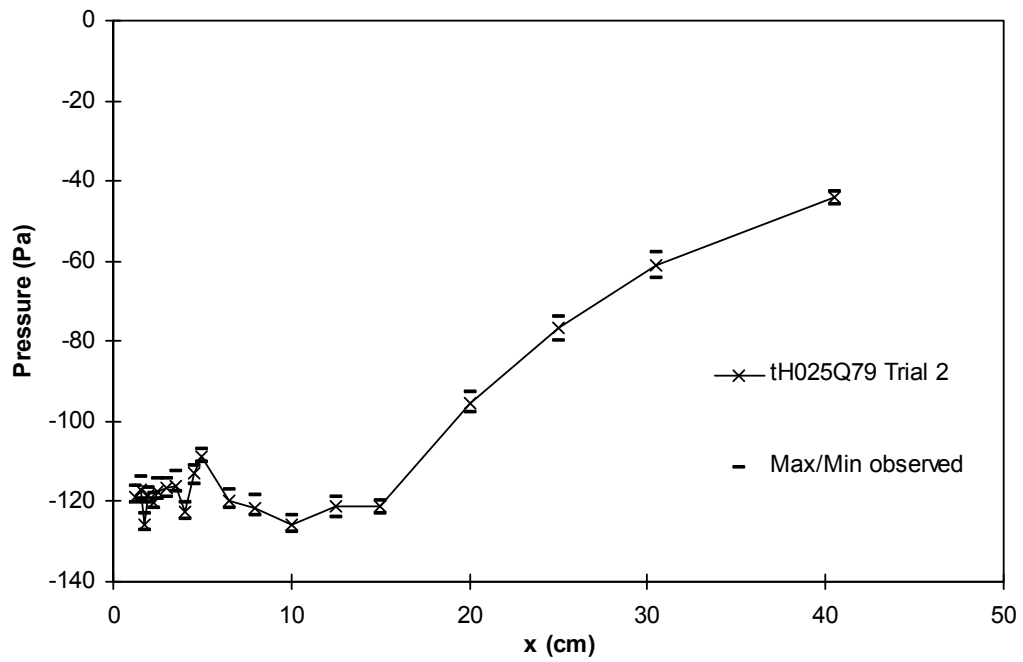
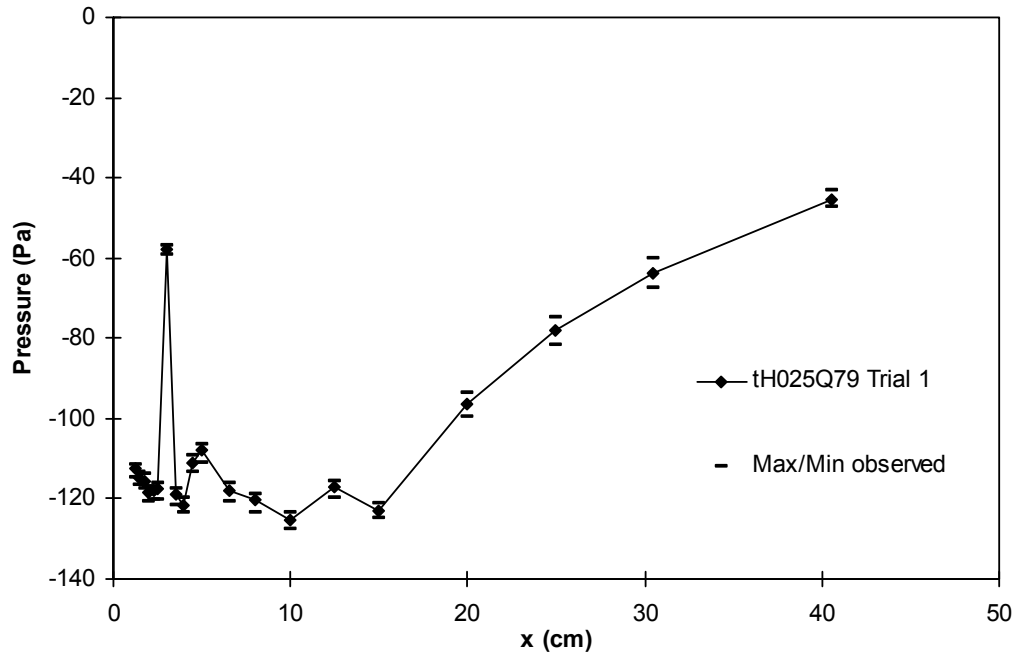
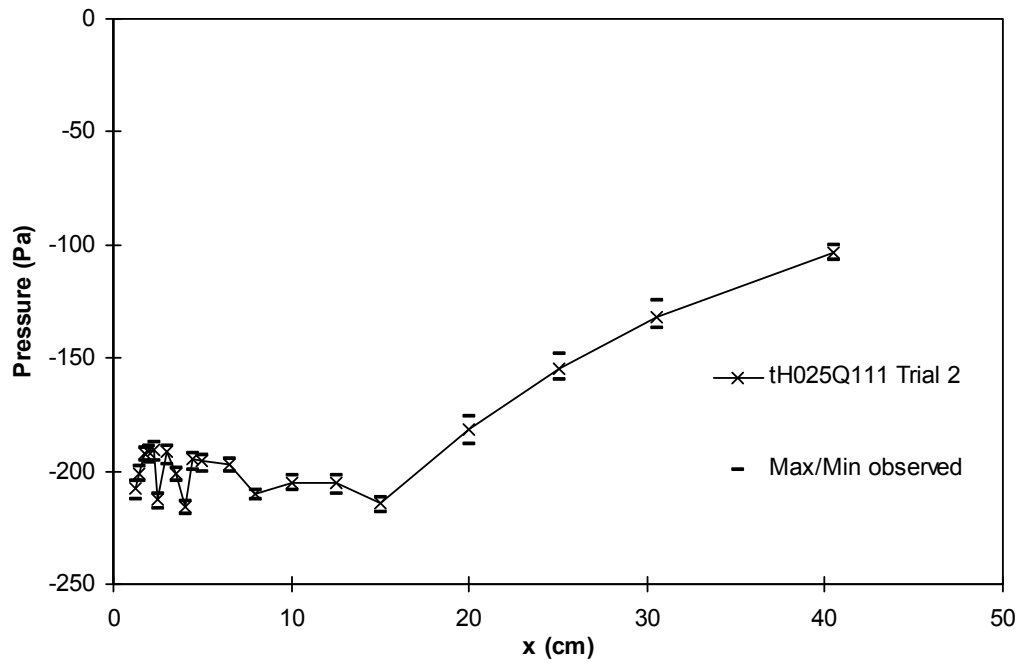
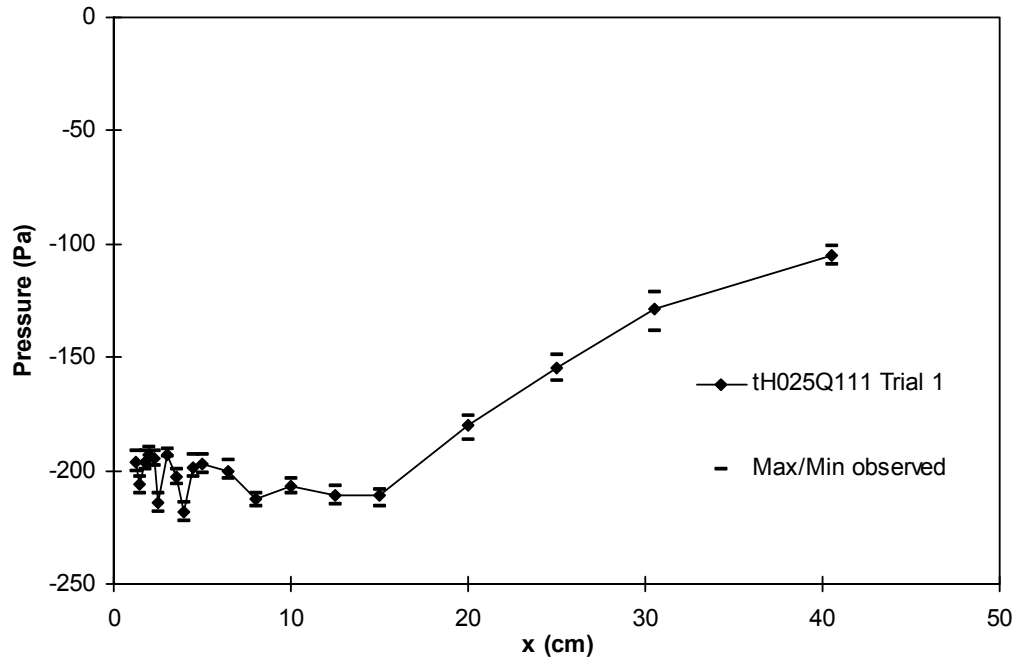


Figure C-4: Pressure measurements for $t/H = 0.2$.





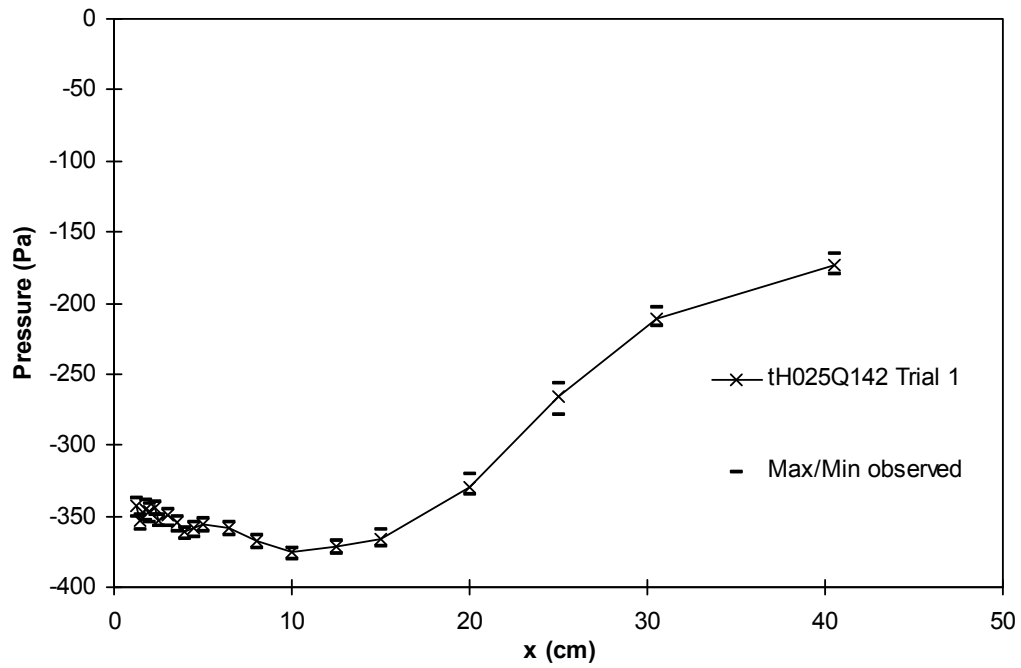
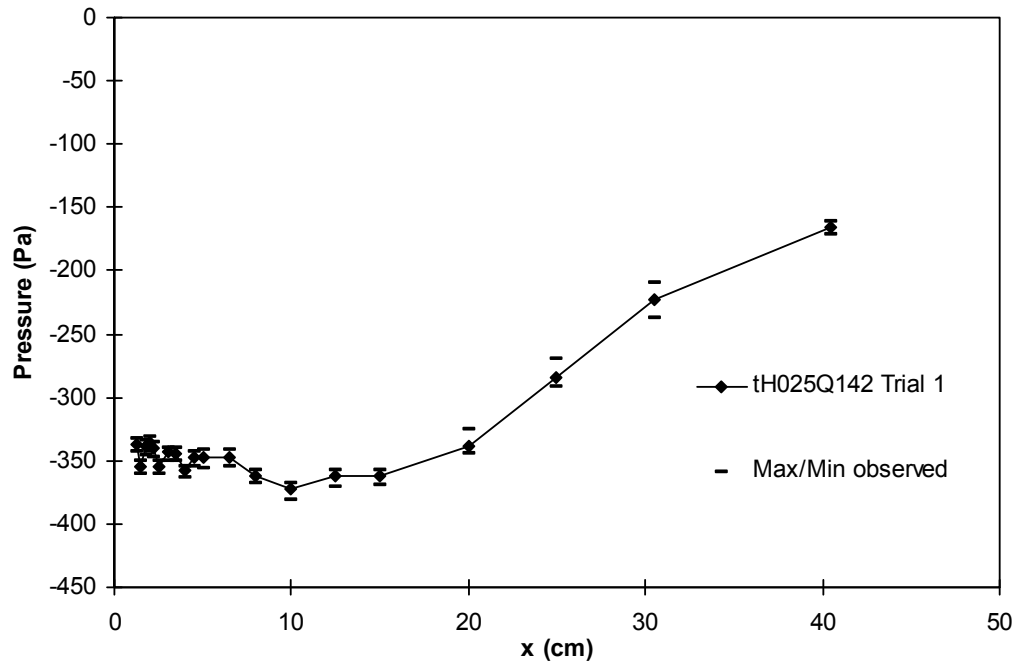
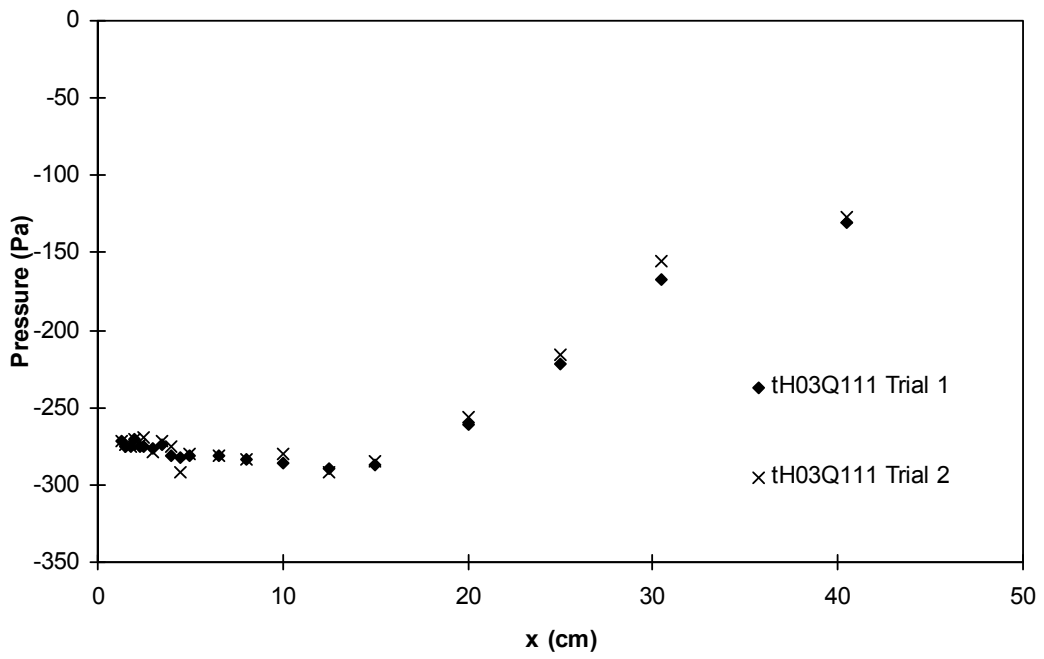
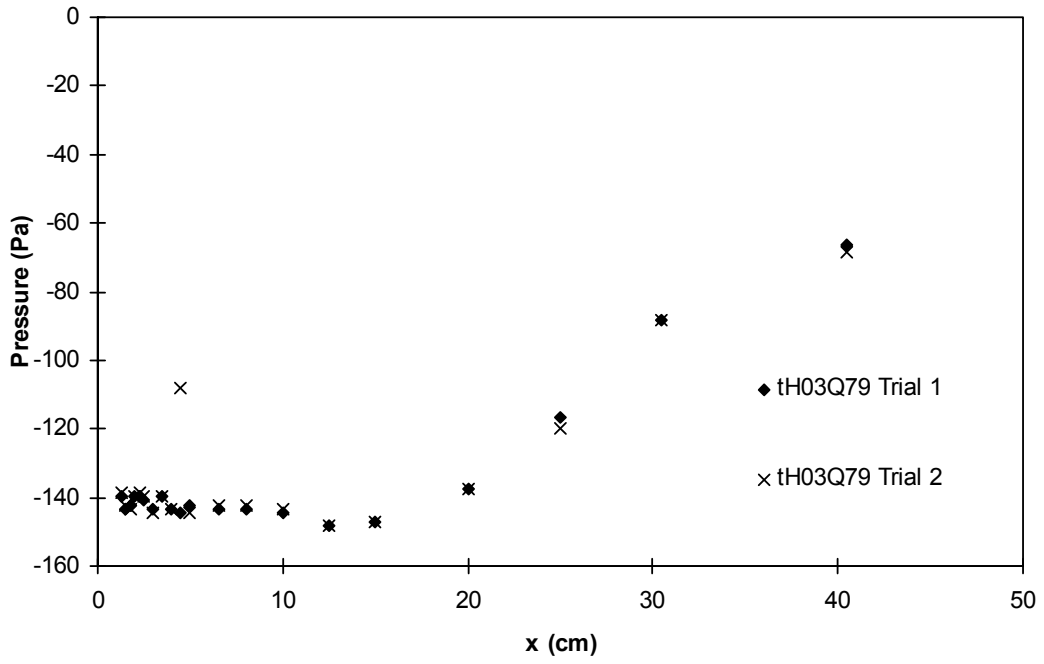


Figure C-5: Pressure measurements for $t/H = 0.25$.



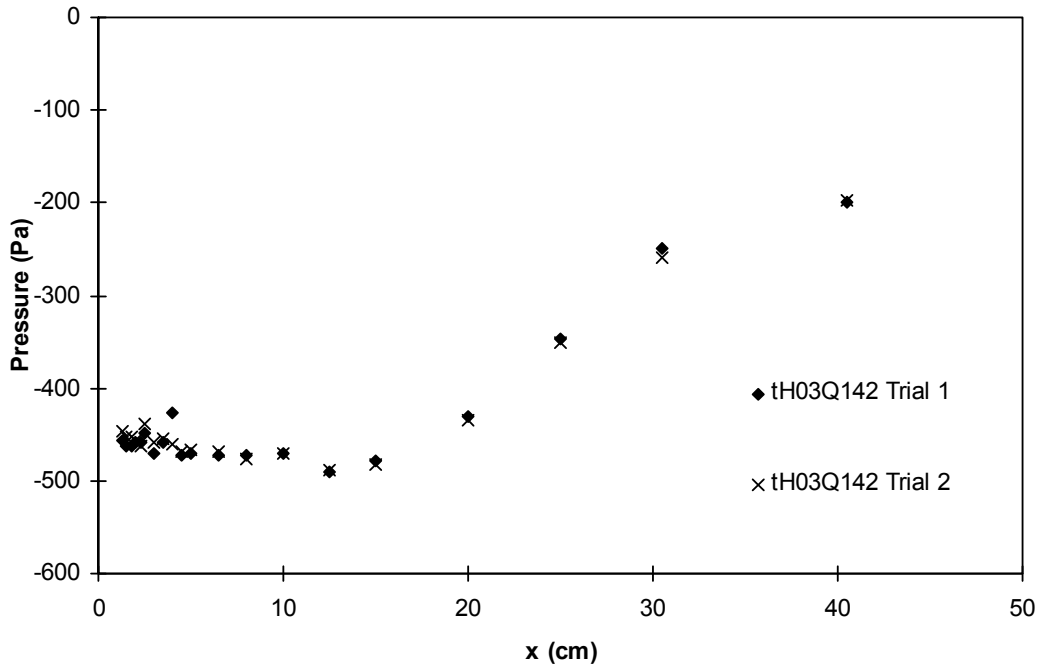
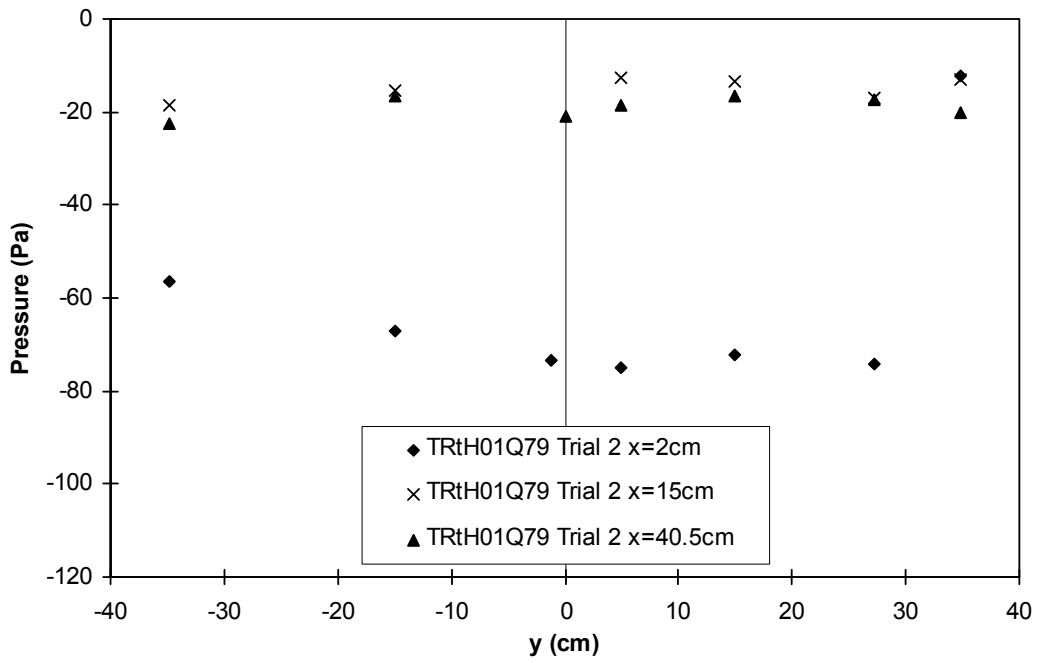
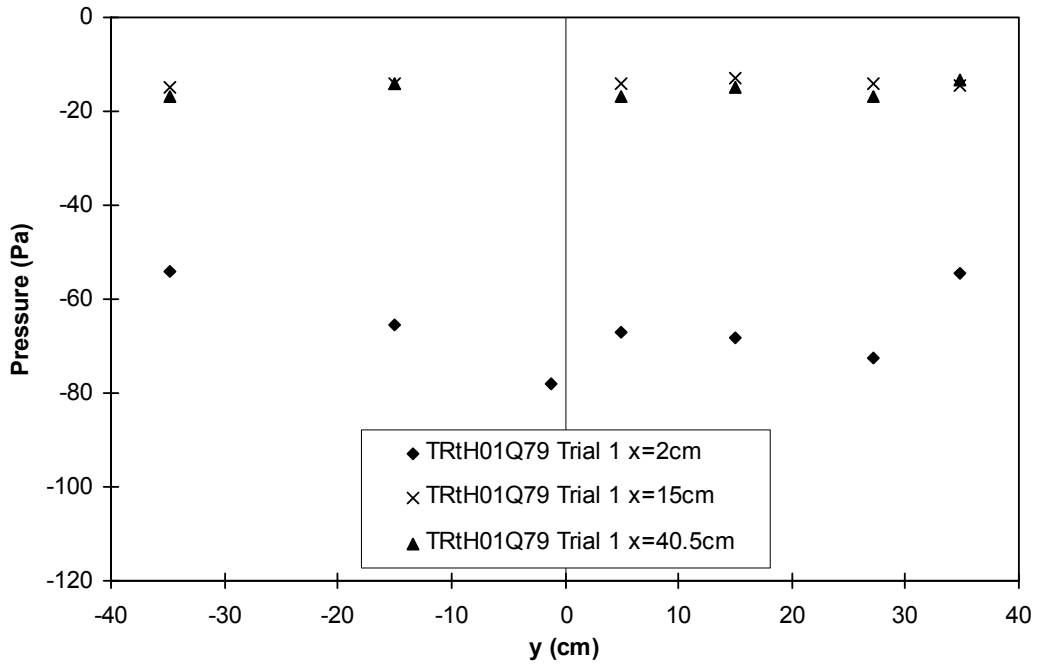


Figure C-6: Pressure measurements for $t/H = 0.3$.



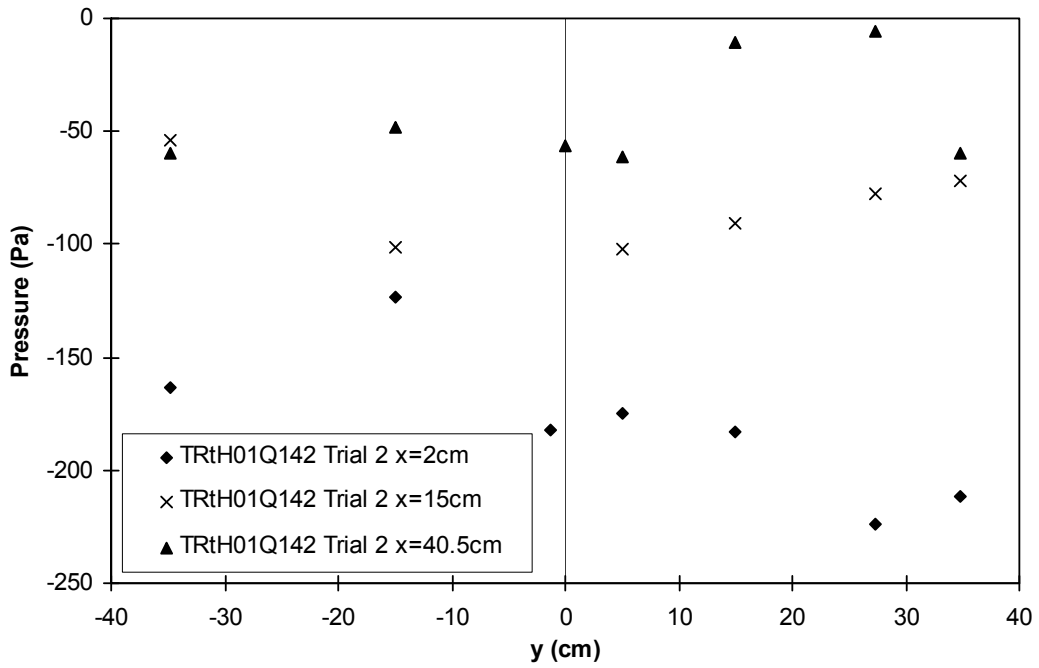
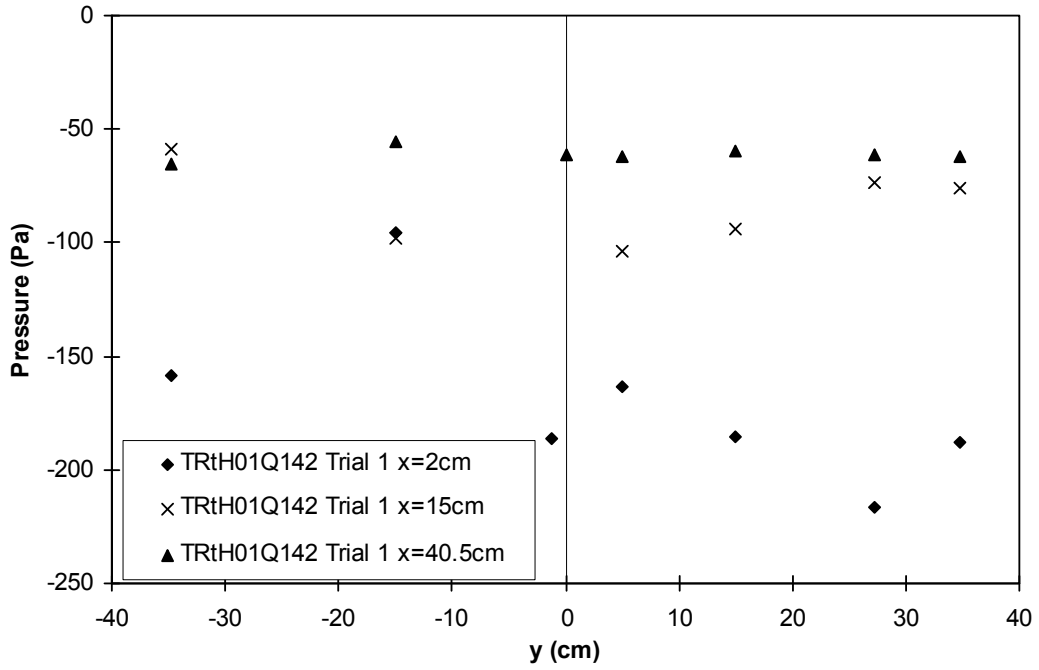
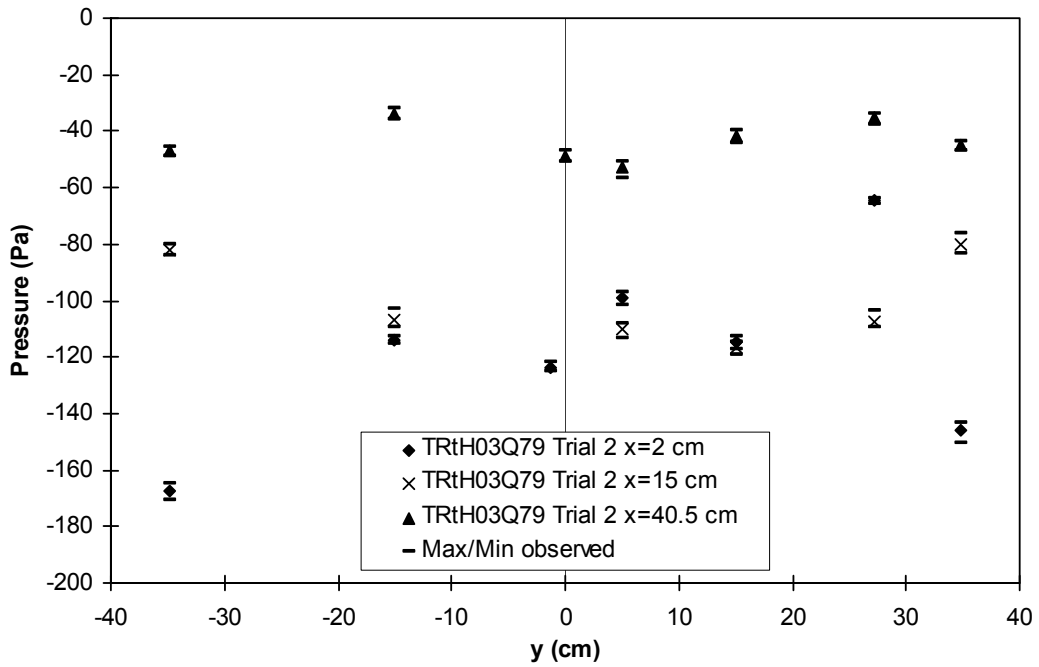
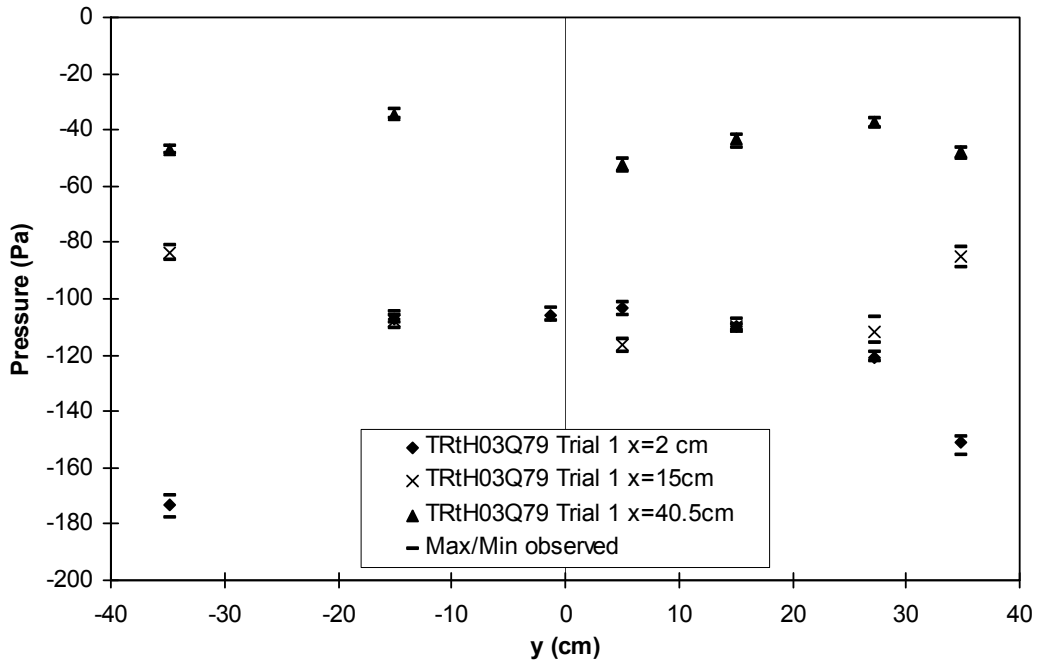


Figure C-7: Pressure measurements for transverse case $t/H = 0.1$.



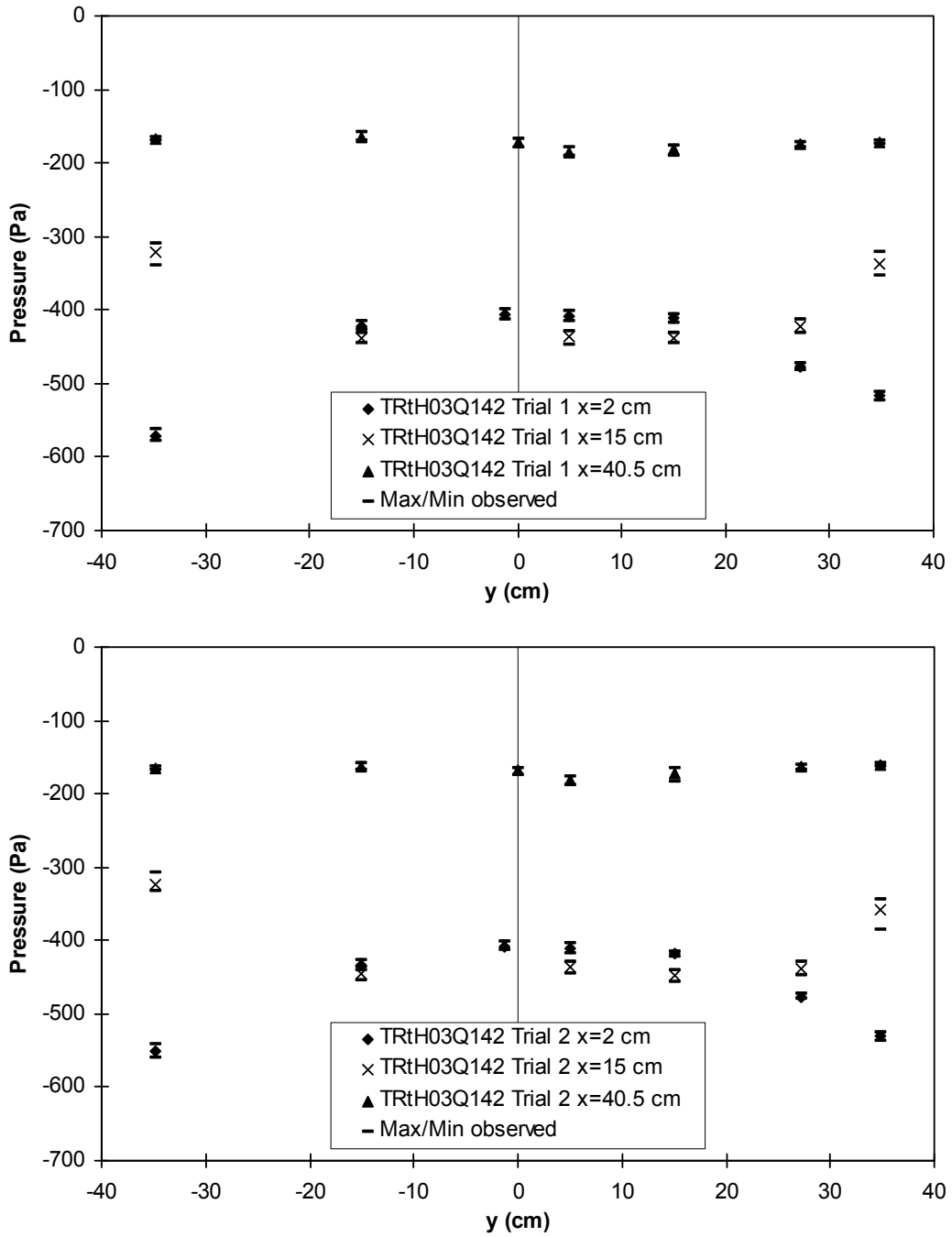
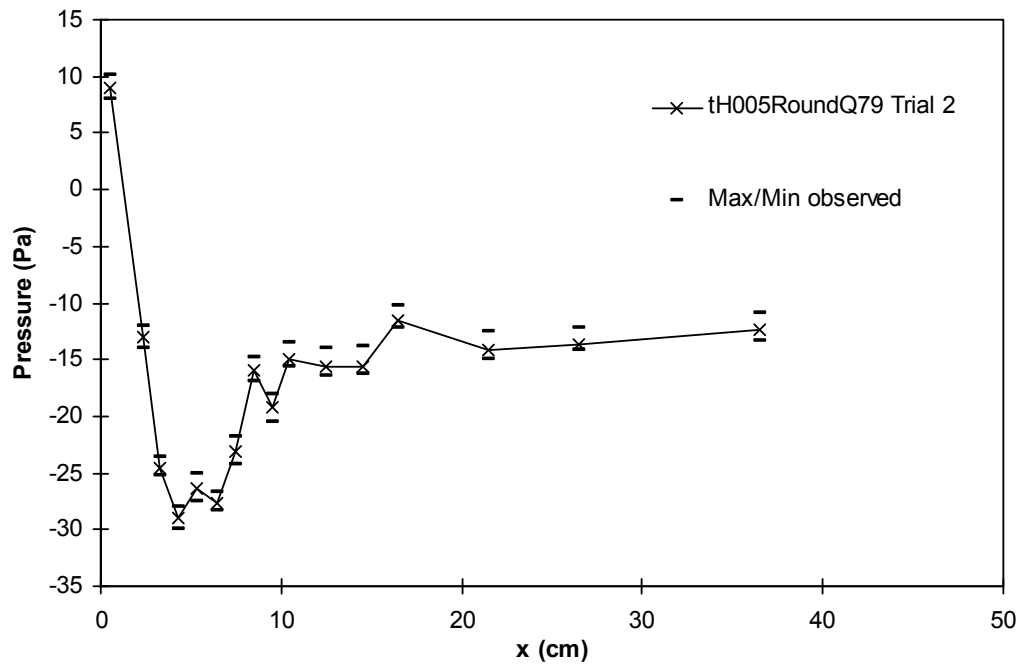
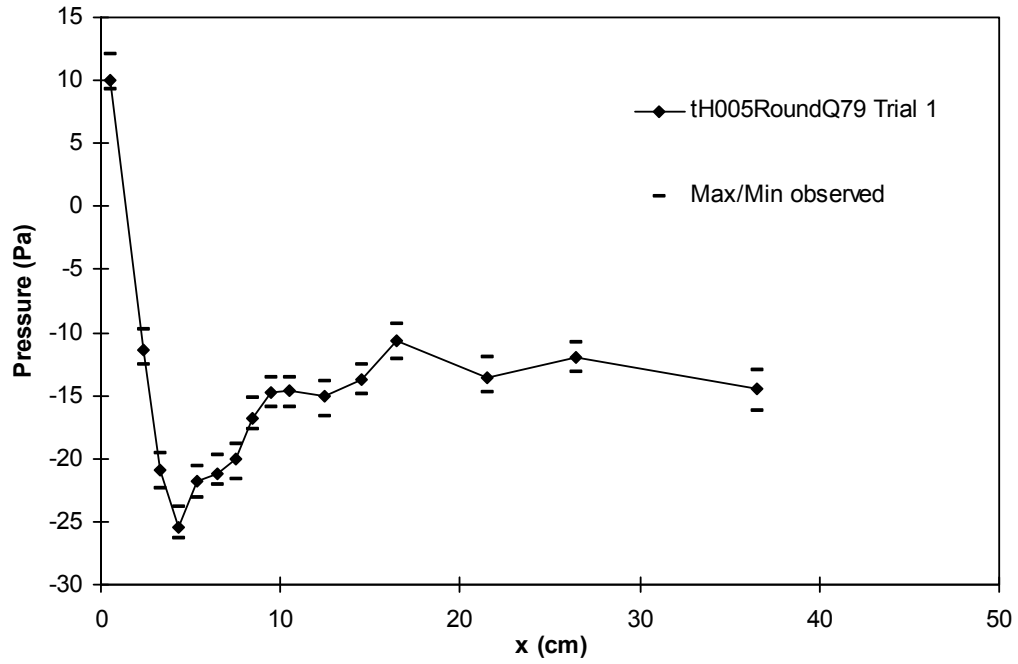
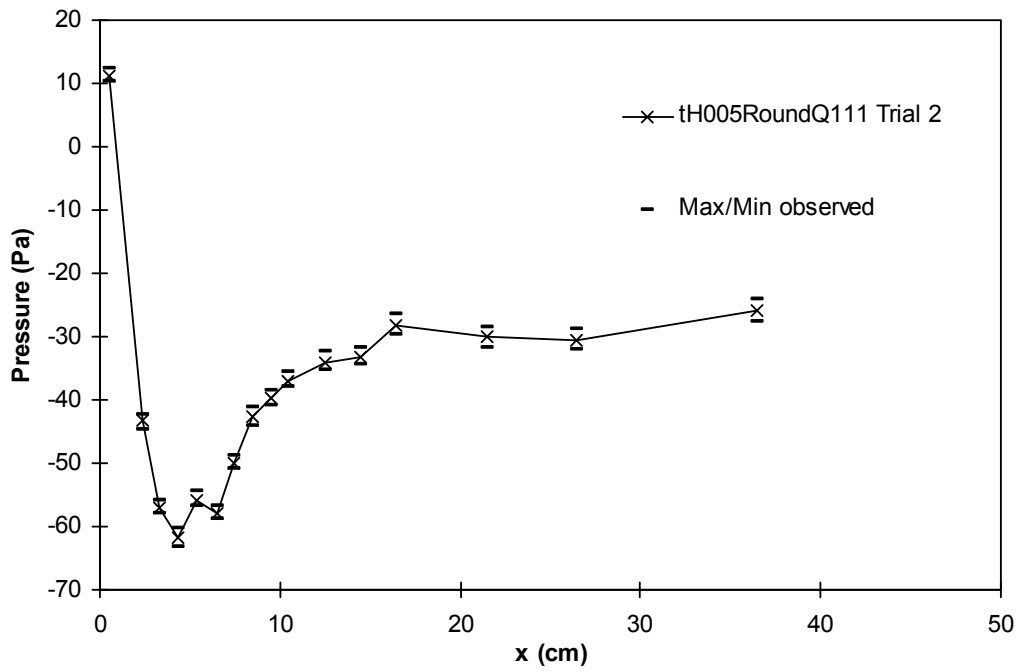
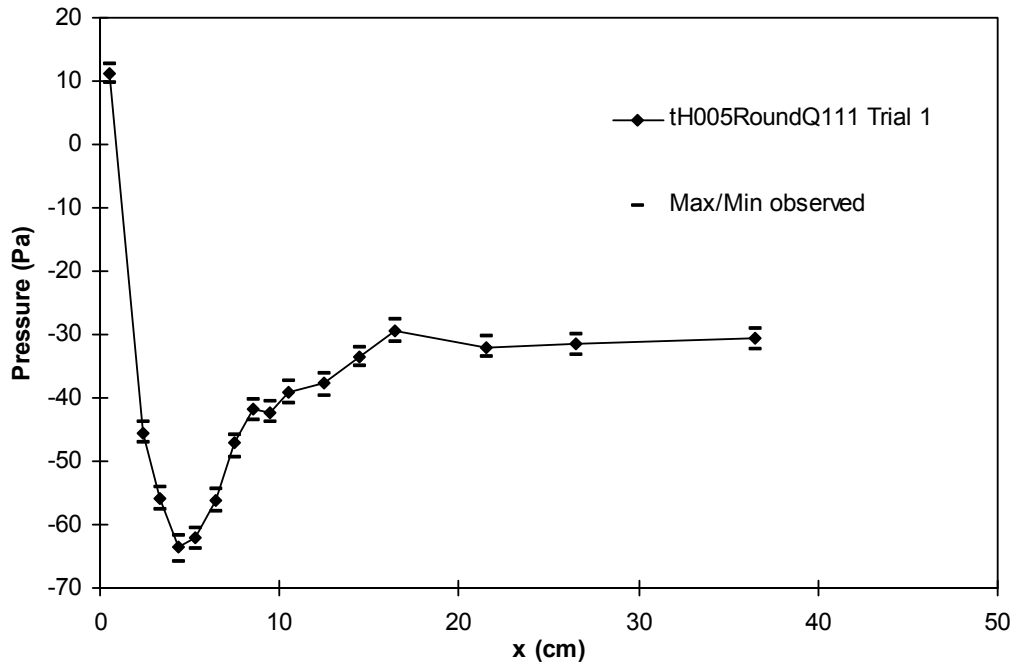


Figure C-8: Pressure measurements for transverse case $t/H = 0.3$.





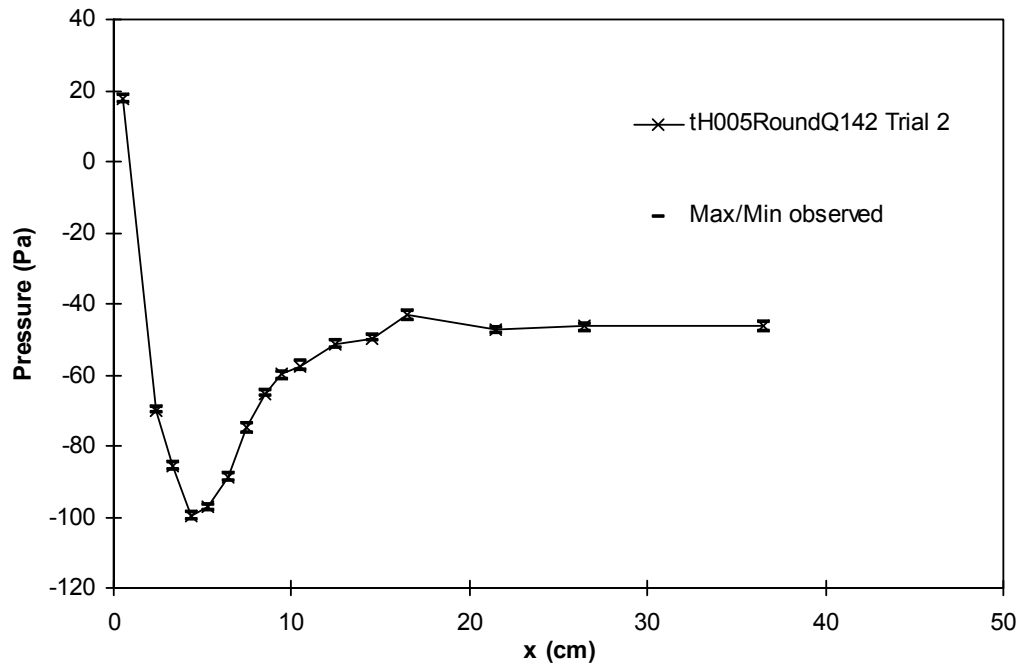
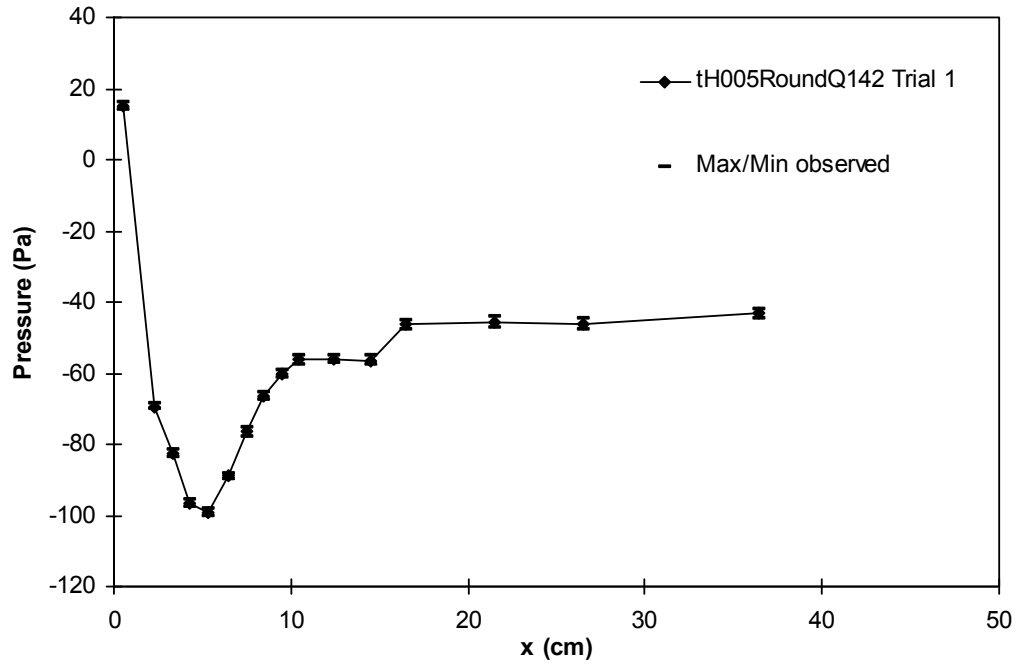
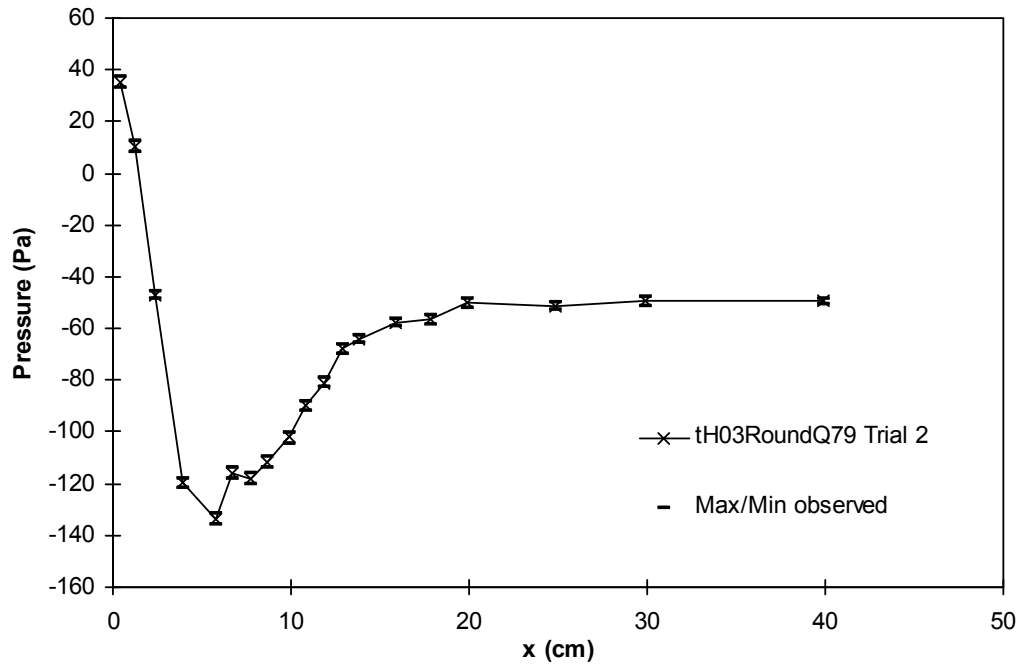
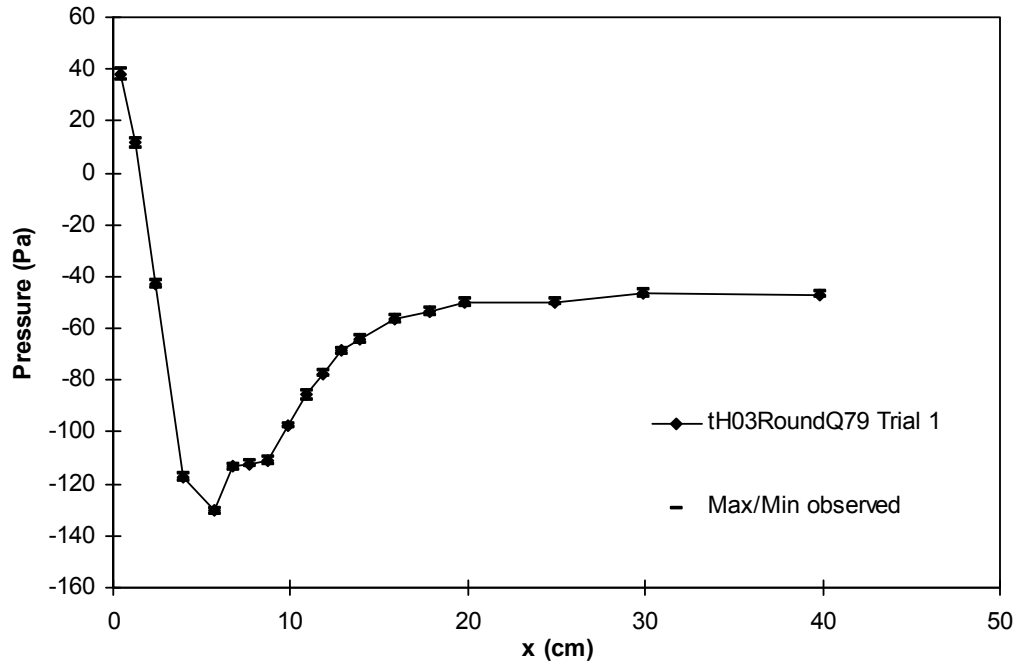
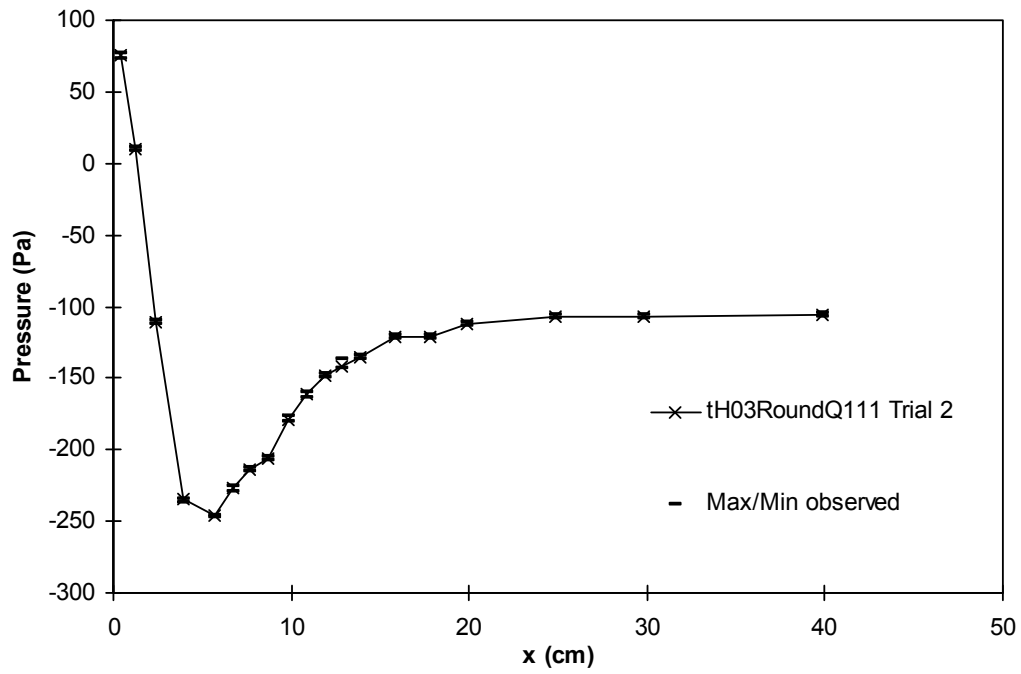
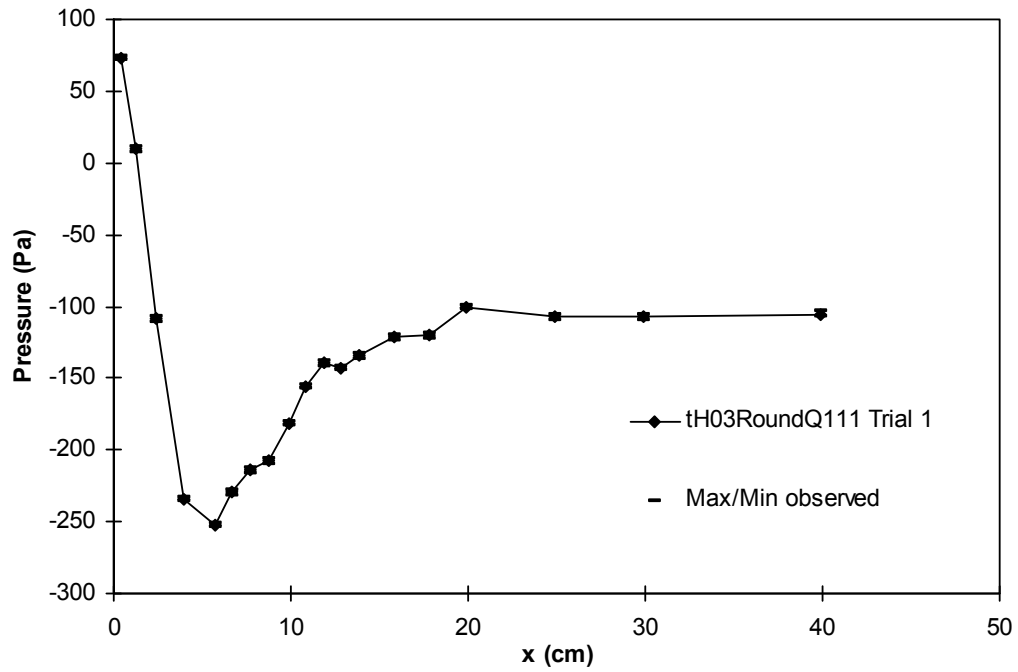


Figure C-9: Pressure measurements for rounded block $t/H = 0.05$.





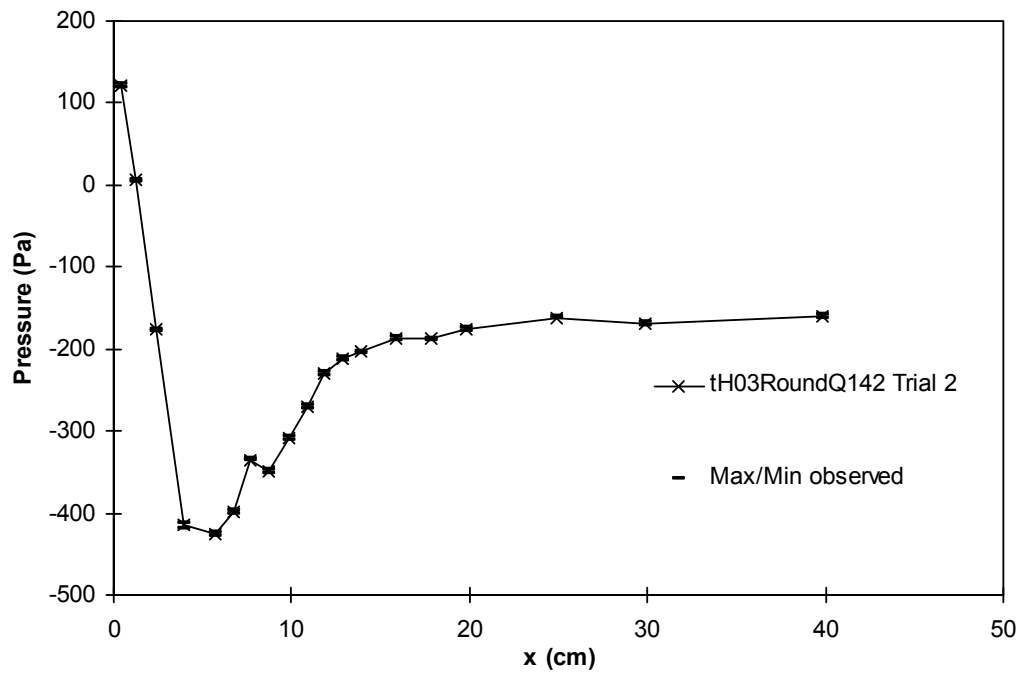
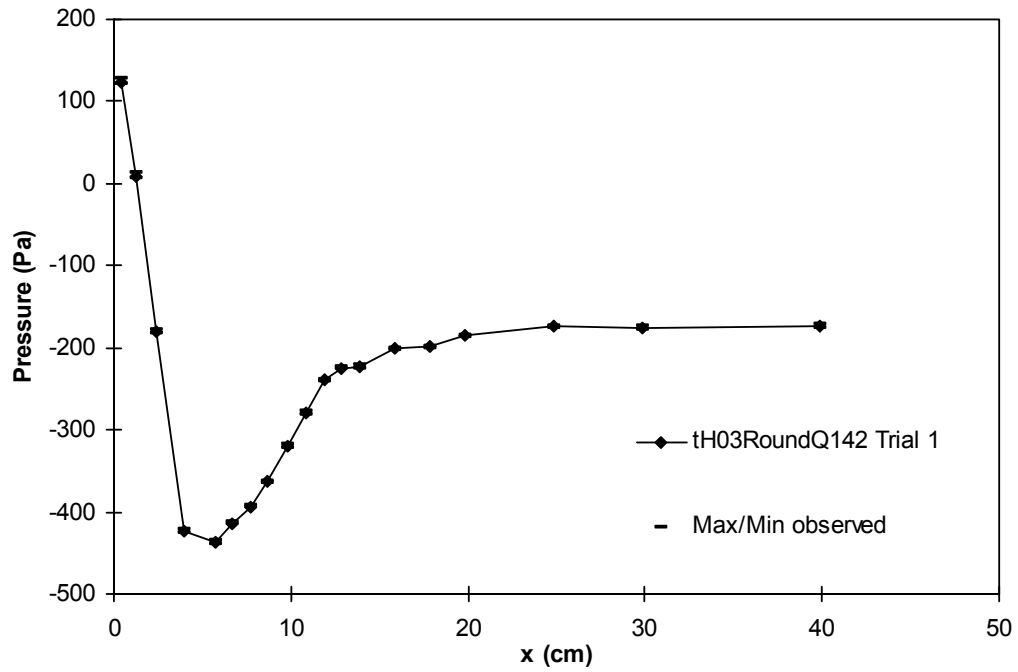
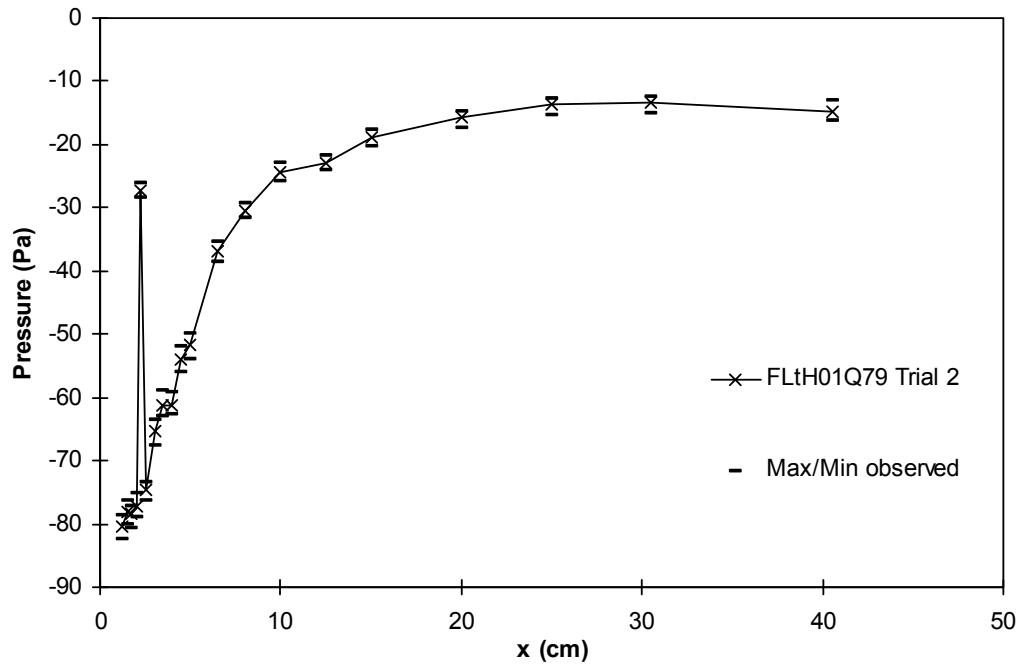
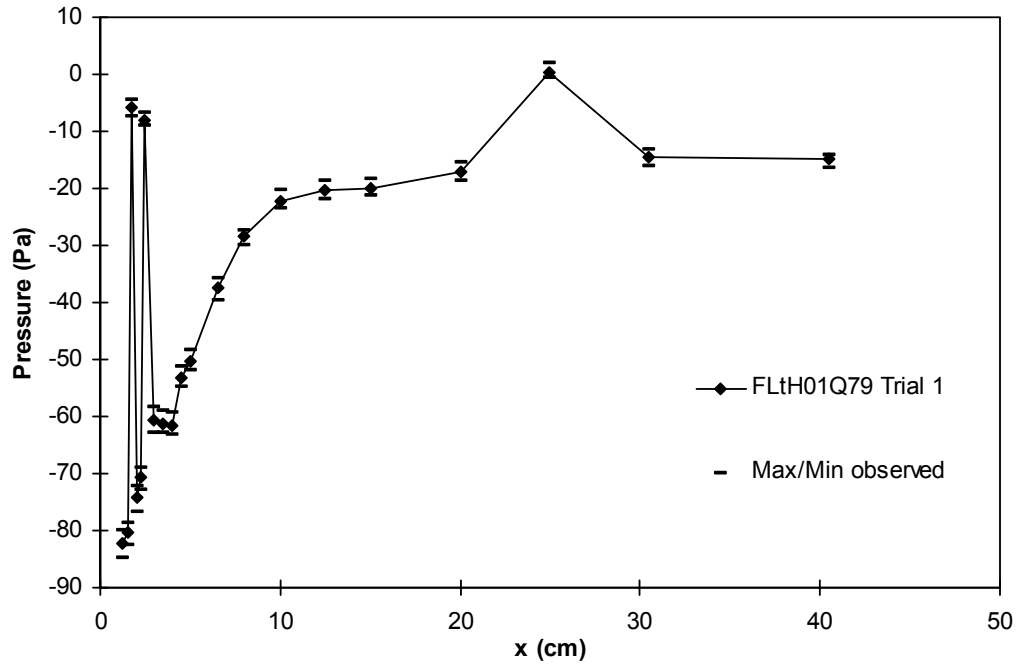


Figure C-10: Pressure measurements for rounded block $t/H = 0.3$.



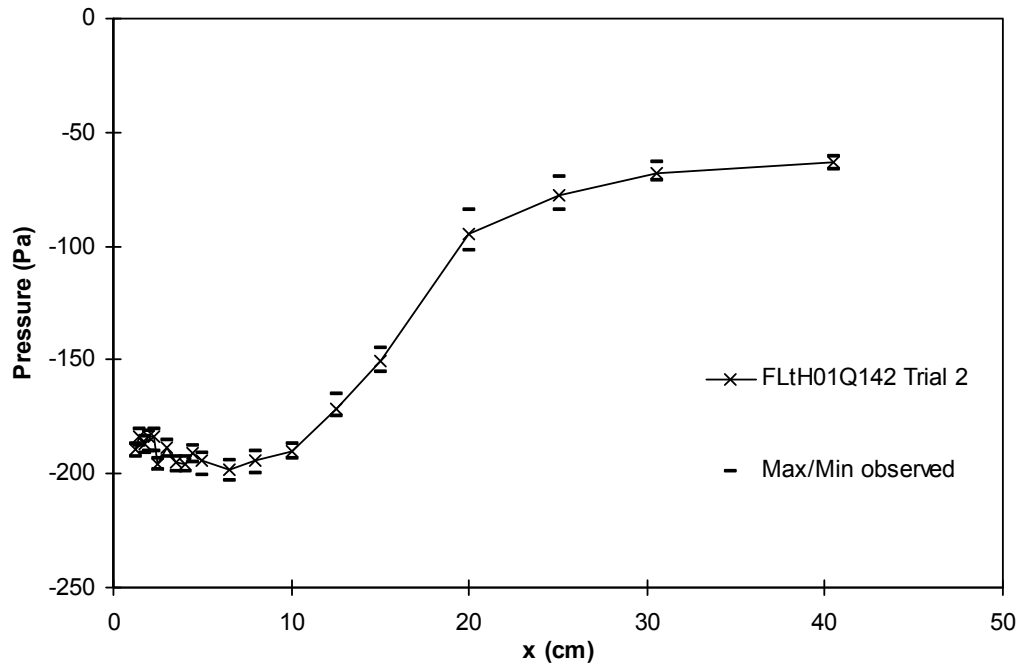
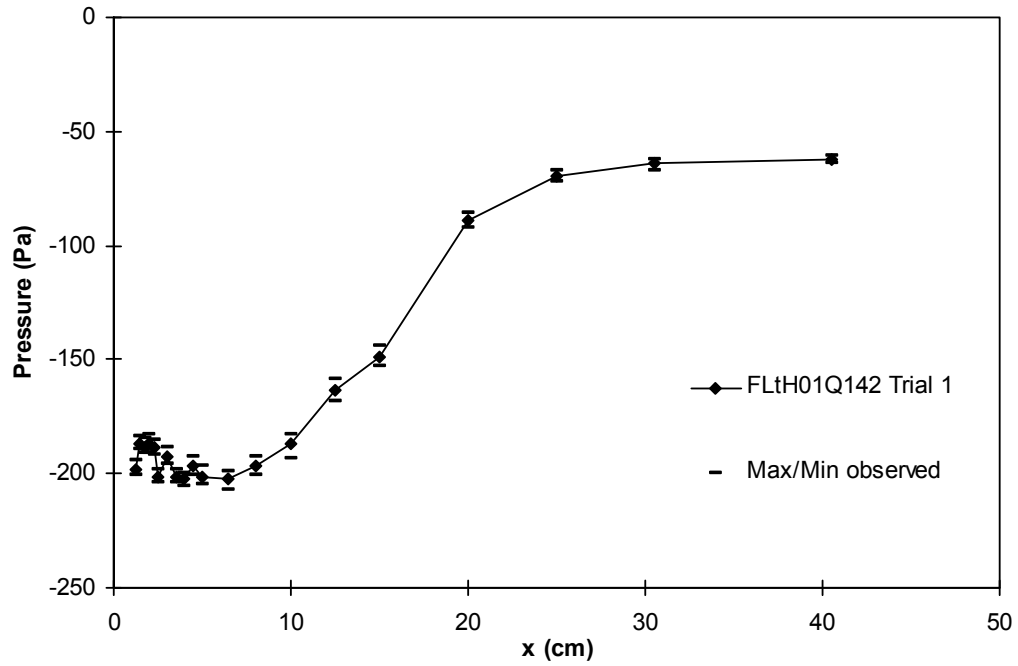
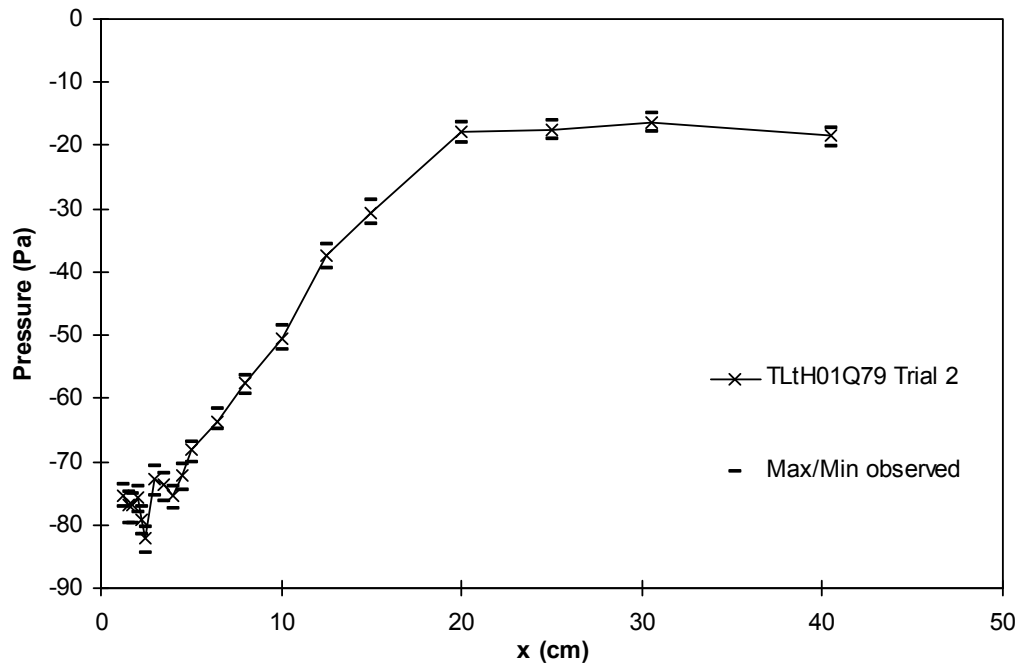
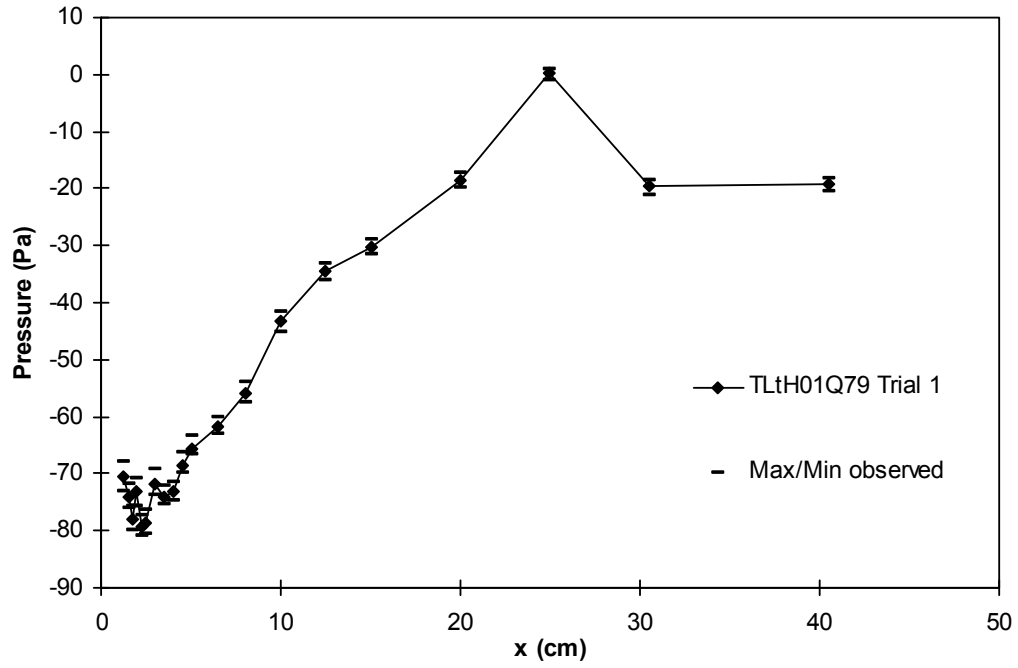


Figure C-11: Pressure measurements for flat block case $t/H = 0.1$.



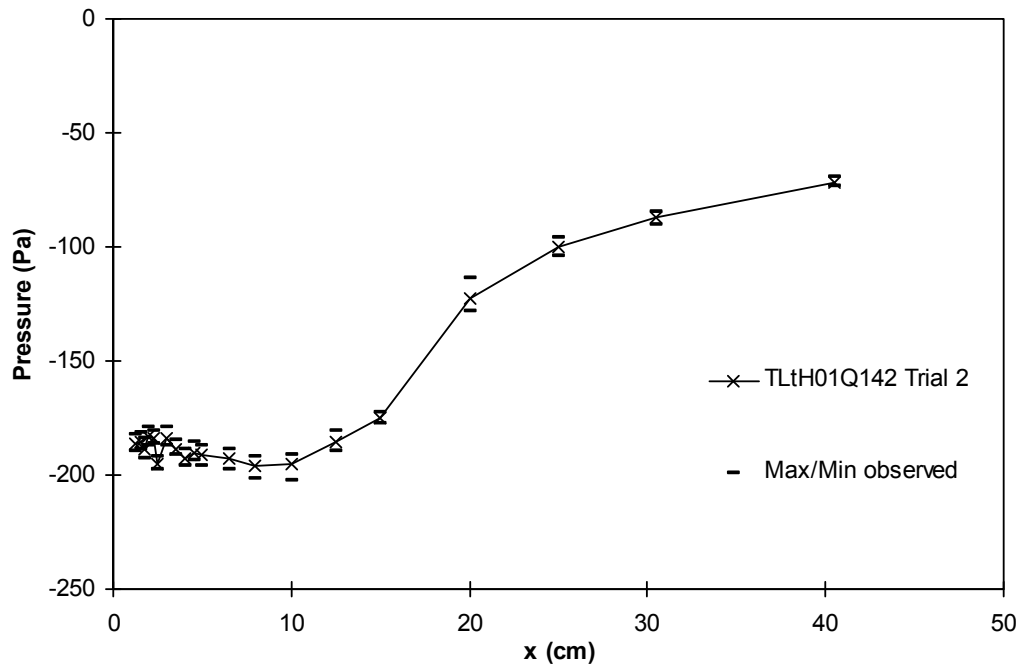
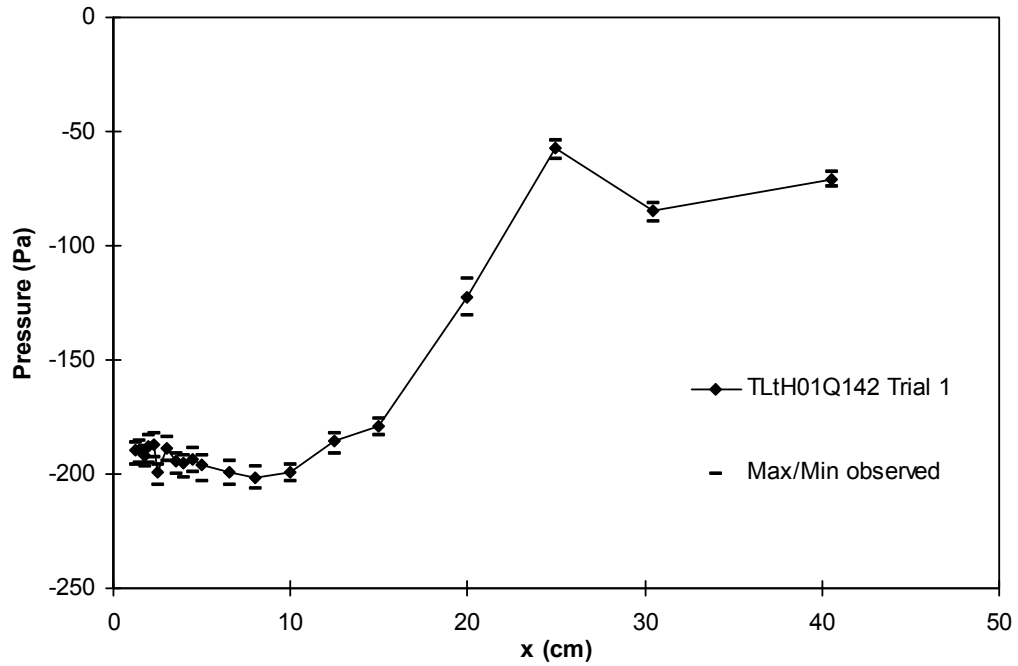


Figure C-12: Pressure measurements for tilted block case $t/H = 0.1$.